

**ELECTROMAGNETIC WAVEFRONT MANIPULATION WITH  
MINIATURIZED-ELEMENT FREQUENCY SELECTIVE SURFACES**

by

Seyed Mohamad Amin Momeni Hasan Abadi

A dissertation submitted in partial fulfillment of  
the requirements for the degree of

Doctor of Philosophy

(Electrical and Computer Engineering)

at the

UNIVERSITY OF WISCONSIN–MADISON

2016

Date of final oral examination: 07/25/2016

The dissertation is approved by the following members of the Final Oral Committee:

Nader Behdad, Associate Professor, Electrical and Computer Engineering

John Booske, Professor, Electrical and Computer Engineering

Susan Hagness, Professor, Electrical and Computer Engineering

Zhenqiang Ma, Professor, Electrical and Computer Engineering

Alan McMillan, Associate Scientist, Radiology

© Copyright by Seyed Mohamad Amin Momeni Hasan Abadi 2016

All Rights Reserved

*To my parents,  
Azar and Mohsen*

*To my sister,  
Hadis*

## ACKNOWLEDGMENTS

I wish to express my sincere appreciation to the following individuals, whose guidance and support made this accomplishment possible.

Foremost, I would like to thank my PhD advisor, Professor Nader Behdad, for his strong support, encouragement, and mentorship both in research and in other aspects of life over the past five years. Working with him has been an incredibly rewarding experience, and his dedication to his work will remain as an invaluable source of inspiration in my career.

I would also like to thank the members of my doctoral committee – Professor John H. Booske, Professor Susan C. Hagness, Professor Zhenqiang Ma, and Dr. Alan McMillan for their service and insightful suggestions towards the completion of this work.

I would also like to extend my gratitude to all my teachers at the University of Wisconsin-Madison and the University of Tehran. Among all, I feel most indebted to Professor Mahmoud Shahabdi from University of Tehran, whose thoughtful guidance and vast knowledge in the field of Electromagnetics inspired me to pursue my doctoral studies in this area.

During the past several years at UW-Madison, I have also been extremely fortunate to be around so many great colleagues and friends. I would like to thank my former and senior colleagues in our research group – Dr. Amir Masoumi, Dr. Chien-Hao Liu, Dr. Meng Li, Dr. Tonmoy Bhattacharjee, Dr. Yazid Yusuf, Dr. Arash Rashidi, and Dr. Suzette Aguilar for generously sharing their experience and assisting me in my research. I would also like to express my appreciation to my fellow labmates – Kasra Ghaemi, Yahya Mohtashami, Ting-Yen Shih, Mohammad Ranjbar Nikkhah, Meng Gao, Konstantinos Mavrakakis, Elham Mohammadi, Bahareh Behzadnezhad, Tyler Rowe, Hung Luyen, Ruyuan Ma, Zhe Yang, Boyu Sima, Shunyong Hu, Dr. Kuang Zhang, and Dr. Mingjian Li for their consistent help and support over the past few years. My sincere thanks also go to all my

friends in Madison, especially Amirhossein Davoody and Ziyi Lu for their invaluable friendship and support in every step of the way.

Last, but certainly not least, I would like to acknowledge my parents and my sister. This accomplishment would never have been possible without their everlasting love, support, and great sacrifices. It is for all of this that I dedicated this dissertation to them.

**DISCARD THIS PAGE**

# TABLE OF CONTENTS

	Page
<b>LIST OF TABLES</b> . . . . .	viii
<b>LIST OF FIGURES</b> . . . . .	x
<b>ABSTRACT</b> . . . . .	xxiii
<b>1 Introduction</b> . . . . .	1
1.1 Motivation . . . . .	1
1.2 Background on Miniaturized-Element Frequency Selective Surfaces . . . . .	2
1.3 Current State-of-the-Art and the Proposed Approach . . . . .	6
1.3.1 Spatial Filters . . . . .	6
1.3.2 Transmitarray and Reflectarrays . . . . .	8
1.3.3 Reconfigurable Periodic Structures . . . . .	8
1.4 Thesis overview . . . . .	10
1.4.1 Chapter 2 . . . . .	10
1.4.2 Chapter 3 . . . . .	11
1.4.3 Chapter 4 . . . . .	11
1.4.4 Chapter 5 . . . . .	12
1.4.5 Chapter 6 . . . . .	12
1.4.6 Chapter 7 . . . . .	13
1.4.7 Chapter 8 . . . . .	14
1.4.8 Chapter 9 . . . . .	14
1.4.9 Chapter 10 . . . . .	15
1.4.10 Chapter 11 . . . . .	16
<b>2 Harmonic-Suppressed Miniaturized-Element Frequency Selective Surfaces with Higher-Order Bandpass Responses</b> . . . . .	17
2.1 Introduction . . . . .	17
2.2 Principles of Operation . . . . .	19
2.2.1 Sources of Harmonics in MEFSSs . . . . .	19

	Page
2.2.2 A Concept for Designing Harmonic-Free MEFSSs . . . . .	23
2.2.3 Practical Implementation of Harmonic-Free MEFSSs . . . . .	25
2.2.4 Approximate Formula for Calculating the Capacitance of Cascade Overlapping Patches . . . . .	29
2.3 Design Procedure and a Design Example . . . . .	30
2.3.1 Design Procedure . . . . .	30
2.3.2 Design Example and Simulation Results . . . . .	32
2.4 Experimental Verification and Measurement Results . . . . .	33
2.5 Conclusions . . . . .	38
<b>3 Inductively-Coupled Miniaturized-Element Frequency Selective Surfaces with Narrowband, High-Order Bandpass Responses . . . . .</b>	<b>40</b>
3.1 Introduction . . . . .	40
3.2 Principles of Operation . . . . .	42
3.3 Design Procedure . . . . .	46
3.4 Experimental Verification and Measurement Results . . . . .	47
3.4.1 Design Example . . . . .	47
3.4.2 Fabrication and Measurement Results . . . . .	50
3.5 Practical Design Considerations . . . . .	53
3.5.1 Fabrication Complexity . . . . .	53
3.5.2 Impact of Losses on the Performance of the Structure . . . . .	54
3.5.3 Sensitivity of the Response to the Uncertainties in Dielectric Constant and Substrate Thickness . . . . .	56
3.6 Conclusions . . . . .	57
<b>4 Wideband Linear-to-Circular Polarization Converters Based on Miniaturized-Element Frequency Selective Surfaces . . . . .</b>	<b>60</b>
4.1 Introduction . . . . .	60
4.2 Principles of Operation . . . . .	62
4.3 Design Procedure . . . . .	67
4.4 A Design Example, Experimental Verification, and Measurement Results . . . . .	70
4.5 Conclusions . . . . .	78
<b>5 A Broadband, Circular-Polarization Selective Surface . . . . .</b>	<b>80</b>
5.1 Introduction . . . . .	80
5.2 Principles of Operation . . . . .	82
5.3 Design Procedure and Design Example . . . . .	88

## Appendix

	Page
5.4 Conclusions . . . . .	93
<b>6 Design of Wideband, FSS-Based Multi-Beam Antennas Using the Effective Medium Approach . . . . .</b>	<b>97</b>
6.1 Introduction . . . . .	97
6.2 Principles of Operation . . . . .	99
6.2.1 Why Use Effective Medium Approach? . . . . .	99
6.2.2 Effective Medium Approach for Modeling True-Time-Delay MEFSSs . . . . .	100
6.2.3 MEFSS-Based Microwave Lens Design Using the Effective Medium Approach . . . . .	103
6.2.4 A Design Example . . . . .	104
6.3 Physical Implementation . . . . .	106
6.4 Experimental Verification and Measurement Results . . . . .	110
6.4.1 Multi-beam Antenna Prototype . . . . .	110
6.4.2 Measurement Results . . . . .	110
6.4.3 Time-Domain Analysis . . . . .	114
6.5 Conclusion . . . . .	115
<b>7 Ultra-Wideband, True-Time-Delay Reflectarray Antennas Using Ground-Plane-Backed, Miniaturized-Element Frequency Selective Surfaces . . . . .</b>	<b>117</b>
7.1 Introduction . . . . .	117
7.2 Reflectarray Elements . . . . .	120
7.3 Design Procedure . . . . .	123
7.4 Design Example . . . . .	124
7.5 Experimental Verification and Measurement Results . . . . .	128
7.5.1 Reflectarray Antenna Prototype . . . . .	128
7.5.2 Measurement Results . . . . .	129
7.6 Conclusions . . . . .	135
<b>8 Broadband True-Time-Delay Circularly-Polarized Reflectarray With Linearly-Polarized Feed . . . . .</b>	<b>136</b>
8.1 Introduction . . . . .	136
8.2 Reflectarray Elements . . . . .	138
8.3 Design Procedure and Design Example . . . . .	141
8.4 Experimental Results . . . . .	144
8.5 Conclusions . . . . .	149

## Appendix

	Page
<b>9 Exploiting Mechanical Flexure as a Means of Tuning the Responses of Large-Scale Periodic Structures</b> . . . . .	151
9.1 Introduction . . . . .	151
9.2 Mechanically-Tunable Periodic Structures with Inductive or Capacitive Responses	153
9.2.1 Overlapping and Relative Movement of Layers . . . . .	156
9.2.2 Stretching . . . . .	158
9.2.3 Mechanical Flexure . . . . .	161
9.3 Design Example . . . . .	166
9.4 Experimental Verification and Measurement Results . . . . .	168
9.5 Discussion . . . . .	171
<b>10 MAcro-Electro-Mechanical Systems (MÆMS) Based Concept for Beam Steering in Reflectarray Antennas</b> . . . . .	173
10.1 Introduction . . . . .	173
10.2 MÆMS-based Spatial Phase Shifters . . . . .	176
10.3 MÆMS-Based Beam Steering . . . . .	181
10.4 Experimental Results . . . . .	184
10.5 Discussion . . . . .	188
<b>11 Future Work</b> . . . . .	192
11.1 Random Frequency Selective Surfaces . . . . .	193
11.2 MÆMS-Based Beam Steering in Leaky-Wave Antennas . . . . .	193
11.3 Infrared Spatial Filters and Lenses . . . . .	194
 <b>APPENDICES</b>	
Appendix A: List of Publications . . . . .	196
Appendix B: List of Acronyms . . . . .	201
<b>LIST OF REFERENCES</b> . . . . .	202

**DISCARD THIS PAGE**

## LIST OF TABLES

Table	Page
2.1 Physical and electrical parameters of the $2^{nd}$ -order MEFSS with a center frequency of 3 GHz and the fractional bandwidth of $\delta = 20\%$ discussed in Section 2.2.1. . . . .	22
2.2 Physical parameters of the $2^{nd}$ -order FSS with a center frequency of 3 GHz, the fractional bandwidth of $\delta = 20\%$ , and no harmonics up to 27 GHz discussed in Section 2.3.2. . . . .	33
3.1 Physical and electrical parameters of the $2^{nd}$ -order MEFSS with the center frequency of 21 GHz and the fractional bandwidth of $\delta = 5\%$ discussed in Section 3.4. . . . .	48
4.1 The element values of circuit models shown in Fig. 4.3 to have third-order responses with $\Delta f_x = 3.75$ GHz-12.25 GHz and $\Delta f_y = 7.75$ GHz - 16.25 GHz for the vertical and horizontal polarizations, respectively. . . . .	70
4.2 The finalized element values of the equivalent circuit models shown in Fig. 4.3 for the polarization converter discussed in Section 4.4. . . . .	72
4.3 Physical parameters of the polarization converter discussed in Section 4.4, with the unit cell shown in Fig. 4.7 and with the equivalent circuit model element values reported in Table 4.2. The unit cell dimension for this structure is $D = 4.5mm$ . . . . .	74
4.4 Comparison between the performance of the proposed structure and few other reported polarization converters. $\lambda_c$ is the wavelength at center frequency. . . . .	79
5.1 Physical parameters of the polarization converters and linear polarizer discussed in Section 5.3. . . . .	90
5.2 Finalized physical parameters of the polarization converters and linear polarizer discussed in Section 5.3. . . . .	91
5.3 Comparison between the performance of the proposed structure and few other reported CPSSs. $\lambda_c$ is the wavelength at center frequency. . . . .	96

Table	Page
6.1 The refractive index profile of the proposed lens composed of the effective media with equal permittivity and permeability.(MF: Matrix Formulation) . . . . .	106
6.2 Physical and electrical properties of the elements that populate each zone of the proposed lens. Time-delay values and physical dimensions are in <i>psec</i> and <i>mm</i> respectively. The lens has unit cell dimensions of $6.5\text{ mm} \times 6.5\text{ mm}$ . The dielectric substrate used is Rogers 5880 and the thickness of all the substrates is $h=3.175\text{ mm}$ . . . . .	108
7.1 Physical parameters of the TDUs that populate each zone of the proposed reflectarray. All physical dimensions are in <i>mm</i> . For all these TDUs, $D_x = D_y = 6.5\text{mm}$ , $h_1 = h_3 = h_5 = 1.524\text{mm}$ , and $h_2 = h_4 = 0.1\text{mm}$ . The dielectric substrates with the thickness of $1.524\text{mm}$ are Rogers RO4003C with the dielectric constant of 3.4. The bonding layers with the thickness of $0.1\text{mm}$ are Rogers 4450F with the dielectric constant of 3.52. . . . .	126
7.2 The refractive index profile of the simplified model of the proposed reflectarray composed of the effective media with the thickness of $4.8\text{ mm}$ . . . . .	129
8.1 Physical properties of the time-delay units that populate each zone of the proposed TTD reflectarray. The unit of all the physical dimensions is <i>mm</i> . The unit cell dimensions for each time-delay unit is $D_x = D_y = 6.5\text{ mm}$ . The substrate thicknesses are $h_1 = h_3 = h_5 = 1.524\text{ mm}$ and $h_2 = h_4 = 0.1\text{ mm}$ . The substrates with the thickness of $1.524\text{ mm}$ are all Rogers RO4003C with the dielectric constant of 3.4. The $0.1\text{-mm}$ -thick bonding layers are Rogers 4450F with the dielectric constant of 3.52.144	144
9.1 The variations of the impedances of the inductive and capacitive metallic sheets with increasing folding angle $\alpha$ . The sheets are composed of periodic arrangement of metallic strips where the folding is along and perpendicular to the direction of the strips. (EQC: Equivalent Circuit Model) . . . . .	165

**DISCARD THIS PAGE**

## LIST OF FIGURES

Figure	Page
1.1 (a) A conceptual depiction of a transmitting bandpass frequency selective surface. (b) A conceptual depiction of a bandpass FSS frequency response. . . . .	2
1.2 (a) Topology of a bandpass FSS with aperture-type elements. (b) Topology of a band-stop FSS with dipole-type elements. . . . .	3
1.3 (a) A capacitive impedance sheet composed of a 2D array of sub-wavelength patches. (b) An inductive impedance sheet composed of a 2D array of sub-wavelength wire grids. . . . .	4
1.4 (a) Topology, equivalent circuit model, and conceptual frequency response of a bandpass-type MEFSS. (b) Topology, equivalent circuit model, and conceptual frequency response of a lowpass-type MEFSS. . . . .	5
2.1 (a) Topology of the bandpass MEFSS presented in [1]. The top view of the unit cells of the capacitive and inductive layers are shown on the right hand side of the figure. (b) Equivalent circuit model of the MEFSS. The structure has $N$ metal layers and acts as an FSS with an $(\frac{N+1}{2})^{th}$ -order bandpass response. . . . .	20
2.2 Calculated transmission coefficient of the $2^{nd}$ -order bandpass FSS discussed in Section 2.2.1 with the parameters shown in Table 2.1. Results are obtained using full-wave EM simulation in CST Microwave Studio. . . . .	22
2.3 The unit cell of the $2^{nd}$ -order bandpass MEFSS with the lumped capacitors loading the capacitive patch layers. . . . .	24
2.4 Calculated transmission coefficients of the $2^{nd}$ -order bandpass MEFSS discussed in Section 2.2.2 where the capacitive patches are loaded with lumped-element capacitors. Results are obtained using full-wave EM simulation in CST Microwave Studio. . . . .	24

Figure	Page
2.5 (a) Multiple closely-spaced capacitive patch layers are used to synthesize a single effective capacitive layer. The dielectric substrates are extremely thin. The unit cells of the patches used in different layers can overlap with each other and do not necessarily have to be aligned together. (b) The equivalent circuit model of a generalized MEFSS of the type shown in Fig. 2.1 in which each one of the capacitive layers is substituted with a composite, multi-layer effective capacitive layer similar to that shown in Fig. 2.5(a). In this equivalent circuit model $C_{i,eff}$ represents the effective capacitance of each of the composite, multi-layer capacitive structures that are used to synthesize the $i^{th}$ capacitive layer of the MEFSS shown in Fig. 2.1(a). . . . .	26
2.6 (a) The unit cells of the two capacitive layers used to synthesize a single effective capacitive layer of the MEFSS of Fig. 2.1(a) can overlap with each other. This overlap is modeled by the vector $(x_c, y_c)$ . (b) 3D topology of the unit cell of a composite patch layer showing the offset between the capacitive patches and the dielectric slab that separates them. (c) The equivalent circuit model of the capacitive structure shown in Fig. 2.6(b). (d)-(e) The extracted effective capacitance of the capacitive structure shown in Fig. 2.6(b) consisting of two cascaded capacitive patches and a thin substrate separating them. The structure has the unit cell dimensions of $6.5 \text{ mm} \times 6.5 \text{ mm}$ . The gap size for both layers is $s = 0.5 \text{ mm}$ and the patch size is $P = 6 \text{ mm}$ . The thickness of the substrate is $h = 0.2 \text{ mm}$ . The study has been done for both (d) Vertical and (e) Horizontal polarizations. . . . .	28
2.7 (a) The capacitive structure composed of two cascaded capacitive layers can be modeled as four capacitors with capacitance values of $C_c$ and one capacitor with a capacitance value of $C_i$ as depicted. (b) The equivalent circuit model of the capacitive structure showing the relative arrangement of $C_c$ and $C_i$ capacitors. . . . .	31
2.8 Comparison between the capacitance values predicted using the analytical method and those extracted from full-wave EM simulations. The results are shown for the structure examined in section 2.2.3. . . . .	32
2.9 Unit cell of the proposed harmonic-suppressed $2^{nd}$ -order bandpass FSS discussed in Section 2.3.2. . . . .	34
2.10 Measured and calculated transmission coefficients of the FSS prototype discussed in Section 2.3.2 and shown in Fig. 2.11. The MEFSS is composed of the unit cells shown in Fig. 2.9 with physical dimensions reported in Table 2.2. . . . .	34
2.11 (a) Photograph of the fabricated harmonic-suppressed MEFSS prototype. (b) Side view of the fabricated prototype. . . . .	35

Appendix	Page
Figure	
2.12 (a)-(b) Measured transmission coefficients of the fabricated harmonic-suppressed MEFSS prototype discussed in Section 2.3.2 and shown in Fig. 2.11 for oblique incidence angles for the (a) TE and (b) TM polarization of incidence. . . . .	37
3.1 (a) Generalized bandpass filter circuit using a number of parallel resonators separated from each other by admittance inverters (J-type inverters). (b) Generalized bandpass filter circuit that consists of series resonators coupled together using K-type impedance inverters. . . . .	43
3.2 (a) The equivalent circuit model of the transmission-line resonators (dielectric spacers) used as the resonators of the proposed frequency selective surface. (b) The circuit model of the admittance inverters used to couple the resonators of Fig. 3.2(a) together in the present circuit model. (c) The equivalent circuit model of the proposed frequency selective surface when the resonators and the admittance inverters of Fig. 3.2(a)-(b) are put together in a ladder network. In this circuit, the negative lengths of the admittance inverters of Fig. 3.2(b) are absorbed in the positive lengths of the transmission-line resonators shown in Fig. 3.2(a). . . . .	44
3.3 Topology of the proposed bandpass FSS. The structure has $N + 1$ metal layers that are separated from one another by $N$ dielectric spacers and acts as an FSS with $N^{th}$ -order bandpass response. . . . .	45
3.4 Unit cell of the proposed second-order bandpass MEFSS discussed in Section 3.4. Notice that the two inductive wire grids placed in the center are separated from one another by a thin prepreg layer. These two inductive layers constitute a single hybrid inductive layer. This arrangement is used to maintain the symmetry of the structure as discussed in Section 3.4. . . . .	49
3.5 Simulated and measured transmission coefficients of the MEFSS discussed in Section 3.4. The results from the equivalent circuit model and full-wave simulations are compared with the free-space measurement results. . . . .	50
3.6 (a) Photograph of the fabricated MEFSS prototype. (b) Side view of the fabricated prototype. . . . .	51
3.7 Measured and simulated transmission coefficients of the fabricated MEFSS prototype discussed in Section 3.4 and shown in Fig. 3.6 for oblique incidence angles for (a) TE and (b) TM polarizations of incidence. . . . .	52

Appendix Figure	Page
3.8 Simulated transmission coefficients of the MEFSS discussed in Section 3.4.1 for various scenarios of misalignments between different metallic layers. $\Delta_{j,j+1}$ represents the misalignment for the inductor $L_{j,j+1}$ . Here, we assume that the location of the center wire grid is fixed and the inductors at two sides of the FSS are misaligned diagonally in $x - y$ plane with respect to the center wire grid. . . . .	55
3.9 Simulated transmission coefficients of the MEFSS discussed in Section 3.4.1 for various loss tangent values of the dielectric substrates. . . . .	56
3.10 Sensitivity of the frequency response of the structure discussed in Section 3.4.1 to the variations of (a) the thickness and (b) the dielectric constant of the substrates from assumed values in the design process. . . . .	58
4.1 Schematic model of a linear-to-circular polarization converter. In this configuration, the incident electric field vector is tilted $45^\circ$ relative to $\hat{x}$ and $\hat{y}$ directions. After passing through the converter, the transmitted signal is right-handed circularly polarized. 63	63
4.2 Topology of the proposed polarization converter based on bandpass miniaturized-element frequency selective surfaces. The unit cells of the capacitive patches and the inductive wire grids are shown on the right hand side of the figure. . . . .	65
4.3 Equivalent circuit model of the converter shown in Fig. 4.2 for (a) the vertical ( $\hat{x}$ -directed) and (b) the horizontal ( $\hat{y}$ -directed) polarizations. . . . .	66
4.4 The concept of de-tuning to design a wideband polarization converter. $T_x$ and $T_y$ show the frequency responses of the device for vertical ( $\hat{x}$ ) and horizontal ( $\hat{y}$ ) polarizations, respectively. The transmission windows for $\hat{x}$ and $\hat{y}$ polarizations are respectively $\Delta f_t^x = f_H^x - f_L^x$ and $\Delta f_t^y = f_H^y - f_L^y$ . In this configuration, $\Delta f_d$ is the overlap region between the two responses and $\Delta f_{opt}$ shows the operational band of interest in which the structure is impedance matched for both orthogonal polarizations while there is a $90^\circ$ phase difference between their corresponding transmission phases. . . . .	68
4.5 Calculated transmission coefficients of the polarization converter discussed in Section 4.4 as well as the difference between the corresponding transmission phases with the parameters shown in Table 4.1. . . . .	71

Appendix	Page
Figure	
4.6 Simulated and measured transmission characteristics of the polarization converter discussed in Section 4.4. These characteristics include (a) transmission coefficients for the two orthogonal polarizations and (b) the difference between their corresponding transmission phases. Simulated results based on the equivalent circuit model are calculated using the values listed in Table 4.2. The full-wave simulated results are obtained based on the values reported in Table 4.3. . . . .	73
4.7 Unit cell of the proposed polarization converter discussed in Section 4.4. Notice that the two capacitive patches placed in the center are separated from one another by a thin prepreg layer. These two layers constitute a single hybrid capacitive layer. This arrangement is used to maintain the symmetry of the structure as discussed in Section 4.4. . . . .	74
4.8 Simulated and measured axial ratios of the polarization converter discussed in Section 4.4. These results are obtained using Eq. (4.6) with the values obtained from the simulated and measured magnitude and phase of the response of the FSS for both $\hat{x}$ and $\hat{y}$ polarizations. . . . .	75
4.9 (a) Photograph of the fabricated polarization converter. (b) Side view of the fabricated prototype. . . . .	75
4.10 (a),(c) Simulated and (b),(d) measured total transmission coefficients of the transmitted wave passed through the polarization converter for an incident wave propagating in (a),(b) $y - z$ and (c),(d) $x - z$ planes of incidence. . . . .	76
4.11 (a),(c) Simulated and (b),(d) measured axial ratios of the transmitted wave passed through the polarization converter for an incident wave propagating in (a),(b) $y - z$ and (c),(d) $x - z$ planes of incidence. . . . .	77
5.1 Schematic models of (a) right-handed and (b) left-handed circular-polarization selective surfaces. . . . .	82
5.2 (a) Schematic model of an RH-CPSS. This CPSS is composed of two LP-to-CP polarization converters that are separated by a linear polarizer. (b) This structure is transparent to left-handed circularly-polarized waves and (c) it reflects the right-handed circularly polarized waves. . . . .	85

Appendix	Page	
Figure		
5.3	Topology of the proposed CPSS composed of two LP-to-CP polarization converters and a linear polarizer. The polarization converters are composed of two-dimensional arrays of sub-wavelength capacitive patches and inductive wire grids having different dimensions along the $x$ and $y$ directions. The layers are separated from each other by thin dielectric slabs. The linear polarizer is composed of an array of sub-wavelength strips that are tilted $45^\circ$ with respect to $\hat{x}$ - and $\hat{y}$ -directions and is sandwiched between two thin substrates. . . . .	87
5.4	Unit cell of the proposed CPSS discussed in Section 5.3. The two middle capacitive patches for each converter are separated from one another by a thin bonding layer. This arrangement is used to maintain the symmetry in the structure. . . . .	89
5.5	(a) Transmission characteristics of the polarization converter part of the proposed CPSS discussed in Section 5.3. These characteristics include the transmission coefficients for both vertical and horizontal polarizations as well as the difference between their corresponding transmission phases. (b) The total transmission coefficient and the axial ratio of the polarization converter used in the architecture of the CPSS described in Section 5.3. These results are all obtained based on the values reported in Table 5.1. . . . .	92
5.6	Transmission characteristics of the linear polarizer used in the design of the CPSS discussed in Section 5.3. The magnitude of the transmission responses are shown for two cases where the linear polarizer is illuminated with an E-field that is aligned with and perpendicular to the strips. These results are calculated based on the values listed in Table 5.1. . . . .	93
5.7	Transmission and reflection coefficient of the RH-CPSS prototype discussed in Section 5.3 for (a) LHCP and (b) RHCP incoming waves. These results are obtained with the parameter values listed in Table 5.2. . . . .	94
5.8	(a) Transmission characteristics of RH-CPSS prototype discussed in Section 5.3 for oblique incidence angles. (a) Transmission coefficient for incoming LHCP waves. (b) Transmission coefficient for incoming RHCP waves. The results are obtained with the parameters reported in Table 5.2. . . . .	95
6.1	(a) Topology of a unit cell of lowpass MEFSS. (b) Equivalent circuit model of the MEFSS. The structure has $\frac{N+1}{2}$ metal layers and acts as an FSS with an $N^{th}$ -order lowpass response. . . . .	100
6.2	Lumped-element circuit model of a classical $N^{th}$ order lowpass filter. . . . .	101

Appendix	Page
Figure	
6.3 (a) Magnitude and phase of the transmission coefficient of a lumped-element third-order lowpass filter with cutoff frequency $f_c = 8$ GHz. (b) Real and imaginary parts for the permittivity and permeability of a homogeneous slab with the same frequency response as the one shown in Fig. 6.3(a). The results are derived from calculated S-parameters for the third-order filter shown in Fig. 6.3(a). The thickness of the equivalent slab is considered to be 1 mm. . . . .	102
6.4 Topology of the proposed multi-beam antenna consisting of a zoned flat TTD lens and planar feed antenna. $d_i$ is the radius of $i^{th}$ zone. (a) Front view. (b) Side view. . . . .	104
6.5 (a) Photograph of the fabricated lens. (b) Side view of the fabricated prototype. . . . .	109
6.6 Measured and simulated power patterns on the focal line of the lens at the center frequency of 9 GHz. The results are shown for plane waves arriving from various incidence angles of $0^\circ$ , $15^\circ$ , $30^\circ$ , and $45^\circ$ . The point on the focal plane that results in maximum power level for a given incidence angle is the location where the the feed antenna needs to be placed to get a beam in the desired direction in the far field. . . . .	111
6.7 Measured and simulated radiation patterns of the proposed antenna at the center frequency of operation(9 GHz). The feed antennas are placed at locations $x_{\theta=0^\circ}$ , $x_{\theta=15^\circ}$ , $x_{\theta=30^\circ}$ , and $x_{\theta=45^\circ}$ , obtained using the measurement results shown in Fig. 6.6. (a) $0^\circ$ , (b) $15^\circ$ , (c) $30^\circ$ , and (d) $45^\circ$ . The measurements were carried out using a multi-probe near field system. The simulated results are obtained using full-wave simulations of the structure using the effective medium technique presented in Section 6.2.2. . . . .	112
6.8 Measured realized gain and directivity of the proposed antenna for different beam directions of (a) $0^\circ$ , (b) $15^\circ$ , (c) $30^\circ$ , and (d) $45^\circ$ . . . . .	114
6.9 (a) Measured aperture efficiency as a function of the frequency. (b) Measured fidelity factors of the proposed lens under oblique angles of incidence for a modulated Gaussian pulse centered at 9 GHz and the bandwidth of 8-10 GHz. . . . .	115
7.1 (a) Topology of the proposed reflectarray antenna. (b) The composition of each TDU and its equivalent circuit model. . . . .	121
7.2 The time-delay profile required from the TDUs distributed over the aperture of the reflectarray. The values are in psec. . . . .	124
7.3 The composition of TDUs populating the proposed reflectarray aperture discussed in Section 7.4. . . . .	126

Appendix	Page
Figure	
7.4 The comparison between the full-wave simulated phase responses of the designed elements and the desired ideal responses for each TDU occupying different zones. The topology of the designed elements is shown in Fig. 7.3 and their dimensions are reported in Table 7.1. The ideal case represents the desired linear reflection phase with the desired time delay. (a) The responses for the TDUs occupying the odd zones. (b) The responses for the TDUs occupying the even zones. . . . .	127
7.5 (a) Photograph of the fabricated reflectarray. (b) Side view of the fabricated prototype.	130
7.6 Measured and simulated normalized radiation patterns of the proposed reflectarray antenna described in Section 7.4 and shown in Fig. 7.5 in the (a)-(c) $xz$ - and (d)-(e) $yz$ -planes at (a), (d) 8 GHz, (b), (e) 10 GHz, and (c), (f) 12 GHz. The measurements were carried out using a multi-probe spherical near field system. The simulated results are obtained using full-wave EM simulations of simplified model of the reflectarray using effective medium approach. All the patterns are normalized to the peak values of their corresponding co-polarized components. . . . .	131
7.7 Measured and simulated realized gain and directivity of the proposed antenna shown in Fig. 7.5 across the band of interest. The measurements are done using a multi-probe near-field system and the full-wave EM simulation results are obtained by simulating the reflectarray antenna, using the effective medium approach, in CST Microwave Studio. . . . .	132
7.8 Measured co-polarized components of the gain patterns of the proposed reflectarray antenna at (a) 8 GHz, (b) 10 GHz, and (c) 12 GHz in the H-plane ( $xz$ -plane). For each frequency, four feed antennas are located on the focal arc illuminating the reflectarray at incident angles of $0^\circ$ , $15^\circ$ , $30^\circ$ , and $45^\circ$ to steer the main beam towards $0^\circ$ , $15^\circ$ , $30^\circ$ , and $45^\circ$ , respectively. . . . .	133
7.9 (a) The measurement setup used to experimentally characterized the time-domain performance of the proposed reflectarray. (b) Measured fidelity factor of the proposed reflectarray when it is illuminated with a modulated Gaussian pulse centered at 10 GHz with different fractional bandwidths up to 6 GHz. . . . .	134
8.1 (a) Topology of the proposed reflectarray whose aperture is populated with FSS-based spatial TDUs. (b) The composition of each TDU. (c)-(d) The equivalent circuit model of each TDU for the two orthogonal ( $\hat{x}$ - and $\hat{y}$ -directed) polarizations. . . . .	138

Appendix	Page
Figure	
8.2 Conceptual depiction of the idealized response needed from the TDUs populating the aperture of the proposed reflectarray. The magnitudes and phases of the reflection coefficient of each TDU for the two orthogonal polarizations are shown. . . . .	140
8.3 (a)-(b) The phase-delay profile required from the pixels distributed over the aperture of the reflectarray for (a) $\hat{x}$ - and (b) $\hat{y}$ -directed polarizations. (c) The time-delay profile required by the time delay units populating the reflectarray aperture. . . . .	142
8.4 Topology of the TDUs used in the design of the prototype reflectarray discussed in Section 8.3. . . . .	144
8.5 The full-wave simulated phase responses alongside the desired ideal phase responses for time-delay units populating different zones. (a) The phase responses of TDUs occupying the odd zones for $\hat{x}$ -polarization. (b) The phase responses of TDUs occupying the odd zones for $\hat{y}$ -polarization. Solid line: ideal phase response. Dashed line: full-wave simulated phase responses. . . . .	145
8.6 Full-wave simulated and measured normalized radiation patterns of the prototype discussed in Section 8.3 at (a), (d) 8 GHz, (b), (e) 10 GHz, and (c), (f) 12 GHz in both (a)-(c) $x - z$ - and (d)-(f) $y - z$ -planes. The full-wave simulated results were obtained using CST Microwave Studio and the experiments were carried out using a multiprobe spherical near-field system. . . . .	147
8.7 (a) Photograph of the fabricated reflectarray prototype. In this prototype, $L = 253.5$ mm, $h = 4.8$ mm, and $D = 6.5$ mm. (b) Full-wave simulated and measured directivity and realized gain of the prototype discussed in Section 8.3 and shown in Fig. 8.7(a). .	148
8.8 (a) Measured RHCP gain pattern of the prototype discussed in Section 8.3 at 10 GHz in the $x - z$ plane. These patterns are measured when the feed is moved on the focal arc to illuminate the aperture off axis with angles of $0^\circ$ , $15^\circ$ , $30^\circ$ , and $45^\circ$ . This steers the beam toward $0^\circ$ , $15^\circ$ , $30^\circ$ , and $45^\circ$ , respectively. (b) Measured axial ratios of the radiated beams in all these four cases over the entire band of operation. . . . .	149
8.9 Measured fidelity factor of the prototype discussed in Section 8.3 when the antenna transmits modulated Gaussian pulses with a center frequency of 10 GHz and the fractional bandwidths up to 6 GHz. . . . .	150

Appendix	Page
Figure	
9.1	Topology of a periodic arrangement of metallic strips. (a) If the incident electric field is perpendicular to the strips, the plane wave creates positive and negative charges on the edges of adjacent strips, which produces a capacitive effect. (b) If the electric field is parallel to the strips, the structure acts as a reactive impedance surface with inductive impedance. The metallic pattern and the substrate are shown in brown and gray, respectively. . . . . 154
9.2	Illustration of the three concepts of (a) overlapping along with relative movement, (b) stretching and contraction, and (c) deforming used to mechanically tune the frequency responses of reactive impedance sheets shown in Fig.9.1. The metallic pattern and substrates are respectively shown in brown and gray. . . . . 155
9.3	(a) Transmission coefficients of the structure shown in Fig. 9.2(a) with $w = 2$ mm, $g = 3$ mm, and $h = 0.1$ mm and different overlappings once excited by a plane wave with a polarization aligned with the direction of strips. (b) Calculated effective inductance using the full-wave simulation results shown in Fig. 9.3(a) and equation (9.3). $L_0$ refers to the effective inductance value at $O=0$ mm. (c) Transmission coefficients of the same structure with $w = 2$ mm and $g = 3$ mm where the incident electric field is perpendicular to the direction of strips. (d) The effective capacitance computed using the simulated results shown in Fig. 9.3(c) alongside the calculated values using equation (9.4). $C_0$ refers to the capacitance inductance value at $O=0$ mm. . . . . 158
9.4	(a) Transmission coefficients of the stretched reactive surface, shown in Fig. 9.2(b) composed of inductive strips with $w_1 = 2$ mm and $g_1 = 3$ mm for $g_2/g_1 = 1, 1.1, 1.2,$ and $1.3$ . (b) The calculated effective inductance using the full-wave simulation results shown in Fig. 9.4(a) alongside the predicted value from $L_{eff}/L_0 = g_2/g_1$ . $L_0$ refers to the effective inductance value at $g_2/g_1=1$ . (c) Transmission coefficients of the stretched impedance sheet, shown in Fig. 9.2(b) composed of capacitive strips with $w_1 = 2$ mm and $g_1 = 3$ mm for $g_2/g_1 = 1, 1.1, 1.2,$ and $1.3$ . (d) The effective capacitance computed using the simulated results shown in Fig. 9.4(c) alongside the calculated values using $C_{eff}/C_0 = g_2/g_1$ . $C_0$ refers to the effective capacitance value at $g_2/g_1=1$ . . . . . 159
9.5	A method for emulating stretching in the periodic structures shown in Fig. 9.1. This method does not rely on stretching of an elastic substrate to change the $w/D$ ratio. . . 160

## Appendix

## Figure

## Page

- 9.6 Different cases for folding an impedance sheet composed of parallel metallic strips in an accordion-like fashion. Case (a): The incident electric field is along the direction of strips (inductive) and folding is parallel to the metallic strips. Case (b): The incident electric field is along the direction of strips (inductive) but the surface is folded perpendicular to the strips. Case (c): The incident electric field and the folds are both perpendicular to the direction of strips. Case (d): The incident electric field is perpendicular to the direction of the strips (capacitive) and the folds are parallel to the metallic strips. The metallic pattern and the substrate are shown in brown and gray, respectively.  $\alpha$  is the folding angle. . . . . 161
- 9.7 (a), (c), (e), and (g) The transmission coefficients of the structures shown in Figs. 9.6(a), 9.6(b), 9.6(c), and 9.6(d), respectively. In all cases,  $w = 2$  mm and  $g = 3$  mm. (b), (d), (f), and (h) The effective reactance values calculated using simulated results shown in Figs. 9.7(a), 9.7(b), 9.7(c), and 9.7(d), respectively. These results are also compared with the predicted values calculated from equations (9.5), (9.6), (9.7), and (9.8), respectively. In (b) and (d),  $L_0$  refers to the effective inductance value at  $\alpha = 0^\circ$ . In (f) and (h),  $C_0$  refers to the effective capacitance value at  $\alpha = 0^\circ$ . . . . . 162
- 9.8 (a) The unit cell of a bandstop frequency selective surface formed by combining the inductive and capacitive strips discussed in Section 9.2 in series on a single layer. (b) The equivalent-circuit model of the structure shown in part (a). . . . . 166
- 9.9 The bandstop FSS composed of metallic squares of the type shown in Fig. 9.8(a) can be folded to tune its frequency response.  $\alpha$  is the folding angle. . . . . 167
- 9.10 (a) Effective inductance and capacitance values of the structure shown in Fig. 9.8(a) as a function of folding angle. The results obtained using full-wave EM simulations and those predicted using equations (9.5) and (9.7) are shown. Physical dimensions of the structure are  $w = 1.5$  mm,  $g = 1$  mm, and unit cell dimensions of  $15$  mm  $\times$   $15$  mm. (b) The predicted resonant frequency of the bandstop FSS shown in Fig. 9.9 based on the calculated effective reactance values shown in Fig. 9.10(a). . . . . 167
- 9.11 (a) Full-wave simulated and (b) measured frequency responses of the mechanically-tunable bandstop FSS prototype shown in Fig. 9.9 having folding angles of  $\alpha = 0^\circ$ ,  $15^\circ$ ,  $30^\circ$ ,  $45^\circ$ , and  $60^\circ$ . . . . . 168
- 9.12 The photographs of the fabricated prototype of the mechanically-tunable bandstop FSS where the folding angle is (a)  $0^\circ$  and (b)  $45^\circ$ . . . . . 169

Appendix Figure	Page
9.13 Measured transmission coefficients of the fabricated prototype shown in Fig. 9.12 with three folding angles of $0^\circ$ , $30^\circ$ , and $60^\circ$ . (a) Polarization: TE, $\alpha = 0^\circ$ , (b) Polarization: TE, $\alpha = 30^\circ$ , (c) Polarization: TE, $\alpha = 60^\circ$ , (d) Polarization: TM, $\alpha = 0^\circ$ , (e) Polarization: TM, $\alpha = 30^\circ$ , and (f) Polarization: TM, $\alpha = 60^\circ$ . . . . .	170
10.1 (a) Topology of a phase shifting surface composed of an array of sub-wavelength capacitive patches backed with a ground plane. Each unit cell of this phase shifting surface is considered to be a single spatial phase shifter. (b) The equivalent circuit model of the spatial phase shifter and the phase shifting surface shown in Fig. 10.1(a). (c) Topology of the MÆMS-based phase shifting surface and its equivalent circuit model. . . . .	178
10.2 (a) The phase of the reflection coefficient of the spatial phase shifters discussed in Section 10.2 as a function of frequency and for different $h$ values. $h$ represents the separation between the ground plane and the bottom of the dielectric substrate on the top surface of which the two-dimensional array of sub-wavelength capacitive patches are printed. (b) The reflection phase of the SPS described in Section 10.2 at the operating frequency of 9.5 GHz as a function of the tuning parameter, $h$ . . . . .	179
10.3 A possible implementation of a MÆMS-based beam-steerable reflectarray antenna. In this structure, the ground plane underneath the array of capacitive patches can be freely tilted in two dimensions along a pivot point located at its center. This locally changes the resonant frequencies of the spatial phase shifters occupying different locations in the aperture and the phase shift that they provide. The phase shift gradient created by this technique will determine the direction of the radiated beam in the far field. Using this approach the radiated beam can be steered in two dimensions using a single control variable. . . . .	183
10.4 (a) Phase profile over the aperture for three cases where the ground plane is not-tilted and fully-tilted along the $\hat{x}$ or the $-\hat{x}$ axes. (b) Simulated and measured far field radiation patterns of the structure shown in Fig. 10.3 and described in Section 10.3 for the three tilting cases described earlier. . . . .	184
10.5 Photograph of the fabricated prototype. . . . .	185

Appendix Figure	Page
10.6 Illustration of a potential implementation of a MÆEMS-based reflectarray antenna with dynamic beam steering. Four piezo-electric actuators are placed on the corners of the ground plane of the structure below the ground plane. By applying a DC bias voltage to each actuator, its height can be controlled. Changing the relative heights of the piezoelectric actuators allows for tilting the ground plane in any desired direction. This can be used to control the phase shift gradient vector over the aperture of the structure in the $x - y$ plane and achieve the desired two-dimensional steering. Finally, placement of the actuators below the ground plane shields the from the incident antenna thereby ensuring that they do not impact the radiation patterns of the reflectarray antenna. . . . .	187
10.7 Topology of a MÆEMS based reflecting surface with a segmented ground plane. In this structure the continuous ground plane is replaced with three segments of independently controllable ground planes. This allows for creating phase wrapping over the aperture of the reflectarray and widening the beam scanning range of the structure. . . . .	188
10.8 (a) Phase profiles over the aperture of the structure shown in Fig. 10.6 for the two cases where none of the three ground planes are tilted or all of them are tilted with the maximum values of tilt. (b) The simulated and measured far field patterns of the structure for these two different tilt conditions. . . . .	189
11.1 (a) A random frequency selective surface whose aperture is populated with two resonant slot elements. Black pixels represent “Element 1” and white pixels represent “Element 2”. (b) The frequency response of a frequency selective surface with pattern shown in Fig. 11.1(a). The transmission coefficient is compared with two cases in which the aperture is uniformly populated. . . . .	194

## ABSTRACT

Miniaturized-element frequency selective surface (MEFSS) is a class of sub-wavelength periodic structures that is entirely composed of non-resonant elements. This dissertation investigates the application of MEFSSs in designing various wavefront-manipulating structures including spatial filters, polarization converters, polarization selective surfaces, transmitarrays, and reflectarrays. These structures are presented in four parts of this dissertation. The focus of the first part is primarily on the design of low-profile spatial filters for reducing the radar signature of antennas mounted on military platforms. Broadband harmonic-free operations and narrowband highly-selective frequency responses are two important features of the presented spatial filters. These features are highly desired in low-observable antenna systems. In the second part, anisotropic versions of MEFSSs were employed in designing linear-to-circular polarization converters and circular-polarization selective surfaces (CPSS). Broad bandwidths and wide angular stability of the frequency responses are some of the key advantages of the proposed devices compared to the current state-of-the-art. The third part of this dissertation presents the design of wideband true-time-delay (TTD) transmitarrays and reflectarrays. The proposed transmitarrays and reflectarrays exploit the unit cells of appropriately designed MEFSSs as their spatial time-delay-units (TDUs), and are extremely suitable for broadband pulsed applications. Finally, in the last part, several mechanical tuning techniques are proposed as potential ways to make the presented wavefront-manipulating structures tunable. The proposed techniques do not require any electronic tunable devices and only rely on exploiting mechanical movements or deformations in the fabric of the structure to achieve tunability over a wide range.

# Chapter 1

## Introduction

### 1.1 Motivation

Frequency selective surfaces (FSS) are engineered surface constructions designed to control the wavefront of the propagating electromagnetic waves. If illuminated by an electromagnetic wave, these surfaces act as barriers for the propagating waves and can modify the spectral content of the waves as desired. For instance, they can be designed to engineer the magnitude and/or the phase of the transmitted or reflected waves in any desired fashion to obtain certain functionalities. Fig. 1.1 shows a conceptual depiction of an FSS and its frequency response. Due to their versatile functionality, FSSs have been employed in a wide range of applications in physics and engineering ranging from low radio frequencies [2] to infrared [3–6] and optical frequencies [7]. These applications include spatial filters [2, 8], metamaterials and metasurfaces [9, 10], artificial magnetic conductors [11, 12], transmitarrays [13–15], and reflectarrays [16]. All these applications play significant roles in both civilian and military sectors. For instance, as spatial filters, frequency selective surfaces have been extensively used in various stealth applications such as reducing the RF signature in low-observable platforms [2], reducing interference in indoor wireless environment [17, 18], and shielding sensitive electronic devices from unwanted interference and jamming signals. Reflectarrays and transmitarrays have also emerged as a potential replacement for the traditional reflectors and dielectric lenses as well as the flat phase arrays in many high-gain, pencil beam antenna applications. With the ongoing proliferation of commercial and military systems, a significant amount of research has been devoted to the development of these systems over the past few decades. However, as with any technology, there are still many challenges remain unsolved. The focus of this

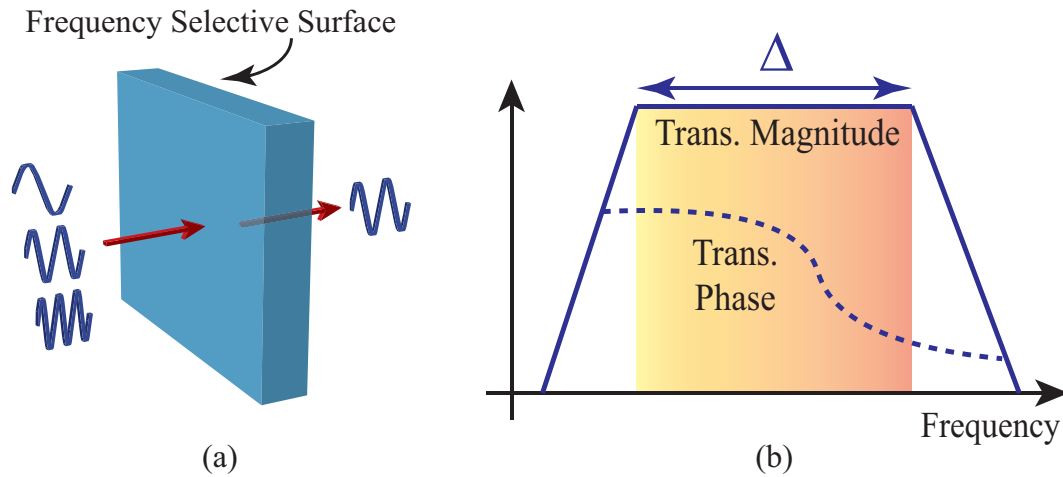


Figure 1.1 (a) A conceptual depiction of a transmitting bandpass frequency selective surface. (b) A conceptual depiction of a bandpass FSS frequency response.

dissertation is to introduce novel approaches and techniques to address the existing limitations and to advance the current state-of-the-art in various planar microwave devices. These devices are all designed based on a new class of sub-wavelength frequency selective surfaces – referred to as miniaturized-element frequency selective surfaces (MEFSS) [1, 19–27]. In the following section, a brief background review on miniaturized-element frequency selective surfaces is presented. This review is then followed up by the description of the current state-of-the-art and the proposed solutions. Finally, in the last section, an overview of the dissertation and the following chapters is presented.

## 1.2 Background on Miniaturized-Element Frequency Selective Surfaces

Traditionally, frequency selective surfaces are implemented using periodic arrangements of resonant elements. The elements used in such FSS can generally be categorized into two major types of dipole-type and aperture-type elements [28–32]. Because of the duality principle, the frequency responses of these two structures are expected to be dual of each other as shown in Fig. 1.2. The FSS with dipole-type elements demonstrates a bandstop filtering performance while that with aperture-type elements shows a bandpass response. Despite the differences in their performance, these two types of FSSs share the same feature that their elements are resonant near the frequency

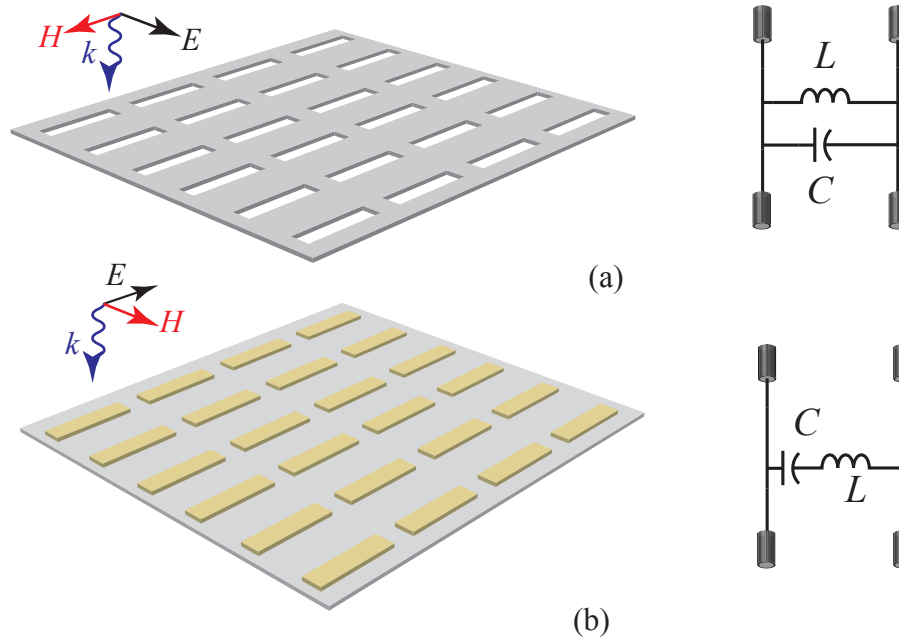


Figure 1.2 (a) Topology of a bandpass FSS with aperture-type elements. (b) Topology of a bandstop FSS with dipole-type elements.

of operation. It means that the length of either dipole or aperture is around half of the wavelength at the frequency of operation. The higher-order frequency responses of such structures are also achieved through cascading of these single-resonant FSS panels with the quarter wavelength spacing between adjacent panels. A major drawback of resonant-type FSSs is the poor angular performance. This sensitivity to the angle and polarization of the incoming waves originates from the large variations of the induced electric currents on the elements, which is mainly due to the bulkiness of the overall profile of the structures. Therefore, an intuitive method to improve the angular performance of the FSSs is to miniaturize the overall profile of these structures. To this end, over the past few years, a new class of frequency selective surfaces with sub-wavelength unit cell dimensions - referred to as miniaturized-element frequency selective surfaces (MEFSS) is introduced [1, 19–27]. In a contrast with traditional FSSs, these structures are entirely composed of non-resonant elements. The unit cell sizes of MEFSSs is around  $0.1\lambda_0 \sim 0.15\lambda_0$ , with  $\lambda_0$  being the operating wavelength [19]. The building blocks of MEFSSs are capacitive and inductive

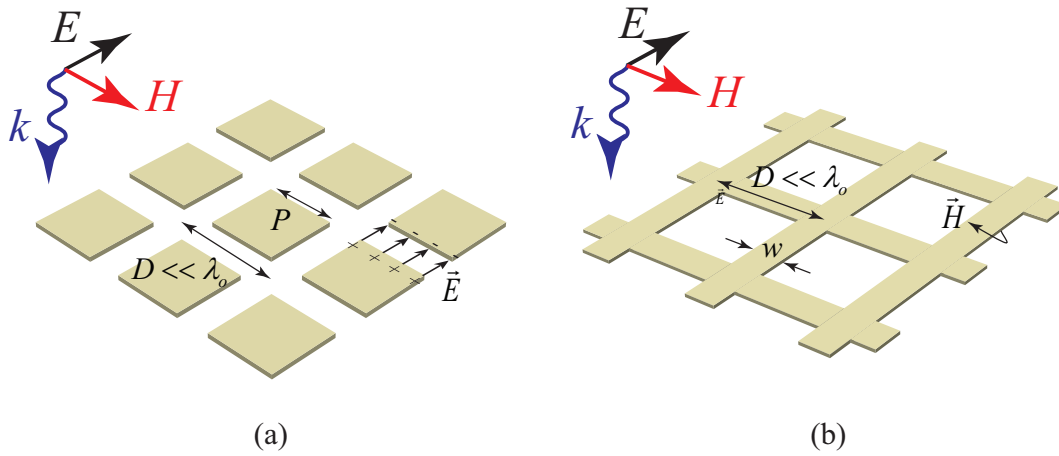


Figure 1.3 (a) A capacitive impedance sheet composed of a 2D array of sub-wavelength patches. (b) An inductive impedance sheet composed of a 2D array of sub-wavelength wire grids.

impedance sheets that are implemented using 2D periodic arrangements of sub-wavelength elements. In this MEFSS configuration, each capacitive layer is typically in the form of a 2D periodic arrangement of the sub-wavelength capacitive patches and each inductive layer is in the form of a 2D periodic arrangement of inductive wire grids. Fig. 1.3 explains the behaviour of these two surface through a quasi-static analysis. Employing these impedance sheets, any desired filtering response can be synthesized. For instance, Fig. 1.4(a) shows the topology and the equivalent circuit model of an MEFSS structure with a bandpass response. In this structure, the capacitive and inductive impedance sheets are repeated sequentially and separated from one another using thin dielectric substrates. Fig. 1.4(a) also shows the equivalent circuit model of this MEFSS, which is a bandpass coupled resonator filter. In this circuit model, the sub-wavelength capacitive patches are modeled with parallel capacitors and the sub-wavelength inductive wire grids are modeled using parallel inductors. The thin dielectric substrates separating the layers are also modeled with short sections of the transmission lines. Another example of MEFSS structures is shown in Fig. 1.4(b). This MEFSS structure has a low-pass type response and is composed of a number of capacitive impedance sheets that are separated from one another using thin dielectric substrates. Fig. 1.4(b) also shows the equivalent circuit model of the low-pass type MEFSS. Since the thin dielectric substrates can be modeled as series inductors, this circuit model is practically a classic low-pass type

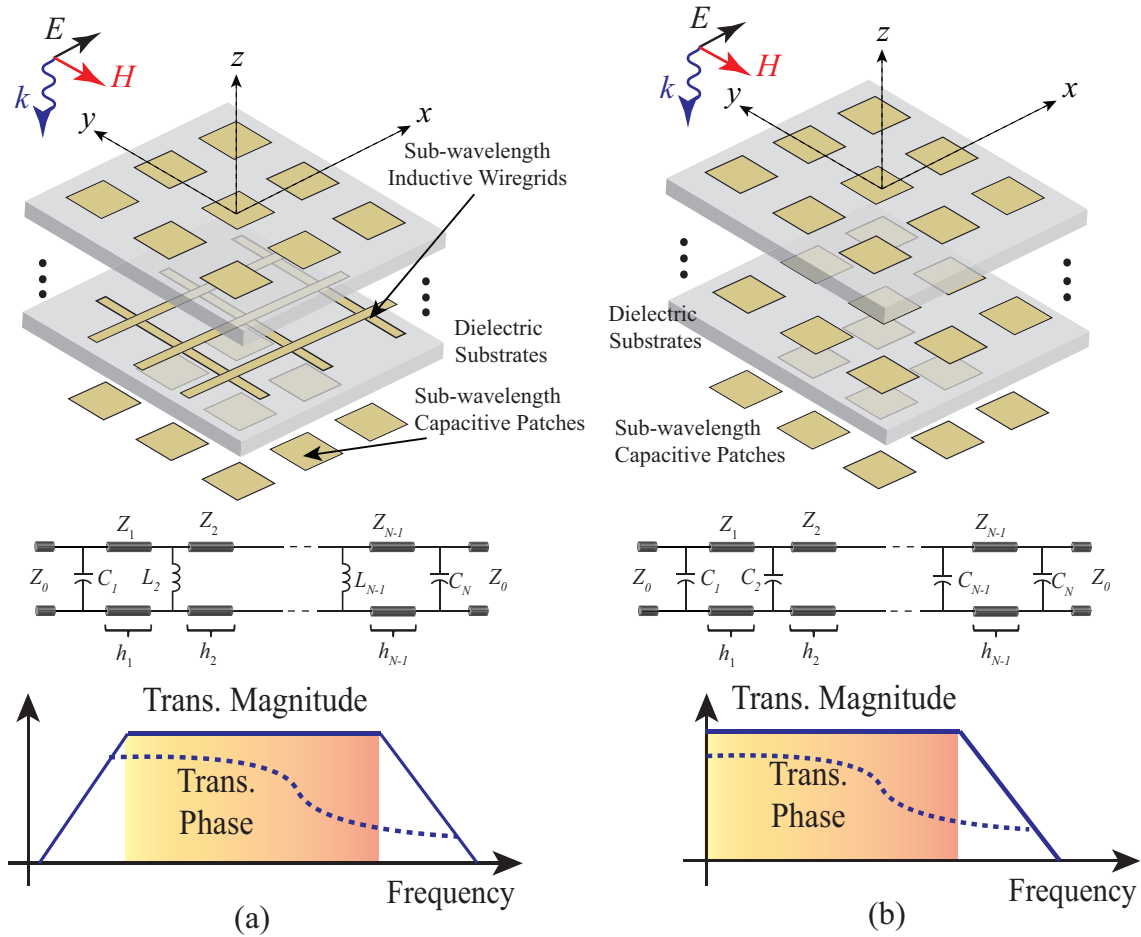


Figure 1.4 (a) Topology, equivalent circuit model, and conceptual frequency response of a bandpass-type MEFSS. (b) Topology, equivalent circuit model, and conceptual frequency response of a lowpass-type MEFSS.

filter. As discussed in Section 1.1, frequency selective surface can be used to manipulate the magnitude and/or the phase of the wave to obtain desired functionalities. This is also the case for the band-pass type and low-pass type MEFSSs shown in Fig. 1.4 since they selectively filter out the waves outside the transmission window and introduce a phase shift/time delay to the passing wave. Depending on the application, therefore, these two structures can be used either as spatial filters or as spatial phase shifters (SPS)/time-delay units (TDU). Due to such versatility, the band-pass type and low-pass type MEFSSs are employed as the building blocks in majority of the structures presented in this dissertation.

## 1.3 Current State-of-the-Art and the Proposed Approach

The main goal of this dissertation is to introduce novel approaches to address the existing challenges and to advance the current state-of-the-art in FSS-based microwave devices. Before describing each new finding in great detail, a brief background on the existing challenges in each category of these devices is presented in this section. In the following subsections, the current state-of-the-art and its corresponding practical challenges in spatial filters, reflectarrays and transmitarrays, and reconfigurable periodic structures is reviewed.

### 1.3.1 Spatial Filters

Based on the spatial filtering characteristics of frequency selective surfaces, they have been extensively used for numerous applications. One common application of FSS is to use them to reduce the radar cross section (RCS) of antennas used in low-observable or stealth platforms. In such applications, the RCS of the antenna is reduced by shielding it from the outside environment using a shaped bandpass FSS that is transparent within the desired frequency of operation of the antenna and opaque at other frequencies. While this approach works in principle, it suffers from few practical design problems. One important practical challenge is the existence of multiple spurious transmission windows occurring at frequencies higher than the main one in most FSSs reported in the literature (e.g. see pp. 26-62 of [2]). Although the high frequency harmonics will not impact the in-band performance, they could become critically important in certain stealth applications in which they coincide with a frequency at which the antenna presents a high RCS value. Another important challenge in using FSSs to reduce the RF signature of the platforms is achieving a narrow-band and highly-selective filtering performance. Such a response is maybe useful in designing radomes used for reducing the out-of-band RCS of a narrowband antenna. In addition to having narrow bandwidth, to sufficiently attenuate strong out-of-band signals, such FSSs should provide highly-selective responses with enough out-of-band rejection to perform the desired task. To achieve such operation in FSS, quality factors of their resonators must be increased. The existing solution to this problem is the miniaturization of the elements [33]. However, there is a limit

to the miniaturization levels that can be achieved using conventional printed circuit board (PCB) fabrication technology. These two practical challenges are respectively addressed in chapter 2 and 3 of this dissertation by introducing two new types of MEFSS structures. To achieve harmonic-free operation, a new miniaturization technique based on using multiple closely-spaced capacitive layers is introduced. A new type of MEFSSs synthesized based on inductively-coupled resonator filters is also presented to achieve narrowband, highly-selective responses.

As spatial filters, frequency selective surface are also employed to control and engineer the polarization of the waves in many applications. For instance, they have been used to design polarization converters and polarization selective surfaces. A polarization converter is a planar anisotropic structure that converts an incident wave with a given polarization to a reflected or transmitted wave with a different polarization. The function of a polarization selective surface, on the other hand, is to reflect one polarization of the wave while being transparent to the orthogonal polarization. In this category of devices, the focus of this dissertation is on two specific structures including linear-to-circular polarization selective surfaces and circular-polarization selective surfaces. Both devices are of particular interest in applications requiring circularly-polarized waves such as satellite communications. To date, many FSS-based polarization converters and polarization selective surfaces have been reported in the literature [34–48], [49–60]. However, these structures generally use resonant constituting elements and hence, they tend to be narrowband structures. Moreover, their performance degrades significantly when illuminated with obliquely incident waves. These deficiencies are not desired in many applications for which broadband performance with a wide range angular stability is required. These issues are addressed in Chapter 4 and 5 of this dissertation. First, a new technique for designing broadband linear-to-circular polarization converters based on anisotropic MEFSSs is introduced in chapter 4. Then, in Chapter 5, two of these polarization converts were combined with a linear polarizer to implement broad circular-polarization selective surfaces.

### 1.3.2 Transmitarray and Reflectarrays

Reflectarrays and transmitarrays have emerged as a competitive alternative to traditional reflectors and dielectric lenses as well as the flat phased arrays in many high-gain, pencil beam antenna applications. Planar apertures and the ability to conveniently shape the aperture phase and magnitude distributions are among the advantages of reflectarrays and transmitarrays over traditional bulky three-dimensional structures such as reflector or lens antennas. Reflectarrays and transmitarrays are generally composed of locally-periodic structures with unit cells that act as spatial phase shifters or time-delay units. These unit cells are commonly implemented from resonant building blocks (e.g. patch, dipole, or slot antennas) [61–70], [71–77]. Reflectarrays and transmitarrays designed based on these elements generally suffer from relative small bandwidths and tend to be highly dispersive when illuminated with broadband pulses. Therefore, they are not suitable for applications where signals with instantaneously broad bandwidths are used. In such applications, wideband reflectarrays and transmitarrays free of any chromatic aberration must be employed [14, 15]. The aforementioned issues are addressed in this dissertation by introducing new techniques to design broadband true-time-delay collimating surfaces. The proposed structures consist of planar aperture populated with miniature, sub-wavelength time-delay units. Each time delay unit is a unit cell of appropriately designed MEFSS and it is designed to provide a constant time delay over the frequency range at which the array operates. The local transfer function of these time-delay units may then be tailored to allow the reflectarray or transmitarray to convert the electric field distribution of the electromagnetic wave impinging on its aperture to a desired electric field distribution over the output aperture. Based on this concept, the design of a transmitarray-based antenna composed of a true-time-delay transmitarray and a focal plane array is presented in chapter 6. Then, the design of linearly-polarized and circularly-polarized true-time-delay reflectarrays is presented in chapters 7 and 8 of this dissertation.

### 1.3.3 Reconfigurable Periodic Structures

With the ever-growing development and deployment of multifunctional systems, the need for designing periodic structures (e.g. frequency selective surfaces) with agile frequency responses is

also growing. To date, significant amount of research has been devoted towards achieving this goal and various techniques have been proposed so far. The most common approach used in the design of a reconfigurable periodic structure is to incorporate electronically-tunable elements (e.g. solid state or MEMS varactors, switches, etc.) into its unit cells in order to tune its response [78–82]. However, this approach suffer from several challenges. First, using this approach is not practical for large-scale periodic structures. This is due to the fact that a moderately-sized section of a periodic structure can easily contain tens of thousands of unit cells (and hence, several tens of thousands of lumped-elements) that must be controlled together to achieve dynamic reconfiguration. The integration, biasing, and RF/DC isolation of all these elements within the structure present a significant challenge. The nonlinearity of the electronic elements as well as the difficulties in thermal managements are also other existing issue especially in high power applications. These issue significantly exacerbate as we move from microwave frequencies to millimeter-wave (MMW) and sub-MMW frequencies. In addition to electronic tuning, other tuning techniques used to tune the responses of periodic structures have included using ferroelectric dielectrics [83], magnetically controlled materials [84], liquid crystals [85], optically controlled materials [86], graphene [87,88], and fluidic tuning techniques [89,90]. While these techniques have certain advantages that make them interesting for particular applications, they are not as widely studied as electronic tuning techniques. Consequently, more research and development is needed to determine whether or not they can be suitable to design large-scale tunable periodic structures.

The proposed approach in this dissertation to overcome the aforementioned challenges is to exploit mechanical movements or deformations in the fabric of the structure to achieve tunability. This eliminates the need for integrating any additional elements with the individual unit cells of the structure and can easily be applied to very large-scale structures. In chapter 9 of this dissertation, three different mechanical techniques are examined which can be used to tune the responses of two elementary types of periodic structure with non-resonant capacitive or inductive response types which are shown in Fig 1.3. These techniques include overlapping combined with relative movement, stretching/compression, and flexure. The importance of the elementary capacitive and inductive structures examined here is that they are the fundamental building blocks of a wide range

of other different periodic structures with more complex unit cells and response types including spatial filters, reflectarrays, and transmitarrays. Then, in chapter 10, a new mechanical beam steering technique referred to as Macro-Electro-Mechanical Systems (MÆMS) is introduced. This technique exploits macro-scale mechanical movements over parts of an aperture to achieve beam steering. The attributes of this technology are expected to make this technology a promising candidate for development of affordable phased-array antennas at microwave, millimeter-wave, and THz frequency bands.

## **1.4 Thesis overview**

As discussed in earlier sections, the aim of this research to advance the current state-of-the-art in spatial filters, transmitarrays, and reflectarrays by addressing the existing limitations. The efforts undertaken to accomplish this research goal have been presented in detail in several chapters of this dissertation. A brief overview of each chapter follows in the later subsections.

### **1.4.1 Chapter 2**

In this chapter, a new technique for designing miniaturized-element frequency selective surfaces with bandpass responses and no spurious transmission windows over extremely large bandwidths is presented. The proposed harmonic-suppressed MEFSSs consist of multiple metallic and dielectric layers. Each metallic layer is in the form of a two-dimensional arrangement of capacitive patches or an inductive wire grid with extremely sub-wavelength periods. Harmonic-free operation in these structures is achieved by using multiple, closely-spaced capacitive layers with overlapping unit cells to synthesize a single, effective capacitive layer with a larger capacitance value. This allows for reducing the unit cell size of a conventional MEFSS considerably and moving the natural resonant frequencies of its constituting elements to considerably higher frequencies. Consequently, the spurious transmission windows of such MEFSSs, which are caused by these higher-order harmonics, can be shifted to very high frequencies and an extremely broad frequency band free of any spurious transmission windows can be obtained. Using this technique, an MEFSS with a second-order bandpass response is designed to operate at 3.0 GHz with 20% fractional bandwidth and be

free of spurious transmission bands up to 27.0 GHz. A prototype of this harmonic-free MEFSS is fabricated and experimentally characterized in the lab. Measurement results confirm harmonic-free operation of the proposed FSS for incidence angles in the  $\pm 60^\circ$  range for both the TE and TM polarizations of incidence.

### 1.4.2 Chapter 3

In this chapter, a new method for designing miniaturized-element frequency selective surfaces with narrowband, bandpass responses of order  $N \geq 2$  is presented. The proposed structure is composed of two-dimensional periodic arrays of sub-wavelength inductive wire grids separated by dielectric substrates. A simple equivalent circuit model, composed of transmission line resonators coupled together with shunt inductors, is presented for this structure. Using this equivalent circuit model, an analytical synthesis procedure is developed that can be used to synthesize the MEFSS from its desired system level performance indicators such as the center frequency of operation, bandwidth, etc. Using this synthesis procedure, a prototype of the proposed MEFSS with a second-order bandpass response, center frequency of 21 GHz, and fractional bandwidth of 5% is designed, fabricated, and experimentally characterized. The measurement results confirm the theoretical predictions and the design procedure of the structure and demonstrate that the proposed MEFSS has a stable frequency response with respect to the angle of incidence of the EM wave in the  $\pm 40^\circ$  range for both TE and TM polarizations of incidence.

### 1.4.3 Chapter 4

A new technique for designing wideband polarization converters based on miniaturized-element frequency selective surfaces is presented in this chapter. The proposed structure is a two-dimensionally anisotropic periodic structure composed of arrays of sub-wavelength capacitive patches and inductive wire grids separated by thin dielectric substrates. The structure is designed to behave differently for field components of the two orthogonal polarizations and transmits a circularly-polarized wave once illuminated by a linearly-polarized plane wave. Using equivalent circuit models for MEFSSs, a synthesis procedure is developed that can be used to design the polarization converter

from its required bandwidth and center frequency of operation. Using this procedure, a prototype of the proposed polarization converter operating within the X-band is designed, fabricated, and experimentally characterized using a free-space measurement system. The measurement results confirm the theoretical predictions and the design procedure of the structure and demonstrate that the proposed MEFSS-based polarization converter operates in a wide field of view of  $\pm 45^\circ$  with a fractional bandwidth of 40%.

#### **1.4.4 Chapter 5**

In this chapter, a new technique for designing wideband circular-polarization selective surfaces (CPSSs) based on anisotropic miniaturized element frequency selective surfaces is introduced. The proposed structure is a combination of two linear-to-circular polarization converters, presented in chapter 4, sandwiching a linear polarizer. This CPSS consists of a number of metallic layers separated from each other by thin dielectric substrates. The metallic layers are in the form of two-dimensional arrays of subwavelength capacitive patches and inductive wire grids with asymmetric dimensions and a wire grid polarizer with sub-wavelength period. The proposed device is designed to offer a wideband circular-polarization selection capability allowing waves with left-hand circular polarization to pass through while rejecting those having right-hand circular polarization. A synthesis procedure is developed that can be used to design the proposed CPSS based on its desired band of operation. Using this procedure, a prototype of the proposed CPSS operating in the 12-18 GHz is designed. Full-wave electromagnetic simulations are used to predict the response of this structure. These simulation results confirm the validity of the proposed design concept and synthesis procedure and show that proposed CPSS operates within a fractional bandwidth of 40% with a co-polarization transmission discrimination of more than 15 dB. Furthermore, the proposed design is shown to be capable of providing an extremely wide field of view of  $\pm 60^\circ$ .

#### **1.4.5 Chapter 6**

In this chapter, the design, simulation, and measurement results of a broadband, low-profile, multi-beam antenna is presented. The antenna uses multiple feed elements placed on the focal

plane of a planar microwave lens to achieve high-gain, multi-beam operation with a wide field of view. The lens employs the constituting unit cells of appropriately designed miniaturized-element frequency selective surfaces as its spatial time-delay units. A new technique for modeling such lenses is also presented that greatly simplifies the full-wave electromagnetic simulation of MEFSS-based lenses. This technique is based on treating the pixels of the lens as effective media with the same effective permittivity and permeability and significantly reduces the difficulty of modeling and optimizing the proposed multi-beam antenna with its relatively large aperture size in a full-wave electromagnetic simulation tool. Using this procedure, a prototype multi-beam antenna operating in the 8-10 GHz range is designed. The prototype is fabricated and characterized using a multi-probe, spherical near field system. The measurement results are in good agreement with the simulation results obtained using the proposed simplified modeling technique. Measurements demonstrate consistent radiation characteristics over the antenna's entire operational band with multiple beams in a field of view of  $\pm 45^\circ$ .

#### **1.4.6 Chapter 7**

A new method for designing low-profile reflectarray antennas with broadband, true-time-delay (TTD) responses is presented in this chapter. Such structures are composed of numerous reflective spatial time delay units distributed over a planar surface. Each spatial time delay unit is a unit cell of a ground-plane-backed miniaturized-element frequency selective surface composed of non-resonant elements. Each element is a lowpass type MEFSS composed of a stack of non-resonant patches separated from one another by thin dielectric substrates and the whole structure is backed with a ground plane. A prototype of the proposed MEFSS-based TTD reflectarray with the focal length to aperture diameter ratio ( $f/D$ ) of 0.87 operating at the center frequency of 10 GHz is designed, fabricated, and experimentally characterized both in time and frequency domains. It is demonstrated that the fabricated TTD reflectarray operates over a bandwidth of 40% without any significant chromatic aberrations. The proposed antenna provides a realized gain of 23 dB when fed with an X-band horn antenna and shows a gain variation of about 4 dB in the 8-12 GHz

range. The antenna also shows consistent radiation characteristics and relatively low side-lobe levels across its entire band of operation.

### **1.4.7 Chapter 8**

In this chapter, a new technique for designing low-profile circularly-polarized reflectarray antennas with ultra-wideband, true-time-delay responses is presented. The proposed reflectarray uses the unit cells of ground-plane-backed, anisotropic miniaturized-element frequency selective surfaces as its spatial time-delay units (TDUs). Each TDU is composed of a stack of non-resonant rectangular-shaped capacitive patches featuring asymmetric gap spacings and separated from one another by thin dielectric substrates. The TDUs are designed to provide a reflection phase difference of  $90^\circ$  between the horizontal and vertical components of the incident wave over a wide bandwidth. This way, a linearly-polarized incident field is converted to a circularly-polarized radiated wave. A device prototype that operates at X band is designed, fabricated, and measured. Measurement results demonstrated that the reflectarray antenna provides a gain of 23.7 dB with variations less than 3 dB within the 8-12 GHz operating frequency range or equivalently 40% bandwidth. Time-domain measurement results demonstrate the suitability of this device for operation with wideband pulses. The reflectarray is also used in a multi-beam antenna and it is shown that the structure provides a wide-angle scanning performance with a field of view of  $\pm 45^\circ$ .

### **1.4.8 Chapter 9**

Various techniques for designing large-scale, mechanically-tunable periodic structures (PSs) is presented in this chapter. Overlapping combined with relative movement, stretching/compression, and flexure are the three mechanical tuning techniques studied in this chapter. We demonstrate that all of these mechanical movements may be used to tune the capacitance and inductance of elementary periodic structures with capacitive and inductive surface impedances over wide ranges of values. Analytic formulas for calculating the variable inductance and capacitance of these tunable PSs are also provided. These elementary PSs are the building blocks of a wide range of other PSs with more complicated unit cells and response types. One such structure — a frequency selective

surface composed of series combination of these inductive and capacitive structures — is also examined to demonstrate the application of the proposed tuning and analysis concepts. The FSS is fabricated on an accordion-like substrate that can be contracted or stretched to change its frequency of operation. The response and tuning properties of this structure are experimentally characterized using a free-space measurement system. A very good agreement between theory and experiment is obtained. This demonstrates that the behavior of such complex mechanically-tunable PSs can be analyzed by examining the behavior of their constitutive inductive and capacitive elements.

### **1.4.9 Chapter 10**

In this chapter, a new approach to perform beam steering in reflecting type apertures such as reflectarray antennas is presented. The proposed technique exploits macro-scale mechanical movements of parts of the structure to achieve two-dimensional beam steering without using any solid-state devices or phase shifters integrated within the aperture of the antenna. The principles of operation of this beam steering technique are demonstrated in an aperture occupied by ground-plane-backed, sub-wavelength capacitive patches with identical dimensions. We demonstrate that by tilting the ground plane underneath the entire patch array layer, a phase shift gradient can be created over the aperture of the reflectarray that determines the direction of the radiated beam. Changing the direction and slope of this phase shift gradient on the aperture allows for performing beam steering in two dimensions using only one control parameter (i.e., tilt vector of the ground plane). A proof-of-concept prototype of the structure operating at X-band is designed, fabricated, and experimentally characterized. Experiments demonstrate that small mechanical movements of the ground plane (in the order of  $0.05\lambda_0$ ) can be used to steer the beam direction in the  $\pm 10^\circ$  in two dimensions. It is also demonstrated that this beam scanning range can be greatly enhanced to  $\pm 30^\circ$  by applying this concept to the same structure when its ground plane is segmented.

### **1.4.10 Chapter 11**

The objective of this chapter is to provide some insight with respect to the future work of this dissertation. The presented ideas include random frequency selective surfaces, MÆEMS-based beam steering leaky wave antennas, and infrared spatial filters and lenses.

## Chapter 2

# Harmonic-Suppressed Miniaturized-Element Frequency Selective Surfaces with Higher-Order Bandpass Responses

### 2.1 Introduction

Frequency selective surfaces (FSSs) have been the subject of numerous studies so far. At microwave and millimeter-wave frequencies, FSSs are used in a wide range of applications including spatial filters [2], [8], radar absorbing materials [91], [92], artificial magnetic conductors [11], [12], planar lenses [13], [14] and reflectarrays [16]. One common application of FSSs is to use them to reduce the radar cross section (RCS) of antennas used in low-observable or stealth platforms. Most antennas act as efficient scatterers both at the frequency band(s) that they are designed to operate in and at other frequency bands that fall outside of their desired frequency range of operation. A typical low-observable platform may have several low-frequency antennas operating at VHF and UHF bands. These antennas act as very efficient scatterers at higher frequencies where many radars operate at. In such applications, the RCS of the antenna can be reduced by shielding it from the outside environment using a shaped bandpass FSS that is transparent within the desired frequency of operation of the antenna and opaque at other frequencies. While the aforementioned RCS reduction approach works in principle, it suffers from a practical design problem. Namely, most FSSs reported in the literature have multiple spurious transmission windows occurring at frequencies higher than that of the main one (e.g. see pp. 26-62 of [2]). Although the high frequency harmonics typically will not impact the in-band performance of these FSSs, they could become critically important in certain stealth applications in which they coincide with a frequency at which the antenna presents a high RCS value. For an FSS designed to work at a low frequency

(e.g. UHF), a number of these spurious transmission windows can fall within the 1-20 GHz range where many radars operate. Thus, in such applications, suppression of the spurious harmonics of the FSS is highly desired.

A number of previous studies has been conducted in this area [93–95]. In [93], an absorptive/transmissive radome is presented. The presented multilayer structure is formed by placing an artificial absorbing coating on a frequency selective surface. This structure, however, achieves absorption properties by using a uniform resistive layer of conductive fiber, which deteriorates the in-band performance of the radome as well. In [94], a bandpass FSS with quasi-elliptic response and wide-stopband characteristics is reported. The structure is formed by cascading periodic arrays of double square loops and gridded square loops. However, this approach requires using several metallic layers separated from one another by rather thick dielectric substrates to design a low-frequency (e.g. UHF) FSS. This leads to a relatively large overall thickness for the FSS (compared to the wavelength) that makes the response of the structure sensitive to the angle and polarization of incidence of the EM wave. In [95], a bandpass FSS with wideband absorbing properties is presented. The reported structure behaves as a bandpass filter in the main band of operation, while behaving as an absorber above the main band. This is realized by cascading a bandpass FSS and a resistive high-impedance surface which uses the FSS as the ground plane within its total reflection band. Although a relatively good performance was observed under normal incidence of the EM wave, the performance of this structure degrades when the structure is illuminated with an obliquely incident wave. The problem can be attributed to the absorption properties of the resistive surface which degrade as a function of the incident angle. As a result, some harmonics appear within the absorption band. This is not desirable in low-observable FSS and radome applications.

Over the past few years, several new classes of frequency selective surfaces with sub-wavelength unit cells dimensions are reported [1, 19–27]. These structures are referred to as miniaturized element frequency selective surfaces (MEFSSs)<sup>1</sup>. Depending on the specific design process, MEFSSs are composed of entirely non-resonant constituting elements (e.g., [1, 19–22]), or a combination of

---

<sup>1</sup>While FSSs that have miniaturized unit cell dimensions have been studied for a long time (e.g. [96]), we use the term MEFSS to refer to FSSs with unit cells that are composed of primarily non-resonant elements (e.g., sub-wavelength capacitive patches or wire grids).

resonant and non-resonant elements (e.g. [23, 24], [25–27]). MEFSSs are shown to have very stable responses for a wide range of incidence angles and polarizations of incidence [1, 19–24]. They also have been used to design tunable FSSs [81], [89] as well as FSSs for high-power microwave (HPM) applications [89, 97].

In this chapter, we present a new type of MEFSS that shows a bandpass response, which is free of spurious transmission windows over an extremely wide frequency band. The proposed harmonic-free MEFSS is composed of multiple metallic layers separated from one another by thin dielectric substrates. Each metallic layer is a two-dimensional periodic structure composed of capacitive patches or inductive wire grids with extreme sub-wavelength dimensions. A prototype of the proposed harmonic-free MEFSS with a second-order bandpass response, center frequency of operation of 3.0 GHz, and fractional bandwidth of 20% is designed and is shown to be harmonic free up to approximately 27 GHz<sup>2</sup>. A prototype of the proposed structure is also fabricated and experimentally characterized in the lab. It is demonstrated that the proposed structure maintains its harmonic-free, second-order bandpass response for both the TE and TM polarizations with incidence angles in the  $\pm 60^\circ$  range up to 27 GHz.

## 2.2 Principles of Operation

### 2.2.1 Sources of Harmonics in MEFSSs

Fig. 2.1(a) shows the three-dimensional topology of different layers of a miniaturized element frequency selective surface with an  $(\frac{N+1}{2})^{th}$ -order bandpass response ( $N$  is the number of metallic layers used in this structure and is always an odd number [1]). The structure consists of two-dimensional periodic arrangements of sub-wavelength capacitive patches and planar wire grids, separated from one another by thin dielectric substrates. Assuming that the thickness of the substrate between two consecutive metal layers is  $h$ , the overall thickness of the FSS is  $(N - 1) \times h$ . The top views of one unit cell of a capacitive layer and that of an inductive layer are shown in the inset of Fig. 2.1(a). The dimension of each unit cell along the  $x$  and  $y$  directions is  $D$ . The

---

<sup>2</sup>The frequency of main transmission window is chosen primarily for ease of measurement. The concepts proposed in this chapter can easily be applied to MEFSSs operating at the VHF and lower UHF frequencies as well.

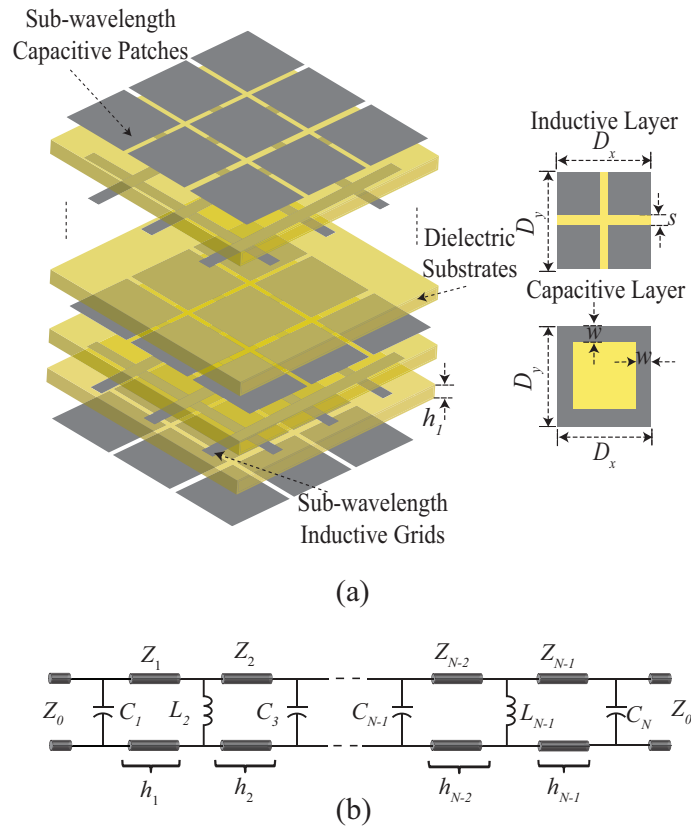


Figure 2.1 (a) Topology of the bandpass MEFSS presented in [1]. The top view of the unit cells of the capacitive and inductive layers are shown on the right hand side of the figure. (b) Equivalent circuit model of the MEFSS. The structure has  $N$  metal layers and acts as an FSS with an  $(\frac{N+1}{2})^{th}$ -order bandpass response.

capacitive patches are in the form of square metallic patches with dimensions of  $D - s_i$ , where  $s_i$  is the gap between the two adjacent patches in the  $i^{th}$  layer. The inductive wire grids are the combination of two metallic strips with the width of  $w$  oriented perpendicularly to each other. Assuming the same periodicity in both  $x$  and  $y$  directions, the frequency responses of the capacitive and inductive layers (and that of the FSS) are insensitive to the polarization of the incident wave for normal incidence.

This FSS can be modeled with the equivalent circuit model shown in Fig. 2.1(b), which is valid for a normally incident plane wave. In this circuit model, the capacitive patch layers are modeled

with parallel capacitors  $C_1, C_3, \dots, C_N$ . The inductive wire grids are represented by parallel inductors  $L_2, \dots, L_{N-1}$ , and the thin dielectric substrates separating the inductive and capacitive layers are modeled with transmission lines with the characteristic impedances of  $Z_1, \dots, Z_{N-1}$  and lengths of  $h_1, \dots, h_{N-1}$ . Free space on each side of the FSS is modeled with semi-infinite transmission lines with characteristic impedances of  $Z_o = 377\Omega$ . The design procedure of this device is based on synthesizing the desired filter response from the equivalent circuit model presented in Fig. 2.1(b), and mapping these equivalent circuit parameter values to the physical parameters of the FSS. This can be done using the procedure described in [1] and will not be repeated here for brevity.

Using the design procedure reported in [1], an MEFSS with a second-order bandpass response having a center frequency of operation of 3.0 GHz and a fractional bandwidth of 20% is designed. This structure is composed of two capacitive layers, one inductive layer, and two dielectric substrates. The physical parameters of this structure as well as the parameters of its equivalent circuit model are presented in Table 2.1. This MEFSS is simulated using full-wave electromagnetic (EM) simulations in CST Microwave Studio and its frequency response is calculated over an extremely broad frequency band. Fig. 2.2 shows the calculated transmission coefficient of this structure for a normally-incident plane wave in the frequency range of 0-30 GHz. As can be seen, in addition to the main transmission band centered at 3.0 GHz, there are multiple spurious transmission windows occurring at higher frequencies than that of the main one. The primary contributors to these harmonics are the resonances of the patches in the capacitive layers and the slots in the inductive layer that occur at higher frequencies. For example, the frequency of the first resonance of the capacitive patches in the capacitive layer and the slots in the inductive layer can be approximated using equations (2.1)-(2.2):

$$f_{r,cap} = \frac{c}{2(D - s)\sqrt{\epsilon_{r,eff,i}}} \quad (2.1)$$

$$f_{r,ind} = \frac{c}{2(D - w)\sqrt{\epsilon_{r,eff,i}}} \quad (2.2)$$

where  $D$ ,  $s_i$ , and  $w_i$  are the physical parameters of the FSS unit cell shown in Fig. 2.1,  $c$  is the speed of light, and  $\epsilon_{r,eff,i}$  is the effective dielectric constant for the  $i^{th}$  metallic layer of the FSS. In

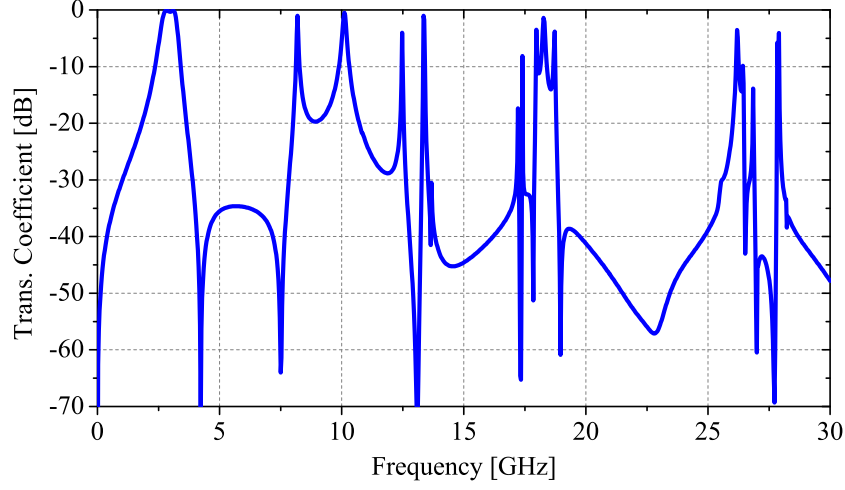


Figure 2.2 Calculated transmission coefficient of the 2<sup>nd</sup>-order bandpass FSS discussed in Section 2.2.1 with the parameters shown in Table 2.1. Results are obtained using full-wave EM simulation in CST Microwave Studio.

Table 2.1 Physical and electrical parameters of the 2<sup>nd</sup>-order MEFSS with a center frequency of 3 GHz and the fractional bandwidth of  $\delta = 20\%$  discussed in Section 2.2.1.

<i>Parameter</i>	$D_x$	$D_y$	$s$	$w$
<i>Value</i>	24 mm	24 mm	0.35 mm	11 mm
<i>Parameter</i>	$h$	$C_1$	$L_2$	$C_3$
<i>Value</i>	1.575 mm	1.18 pF	0.34 nH	1.18 pF

the second-order MEFSS example under discussion in this section,  $\epsilon_{r,eff,1} = \epsilon_{r,eff,3} \approx \frac{\epsilon_r + 1}{2}$  for the capacitive layers and  $\epsilon_{r,eff,2} \approx \epsilon_r$  for the inductive layer. Notice that in equations (2.1)-(2.2) the effect of the interaction between different layers on the higher-order resonances of the constituting elements in each unit cell is ignored. Therefore, these formulas represent approximations of the actual resonant frequencies of the capacitive patches and apertures in the inductive layers. Using equations (2.1)-(2.2) along with the physical parameters of the MEFSS provided in Table 2.1, the first resonant frequencies of the capacitive patches and the slots in the inductive layers are calculated to be 5.0 GHz and 7.8 GHz, respectively. At their first resonance, the patches in the capacitive layers act as band-stop elements, whereas the apertures in the inductive layer act as

bandpass elements (see pp. 26-62 of [2]). Therefore, the first spurious transmission window of this second-order MEFSS is expected to occur at a frequency close to the resonant frequency of the apertures in the inductive layer. Fig. 2.2 shows that this is indeed the case. At higher frequencies, the higher-order resonant modes of the elements, the complex interactions between different layers, as well as the grid resonances (grating lobes) occurring at  $D = n\lambda$  (e.g. see pp. 26-62 of [2]) result in additional transmission windows and transmission nulls in the transmission coefficient of this device as can be observed in Fig. 2.2.

### 2.2.2 A Concept for Designing Harmonic-Free MEFSSs

Since the first spurious passband of this MEFSS is caused by the natural harmonics of its constituting elements, an effective method for removing that from the desired frequency band of operation is to reduce the unit cell size of the structure. From (1)-(2), it can be seen that reducing  $D$  shifts these resonant frequencies to higher values. In doing this, however, the effective inductance and capacitance values provided from the metallic layers of the MEFSS must not change in order to maintain the frequency response of the structure within the desired transmission band (i.e., the element values of the equivalent circuit model of the MEFSS must not change). This shifts the spurious transmission bands to higher frequencies without disturbing the frequency response of the FSS within the desired operating band. However, implementing this in practice can be challenging, since reducing the period of the MEFSS while maintaining the desired capacitance and inductance values results in significant reduction of the minimum feature sizes of the unit cell of the MEFSS (i.e., the gap size between capacitive patches  $s_i$  and the width of the inductive wires  $w_i$ ) [1]. For MEFSSs of the type shown in Fig. 2.1, however, this problem is more severe for the capacitive patch layers and the gap spacing between adjacent capacitive patches in these layers is the bottleneck in the process of miniaturization of the MEFSS unit cell [98]. In practice, the minimum spacing between the adjacent capacitive patches in each capacitive layer of the FSS,  $s_i$ , is determined by the minimum feature size that can be reliably fabricated using any given fabrication procedure. For most standard lithography techniques used in printed circuit board

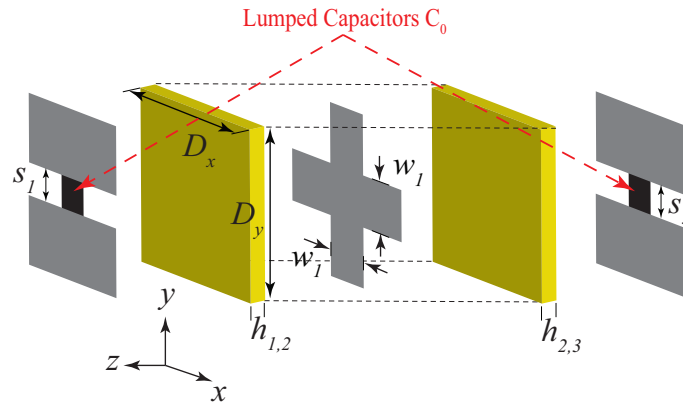


Figure 2.3 The unit cell of the  $2^{nd}$ -order bandpass MEFSS with the lumped capacitors loading the capacitive patch layers.

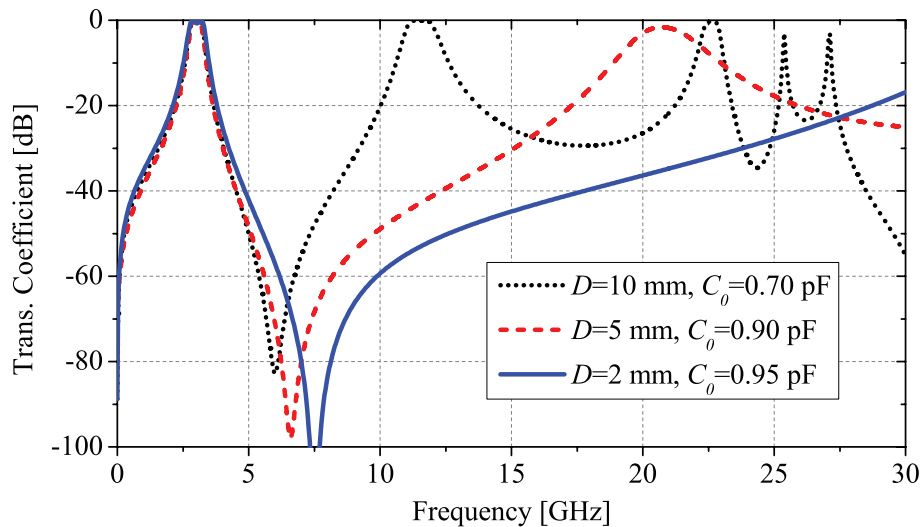


Figure 2.4 Calculated transmission coefficients of the  $2^{nd}$ -order bandpass MEFSS discussed in Section 2.2.2 where the capacitive patches are loaded with lumped-element capacitors. Results are obtained using full-wave EM simulation in CST Microwave Studio.

(PCB) fabrication, this minimum feature size is about 0.15 mm. Therefore, achieving the desired capacitance value from an extremely sub-wavelength periodic structure is rather challenging.

One technique for achieving the desired capacitance value in such situations is shown in Fig. 2.3. In this case, lumped-element capacitors  $C_0$  are placed in parallel between the two adjacent edges of nearby capacitive patches. Taking the intrinsic capacitance of the unloaded capacitive patch layer,  $C_i$ , into account, the total capacitance of each capacitive layer in this structure can be

modeled with a parallel combination of  $C_0$  and  $C_i$ . Using this topology, the unit cell size of the capacitive patches of the structure can be reduced while maintaining the required capacitance value. To demonstrate this in practice, three different MEFSSs of the type shown in Fig. 2.3 are designed and simulated. All of these MEFSSs have second-order bandpass responses centered at 3.0 GHz and a fractional bandwidth of 20%. For all three cases, the gap sizes in the capacitive layers are  $s = s_1 = s_3 = 0.35$  mm, and the thicknesses of the substrates are  $h_{1,2} = h_{2,3} = 1.575$  mm. However, these MEFSSs have different periods and consequently, use different lumped-element capacitor values to maintain the desired frequency response. Fig. 2.4 shows the transmission coefficients of these three MEFSSs obtained using full-wave EM simulations in CST Studio. As expected, the frequencies of the spurious transmission windows increase as the unit cell sizes of the MEFSSs decrease. For example, for the structure with the unit cell size of  $D = 10$  mm, and the lumped capacitor value of  $C_0 = 0.7$  pF, the first spurious transmission window occurs at 11.5 GHz. As the unit cell size is decreased (and  $C_0$  is increased), the frequency of the first spurious transmission window increases as well and in the extreme case of  $D = 2$  mm and  $C_0=0.95$  pF, the first spurious transmission window occurs at a frequency above 30 GHz.

### 2.2.3 Practical Implementation of Harmonic-Free MEFSSs

While this design example confirms the feasibility of removing spurious transmission bands from the responses of MEFSSs over a very wide frequency range, a major challenge limits the practicality of implementing MEFSSs of the type shown in Fig. 2.3. Specifically, the number of lumped elements needed to achieve the desired response can become extremely large, even in small FSS panels. For example, for  $D = 2$  mm, a 10 cm  $\times$  10 cm panel of the second-order MEFSS whose response is shown in Fig. 2.4 requires about 10,000 lumped capacitors (2 capacitive layers, 2500 capacitive patches per layer, and 2 lumped capacitors per patch to ensure polarization insensitivity). This becomes even more challenging when a higher-order filter response is required, since the number of capacitive layers in these filters increases [1]. Additionally, in MEFSSs with bandpass responses of order  $P \geq 3$ ,  $P - 2$  capacitive layers are sandwiched by dielectric substrates on both sides and are not directly accessible [1].

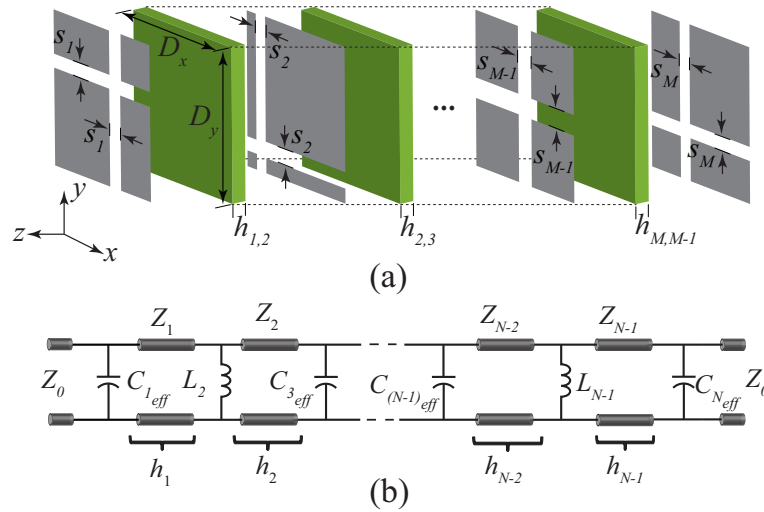


Figure 2.5 (a) Multiple closely-spaced capacitive patch layers are used to synthesize a single effective capacitive layer. The dielectric substrates are extremely thin. The unit cells of the patches used in different layers can overlap with each other and do not necessarily have to be aligned together. (b) The equivalent circuit model of a generalized MEFSS of the type shown in Fig. 2.1 in which each one of the capacitive layers is substituted with a composite, multi-layer effective capacitive layer similar to that shown in Fig. 2.5(a). In this equivalent circuit model  $C_{i,eff}$  represents the effective capacitance of each of the composite, multi-layer capacitive structures that are used to synthesize the  $i^{th}$  capacitive layer of the MEFSS shown in Fig. 2.1(a).

While the direct implementation of the MEFSS shown in Fig. 2.3 using lumped elements is challenging, alternative implementation techniques can be envisioned that address the practical problems of using lumped elements in a periodic structure. One such technique is to use cascaded capacitive patches separated by very thin dielectric substrates to synthesize a single capacitive layer with an effectively larger capacitance. In such an arrangement, each capacitive layer of the original MEFSS shown in Fig. 2.1 is replaced with multiple, closely-spaced capacitive patch layers. In general, as the period of the MEFSS is reduced, the number of closely-spaced capacitive patch layers needed to synthesize an effective capacitance layer will increase. Fig. 2.5(a) shows the unit cell of an effective capacitive layer composed of  $M$  individual capacitive patches separated from one another by  $M - 1$  extremely thin dielectric substrates. For small substrate thicknesses, all these capacitive patches can be considered to be in parallel with one another and hence, they constitute a single composite capacitive layer with a larger capacitance value. Additionally, different capacitive

patch layers that constitute the composite capacitive layer can overlap with each other to further increase the capacitance of the composite structure. Using  $M$  closely-spaced capacitive patch layers to implement each single capacitive layer of the MEFSS shown in Fig. 2.1 will increase the total number of metallic layers of the MEFSS to  $M \times P + P - 1$ , where  $P = \frac{N+1}{2}$  is the order of the filter, and  $N$  is the total number of metallic layers of the original MEFSS shown in Fig. 2.1. The equivalent circuit model of the whole structure is shown in Fig. 2.5(b). Here, the combination of cascaded capacitive patches are modeled with  $C_{1_{eff}}, \dots, C_{N_{eff}}$ . Each capacitor in this equivalent circuit represents the effective capacitance obtained from one combination of  $M$  closely-spaced capacitive layers. The sub-wavelength inductive wiregrids are modeled with  $L_2, \dots, L_{N-1}$  and the dielectric substrates separating the inductive layers and combined capacitive layers are modeled with the transmission lines with the lengths of  $h_1, \dots, h_{N-1}$  and the characteristic impedances of  $Z_1, \dots, Z_{N-1}$ . Free space on each side of the FSS is modeled with semi-infinite transmission lines with the characteristic impedances of  $Z_o = 377\Omega$ .

There are a number of parameters that influence the effective capacitance obtained from the combination of cascaded patches. These include the number of capacitive layers in the cascade arrangement, the gap size between the adjacent capacitive patches in each layer, and the thickness and the dielectric constants of the separating substrates. Increasing the number of layers increases the effective capacitance but it will also increase the total number of layers used in the MEFSS and increases the overall thickness and the complexity of the design. Therefore, in the rest of this chapter, we focus on designs that use only two cascaded capacitive layers to synthesize each of the constituting capacitive layers of the MEFSS of Fig. 2.1. Decreasing the gap size, increasing the dielectric constant value of the separating substrates, and decreasing their thicknesses will all increase the effective capacitance value. However, these parameters are primarily determined by the fabrication technology or the availability of commercially available substrates. In addition to these parameters, the capacitance value also depends on the offset overlap between two cascaded patches in the capacitive layer.

To demonstrate the effect of offset overlapping, we have examined a periodic structure composed of two capacitive patch layers with unit cell dimensions of  $D = 6.5$  mm and the gap spacing

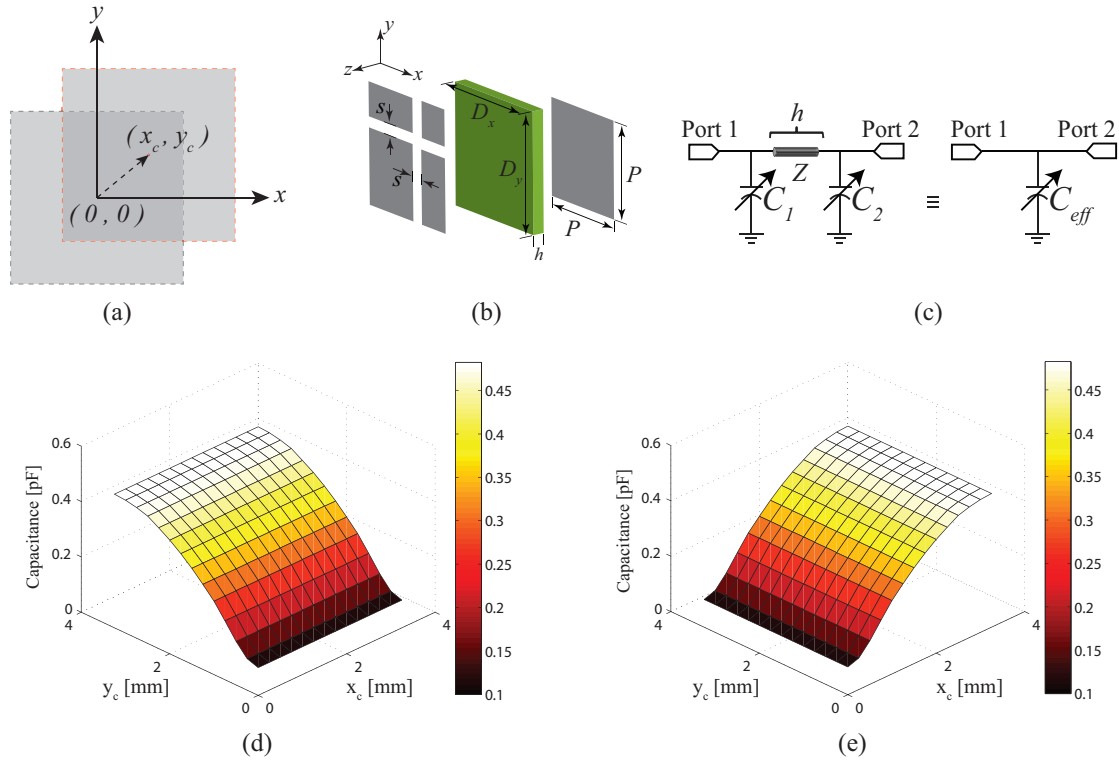


Figure 2.6 (a) The unit cells of the two capacitive layers used to synthesize a single effective capacitive layer of the MEFSS of Fig. 2.1(a) can overlap with each other. This overlap is modeled by the vector  $(x_c, y_c)$ . (b) 3D topology of the unit cell of a composite patch layer showing the offset between the capacitive patches and the dielectric slab that separates them. (c) The equivalent circuit model of the capacitive structure shown in Fig. 2.6(b). (d)-(e) The extracted effective capacitance of the capacitive structure shown in Fig. 2.6(b) consisting of two cascaded capacitive patches and a thin substrate separating them. The structure has the unit cell dimensions of  $6.5 \text{ mm} \times 6.5 \text{ mm}$ . The gap size for both layers is  $s = 0.5 \text{ mm}$  and the patch size is  $P = 6 \text{ mm}$ . The thickness of the substrate is  $h = 0.2 \text{ mm}$ . The study has been done for both (d) Vertical and (e) Horizontal polarizations.

of  $s = 0.5 \text{ mm}$ . Both layers are assumed to be in free space and the spacing between them is  $h = 0.2 \text{ mm}$ . As shown in Fig. 2.6(a), the overlap between two patch layers is modeled with a vector  $(x_c, y_c)$  connecting the centers of the two patches, within each unit cell of the structure, together.  $x_c$  refers to the horizontal offset between the positions of the two patches and  $y_c$  refers to the vertical offset between them. The structure is simulated using full-wave EM simulations in CST Studio to compute its effective capacitance as a function of the vector  $(x_c, y_c)$ . To do this, the unit cell of the structure shown in Fig. 2.6(b) is simulated using the periodic boundary conditions.

The transmission and reflection coefficients of the structure for a normally incident wave are calculated for the two orthogonal polarizations. These include the vertical and horizontal polarizations in which the electric field is respectively oriented along the  $\hat{y}$  and  $\hat{x}$  directions. Subsequently, the simplified equivalent circuit model of the structure, shown in Fig. 2.6(c) (right), is simulated in a circuit simulation software (Agilent Advanced Design System) and the transmission coefficient of the equivalent circuit model is calculated. Finally, the value of  $C_{eff}$  is tuned in ADS to match the magnitudes and the phases of the transmission and reflection coefficients obtained from the full-wave simulation and the simplified circuit model together. This way, the effective capacitance is calculated.

Figs. 2.6(d)-2.6(e) show the results obtained from these case studies for the aforementioned structure for both the vertical and horizontal polarizations. For both polarizations, the capacitance value is calculated as a function of  $x_c$  and  $y_c$ . For the vertical polarization,  $y_c$ , which represents the vertical offset between two patches, has the most significant effect on the capacitance value while  $x_c$ , which represents the horizontal offset between two patches, only has a negligible effect. However, for the horizontal polarization,  $x_c$  has the major effect and  $y_c$  only affects the capacitance negligibly. These can be described easily by the alignment of the direction of the electric field vector of the incident wave and the gap between two adjacent patches. Combining these two figures, we can find out that the maximum capacitance happens when the offset vector is equal to  $(x_c, y_c) = (D/2, D/2)$ . For this structure, the maximum value of the capacitance is 0.48 pF. The minimum capacitance value of 0.09 pF is obtained for the case when both patches are aligned together and  $(x_c, y_c) = (0, 0)$ .

#### 2.2.4 Approximate Formula for Calculating the Capacitance of Cascade Overlapping Patches

To better understand the impact of the offset overlap on the capacitance of the cascaded patches and facilitate the design process of such structures, we have developed an analytical formula that can be used to approximate the effective capacitance of a two layer stack of cascaded capacitive patches with the offset vector of  $(x_c, y_c) = (D/2, D/2)$ . Fig. 2.7 shows a unit cell of such a

structure. Observe that four parts of the upper patch layer form effective parallel plate capacitors of  $C_c$  with the bottom patch layer.  $C_c$  can be easily approximated by the following formula:

$$C_c = \frac{\epsilon_o \epsilon_{r_{eff}} (D - s)^2}{4h} \quad (2.3)$$

Where  $D$  is the unit cell size,  $s$  is the gap size between two adjacent patches,  $h$  is the thickness of the dielectric between two patch layers, and  $\epsilon_{eff}$  represents the effective dielectric constant between the two layers. The total capacitance is modeled as the parallel combination of the intrinsic capacitance  $C_i$ , brought by the capacitive gap, in parallel with the series-parallel network of  $C_c$  capacitors as shown in Fig. 2.7(b). Therefore,

$$C_{total} = C_c + C_i \quad (2.4)$$

where

$$C_i = \epsilon_o \epsilon_{r_{eff}} \frac{2D}{\pi} \ln\left(\frac{1}{\sin\left(\frac{\pi s}{2D}\right)}\right) \quad (2.5)$$

These analytical formulas are used to calculate the effective capacitance of the two layer stack of capacitive patches examined in Section 2.2.3 as a function of the unit cell size. Fig. 2.8 shows the capacitance values calculated using equations (2.3)-(2.5) alongside the values extracted from full-wave EM simulations. As can be observed, both results are in good agreement. Thus, the analytical formula can be used in a design procedure of the proposed harmonic-free FSS to predict the capacitances to a first order approximation.

## 2.3 Design Procedure and a Design Example

### 2.3.1 Design Procedure

The design procedure of the proposed structure is based on synthesizing the desired filter response of the equivalent circuit model of Fig. 2.5(b) and mapping the equivalent circuit parameters to the physical parameters of the proposed MEFSS. All the steps are similar to the procedure described in Section 2.2.1 and also that reported in [1] except the mapping of the effective parameters

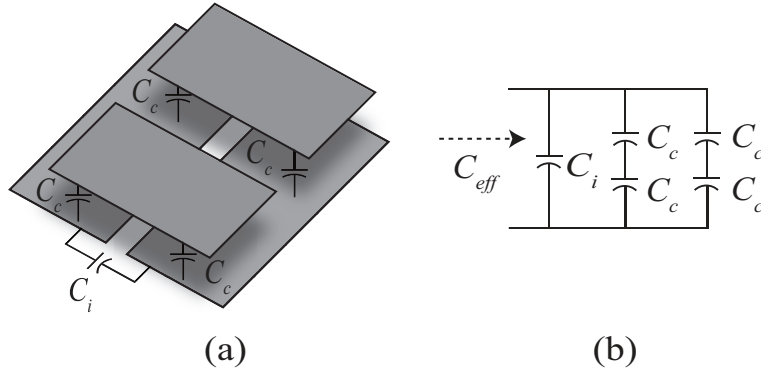


Figure 2.7 (a) The capacitive structure composed of two cascaded capacitive layers can be modeled as four capacitors with capacitance values of  $C_c$  and one capacitor with a capacitance value of  $C_i$  as depicted. (b) The equivalent circuit model of the capacitive structure showing the relative arrangement of  $C_c$  and  $C_i$  capacitors.

of the equivalent circuit model to the geometrical parameters of the capacitive layers constituting the FSS. In the mapping step, the desired values of the capacitors and inductors obtained from the equivalent circuit model are mapped to the geometrical parameters of the proposed structure. We assume that the dielectric constant of all the substrates used in the FSS are known. For simplicity, we also assume that all substrates used in the FSS have the same dielectric constants and that the thicknesses of the substrates used in between the capacitive multilayers are also equal and known. The gap size between the sub-wavelength capacitive patches in each capacitive layer is primarily determined by the minimum feature size that can be reliably fabricated using the fabrication technology of choice. In general, the smallest gap size is chosen to ensure that the unit cell dimensions of the FSS can be reduced as much as possible. This will increase the bandwidth over which no spurious transmission window occurs. Assuming that the gap size,  $s$ , is known and fixed, the unit cell size,  $D$ , can be obtained using equations (2.3)-(2.5). Then, the width of the wire grids is determined from:

$$L = \mu_0 \mu_{r_{eff}} \frac{D}{2\pi} \ln\left(\frac{1}{\sin\left(\frac{\pi w}{2D}\right)}\right) \quad (2.6)$$

Due to the close proximity of the metal layers, the presence of each layer will affect the capacitance or inductance of the other layers. Therefore, physical parameters obtained using this design process

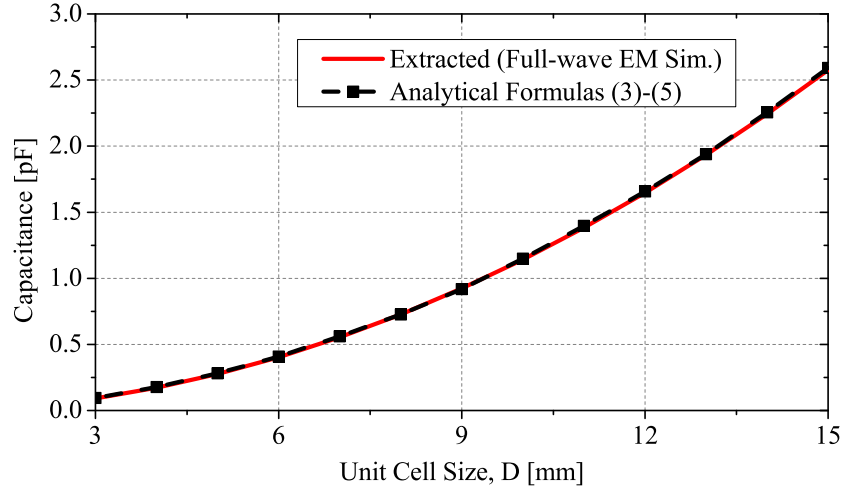


Figure 2.8 Comparison between the capacitance values predicted using the analytical method and those extracted from full-wave EM simulations. The results are shown for the structure examined in section 2.2.3.

may need to be tuned slightly to achieve the desired response. This can be done by following an iterative procedure similar to the one described in [98] and [1] and will not be repeated here.

### 2.3.2 Design Example and Simulation Results

The procedure presented in Section 2.3.1 was followed to design an MEFSS prototype with a second-order bandpass response having a center frequency of  $f_0=3.0$  GHz, a fractional bandwidth of  $\delta = 20\%$ , and no spurious transmission bands up to approximately 27 GHz. The equivalent circuit parameters of the structure (shown in Fig. 2.5(b)) were first determined following the design procedure described in [1]. In doing so, we assumed that dielectric substrates are non magnetic and have a dielectric constant of  $\epsilon_r = 2.2$  (Rogers RT/duroid 5880). A conventional second-order MEFSS (of the type shown in Fig. 2.1(a)) has two capacitive layers and one inductive layer as shown in Fig. 2.1. In this harmonic-suppressed MEFSS, each of the capacitive layers were implemented by using two closely-spaced, overlapping capacitive layers as described in Section 2.2.3. The physical parameters of the MEFSS were obtained using the design procedure discussed in Section 2.3.1. The structure has unit cell dimensions of  $D = 5.2$  mm which is equivalent to approximately  $\lambda_0/20$ , where  $\lambda_0$  is the free space wavelength at  $f_0=3.0$  GHz. Since this MEFSS is

Table 2.2 Physical parameters of the 2<sup>nd</sup>-order FSS with a center frequency of 3 GHz, the fractional bandwidth of  $\delta = 20\%$ , and no harmonics up to 27 GHz discussed in Section 2.3.2.

<i>Parameter</i>	$D$	$w_1$	$w_2$	$h_b$
<i>Value</i>	5.2 mm	2 mm	2 mm	0.101 mm
<i>Parameter</i>	$P_1$	$s_1$	$P_2$	$s_2$
<i>Value</i>	4.85 mm	0.35 mm	4.85 mm	0.35 mm
<i>Parameter</i>	$h_1$	$h_2$	$h_3$	$h_4$
<i>Value</i>	1.575 mm	1.575 mm	0.127 mm	0.127 mm

composed of multiple substrates that need to be bonded together, the effect of the bonding material on the response of the MEFSS must also be taken into account. The bonding material used here was Rogers 4450F prepreg with the dielectric constant of  $\epsilon_r = 3.58$  and a thickness of 0.1 mm. Introduction of the bonding layers creates an asymmetry in the topology of the proposed MEFSS, which slightly changes its response. This asymmetry was eliminated by using two closely-spaced wire grids on the two sides of the middle bonding layer instead of using just one wire grid on one side as shown in Fig. 2.9. Using this strategy, the two inductive layers in the middle, which are separated by a thin prepreg layer, act as a single composite inductive layer. This way, the symmetry of the structure is maintained and impact of the prepreg layers on the response of the MEFSS can be minimized. The final physical parameters of the structure are listed in Table 2.2. This structure was simulated in CST Microwave Studio and its frequency response was calculated. Fig. 2.10 shows the transmission coefficient of this FSS in the 0-27 GHz range. As can be observed, a transmission window centered at 3.0 GHz is achieved and the FSS does not have any spurious transmission bands up to 27 GHz as expected.

## 2.4 Experimental Verification and Measurement Results

A prototype of the aforementioned harmonic-suppressed MEFSS (discussed in Section 2.3.2) was fabricated using standard PCB lithography and substrate bonding techniques. The fabricated

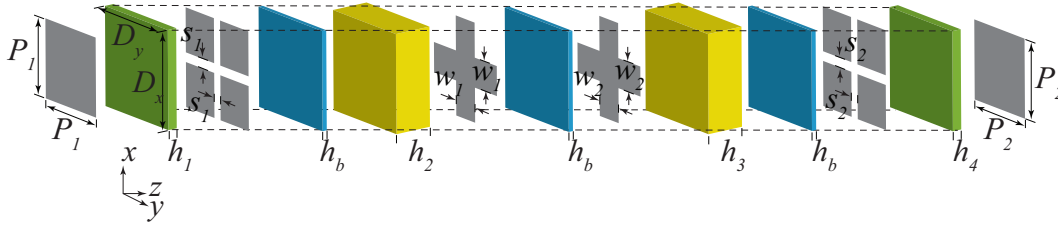


Figure 2.9 Unit cell of the proposed harmonic-suppressed 2<sup>nd</sup>-order bandpass FSS discussed in Section 2.3.2.

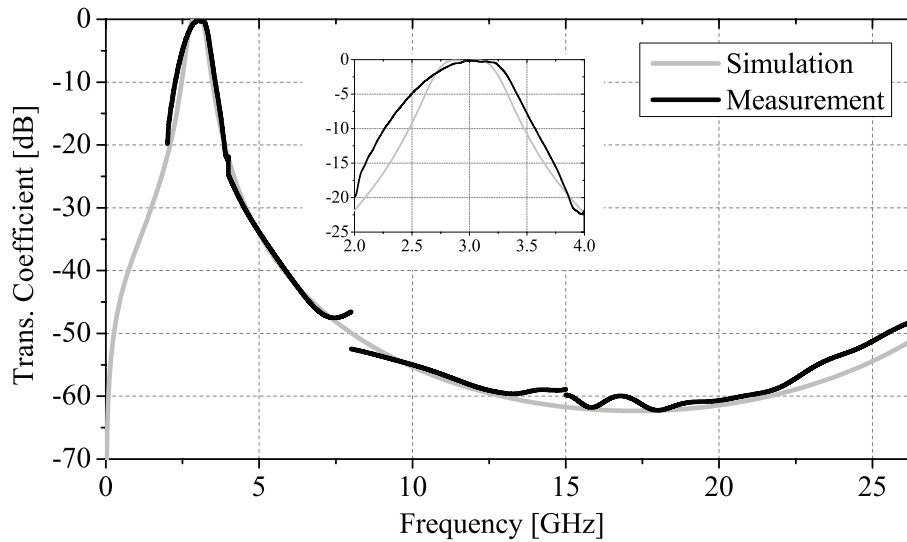


Figure 2.10 Measured and calculated transmission coefficients of the FSS prototype discussed in Section 2.3.2 and shown in Fig. 2.11. The MEFSS is composed of the unit cells shown in Fig. 2.9 with physical dimensions reported in Table 2.2.

prototype has six metal layers, four dielectric substrates, and panel dimensions of 50 cm  $\times$  37 cm. Rogers RT/duroid 5880 substrates ( $\epsilon_r = 2.2$ ), with the thickness of 1.575 mm is used between inductive layers and capacitive multilayers. The same substrate material with the thickness of 0.127 mm is used between two cascaded captive patches. All the dielectric substrates are bonded together using a 0.1 mm thick Rogers 4450F binding film with  $\epsilon_r = 3.58$ . The total thickness of the structure, including the bonding layers, is 3.7 mm which is less than  $\lambda_0/25$  at 3.0 GHz. Fig. 2.11 shows a photograph of the fabricated harmonic-suppressed MEFSS.

The measurement setup consisted of a large metallic screen with the dimensions of 1.8 m  $\times$  1.2 m with a rectangularly shaped opening having the same dimensions as those of the FSS at its center.

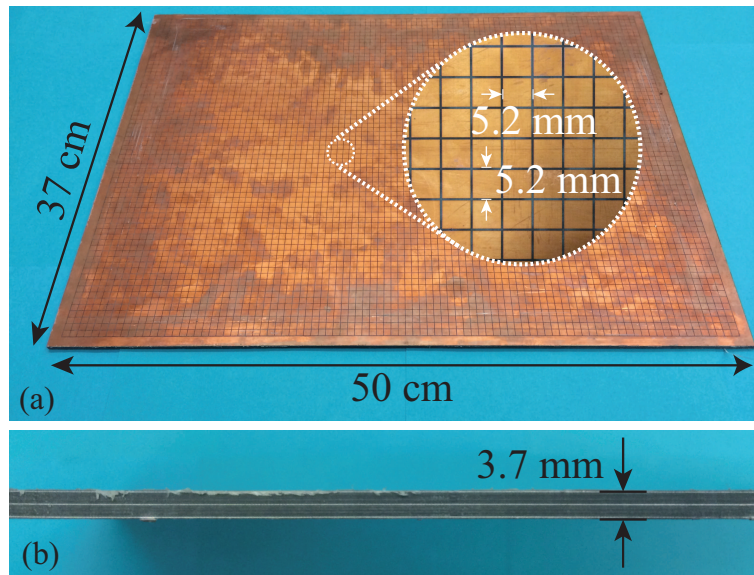
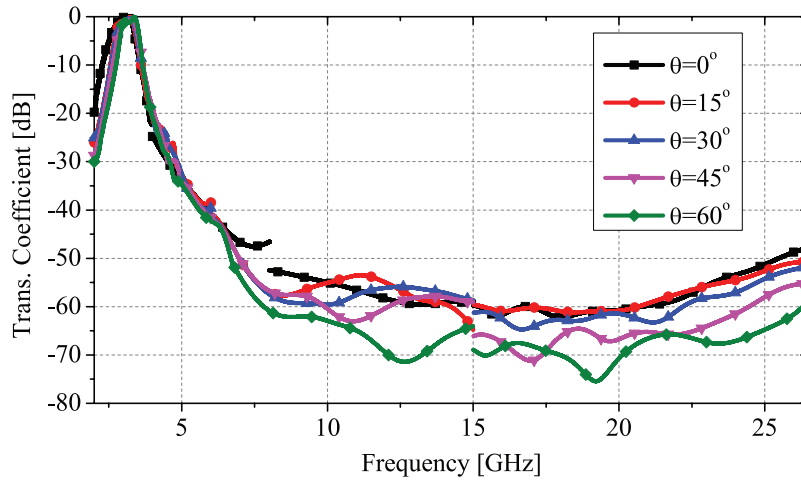


Figure 2.11 (a) Photograph of the fabricated harmonic-suppressed MEFSS prototype. (b) Side view of the fabricated prototype.

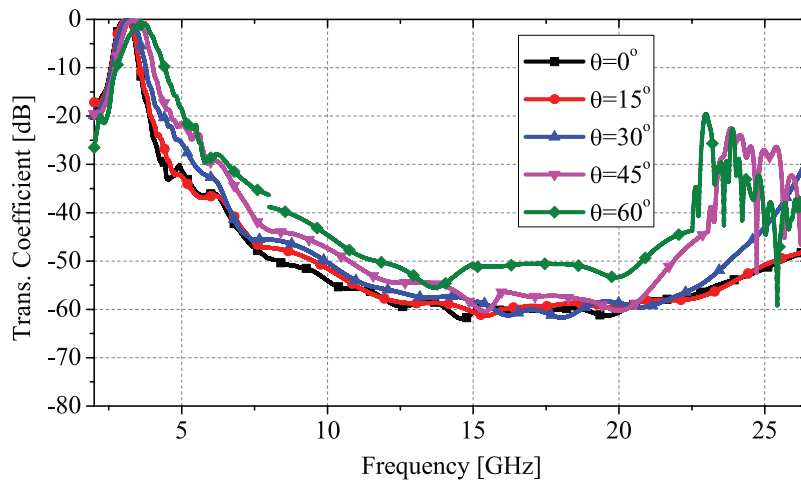
This screen was placed between the transmitting and receiving antennas both connected to the two ports of a vector network analyzer (VNA). The large metallic fixture ensures that a transmitted EM wave must pass through the FSS to arrive at the receiver. Absorbers were used to cover points of specular reflection in the surrounding environment (e.g. on the ground and side walls of the room). Additionally, range gating in the VNA was used to eliminate the effects of scattering and diffraction of the EM waves from the edges of the metallic fixture that host the FSS as well as the effects of the multiple reflections between two antennas as discussed in [98]. Transmission coefficient measurements were carried out in two steps. First, the transmission coefficient of the screen without the FSS was measured and used for calibration. Then, the FSS was placed in the opening and its transmission coefficient was measured once again. The transmission coefficient of the MEFSS was obtained using these two measurement results. Measurements were performed in 2 GHz - 27.0 GHz frequency range using multiple pairs of transmitting and receiving antennas that cover different parts of this frequency range. Over the 2 GHz - 8 GHz frequency band, a pair of dual ridge horn antennas were used. A pair of X-band and a pair of K-band horn antennas were used to do the measurements in the 7.0 GHz - 15 GHz and 15 GHz - 27.0 GHz frequency bands

respectively. In these measurements, the X-band and K-band horn antennas were used outside of their recommended frequency bands of operation (e.g., 7.0-8.0 GHz and 12-15 GHz for the X-band horns and 15 GHz-18 GHz for the K-band horns). This was done primarily due to the unavailability of other standard antennas that were specifically designed for operation at these bands during our measurements. Fig. 2.10 shows the measured frequency response of the MEFSS along with the full-wave simulation results. As can be observed, a relatively good agreement between the measured and simulated results is observed. The discrepancies observed between the measurement and simulation results in the vicinity of 7.0 GHz and 15.0 GHz are primarily attributed to using the receive and transmit antennas outside of their recommended frequency bands. Nonetheless, the measured result demonstrates clearly that the FSS does not have any spurious transmission windows up to 27.0 GHz.

The response of the fabricated prototype was also measured for oblique incidence angles for the TE and TM polarizations of incidence. Fig. 2.12(a) shows the transmission coefficients of the structure measured for the TE polarization for incidence angles in the range of  $0^\circ - 60^\circ$ . As can be observed, the FSS response is stable for such large incidence angles. Additionally, the structure maintains its harmonic suppressed operation for the TE polarization up to 27.0 GHz for incidence angles in the range of  $\pm 60^\circ$ . Fig. 2.12(b) shows the measured transmission coefficients of the structure for the TM polarization of incidence in the range of  $0^\circ - 60^\circ$ . Similar to the previous case, the FSS maintains its second-order bandpass response. However, the center frequency of operation of the structure shifts higher than 3.0 GHz for incidence angles exceeding  $45^\circ$ . This is also observed in other MEFSSs of the type shown in Fig. 2.1 (e.g., see [98]). This behavior can be explained by examining the variations of the parameters of the equivalent circuit model of the FSS under oblique incidence angles. Specifically, for the TE polarization of incidence, the capacitance values of the patch layers decrease as the angle of incidence increases while the inductance value of the wire grid does not change [99]. For the TE polarization, the series inductances - associated with small transmission lines representing the dielectric substrates of the MEFSS - increase as the incidence angle increases. These two effects compensate each other resulting in a stable center frequency of operation as the angle of incidence changes. For the TM polarization, however, the



(a)



(b)

Figure 2.12 (a)-(b) Measured transmission coefficients of the fabricated harmonic-suppressed MEFSS prototype discussed in Section 2.3.2 and shown in Fig. 2.11 for oblique incidence angles for the (a) TE and (b) TM polarization of incidence.

inductance of the wire grid in the middle layer decreases as the incidence angle increases while the capacitance values of the patch layers do not change [99]. The values of the series inductances representing the short transmission lines modeling the dielectric substrates, however, decrease as the angle of incidence increases. The reduction of these inductance values results in increasing

the center frequency of operation of the MEFSS for the TM polarization as the incidence angle increases. This effect, however, becomes significant only when the incidence angle increases beyond  $45^\circ$  as seen in Fig. 2.12. Additionally, for the TM polarization, as the angle of incidence is increased, one of the higher spurious transmission windows starts to shift towards lower frequencies and is observed in the results shown in Fig. 2.12(b) for  $\theta = 45^\circ$  and  $\theta = 60^\circ$ . The peak transmission coefficient of this spurious band, however, remains below -20 dB for incidence angles up to  $60^\circ$ . Thus, the MEFSS maintains its desired harmonically-suppressed transfer function for the TM polarization for incidence angles in the  $\pm 60^\circ$  range as well.

## 2.5 Conclusions

We presented a new method for designing miniaturized-element frequency selective surfaces with higher-order bandpass responses, which are free of spurious transmission windows over an extremely wide frequency band. The proposed harmonic-suppressed MEFSSs take advantage of the concept of cascaded, overlapping capacitive patch layers to drastically reduce the unit cell size of the structure. Using multiple closely-spaced capacitive layers with overlapping unit cells to synthesize a single effective capacitive layer leads to a larger capacitance value for given unit cell dimensions. As a result, the natural resonant frequencies of these patches and the apertures within the wire grids shift to higher frequencies and a harmonic-free response over an extremely large bandwidth can be achieved. The proposed concept was experimentally verified by designing an MEFSS prototype having a second-order bandpass response with a fractional bandwidth of 20% at 3.0 GHz, which does not demonstrate any spurious transmission windows up to 27 GHz. This MEFSS was also fabricated and experimentally characterized using a free-space measurement setup. Measurements confirmed that the fabricated structure is indeed free of spurious transmission windows over the expected frequency band of operation. Additionally, we examined the performance of this prototype for various incidence angles and polarizations of the incident EM wave. The fabricated MEFSS prototype demonstrates a stable frequency response for both the TE and TM polarizations of incidence and maintains its harmonic free operation for incidence angles in the  $\pm 60^\circ$  range for both the TE and TM polarizations of incidence. The concept presented in this

chapter can also be expanded to design MEFSSs for the VHF and lower UHF frequency bands. If the MEFSS design presented in this chapter is directly scaled, it is expected that it will maintain the same harmonic free bandwidth (i.e. a 9:1 bandwidth). However, as the center frequency of operation of the MEFSS decreases, it may be necessary to extend the harmonic-free range of operation of the device to ensure that the device does not show any spurious transmission windows up to high frequencies (e.g. 20 GHz). In such situations, the harmonic-free bandwidth of the MEFSS can be increased by using more cascaded capacitive layers with smaller unit cell dimensions. For example, computer simulations of an MEFSS with three cascaded capacitive patches operating in the 500 – 700 MHz range indicate that it remains free of spurious transmission windows up to 18.0 GHz, or equivalently a 30:1 bandwidth.

## Chapter 3

# Inductively-Coupled Miniaturized-Element Frequency Selective Surfaces with Narrowband, High-Order Bandpass Responses

### 3.1 Introduction

Frequency selective surfaces are engineered surface constructions designed to control the flow of a propagating electromagnetic wave by modifying its phase, amplitude, or polarization in a desired and controlled way. These structures have brought unique capabilities to a wide range of systems operating from low radio frequencies [2] to the infrared [3], [4] and optical frequencies [5], [7]. Over the past few decades, frequency selective surfaces have been employed in a wide range of devices including spatial filters [2, 8], artificial magnetic conductors [11, 12], transmitarrays [13–15, 100], and reflectarrays [16, 101]. As spatial filters, they are used to reduce the radar cross sections (RCS) of objects mounted on stealth platforms [2, 102], reduce interference in indoor wireless environments [17, 18], and shield sensitive electronic devices from unwanted interference and jamming signals. One important factor that determines the suitability of a frequency selective surface in a given application is the selectivity of its frequency response. In certain applications, narrowband and highly-selective filtering performances are required. For instance, such a response may be useful in designing radomes used for reducing the out-of-band RCS of a narrow-band antenna. In addition to having narrow bandwidth, to sufficiently attenuate strong out-of-band interference/jamming signals, such FSSs should provide highly-selective responses with enough out-of-band rejection to perform the desired filtering task.

The operation of most bandpass or bandstop FSSs with response orders of  $N \geq 2$  can be described using the coupled-resonator filter theory. The bandwidth of such filters is determined

by the quality factors of their constituting resonators as well as the coupling coefficients between the resonators. In antenna-based FSSs, resonant-type elements (e.g. dipole, tri-pole, Jerusalem cross, etc.) are used as the constituting elements of the structure [2]. In the filter analogy, these resonant-type unit cells act as the resonators of the filter. To achieve a filter with higher-order (i.e.,  $N \geq 2$ ) response, these elements are then cascaded using quarter-wavelength spacers that act as impedance inverters. To achieve narrowband operation in these FSSs, the quality factors of their resonators must be increased. Since antennas are the constituting elements of these structures, this requires using miniaturized antennas (with high  $Q$ ) in each unit cell. To increase the  $Q$  of such an antenna, its occupied area must be decreased while maintaining its resonant frequency. For a dipole antenna for example, this requires maintaining the overall electrical length of the dipole to around  $\lambda/2$  while decreasing the overall occupied area (by bending or meandering the dipole). However, using conventional PCB fabrication technology, there is a limit to the miniaturization levels that can be achieved using techniques like this (for an expanded discussion see Section II of [103]). Therefore, achieving narrowband, highly-selective FSSs using conventional FSS design approaches is very challenging.

To address these challenges, a number of previous studies have been conducted and reported in the literature [33, 104–109]. In [104], it is shown that a periodic arrangement of strips loaded periodically with closed or open ended stubs is capable of offering passbands narrower than what can be achieved using a traditional single layer FSS. In [105], a narrowband FSS based on aperture coupled microstrip patches is presented. A closely coupled two layer aperture FSS capable of offering a relatively narrow passband is reported in [106]. In [33], a first-order FSS with very high- $Q$  bandpass response is presented. A narrowband band-reject FSS with pseudo-elliptic response is reported in [107]. Finally, highly-selective FSSs based on substrate integrated waveguide techniques are presented in [108], [109].

In this chapter, we propose a new design approach that is particularly suited for designing narrowband, highly-selective FSSs (i.e. FSSs having fractional bandwidths of less than 10% and bandpass responses with arbitrarily high orders). The approach is based on using dielectric spacers as the main resonant elements of the filter and coupling them together using shunt inductors.

The inductors are implemented as two-dimensional wire grids with sub-wavelength periods. Thus, the proposed FSS is a periodic structure with sub-wavelength period and does not use any metallic resonant elements to achieve the desired filter response. In that sense, this FSS has many of the features and attributes of miniaturized-element frequency selective surfaces (MEFSSs) of the types reported in [103], [1, 19–27, 81, 98, 103]. Consequently, henceforth we refer to this structure also as an MEFSS. An equivalent-circuit model for this type of FSS is also proposed. Using this equivalent-circuit model, a comprehensive synthesis procedure is developed that allows for designing the FSS from its system level performance indicators such as the center frequency of operation, bandwidth, and response type. This procedure is used to design a prototype of such an FSS with a second-order bandpass response operating at 21 GHz with a fractional bandwidth of 5%. The prototype is fabricated and experimentally characterized. It is demonstrated that the measurement results agree very well with the theoretical predictions and full-wave computer simulations. In what follows the details of the operating principles, design process, and the measurement and simulation results of the fabricated MEFSS are presented and discussed.

### 3.2 Principles of Operation

An intuitive way for analyzing the performance of a frequency selective surface is to examine its equivalent circuit model. This offers useful insight into the performance of the FSS and allows for examining the frequency response of the structure without having to rely on full-wave electromagnetic simulations. Similar to many microwave filters with bandpass frequency responses, a bandpass FSS can also be designed based on the coupled-resonator filter topology. Fig. 3.1 shows two generalized circuit models of bandpass coupled-resonator filters. In these filters, two or more resonators are coupled together using impedance inverters to achieve the desired frequency response. Based on the type of the resonator and the inverter, these filters can be categorized into two classes. Fig. 3.1(a) shows a coupled-resonator filter designed based on parallel resonators that are coupled together using admittance inverters. For a filter with  $N^{th}$ -order response of this type, the resonators are modeled as  $X_1, X_2, \dots, X_N$  and the admittance inverters are shown as

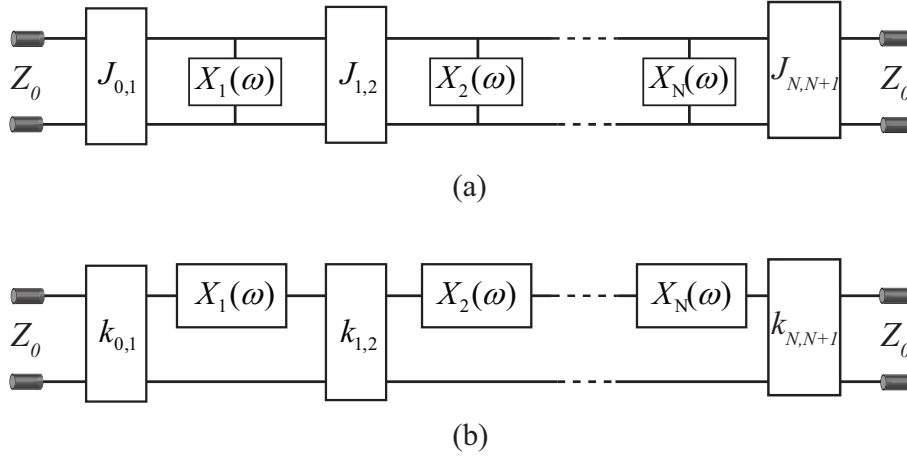


Figure 3.1 (a) Generalized bandpass filter circuit using a number of parallel resonators separated from each other by admittance inverters (J-type inverters). (b) Generalized bandpass filter circuit that consists of series resonators coupled together using K-type impedance inverters.

$J_{01}, J_{12}, J_{N,N+1}$ . The circuit shown in Fig. 3.1(b) is the dual of that shown in Fig. 3.1(a). Therefore, this filter is designed based on resonators in series that are coupled together using impedance inverters. In this case, the inverters are modeled as  $k_{01}, k_{12}, \dots, k_{N,N+1}$  for a filter with  $N^{\text{th}}$ -order response. Most antenna-array-based FSSs (e.g. see [2]) are designed based on the coupled-resonator filter model shown in Fig. 3.1(a). This way, dipole- or aperture-type resonant elements are shaped in such ways that they act as resonators near the intended frequency band of operation. The coupling elements in such FSSs are generally quarter-wavelength dielectric spacers. The equivalent circuit model of most reported MEFSSs [1, 24, 98, 103] is also a converted version of the circuit shown in Fig. 3.1(a). Spatial resonators in such structures are formed by combining non-resonant reactive impedance sheets.

In the method proposed in this chapter, low-loss dielectric spacers are employed as resonators of the FSS, which makes the task of achieving a narrowband bandpass response considerably easier. The resonators are separated from each other by the impedance inverters. The frequency of operation of the filter is determined by the physical dimensions of the resonators and the dielectric constants of the materials used to implement them. In contrast with the previously-reported MEFSSs with higher-order (i.e.,  $N \geq 2$ ) bandpass responses [1, 24, 98, 103], the generalized bandpass

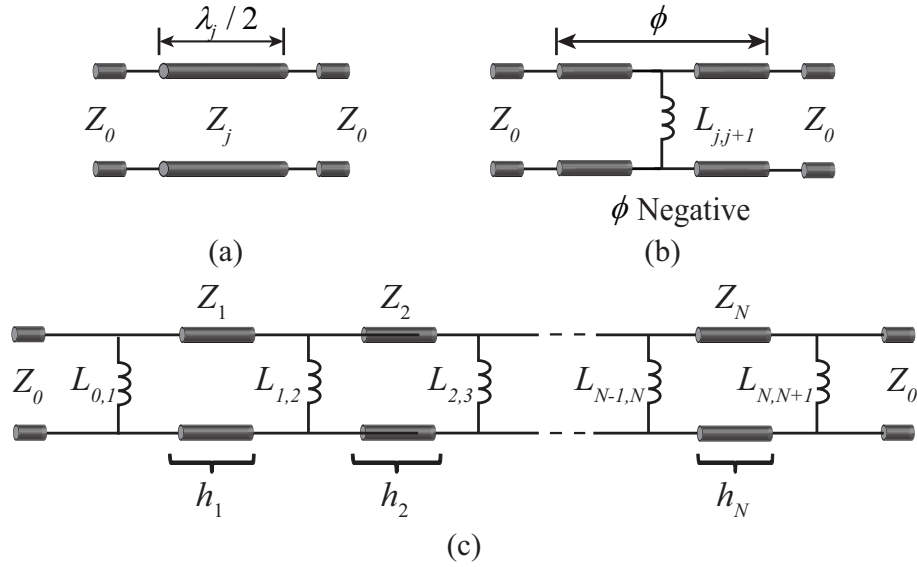


Figure 3.2 (a) The equivalent circuit model of the transmission-line resonators (dielectric spacers) used as the resonators of the proposed frequency selective surface. (b) The circuit model of the admittance inverters used to couple the resonators of Fig. 3.2(a) together in the present circuit model. (c) The equivalent circuit model of the proposed frequency selective surface when the resonators and the admittance inverters of Fig. 3.2(a)-(b) are put together in a ladder network. In this circuit, the negative lengths of the admittance inverters of Fig. 3.2(b) are absorbed in the positive lengths of the transmission-line resonators shown in Fig. 3.2(a).

coupled-resonator filter circuit shown in Fig. 3.1(b), is used in the proposed design. In this configuration, the resonators are in series and they are coupled to each other using  $k$ -type inverters. The resonators in this design are half-wavelength spacers, shown in Fig. 3.2(a), that are modeled with transmission lines with characteristic impedances of  $Z_j = Z_0/\sqrt{\epsilon_{r,j}}$ , where  $Z_0 = 377 \Omega$  is the free-space impedance and  $\epsilon_{r,j}$  is the dielectric constant of the  $j^{th}$  substrate. The resonators are then coupled to each other using the coupling elements shown in Fig. 3.2(b). This impedance inverter is composed of a parallel inductor with two transmission lines with negative electric lengths on its either side. These coupling elements have an overall image phase shift of  $-90^\circ$ . After placing the transmission lines (resonators) and these coupling elements together to form the whole filter, the negative electrical lengths of the transmission lines of the inverters are subtracted from the positive electrical length of the adjacent lines (resonators). Therefore, in the final format of the circuit, the lengths of all transmission lines are positive. Furthermore, the transmission lines will

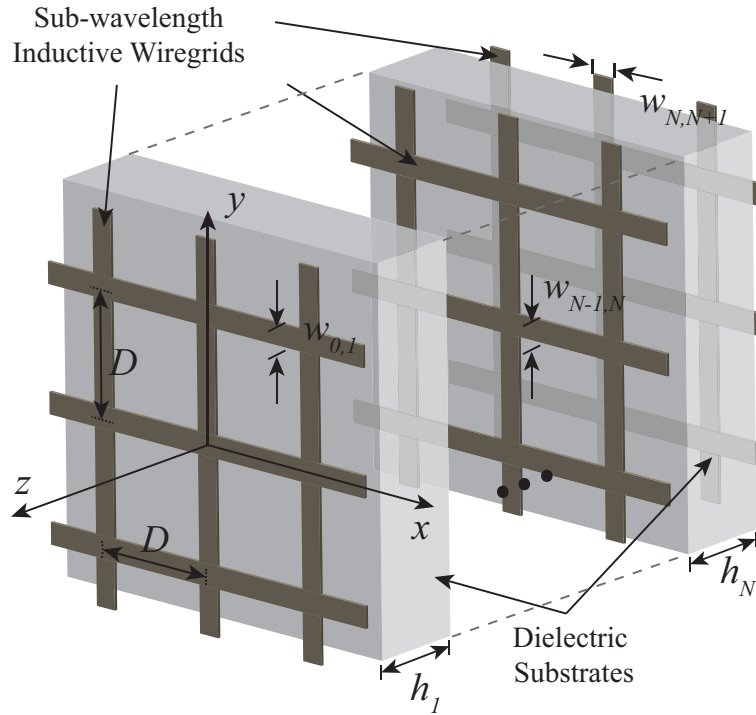


Figure 3.3 Topology of the proposed bandpass FSS. The structure has  $N + 1$  metal layers that are separated from one another by  $N$  dielectric spacers and acts as an FSS with  $N^{th}$ -order bandpass response.

have overall lengths less than half a wavelength, which reduces the overall thickness of the final FSS. Fig. 3.2(c) shows the equivalent circuit model of the proposed spatial filter with  $N^{th}$ -order bandpass response after combining the resonators and the transmission lines. This circuit is an inductively-coupled, coupled-resonator bandpass filter. In this final configuration, the inductors are shown as  $L_{0,1}, L_{1,2}, \dots, L_{N,N+1}$ . The lengths and the characteristic impedances of the transmission lines between the inductors are shown as  $h_1, h_2, \dots, h_N$  and  $Z_1, Z_2, \dots, Z_N$ , respectively.  $Z_0$  is also the termination impedance at both sides of the FSS. Similar to the procedure described in [1], the transmission lines and the inductors then can be implemented using dielectric spacers and two-dimensional periodic arrangement of inductive wire grids, respectively.

Fig. 3.3 shows the three-dimensional (3D) topology of the proposed FSS with  $N^{th}$ -order bandpass response. The structure is composed of 2D periodic arrangement of sub-wavelength inductive wire grids that are separated from one another by dielectric substrates. Assuming the thickness

of the substrate between two consecutive metal layers is  $h$ , the overall thickness of the FSS is  $N \times h$ . The dimensions of each unit cell along  $\hat{x}$  and  $\hat{y}$  directions is  $D$ . The inductive wire grids are also the combination of two metallic strips with the widths of  $w_{j,j+1}$  oriented perpendicularly to each other. Due to symmetry, the response of this structure is insensitive to the polarization of the incident wave for normal incidence.

### 3.3 Design Procedure

The design procedure of the proposed device is based on synthesizing the desired filter response from the equivalent circuit model shown in Fig. 3.2(c) and mapping the equivalent circuit parameter values to the physical and geometrical parameters of the proposed FSS. In this procedure, we assume the FSS has a certain response type (i.e. Butterworth, Chebyshev, etc.), center frequency of operation of  $f_0$ , and fractional bandwidth of  $\delta = BW/f_0$ . For simplicity, we assume that the dielectric constant of the substrates used in the FSS are all the same. As described in Section 3.2, the values of the elements used in the equivalent circuit model of Fig. 3.2(c) can be determined by analyzing this circuit as an inductively-coupled, coupled-resonator bandpass filter [110]. Doing this, the values of the elements of the equivalent circuit model can be calculated using the following procedure. First we calculate the values of the inductors:

$$L_{0,1} = \frac{Z_0}{2\pi f_0 \sqrt{\frac{1+\epsilon_r}{2}}} \frac{\sqrt{\frac{\pi\delta}{2g_0g_1}}}{1 - \frac{\pi\delta}{2g_0g_1}} \quad (3.1)$$

$$L_{N,N+1} = \frac{Z_0}{2\pi f_0 \sqrt{\frac{1+\epsilon_r}{2}}} \frac{\sqrt{\frac{\pi\delta}{2g_Ng_{N+1}}}}{1 - \frac{\pi\delta}{2g_Ng_{N+1}}} \quad (3.2)$$

$$L_{j,j+1} = \frac{Z_0}{2\pi f_0 \sqrt{\epsilon_r}} \frac{\frac{\pi\delta}{2\sqrt{g_jg_{j+1}}}}{1 - \left(\frac{\pi\delta}{2\sqrt{g_jg_{j+1}}}\right)^2}, \quad j = 2, \dots, N-1 \quad (3.3)$$

where  $g_0, \dots, g_{N+1}$  are the element values in the low-pass prototype filter that has the desired response type (e.g. Butterworth, Chebyshev, etc. For more information see pp. 83-157 of [110]).

$Z_0 = 377 \Omega$  is the free space impedance and  $\epsilon_r$  is the permittivity of the dielectric substrates used to implement the FSS. The substrate thicknesses can be obtained from:

$$h_j = \left( \frac{\lambda_0}{2\pi\sqrt{\epsilon_r}} \right) \times \left( \pi - \frac{1}{2} \left[ \tan^{-1} \left( \frac{2L_{j-1,j}\sqrt{\epsilon_{r,eff_{j-1,j}}}}{2\pi f_0 Z_0} \right) + \dots \right] \right) \quad (3.4)$$

where  $c$  is the speed of light and  $\epsilon_{r,eff_{j,j+1}}$  is the effective dielectric constant for  $L_{j,j+1}$ . For the MEFSS under discussion,  $\epsilon_{r,eff_{j,j+1}} = \frac{\epsilon_r+1}{2}$  for the first and last inductors and  $\epsilon_{r,eff_{j,j+1}} = \epsilon_r$  for other inductors. The next step of the design procedure is to map the values of the equivalent circuit model of the FSS to those of the physical and geometrical parameters of the FSS. The values of  $L_{0,1}, \dots, L_{N,N+1}$  can be related to the geometrical parameters of the sub-wavelength inductive wire grids using the following equation [99]:

$$L_{j,j+1} = \mu_0 \mu_{j,j+1} \frac{D}{2\pi} \ln(\csc(\frac{\pi w_{j,j+1}}{2D})) \quad (3.5)$$

where  $D$  is the period of the periodic structure,  $\mu_0$  is the free space permeability,  $\mu_{j,j+1}$  is the effective permeability, and  $w_{j,j+1}$  is the width of the inductive wire grid used in the design. In the design procedure,  $D$  can be chosen arbitrarily as long as the dimensions of the unit cells are small compared to the wavelength.

## 3.4 Experimental Verification and Measurement Results

### 3.4.1 Design Example

The procedure presented in Section 3.3 was followed to design an MEFSS prototype with a second-order bandpass response having a Butterworth response type, a center frequency of  $f_0 = 21$  GHz, and a fractional bandwidth of 5%. For this type of response,  $g_0 = g_3 = 1$  and  $g_1 = g_2 = 1.414$ . These values are obtained from Table 4.05-1(a) of [110]. The equivalent circuit parameters of the structure including the values of the three inductors and the thicknesses of the dielectric substrates are determined using (3.1)-(3.4). In doing so, the dielectric substrate

Table 3.1 Physical and electrical parameters of the 2<sup>nd</sup>-order MEFSS with the center frequency of 21 GHz and the fractional bandwidth of  $\delta = 5\%$  discussed in Section 3.4.

Parameter	$L_{01}$	$L_{12}$	$L_{23}$	$h_1$	$h_2$
value	0.4 nH	0.05 nH	0.4 nH	1.9 mm	1.9 mm
Parameter	$D$	$w_{01}$	$w_{12}$	$w_{23}$	$h_b$
value	3 mm	1.05 mm	1.85 mm	1.05 mm	0.1 mm

used in the design are assumed to be non-magnetic and have a dielectric constant of  $\epsilon_r = 10.2$  (Rogers RT/duroid 6010). The calculated values obtained from (3.1)-(3.4) are then used in a circuit simulation software (Agilent Advanced Design System) to calculate the frequency response of the structure. Since the exact substrate thicknesses calculated using (4) were not available commercially, the closest commercially available thickness was used for the substrates. Doing this necessitated tuning the values of the inductors as well to recover the desired filter response. The optimized circuit values are reported in Table 3.1. The unit cell dimension of the designed structure is selected to be 3 mm, which is equivalent to approximately  $0.21\lambda_0$ , where  $\lambda_0$  is the free space wavelength at the center frequency. Therefore, using  $D=3$  mm and the inductance values reported in Table 3.1 in (3.5), the widths of the inductive wire grids used in the MEFSS can be calculated. Since the proposed MEFSS is a multilayer structure, the effect of bonding materials on its response should also be taken into account. The bonding material used in the design is Rogers 4450F prepreg with the dielectric constant of  $\epsilon_r = 3.52$  and the thickness of  $h_b = 0.1$  mm. Introduction of the bonding layer creates an asymmetry in the topology of the MEFSS, which can slightly change the frequency response of the device. This asymmetry can be eliminated by using two closely spaced wire grids on the two sides of the middle bonding layer as shown in Fig. 3.4 instead of using just one wire grid placed only on one side. The final physical parameters of the structure are listed in Table 3.1.

The structure is simulated in CST Microwave studio and its frequency response is calculated. Fig. 3.5 shows the full-wave simulated transmission coefficient of the FSS in the frequency range of 18-24 GHz alongside the frequency response predicted by the equivalent circuit model shown

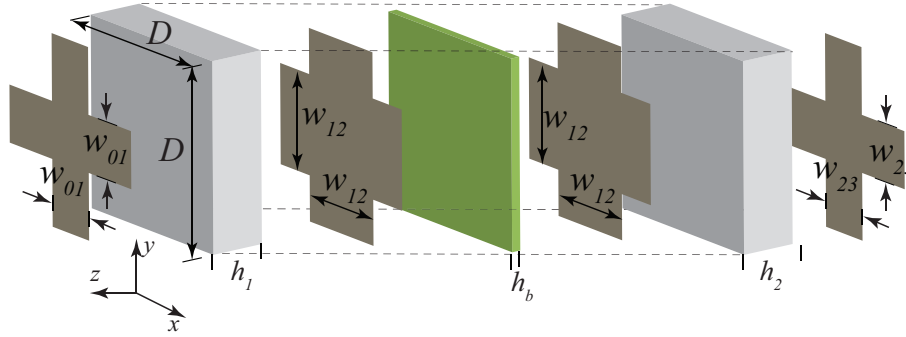


Figure 3.4 Unit cell of the proposed second-order bandpass MEFSS discussed in Section 3.4. Notice that the two inductive wire grids placed in the center are separated from one another by a thin prepreg layer. These two inductive layers constitute a single hybrid inductive layer. This arrangement is used to maintain the symmetry of the structure as discussed in Section 3.4.

in Fig. 3.2(c) using the values reported in Table 3.1. As can be observed, the transmission window centered at 21 GHz is achieved and a good agreement between both simulated responses is achieved. The frequency response of the structure is also simulated for oblique incidence angles for both the TE and TM polarizations of incidence and the results are shown in Fig. 3.7. As can be observed, for incidence angles in the range of  $\pm 40^\circ$ , the FSS is expected to provide a stable frequency response for both polarizations. As the incidence angle is increased beyond  $40^\circ$ , the center frequency of operation of the structure starts to move towards higher frequencies. This shift in the center frequency can be explained by examining the variation of the parameters of the equivalent circuit model of the FSS under oblique incidence angles. Specifically, for the TE polarization of incidence, as the angle of incidence increases, the impedance value of the transmission lines increases (i.e.  $Z_{TE} = Z_0 / \cos(\theta)$ ) while the inductance values of the wire grids remain constant (i.e.  $L_{TE} = L_0$ ). These variations result in the slight shift of the center frequency. For the TM polarization, on the other hand, the inductance values of the wire grids decrease as the incidence angle increases (i.e.  $L_{TM} = L_0(1 - \frac{1}{\epsilon_{r,eff}} \sin^2 \theta)$ ). The impedance value of the transmission lines, however, decreases as the incidence angle increases (i.e.  $Z_{TM} = Z_0 \cos(\theta)$ ). While the inductance values of the wire grids are a major contributor, these two effects compensate each other to some extent resulting in a slight increase in the center frequency of the pass band<sup>1</sup>. Since this MEFSS has

<sup>1</sup>To achieve stability in a wider field of view, both of these variations should be minimized or compensated. Adding dielectric stabilizers at both sides of the FSS [2] or utilizing high-permittivity dielectric substrates in the design of the

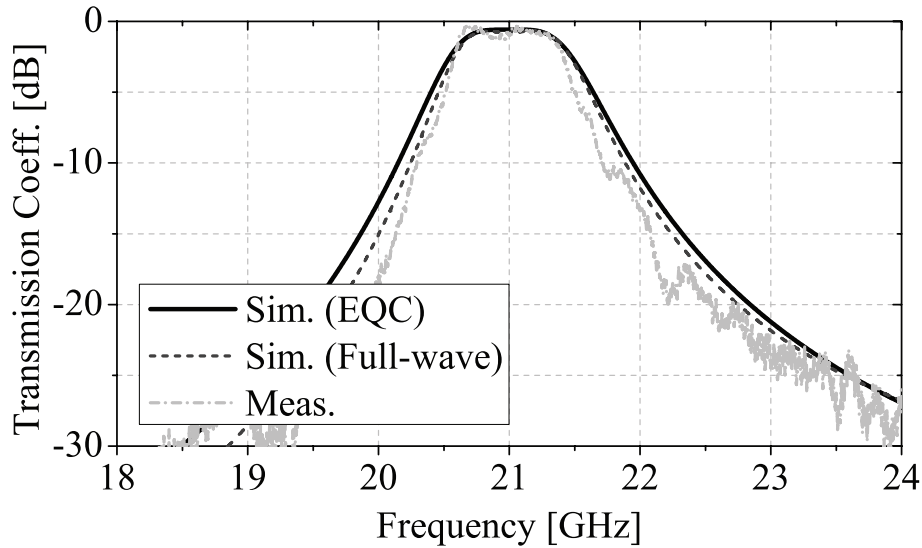


Figure 3.5 Simulated and measured transmission coefficients of the MEFSS discussed in Section 3.4. The results from the equivalent circuit model and full-wave simulations are compared with the free-space measurement results.

a narrowband response, the shifting of the center frequency of operation is the primary parameter that impacts the effective field of view of the structure.

### 3.4.2 Fabrication and Measurement Results

A prototype of the proposed MEFSS was fabricated using standard PCB lithography and substrate bonding techniques. The fabricated prototype has four metallic layers, two dielectric substrates, and panel dimensions of  $13 \text{ cm} \times 13 \text{ cm}$  ( $\approx 9\lambda_0 \times 9\lambda_0$ ). The photograph of the fabricated prototype is shown in Fig. 3.6. The fabricated prototype was characterized using free-space measurement techniques. For brevity, the detailed procedure of the measurements will not be repeated here and the reader is referred to Section III of [102]. Fig. 3.5 shows the measured frequency response of the MEFSS for normal incidence along with the simulation responses obtained using both the equivalent circuit model and the full-wave EM simulations. As can be observed, a good agreement between the measured and simulated results is observed.

---

structure helps to some extent by reducing the angular dependence of the inductance of the wire grids. Using a material with a higher dielectric constant also helps somewhat with reducing the angular dependence of the impedances of the transmission lines under oblique incidence angles.

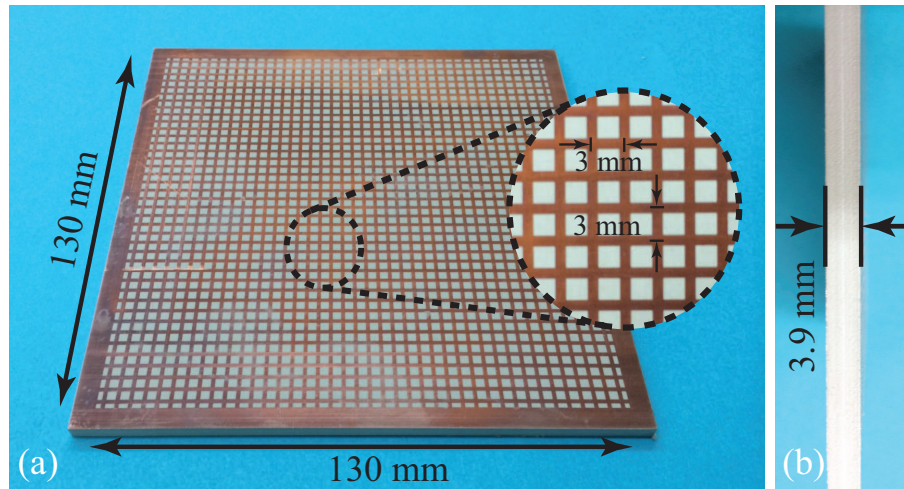


Figure 3.6 (a) Photograph of the fabricated MEFSS prototype. (b) Side view of the fabricated prototype.

The response of the fabricated prototype was also measured for oblique angles of incidence for both the TE and the TM polarizations of incidence. Fig. 3.7(a)-(b) shows the transmission coefficients of the structure for both TE and TM polarizations of incidence in the range of  $0^\circ - 40^\circ$ . Observe that under these illumination conditions, the FSS maintains its second-order response and the response is relatively stable for both polarizations. The variations of the frequency response of the FSS as a function of the polarization and the angle of incidence of the incident wave are similar to those predicted from simulations. Since the structure has a narrowband filter response, the inevitable changes in the inductance values and the effective electrical lengths of the transmission lines that happen when the polarization or angle of incidence change have a more pronounced effect on the frequency response of the structure. Specifically, as can be seen from Fig. 3.7, as the angle of incidence increases up to  $40^\circ$ , the center frequency shifts by approximately 2.5%. From this trend, it is expected that increasing the angle of incidence beyond  $40^\circ$  results in further shifting of the center frequency of operation of the MEFSS. Therefore, the desired field of view of this structure (i.e., the range of incidence angles over which the structure is expected to operate) also impacts the effective usable bandwidth of the FSS. This shift in center frequency, however, is not unique to this type of FSS and is observed in the vast majority of FSSs that have higher-order

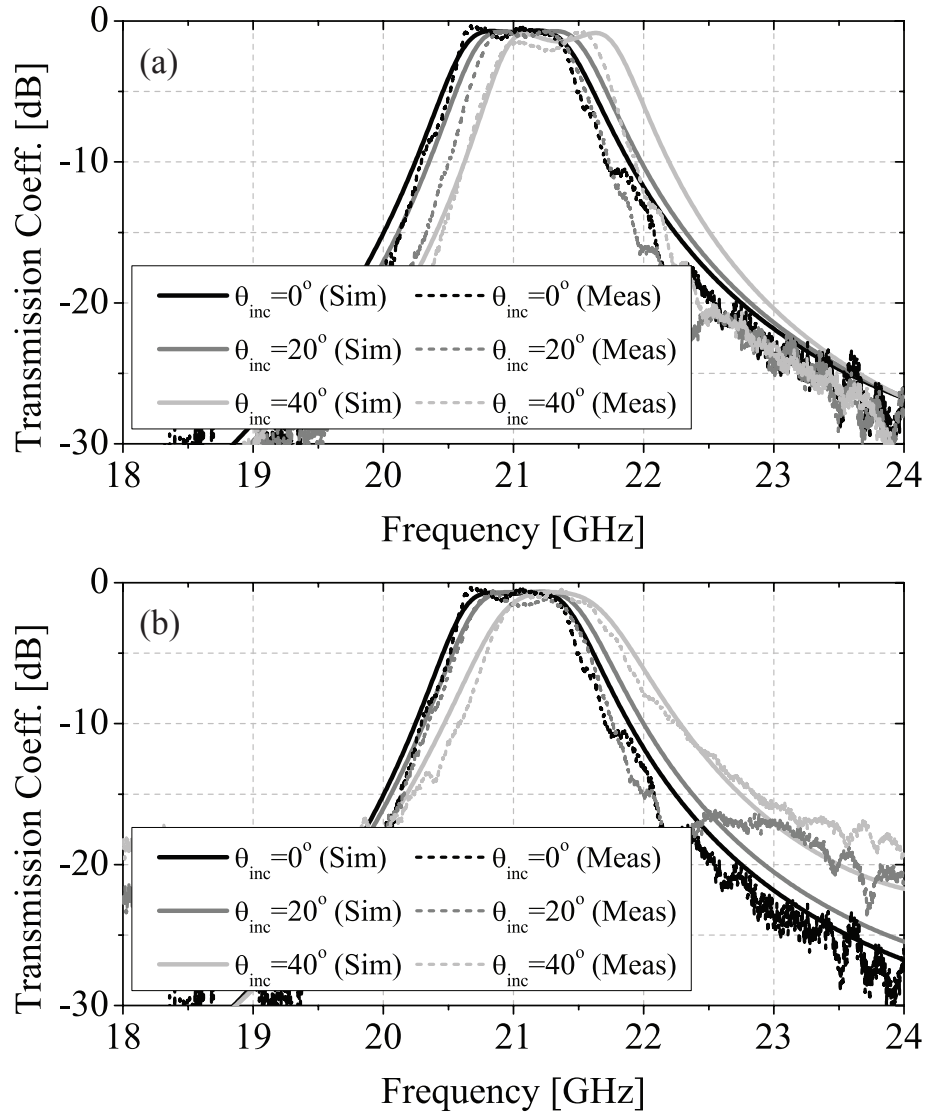


Figure 3.7 Measured and simulated transmission coefficients of the fabricated MEFSS prototype discussed in Section 3.4 and shown in Fig. 3.6 for oblique incidence angles for (a) TE and (b) TM polarizations of incidence.

responses (i.e.,  $N \geq 2$ ). Interested readers are referred to Chapter 7 of [2] for a more detailed discussion of this (Specifically, the interested reader is encouraged to examine Fig. 7.12 of [2]).

## 3.5 Practical Design Considerations

### 3.5.1 Fabrication Complexity

One of the important advantages of the proposed FSS design technique over the previously-reported MEFSS design approaches is the reduction of the fabrication complexity of the structure and the insensitivity of the response of the structure to alignment errors. As described in Section 10.1, the limitations of conventional PCB fabrication technologies all but eliminate the possibility of using the previously-reported FSS design approaches to design FSSs with narrowband, highly-selective bandpass responses. To demonstrate this, let us consider the fabrication complexity of an MEFSS of the type reported in [98] designed to provide the same bandpass response as the structure examined in this chapter (i.e.,  $2^{nd}$ -order response,  $f_0 = 21$  GHz,  $\delta = 5\%$ , and  $D = 3$  mm). This MEFSS was designed using the procedure described in [98]. According to Eqs. (6)-(8) of [98], to achieve this narrow-band response, the gap spacings between capacitive patches of the structure reported in [98] need to be  $5 \mu m$ , which is significantly smaller than the minimum feature size that can be reliably fabricated using standard PCB fabrication technique (approximately  $150 \mu m$ ). Also, according to Eqs. (4)-(5) of [98], the total thickness of this structure is approximately  $150 \mu m$ . While such small overall thickness compared to the wavelength may be advantageous in terms of reducing the sensitivity of the response of this structure with respect to the angle of incidence, it can present problems for the structural rigidity of the FSS. This problem becomes particularly severe if the FSS is to be designed at millimeter-wave or THz frequencies.

Other than the mechanical stability of the structure, such small separations between the different metallic layers of the structure increase the sensitivity of the response of the FSS to the alignment between different layers. This is due to the coupling between the different metal layers of the structure caused by the evanescent higher-order Floquet modes. In the present structure, however, this problem is virtually non-existent. This is due to the all inductive nature of the metallic layers used in the structure as well as the thicker dielectric spacers used between the metallic layers. The latter results in significant reduction of the mutual coupling between the different

metallic layers<sup>2</sup>. To demonstrate the effect of having misalignment between different metallic layers on the performance of the structure discussed in Section 3.4.1, a series of simulations are performed. In these simulations, misalignments are introduced between the different layers of the proposed MEFSS as shown in the inset of Fig. 3.8. In this figure,  $\Delta_{j,j+1}$  refers to the misalignment of the inductor  $L_{j,j+1}$  (shown in Fig.4). Here we assume that the location of the center wire grid is fixed, so the inductors at two sides of the FSS ( $L_{0,1}$  and  $L_{23}$ ) are misaligned with respect to the center wire grid. For simplicity, we have considered the same level of misalignment along the  $x$  and  $y$  directions.  $\Delta = 0$  is considered the perfect alignment case. Fig. 3.8 shows the transmission coefficients of the proposed FSS for a number of different combinations of  $\Delta_{j,j+1}$  values. As can be observed, even for the worst case scenario, where all the metal layers are misaligned compared to one another, the structure's frequency response is practically not changed. This feature is extremely important if the proposed FSS is to be used for millimeter-wave, THz, IR, or visible applications. In such frequency bands, the unit cell dimensions become very small physically and achieving good alignment between multiple metallic layers is extremely difficult. The proposed FSS design virtually eliminates the need for performing any alignment between the different layers at such high-frequency bands. In addition to this, the increased thickness of the proposed structure allows for designing self-standing MEFSS operating at higher frequency bands ranging from the millimeter-wave and THz to infrared and optical bands.

### 3.5.2 Impact of Losses on the Performance of the Structure

The passband bandwidth of a coupled-resonator filter is determined by the loaded quality factor of its resonators as well as the coupling coefficients between the resonators. The loaded quality factor of a resonator can be calculated as the product over sum of the unloaded and the external quality factors. In this context, the unloaded quality factor is associated with the losses of the

---

<sup>2</sup>The mutual coupling between the different metallic layers is predominantly through the higher-order Floquet modes that are evanescent for sub-wavelength periodic structures. Therefore, by using a thicker substrate, the higher-order Floquet modes of each layer will decay considerably before they arrive at the other layer thereby reducing the mutual coupling between the different metallic layers.

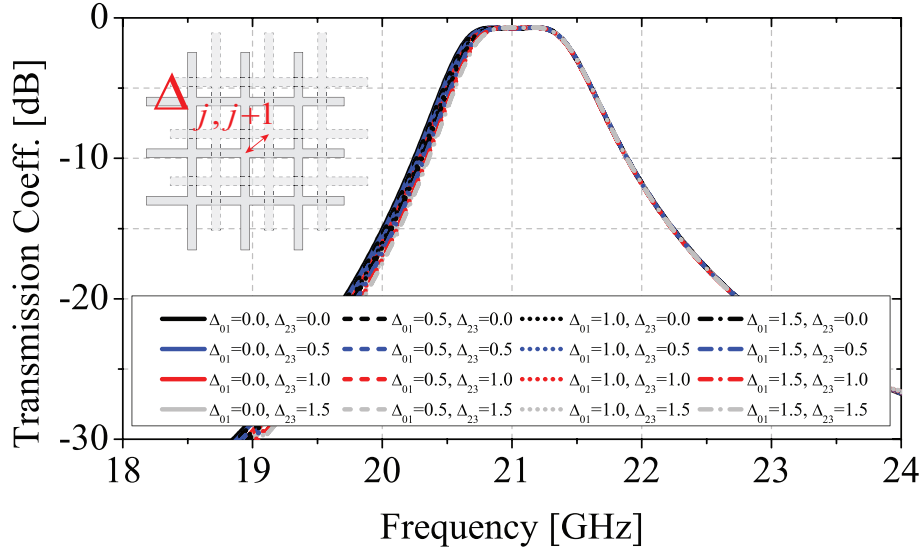


Figure 3.8 Simulated transmission coefficients of the MEFSS discussed in Section 3.4.1 for various scenarios of misalignments between different metallic layers.  $\Delta_{j,j+1}$  represents the misalignment for the inductor  $L_{j,j+1}$ . Here, we assume that the location of the center wire grid is fixed and the inductors at two sides of the FSS are misaligned diagonally in  $x - y$  plane with respect to the center wire grid.

resonator itself including the dielectric and metallic losses while the external quality factor is dependent on the coupling. Therefore, for coupled-resonator filters employing resonators with high unloaded quality factors, the bandwidth is predominantly controlled by the external quality factor of the structure while the internal losses in the resonators mostly impact the insertion loss of the filter in its transmission band. For the MEFSS considered in this chapter, the losses of the substrate primarily impact the insertion loss of the FSS in its pass band. This is shown by conducting a number of full-wave simulations for the structure discussed in Section 3.4.1 in which the loss tangent of the constituting substrates of the MEFSS are increased from 0.002 to 0.010. This range is chosen because it represents the loss range of most commercially available microwave substrates ranging from good to poor. Fig. 3.9 shows the impact of the loss tangent on the performance of the structure. Observe that for these typical  $\tan \delta$  values, the primary impact of increasing the dielectric losses is to increase the insertion loss of the MEFSS in its pass band. Therefore, in designing FSSs of this type, it is important to use low-loss substrates. Finally, for the proposed FSSs with a given response type and order, as the bandwidth of the structure decreases, its insertion loss

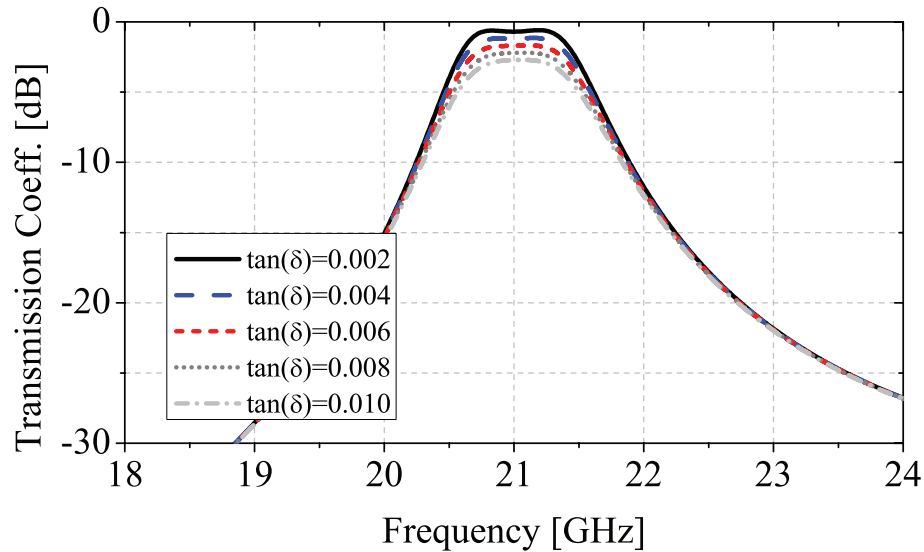


Figure 3.9 Simulated transmission coefficients of the MEFSS discussed in Section 3.4.1 for various loss tangent values of the dielectric substrates.

increases. This phenomenon is well known and understood in the coupled-resonator microwave filter theory and the interested reader is referred to [111, 112] (and the references therein) for an expanded discussion on this.

### 3.5.3 Sensitivity of the Response to the Uncertainties in Dielectric Constant and Substrate Thickness

The resonant frequency of the resonators of the proposed design is mainly determined by the dielectric constant and the thickness of the substrates used in the structure. Therefore, any variations in the values of these parameters from those assumed in the design process can change the operating frequency of the FSS. The impact of these variations on the response of the structure discussed in Section 3.4.1 is demonstrated by conducting a number of full-wave simulations. In these simulations the dielectric constant is considered to change in the range of  $10.2 \pm 0.25$ . Also, the exact thickness of the substrate is allowed to vary in the range of  $1.9 \pm 0.05$  mm. These ranges are the reported values specified by the manufacturer of Rogers RT/duroid 6010. Fig. 3.10(a) shows the impact of the change in the dielectric substrate thickness on the performance of the structure. Observe that the primary impact of variation of the dielectric thickness is to change the

center frequency of the MEFSS. Considering  $h_1 = h_2$  in the structure discussed in Section 3.4.1, the resonant frequency varies within  $\sim 5\%$  of the intended center frequency. Fig. 3.10(b) shows the effect of changing the dielectric constant from the assumed design value on the response of the proposed structure. Observe that as the dielectric constant decreases, the resonant frequency increases. Considering the changes in the dielectric constant is similar in both layers, the resonant frequency varies within  $\sim 2.5\%$  of the expected center frequency.

Since the parameters of the dielectric substrates are among the major factors determining the response of the FSS, it is important to precisely characterize (or determine) the thickness and the dielectric constant of the substrates before a design is performed rather than solely relying on the data provided by the manufacturer. Specifically, if commercially available substrates are used, the thickness of each substrate can be measured using precision digital micrometers with an accuracy better than  $1\text{-}2\ \mu\text{m}$ . The dielectric constant of the substrate can also be characterized experimentally with accuracies in the  $2\text{-}5\%$  range. Since the substrate thickness is generally known with a better degree of accuracy than the dielectric constant, the main source of uncertainty in the design of FSSs of this type is the uncertainties in the exact dielectric constant of the structure. However, the good agreements shown between the measurement and simulation results of the FSS prototype reported in this chapter (see Fig. 3.5) shows that the desired response can be obtained in the first round of fabrication if these issues are taken into account at the design stage.

### 3.6 Conclusions

A new technique for designing low-profile frequency selective surfaces with narrowband, bandpass responses was presented. A comprehensive procedure for synthesizing the proposed FSS was also presented. The technique is based on modeling the FSS with an equivalent circuit model that is a classical inductively-coupled, coupled-resonator bandpass filter. In physical implementation of the FSS, inductive wire grids are used to implement the inductors used in the equivalent circuit model and dielectric spacers are used to implement the series resonators. The proposed design technique allows for designing FSSs with narrowband, bandpass responses with arbitrary orders and response types. Additionally, narrowband operation in the proposed structure is achieved using

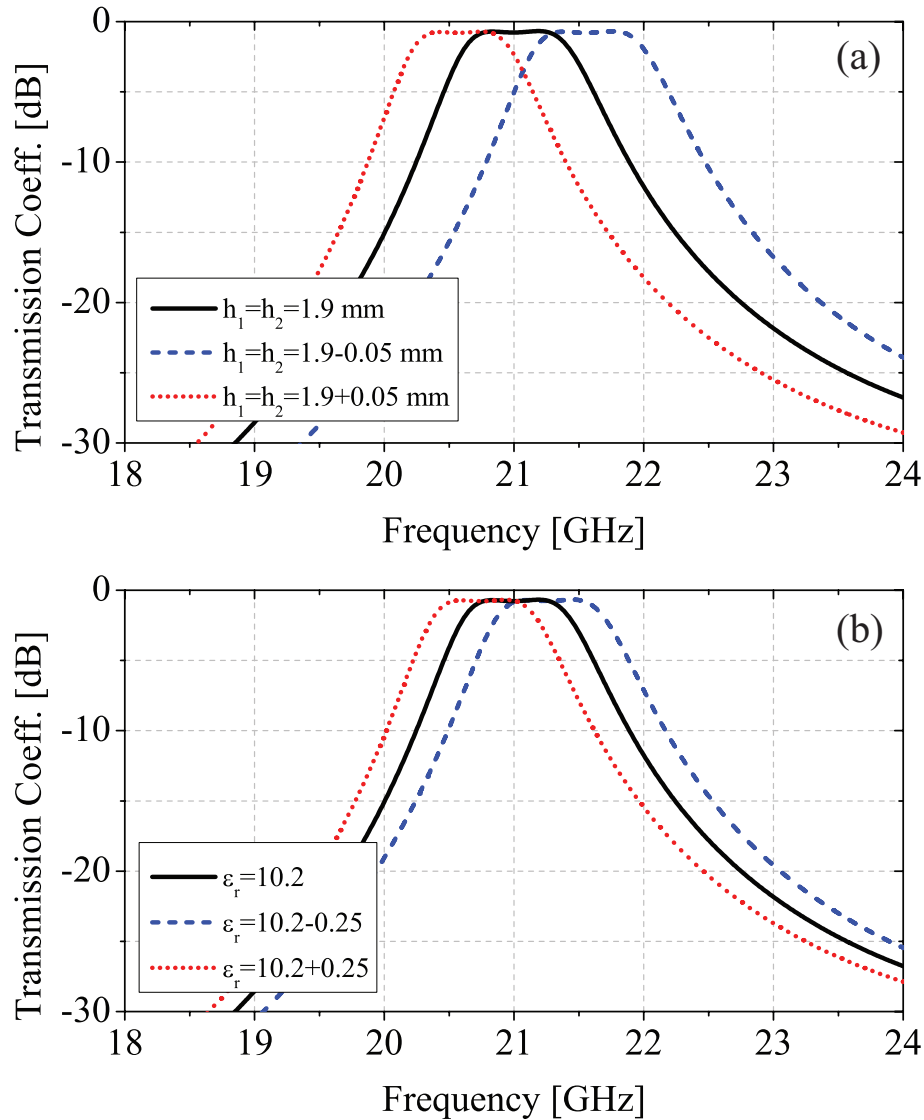


Figure 3.10 Sensitivity of the frequency response of the structure discussed in Section 3.4.1 to the variations of (a) the thickness and (b) the dielectric constant of the substrates from assumed values in the design process.

a simple, planar structure. The introduced concept was also experimentally verified by designing an MEFSS prototype having a second-order bandpass response with a fractional bandwidth of 5% at 21 GHz. The fabricated prototype demonstrated a stable response as a function of the angle of incidence of the electromagnetic wave for both TE and TM polarizations. The main advantages of the proposed FSS include the ability to offer narrowband filtering responses of any arbitrary

order and response type, having a simple design and synthesis procedure that is extremely likely to result in achieving the desired response in the first fabrication iteration, and using simple low-cost fabrication techniques that do not require using through substrate via metallizations.

## Chapter 4

# Wideband Linear-to-Circular Polarization Converters Based on Miniaturized-Element Frequency Selective Surfaces

### 4.1 Introduction

In antenna design, the choice of the polarization of the radiated wave generally depends on the application as well as the propagation environment. For instance, in satellite communications or navigation systems, circularly-polarized waves are preferred due to the advantages such as lower sensitivity to multipath fading and reduced sensitivity to Faraday rotation or the orientation of the receiver's antenna. In communications systems involving satellite-earth links, a linearly-polarized wave experiences an unpredictable rotation as it propagates through the ionosphere. This rotation may cause polarization mismatch at the receiver that impacts the link budget of the system [113]. Circularly-polarized (CP) waves, on the other hand, do not suffer from these issues and have been used in modern satellite and point-to-point communications systems to improve the polarization efficiency and propagation link budget. Over the past several decades, a variety of different circularly-polarized antenna designs have been reported in the literature. An alternative way of generating a circularly-polarized wave is to generate a linearly-polarized wave and pass it through a polarization converter. This technique is particularly attractive in situations where the radiating system consists of a planar array and generating CP waves at the element level may not be convenient. In such a situation, a polarization converter can be placed on top of the linearly-polarized antenna system to produce circularly-polarized waves.

A polarization converter is a slab of an anisotropic medium that converts an incident wave with a given polarization to a reflected or a transmitted wave with a different polarization (e.g. linear

to circular or vertical to horizontal). Planar polarization converters are generally implemented using frequency selective surfaces or other types of periodic structures. These structures normally operate based on dividing a wave into two orthogonal components and generating a  $90^\circ$  phase shift between them. A simple implementation for such a device is a reactive surface having inductive impedance for one component of the field and capacitive impedance for the other. This way, a phase shift of  $90^\circ$  may be obtained between the two components of the emerging transmitted wave. If these two components have equal amplitudes, the incident linearly-polarized wave will be converted to a transmitted circularly-polarized wave at the output.

Over the past several decades, a number of different types of polarization converters operating in such a fashion have been reported in the literature [34–48]. The work reported in [34] is among the first structures designed to perform a conversion between linearly- and circularly-polarized waves. The structure presented in [34] is a multilayer structure consisting of both inductive and capacitive impedance sheets. The dimensions of the structure are chosen in such a way to introduce a  $90^\circ$  phase shift between orthogonal field components to achieve a circularly-polarized transmitted wave when the structure is illuminated with a linear polarization. In [35], a meandered-line polarizer is reported. This polarization converter is a multilayer structure composed of meandered metallic strips. The basic approach in the design of this structure is to make an array that is predominantly inductive to one polarization and capacitive to the orthogonal polarization. This concept was modified and improved in [36] and [37]. Also, the integration of such a converter and a horn antenna was investigated in [38]. Other than the aforementioned structures, two-dimensional arrays of cross-shaped dipoles [39], [40], cross-shaped slots [41], split-ring slots [41–43], and hexagonal-shaped slots [41] with asymmetric features have also been used to design polarization converters. Furthermore, in [44] and [45] polarizers composed of arrays of respectively T-shaped slots and bisected split-ring elements were reported. Despite the advantages offered by these structures, most of them use resonant constituting elements and hence, they tend to be narrowband structures. Furthermore, the relatively large dimensions of the unit cells of most of these structures deteriorates their performances under oblique incidence angle illumination conditions.

Over the past few years, a new class of metamaterial-inspired frequency selective surfaces with sub-wavelength unit cell dimensions - referred to as miniaturized-element frequency selective surfaces (MEFSSs) - has been studied [1, 8, 20–27, 81, 89, 97, 98, 102, 114, 115]. To date, such structures have been employed in a wide range of devices including spatial filters [8, 102], transmitarrays [13–15, 100], and reflectarrays [101, 116]. In this chapter, we present a method for designing wideband polarization converters based on MEFSSs. The proposed converters are composed of two dimensional arrays of capacitive patches and inductive wire grids separated from one another with thin dielectric substrates. Each pixel in the proposed polarization converter is a unit cell of an appropriately-designed MEFSS with different transmission characteristics for the two orthogonal polarizations. Over the band of interest, the structure is impedance matched for both orthogonal polarizations while providing two distinct linear phase responses with a phase difference of  $90^\circ$  between them. With these principles of operation, the proposed device is capable of offering wideband operation. In addition, due to the small unit cell dimensions and the low-profile nature of the proposed structure, this device can demonstrate a stable performance with respect to the incidence angle with a wide field of view. Using this approach, a linear-to-circular polarization converter prototype operating within the X-band (8-12 GHz) was designed, fabricated, and experimentally characterized. The measurement results confirm that the fabricated device operates over a bandwidth of more than 40%. The measurements also demonstrate that the structure has a very consistent frequency response as a function of the angle of incidence of the EM wave, with a field of view of  $\pm 45^\circ$ .

## 4.2 Principles of Operation

Fig. 4.1 presents the topology of a linear-to-circular polarization converter. This device is a slab of anisotropic medium, which converts a linearly-polarized wave to a circularly-polarized one. The device is illuminated with a linearly-polarized incident wave with the electric field vector,  $\vec{E}^i$ , tilted  $45^\circ$  relative to both  $\hat{x}$  and  $\hat{y}$  directions.  $\vec{E}_x^i$  and  $\vec{E}_y^i$  are the vertical and horizontal components of the incident electric field, respectively. This polarization converter behaves differently for these two components. Specifically, the device has different frequency responses for the vertical

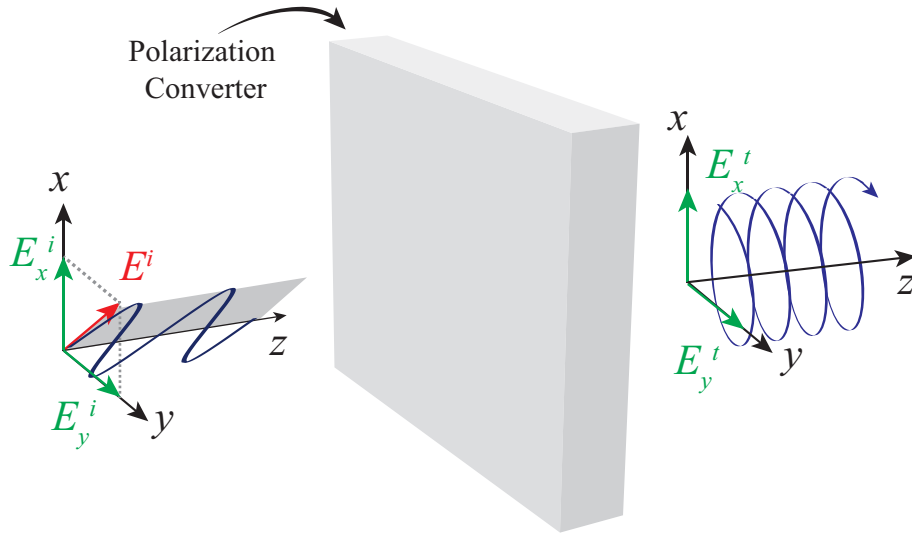


Figure 4.1 Schematic model of a linear-to-circular polarization converter. In this configuration, the incident electric field vector is tilted  $45^\circ$  relative to  $\hat{x}$  and  $\hat{y}$  directions. After passing through the converter, the transmitted signal is right-handed circularly polarized.

and horizontal components of the incident wave. Within the operational band, the magnitude of the transmission coefficient for each component is ideally equal to one and the device passes both components very efficiently within the pass band with little or no attenuation. However, the vertical and horizontal components experience two distinct phase shifts with the phase difference of  $90^\circ$  while propagating through the converter. As a result, within the transmission window, the polarization of the emerging wave on the other side will be circular.  $\vec{E}_x^t$  and  $\vec{E}_y^t$  are the two orthogonal components of the transmitted wave and are expressed in terms of  $\vec{E}_x^i$  and  $\vec{E}_y^i$  using the following formulas:

$$\vec{E}_x^t = T_x \vec{E}_x^i \quad (4.1)$$

$$\vec{E}_y^t = T_y \vec{E}_y^i \quad (4.2)$$

where  $T_x = |T_x|e^{j\angle T_x}$  and  $T_y = |T_y|e^{j\angle T_y}$  are the transmission coefficients of the device for the  $\hat{x}$  and  $\hat{y}$  polarizations, respectively. In (4.1) and (4.2), the cross transmission coefficients (i.e.,  $T_{xy}$  and  $T_{yx}$ ) are considered to be negligible. To achieve a circularly-polarized wave at the output within the operational band,  $T_x$  and  $T_y$  are related based on the following formulas:

$$|T_x| = |T_y| \quad (4.3)$$

$$\angle T_y - \angle T_x = \pm \frac{\pi}{2} \quad (4.4)$$

The sign in (4.4) determines the sense of rotation of the circularly-polarized output wave. The transmitted wave is left-handed circularly polarized if  $\angle T_y - \angle T_x = \frac{\pi}{2}$  and right-hand circularly-polarized if  $\angle T_y - \angle T_x = -\frac{\pi}{2}$ .

The polarization converter shown in Fig. 4.1 is implemented using miniaturized-element frequency selective surfaces. The elements of conventional MEFSSs often have two axes of symmetry (i.e., rotationally symmetric for a rotation angle of  $90^\circ$ ) and hence, are polarization independent for normal incidence angles. Polarization converters, on the other hand, need to have different responses for  $\hat{x}$ - and  $\hat{y}$ -polarized waves. Therefore, the present structure needs to feature asymmetric elements within a unit cell to generate two distinct frequency responses for vertical and horizontal components of the incident wave. Fig. 4.2 shows the three-dimensional topology of the proposed polarization converter. The structure consists of two-dimensional periodic arrangements of sub-wavelength capacitive patches and planar wire grids, separated from one another by thin dielectric substrates. Assuming that the thickness of the substrate between two consecutive metallic layers is  $h$ , the overall thickness of the structure is  $(N - 1) \times h$ , where  $N$  is the total number of metallic layers used to implement the structure. The top view of one unit cell of the capacitive layer and that of an inductive layer are shown in the inset of Fig. 4.2. The dimensions of the unit cell along the  $\hat{x}$  and  $\hat{y}$  directions are  $D_x = D_y = D$ . The capacitive patches are in the form of rectangular metallic patches with dimensions of  $D - s_x^i$  and  $D - s_y^i$ , where  $s_x^i$  and  $s_y^i$  are the gap spacings between two adjacent patches in the  $i^{\text{th}}$  layer in  $\hat{x}$  and  $\hat{y}$  directions, respectively. The inductive wire grids are the combination of two metallic strips with the widths of  $w_x^i$  and  $w_y^i$  oriented perpendicularly to each other. Due to these asymmetric features, this structure will have different responses for incident plane waves polarized along the  $\hat{x}$  and  $\hat{y}$  directions.

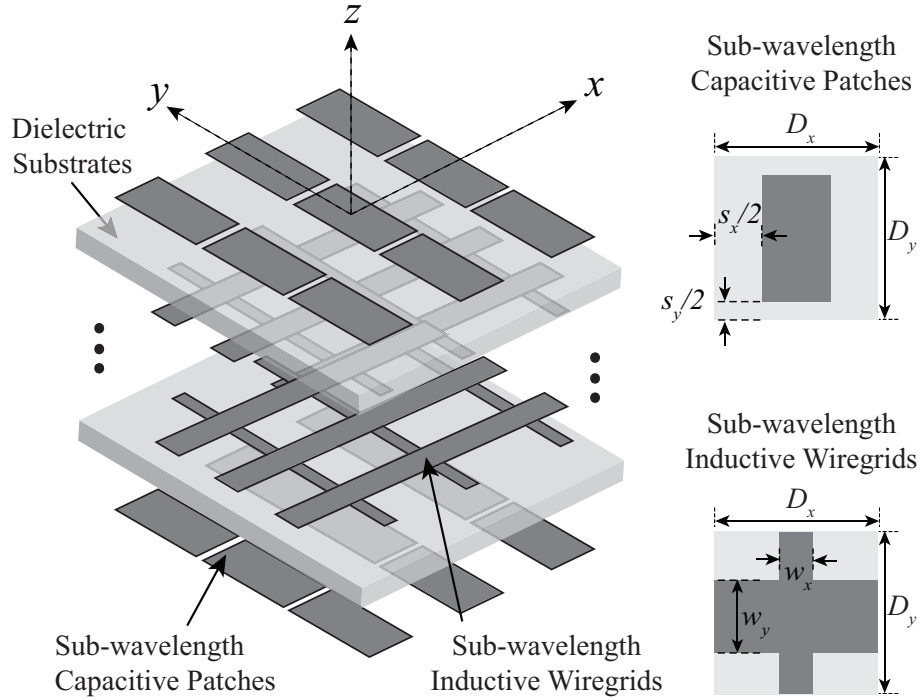


Figure 4.2 Topology of the proposed polarization converter based on bandpass miniaturized-element frequency selective surfaces. The unit cells of the capacitive patches and the inductive wire grids are shown on the right hand side of the figure.

The synthesis procedure of MEFSSs are typically based on a generalized equivalent circuit model whose values are determined from the system level performance indicators such as the center frequency of operation, operational bandwidth, response type, etc. In the proposed device, the structure of the equivalent circuit model is the same for both polarizations with the exception of the element values as shown in Fig. 4.3. In this circuit model, the capacitive patches are modeled with parallel capacitors  $C_x^1, C_x^3, \dots, C_x^N$  for  $\hat{x}$  polarization, while these capacitors are  $C_y^1, C_y^3, \dots, C_y^N$  for  $\hat{y}$  polarization. The inductive wire grids are represented by parallel inductors  $L_x^2, \dots, L_x^{N-1}$  and  $L_y^2, \dots, L_y^{N-1}$  for the  $\hat{x}$  and  $\hat{y}$  polarizations, respectively. Thin substrates separating the inductive and capacitive layers are modeled with transmission lines with characteristic impedances of  $Z_{1,2}, \dots, Z_{N-1,N}$  and lengths of  $h_{1,2}, \dots, h_{N-1,N}$  for both polarizations. For non-magnetic media  $Z_{i,i+1} = Z_0(\epsilon_r^{i,i+1})^{-1/2}$ . Free space on each side of the device is modeled with semi-infinite transmission lines with characteristics impedance of  $Z_0 = 377 \Omega$ .

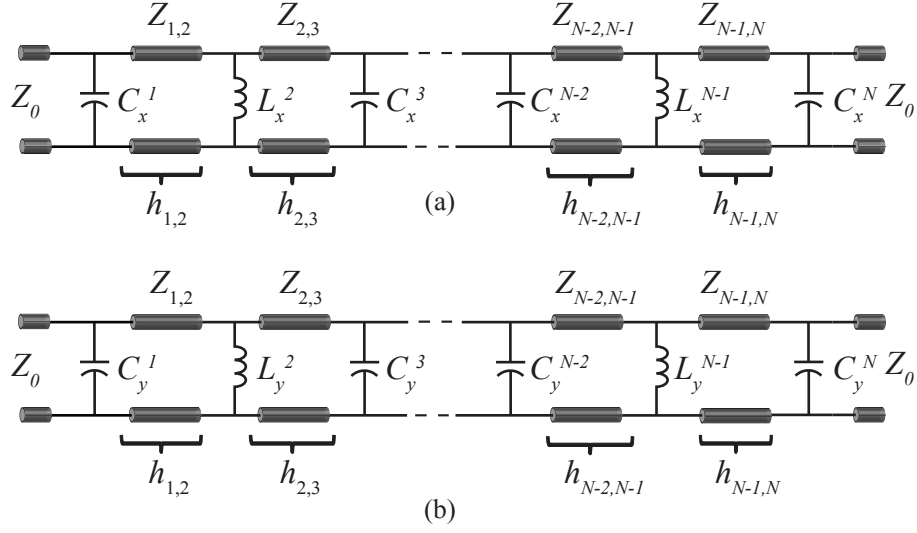


Figure 4.3 Equivalent circuit model of the converter shown in Fig. 4.2 for (a) the vertical ( $\hat{x}$ -directed) and (b) the horizontal ( $\hat{y}$ -directed) polarizations.

As described in [14,15,100], MEFSSs can be used as time delay units. To act in such a manner, they must be designed to provide linear phase responses with desired slopes versus frequency over a wide range of frequencies in their transmission windows (i.e. to provide desired, constant group delays). Therefore, if the proposed structure is designed to exhibit a linear phase response for both  $\hat{x}$  and  $\hat{y}$  polarizations while maintaining a phase difference of  $90^\circ$  between the two responses, a wideband polarization converter can be achieved. This concept is depicted in Fig. 4.4. In this figure,  $T_x$  and  $T_y$  are the transmission coefficients of the polarization converter for  $\hat{x}$  and  $\hat{y}$  polarizations, respectively. The transmission windows for  $\hat{x}$ - and  $\hat{y}$  polarizations are respectively  $\Delta f_t^x = f_H^x - f_L^x$  and  $\Delta f_t^y = f_H^y - f_L^y$ . The overlap frequency band between the two responses is shown as  $\Delta f_d = f_H^x - f_L^y$ . The operational band of interest for the polarization converter is also denoted as  $\Delta f_{opt} = f_H - f_L \leq \Delta f_d$ . Generally  $\Delta f_{opt}$  is smaller than  $\Delta f_d$  because the phase responses of  $T_x$  and  $T_y$  are not linear close to the band edges in most MEFSS implementations [14]. The total phase span within the transmission windows is approximately the same ( $\Delta\phi_t$ ) for both polarizations as this parameter is mainly a function of the order of the response of the MEFSS used to construct the device ( $\frac{N+1}{2}$ , where  $N$  is the number of metallic layers). The relation between these two parameters can be expressed as  $\Delta\phi_t \approx \frac{(N+1)\pi}{4}$ . For an ideal case, the frequency

response for the  $\hat{x}$  polarization is a de-tuned version of the frequency response for the  $\hat{y}$  polarization while ensuring that the desired phase and amplitude responses are maintained. Therefore, the bandwidth of both responses and their total phase shifts within their transmission windows are  $\Delta f_t = \Delta f_t^x = \Delta f_t^y$  and  $\Delta \phi_t$ , respectively. Thus, to achieve an operational bandwidth of  $\Delta f_{opt}$ , the transmission window for each of the two responses can be calculated using the following formula:

$$\Delta f_t \geq \frac{\Delta f_{opt}}{\left(1 - \frac{\Delta \phi_d}{\Delta \phi_t}\right)} \quad (4.5)$$

where  $\Delta \phi_d$  is the desired phase difference of  $90^\circ$  in an ideal situation. For example, if the total phase span of the transmission coefficient for both polarizations is  $270^\circ$ , then, the bandwidth of each response needs be at least 1.5 times the desired bandwidth of the polarization converter; i.e.  $\Delta f_t = 3/2 \times \Delta f_{opt}$ . As described in [14, 15], the total phase shift provided by an MEFSS is a function of the order of the response. Therefore, for a given desired bandwidth of the polarization converter, as the order of the MEFSS responses is increased, a narrower bandwidth for each of the  $T_x$  and  $T_y$  responses of the MEFSS will be required.

### 4.3 Design Procedure

The design procedure of the proposed polarization converter is based on synthesizing the transmission characteristics of the required responses for both vertical and horizontal polarizations. These responses are determined based on the operational band of interest  $\Delta f_{opt} = f_H - f_L$ . To do so, the structure is first designed based on the equivalent circuit model and then the physical and geometrical parameters (e.g. wire widths and gap spacings) are calculated using equations (23)-(24) in [1]. The design procedure of the proposed device consists of a few different steps. This design starts by determining the order of the response of the MEFSS ( $\frac{N+1}{2}$ ) for both polarizations (i.e. number of metallic layers  $N$ ). This parameter must be chosen to satisfy (4.5), given the desired  $\Delta f_{opt}$ . It is recommended that the lowest order of the filter response satisfying (4.5) is used for the design, since the design complexity increases as  $N$  increases. Furthermore, increasing  $N$  increases the overall thickness of the structure, which may cause the deterioration of the response

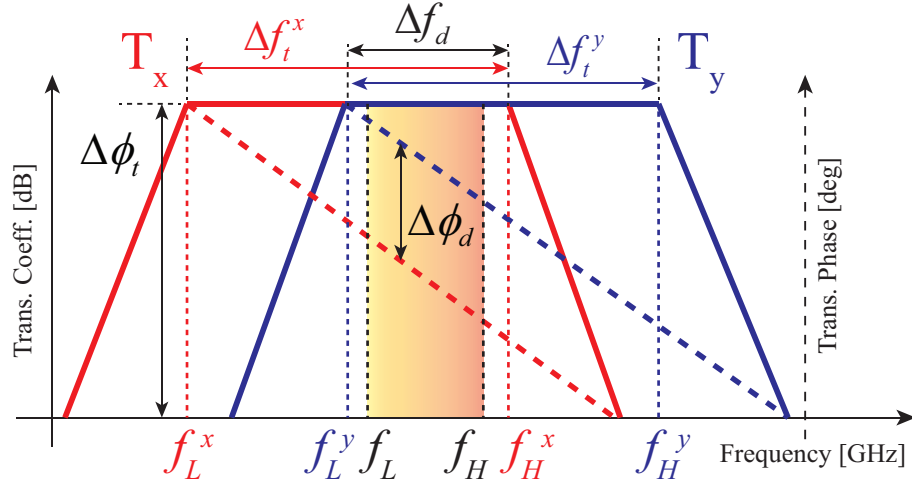


Figure 4.4 The concept of de-tuning to design a wideband polarization converter.  $T_x$  and  $T_y$  show the frequency responses of the device for vertical ( $\hat{x}$ ) and horizontal ( $\hat{y}$ ) polarizations, respectively. The transmission windows for  $\hat{x}$  and  $\hat{y}$  polarizations are respectively  $\Delta f_t^x = f_H^x - f_L^x$  and  $\Delta f_t^y = f_H^y - f_L^y$ . In this configuration,  $\Delta f_d$  is the overlap region between the two responses and  $\Delta f_{opt}$  shows the operational band of interest in which the structure is impedance matched for both orthogonal polarizations while there is a  $90^\circ$  phase difference between their corresponding transmission phases.

of the structure under oblique incidence illumination. Knowing the order of the response,  $\frac{N+1}{2}$ , and  $\Delta f_{opt}$ , the minimum operational bandwidth for responses for the  $\hat{x}$  and  $\hat{y}$  polarizations (i.e.  $\Delta f_t^x$  and  $\Delta f_t^y$ ) can be determined using (4.5). After determining the order of the response and the bandwidth for each polarization, the values of the elements of the circuit models shown in Fig. 4.3 can be calculated using the procedure described in Section II of [1]. However, to ensure that the phase difference between the two components remains  $90^\circ$  over the entire band of interest, a modified procedure needs to be followed. In this procedure, the initial values of the elements of the equivalent circuit model for both polarizations are determined based on the synthesis procedure described in [1]. Then, one of the initial responses is kept the same and the other one is fine tuned to ensure that the design goals are achieved over the entire band. The tuning is performed by optimizing the parallel inductor and capacitor values. The specific design goals for this optimization step are to have a transmission window overlap and a phase difference of  $90^\circ$  over the entire operational band of interest. Alternatively, this goal can be considered as achieving a required axial ratio for

the transmitted signal within the frequency band of operation. This parameter can be determined using the following formula:

$$AR = \left( \frac{|T_x|^2 + |T_y|^2 + \sqrt{a}}{|T_x|^2 + |T_y|^2 - \sqrt{a}} \right) \quad (4.6)$$

$$a = |T_x|^4 + |T_y|^4 + 2|T_x|^2|T_y|^2 \cos(2(\angle T_y - \angle T_x))$$

Assuming that  $T_y$  is synthesized first and  $T_x$  is determined in the de-tuning step, the optimization parameters are the values of the parallel capacitors  $C_x^1, \dots, C_x^N$  and those of the parallel inductors  $L_x^2, \dots, L_x^{N-1}$  in the equivalent circuit model shown in Fig. 4.3. The thicknesses of the substrates are already determined while  $T_y$  is synthesized. This optimization can be performed using two different methods. The first technique is to use a commercially-available circuit simulation and optimization software (e.g. Agilent Advance Design System<sup>®</sup>). Alternatively, the transfer function of an MEFSS can be predicted using its equivalent circuit model:

$$T = \frac{2}{A + \frac{B}{Z_0} + CZ_0 + D} \quad (4.7)$$

where  $A$ ,  $B$ ,  $C$ , and  $D$  are given by:

$$\begin{bmatrix} A & B \\ C & D \end{bmatrix} = \left( \prod_{i=1, i \text{ odd}}^{N-2} \mathbf{T}_C^i \mathbf{T}_h^{i,i+1} \mathbf{T}_L^{i+1} \mathbf{T}_h^{i+1,i+2} \right) \mathbf{T}_C^N \quad (4.8)$$

In (4.8),  $\mathbf{T}_C^i$ ,  $\mathbf{T}_L^i$ , and  $\mathbf{T}_h^{i,i+1}$  can be calculated using the following formulas:

$$\mathbf{T}_C^i = \begin{bmatrix} 1 & 0 \\ j\omega C_x^i & 1 \end{bmatrix} \quad (4.9)$$

$$\mathbf{T}_L^i = \begin{bmatrix} 1 & 0 \\ (j\omega L_x^i)^{-1} & 1 \end{bmatrix} \quad (4.10)$$

$$\mathbf{T}_h^{i,i+1} = \begin{bmatrix} \cos \beta h_{i,i+1} & jZ_{i,i+1} \sin \beta h_{i,i+1} \\ (j/Z_{i,i+1}) \sin \beta h_{i,i+1} & \cos \beta h_{i,i+1} \end{bmatrix} \quad (4.11)$$

Table 4.1 The element values of circuit models shown in Fig. 4.3 to have third-order responses with  $\Delta f_x = 3.75$  GHz-12.25 GHz and  $\Delta f_y = 7.75$  GHz - 16.25 GHz for the vertical and horizontal polarizations, respectively.

Parameter	$C_1^y = C_5^y$	$C_3^y$	$L_2^y = L_4^y$	$L_2^x = L_4^x$
value	23 fF	46 fF	1.1 nH	3.5 nH
Parameter	$C_1^x = C_5^x$	$C_3^x$	$h_{1,2} = h_{4,5}$	$h_{2,3} = h_{3,4}$
value	90 fF	120 fF	1.27 mm	1.27 mm

where  $Z_{i,i+1}$  and  $\beta = \frac{\omega\sqrt{\epsilon_r^{i,i+1}}}{c}$  are respectively the characteristic impedance and propagation constant of the transmission lines. Combination of (4.7)-(4.11) yields a relationship between the phase and magnitude of the frequency response (i.e.  $\angle T_x$  and  $|T_x|$ ) and the element values in the equivalent circuit model shown in Fig. 4.3. Using these equations, a simple computer program can be written (e.g. in MATLAB) to perform the optimization. In the final step, after calculating all the element values of the equivalent-circuit models shown in Fig. 4.3, the geometrical parameters including the strip widths and gap spacings can be determined using equations (23)-(24) of [1].

#### 4.4 A Design Example, Experimental Verification, and Measurement Results

The procedure presented in Section 4.3 was followed to design a polarization converter operating over the frequency range of 8 GHz to 12 GHz or equivalently a 40% fractional bandwidth. The bandwidth is defined as the frequency range over which the axial ratio is below 3 dB and the total transmission coefficient is higher than -3 dB. A third-order bandpass MEFSS with a Chebyshev response was used to design this polarization converter. With this order of response, the total phase shift over the entire main transmission window is  $270^\circ$ . Based on (4.5), designing this polarization converter requires using third-order bandpass MEFSSs with minimum bandwidths of 6 GHz for each of the horizontal and vertical responses. Following the design procedure, to meet the minimum bandwidth requirement and having  $f_L^y \leq f_L$ , a frequency response with center frequency of 12 GHz and the bandwidth between 7.75 GHz to 16.25 GHz for the  $\hat{y}$  polarization was synthesized using the design procedure presented in [1]. In doing so, first the element values of the equivalent

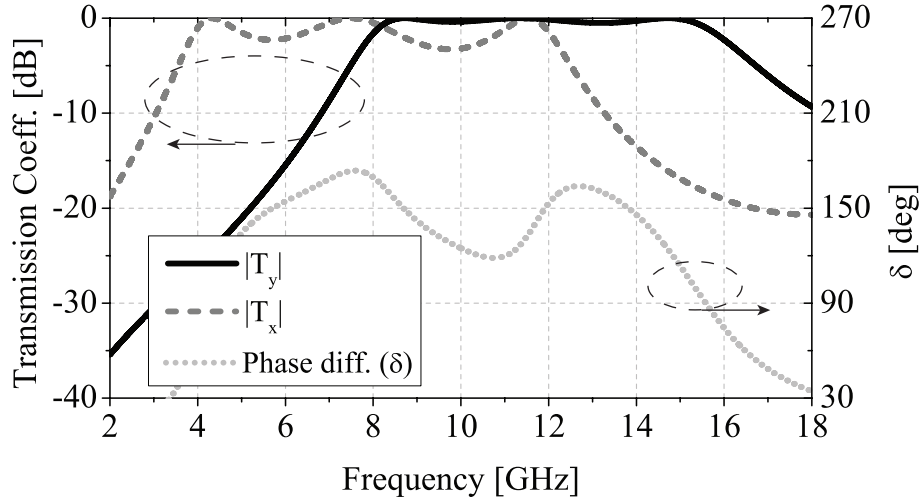


Figure 4.5 Calculated transmission coefficients of the polarization converter discussed in Section 4.4 as well as the difference between the corresponding transmission phases with the parameters shown in Table 4.1.

circuit model of the structure including the values of three capacitors, two inductors, and the thicknesses of the dielectric substrates were determined. In this design, the dielectric substrates were assumed to be non-magnetic having a dielectric constant of  $\epsilon_r=10.2$  (Rogers RT/duroid 6010). These circuit values are reported in Table 4.1. The frequency response of the MEFSS for the  $\hat{x}$  polarization was also synthesized similar to the procedure used to synthesize the MEFSS response for the  $\hat{y}$  polarization. To do so, a frequency response with a center frequency of 8 GHz and the bandwidth between 3.75 GHz and 12.25 GHz was considered. The circuit values used to achieve such a response are listed in Table 4.1. Fig. 4.5 shows the simulated transmission coefficients of the MEFSS for both polarizations as well as the difference between their transmission phases obtained using the circuit values reported in Table 4.1. The structure for both polarizations is assumed to be symmetric with respect to the center capacitive layer. In the next step, the element values of the equivalent circuit model for the  $\hat{x}$  polarization including  $C_1^x = C_5^x$ ,  $C_3^x$ , and  $L_2^x = L_4^x$  were de-tuned to achieve the design goals. As described in Section 4.3, this step can be accomplished using optimization in ADS or simply using equations (4.7)-(4.11) to numerically perform the optimization. In this example, a hybrid optimizer with least squares error function was employed. As discussed, the goal was to achieve axial ratio of below 3 dB within the transmission

Table 4.2 The finalized element values of the equivalent circuit models shown in Fig. 4.3 for the polarization converter discussed in Section 4.4.

Parameter	$C_1^y = C_5^y$	$C_3^y$	$L_2^y = L_4^y$	$L_2^x = L_4^x$
value	23 fF	46 fF	1.1 nH	1.49 nH
Parameter	$C_1^x = C_5^x$	$C_3^x$	$h_{1,2} = h_{4,5}$	$h_{2,3} = h_{3,4}$
value	67 fF	112 fF	1.27 mm	1.27 mm

window overlap of responses for the two orthogonal polarizations. The final element values of the equivalent-circuit model for both the horizontal and the vertical polarizations are listed in Table 4.2. Fig. 4.6(a) shows the magnitudes of the frequency responses predicted using the circuit models with the values reported in Table 4.2. The difference between the transmission phases of responses for the horizontal and the vertical polarizations predicted using circuit models is also shown in Fig 4.6(b).

The unit cell dimension of the designed structure is selected to be 4.5 mm, which is equivalent to approximately  $0.15\lambda_0$ , where  $\lambda_0$  is the free-space wavelength at the center frequency of operation  $f_c = 10$  GHz. Therefore, using  $D = 4.5$  mm and the capacitance and inductance values reported in Table 4.2, the widths of the inductive wire grids and the capacitive gap spacings can be calculated. Since the proposed structure is a multilayer structure, the effect of the bonding layers placed between the adjacent substrates on its response should also be considered. The bonding material used in this design is Rogers 4450F prepreg with the dielectric constant of  $\epsilon_r = 3.52$  and the thickness of  $h_b = 0.1$  mm. Introduction of the bonding layers creates an asymmetry in the topology of the structure, which can slightly change the frequency response of the device. This asymmetry can be eliminated by using two closely-spaced patches on the two sides of the middle bonding layer as shown in Fig. 4.7 instead of using just one patch placed on only one side of this layer. The final physical parameters of the structure are listed in Table 4.3. The structure was simulated in CST Microwave Studio<sup>®</sup> and its frequency responses for both the horizontal and the vertical polarizations were calculated. Fig. 4.6(a) shows the full-wave simulated transmission coefficients of the polarization converter for both polarizations alongside the frequency responses

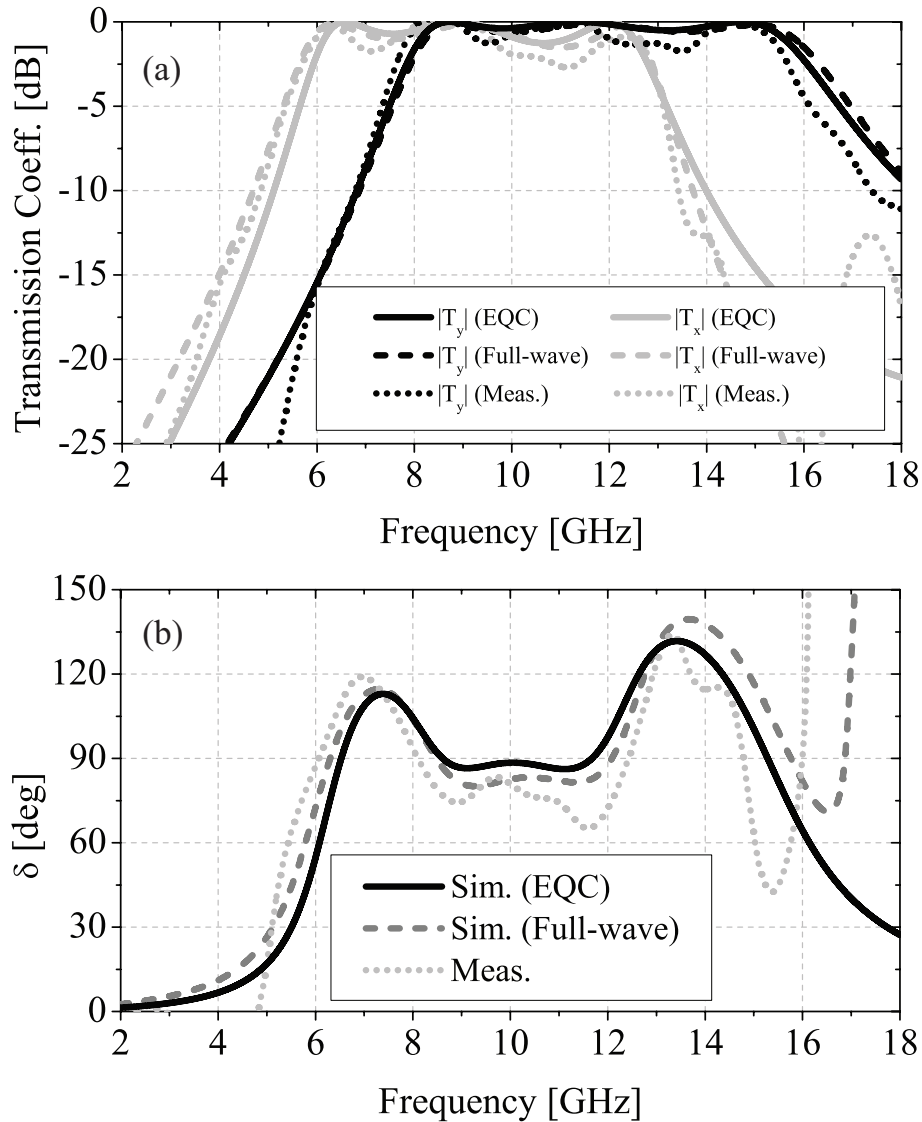


Figure 4.6 Simulated and measured transmission characteristics of the polarization converter discussed in Section 4.4. These characteristics include (a) transmission coefficients for the two orthogonal polarizations and (b) the difference between their corresponding transmission phases. Simulated results based on the equivalent circuit model are calculated using the values listed in Table 4.2. The full-wave simulated results are obtained based on the values reported in Table 4.3.

predicted by the equivalent circuit model. The phase difference between the transmission phases of both polarizations is also shown in Fig. 4.6(b). Using (4.6), the axial ratio of the transmitted signal was also calculated based on the two responses. Fig. 4.8 shows the predicted axial ratio of the transmitted wave based on both the full-wave simulated results and those obtained using

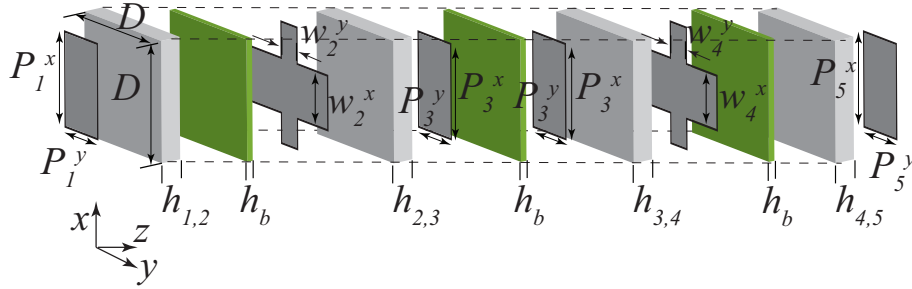


Figure 4.7 Unit cell of the proposed polarization converter discussed in Section 4.4. Notice that the two capacitive patches placed in the center are separated from one another by a thin prepreg layer. These two layers constitute a single hybrid capacitive layer. This arrangement is used to maintain the symmetry of the structure as discussed in Section 4.4.

Table 4.3 Physical parameters of the polarization converter discussed in Section 4.4, with the unit cell shown in Fig. 4.7 and with the equivalent circuit model element values reported in Table 4.2.

The unit cell dimension for this structure is  $D = 4.5\text{mm}$ .

Parameter	$P_1^y = P_5^y$	$P_3^y$	$w_2^x = w_4^x$	$w_2^y = w_4^y$
value	1 mm	1.6 mm	0.8 mm	0.2 mm
Parameter	$P_1^x = P_5^x$	$P_3^x$	$h_{1,2} = h_{4,5}$	$h_{2,3} = h_{3,4}$
value	2.9 mm	2.5 mm	1.27 mm	1.27 mm

the equivalent circuit model. Observe that the full-wave simulated results are consistent with the predictions from the equivalent-circuit model. The axial ratio remains below 3 dB between 7.92 GHz to 12.54 GHz, which successfully covers the entire X-band.

A prototype of the proposed polarization converter was fabricated using standard PCB lithography and substrate bonding techniques. The fabricated prototype has six metallic layers and four dielectric substrates. The panel dimensions of the fabricated prototype are  $33.75\text{ cm} \times 22.5\text{ cm}$  ( $\approx 11.25\lambda_0 \times 7.5\lambda_0$ ). The total thickness of the structure, including the bonding layers, is 5.4 mm which is approximately equivalent to  $0.18\lambda_0$  at 10 GHz. The photograph of the fabricated prototype is shown in Fig. 4.9. The fabricated prototype was characterized using free-space measurement techniques. To do so, the frequency responses of the prototype, for the two orthogonal polarizations, were measured and the axial ratio was calculated in the post processing step using

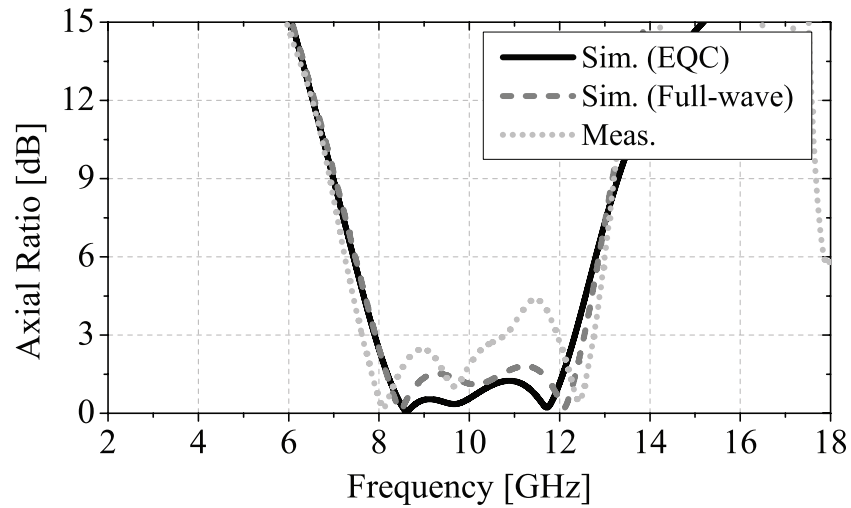


Figure 4.8 Simulated and measured axial ratios of the polarization converter discussed in Section 4.4. These results are obtained using Eq. (4.6) with the values obtained from the simulated and measured magnitude and phase of the response of the FSS for both  $\hat{x}$  and  $\hat{y}$  polarizations.

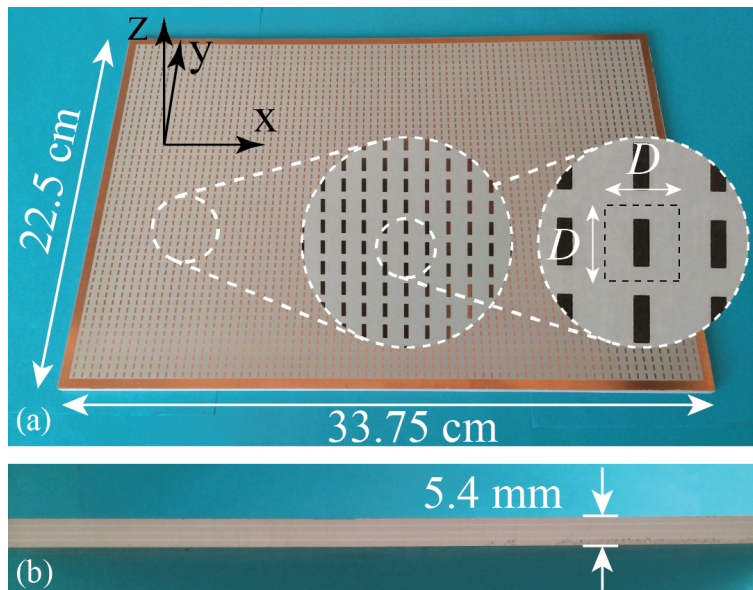


Figure 4.9 (a) Photograph of the fabricated polarization converter. (b) Side view of the fabricated prototype.

(4.6). The measurement setup consisted of a large metallic screen with an opening having the same dimensions as those of the polarization converter at its center. This screen was placed between the transmitting and receiving antennas both connected to the two ports of a vector network analyzer

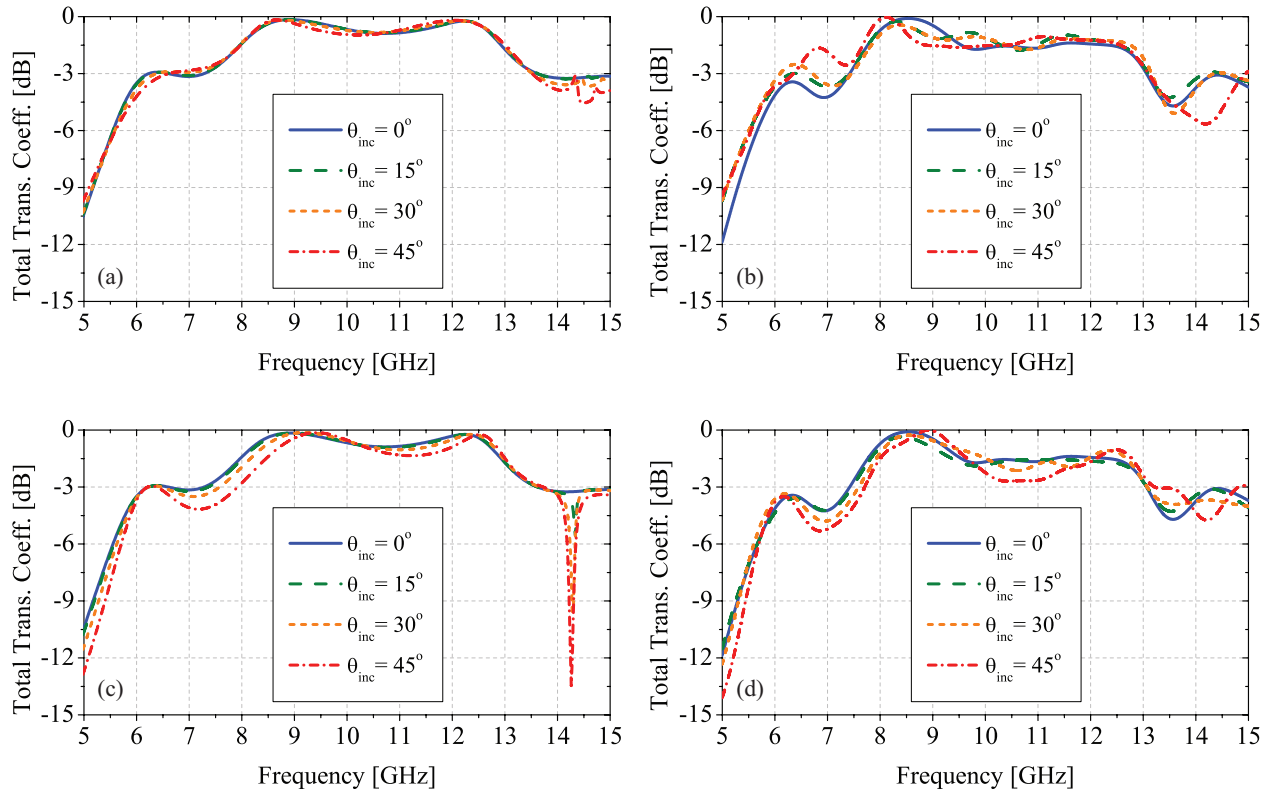


Figure 4.10 (a),(c) Simulated and (b),(d) measured total transmission coefficients of the transmitted wave passed through the polarization converter for an incident wave propagating in (a),(b)  $y - z$  and (c),(d)  $x - z$  planes of incidence.

(VNA). The large metallic fixture ensures that a transmitted EM wave must pass through the device to arrive at the receiver. Transmission coefficient measurement for each of the two orthogonal components were carried out in two steps. First, the transmission coefficient of the screen without the FSS was measured and used for calibration. Then, the converter was placed in the opening and its transmission coefficient was measured once again. The frequency response of the structure for each polarization was obtained using these two measurement results. The measured frequency responses for both the horizontal and the vertical polarizations and the difference between the phase shifts of both responses are shown alongside the simulation results in Figs. 4.6(a) and 4.6(b), respectively. The measured and simulated axial ratios of the device are presented in Fig. 4.8. Observe that a good agreement between the measured and simulated results is achieved.

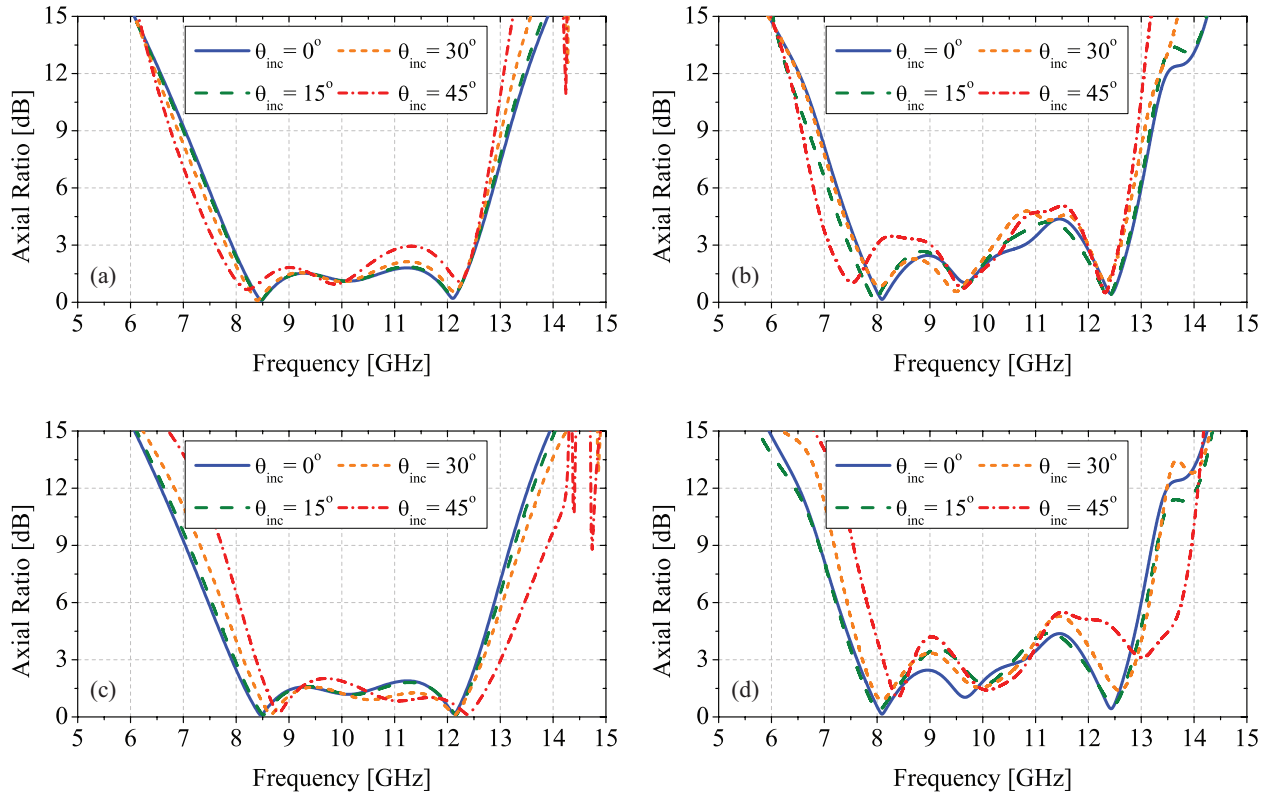


Figure 4.11 (a),(c) Simulated and (b),(d) measured axial ratios of the transmitted wave passed through the polarization converter for an incident wave propagating in (a),(b)  $y - z$  and (c),(d)  $x - z$  planes of incidence.

The sensitivity of the response of the fabricated prototype to the angle of incidence was also examined for various angles of incidence in the range of  $0^\circ$  to  $45^\circ$ . To do this, the transmission coefficients of the polarization converter were measured for both polarizations for various angles of incidence in the  $x - z$  and  $y - z$  incidence planes. Figs. 4.10(a)-(d) show the simulated and measured total transmission coefficients for incident angles in both  $x - z$  and  $y - z$  planes of incidence. Observed that the insertion loss remains below 2.7 dB over the entire band for all cases. The magnitude and phase responses were then combined to obtain the simulated and measured axial ratios of the polarization converter a function of the incidence angles. The simulated and measured results for the axial ratio of the transmitted signal for oblique incidences in the range of  $0^\circ - 45^\circ$  in both  $x - z$  and  $y - z$  planes of incidence are shown in Fig. 4.11(a)-(d). Observe that the structure demonstrates a relatively stable operation both in terms of total transmission coefficient

and axial ratio of the transmitted signal over the entire band of interest for incident angles in the range of  $\pm 45^\circ$ .

The polarization converter presented in this section uses a dielectric substrate with a relative permittivity of 10.2. It is also possible to design the polarization converter presented in this chapter with low-permittivity substrates. In doing so, the same design procedure can be followed and similar results, in terms of bandwidth and axial ratio levels, may be obtained. The primary impact of using substrates with lower dielectric constants is that the dimensions of the capacitive patches used in the structure will change. Specifically, for the same unit cell size, the gap spacing between adjacent capacitive patches in the capacitive patch layers needs to be reduced to provide the desired capacitance value. Alternatively, if reducing the gap spacing is not possible, the unit cell size can be increased to achieve the desired capacitance values while maintaining the gap sizes. Our simulations verify that using substrates with dielectric constant of 2.2, it is possible to design a polarization converter with similar bandwidth and axial ratio as the one presented in this chapter. Therefore, the polarization converter design presented in this chapter is compatible for implementation using almost all commercially-available dielectric substrates.

## 4.5 Conclusions

A new technique for designing low-profile linear-to-circular polarization converters with wide bandwidths was presented. The proposed structure is a multilayer structure composed of reactive impedance surfaces separated from one another by thin dielectric substrates. Providing different transmission characteristics for the two orthogonal polarizations, the proposed device is able to convert a linearly-polarized incident wave with an electric field rotated  $45^\circ$  relative to these orthogonal polarizations to a circularly-polarized wave transmitted at the output aperture. Over the band of interest, the magnitude of the frequency response of the device for two orthogonal polarizations is unity while it introduces a  $90^\circ$  phase difference between these two responses. A design procedure was presented and used to design a prototype capable of operating over the entire X-band in the 8-12 GHz frequency range. A prototype of the device was also fabricated and experimentally characterized using a free-space measurement setup. The measurements confirmed the consistent

Table 4.4 Comparison between the performance of the proposed structure and few other reported polarization converters.  $\lambda_c$  is the wavelength at center frequency.

Ref. Work	Bandwidth	Thickness	Oblique Performance
[34]	20%	$0.35\lambda_c$	N/A
[35]	40%	$0.45\lambda_c$	N/A
[36]	30%	$0.50\lambda_c$	$\pm 45^\circ$
[37]	7%	$0.63\lambda_c$	$\pm 12^\circ$
[39]	0.5%	$0.62\lambda_c$	N/A
[40]	4%	$0.10\lambda_c$	N/A
[41]	12%	$0.30\lambda_c$	$\pm 25^\circ$
[48]	<5%	$0.024\lambda_c$	N/A
Present structure	40%	$0.18\lambda_c$	$\pm 45^\circ$

performance of the polarization converter within over a 40% fractional bandwidth. The performance of this structure for oblique angles of incidence was also experimentally characterized. It was observed that the structure provides a stable frequency response for oblique incidence angles in the  $\pm 45^\circ$ . The comparison between the performance of the proposed polarization converter and a number of other polarization converters reported in the literature is provided in Table 4.4. The proposed structure provides the unique combination of wide bandwidth, thin profile, and stable response with respect to the angle of incidence.

## Chapter 5

# A Broadband, Circular-Polarization Selective Surface

### 5.1 Introduction

Frequency selective surfaces (FSSs) and spatial filters have a wide range of applications in many areas of science and engineering. If illuminated by an electromagnetic wave, these surfaces act as barriers for the propagating waves and can modify the spectral content of the waves as desired. For example, they can be designed to manipulate the magnitude and/or the phase of the transmitted or reflected waves in any desired fashion to obtain certain functionalities. FSSs have been employed in a wide range of applications in physics and engineering ranging from low radio frequencies [2] to infrared [3–6] and optical frequencies [7]. These applications include spatial filtering, high-power microwave filters [97, 117], metamaterials [9], metasurfaces [10], chromatic aberration free lenses [13–15, 100], and true-time-delay reflectarrays [16, 101]. The phase manipulation capability offered by FSSs can be exploited to design polarization selective surfaces. The function of such a device is to reflect one polarization of the wave while being transparent to the orthogonal polarization. A wire grid polarizer [118] is the simplest implementation of such a device for linear polarization. If properly designed, this device reflects the component of the wave whose polarization is parallel to the strips while allowing the orthogonal polarization component of the wave to pass through without any significant attenuation. Achieving similar functionality for circular polarization, however, is not as straightforward. A number of different types of polarization selective surfaces for circular polarization have been reported in the past [49–60]. The structure based on Pierrot unit cell [49] was among the first devices designed to perform as a circular-polarization selective surface (CPSS) [49–52]. Pierrot unit cell is composed of two

orthogonal monopoles connected by a vertical quarter-wavelength segment. Depending on the orientation of monopoles, it can act as left-hand or right-hand circular-polarization selective surfaces. In Ref. [53], a structure with similar functionality based on two orthogonal dipoles and a half-wavelength segment was presented. An improved design employing two closely-helices arranged in one unit cell was reported in Ref. [54]. In Ref. [55], the segment between two monopoles were replaced by coupling elements. These structures generally use resonant constituting elements and hence, they tend to be narrowband structures. Moreover, their performances degrades significantly when illuminated with obliquely incident waves [56]. These deficiencies are not desired in many applications for which broadband performance with a wide range angular stability is required.

The bandwidth issue has been mitigated to some extent using multilayer CPSSs [57–60]. These structures are generally composed of two linear to circular polarization (LP-to-CP) converters that are separated by a linear polarizer. In these CPSSs, the polarization converters and linear polarizers are realized by using arrays of strips or meander lines. The problem associated with them, however, is their large thicknesses when they are designed to provide large bandwidths. The reason for these large thicknesses is that they are composed of numerous layers that are all separated by relatively thick substrates. This large overall thickness generally deteriorates the performances of such CPSSs for obliquely incident electromagnetic waves.

Over the past few years, a new class of frequency selective surfaces with sub-wavelength unit cell dimensions – referred to as miniaturized-element frequency selective surfaces - has been extensively studied. Compared to the resonant-type traditional frequency selective surfaces, the main advantage of such a structure is its much smaller unit cell size and significantly reduced overall thickness. These advantages will in turn contribute to a much more stable frequency response as a function of incident angle. Recently, these structures have been employed to design spatial filters [1,20–27,102,115,119], transmitarrays [13–15,100], reflectarrays [101,116], and polarization converters [120]. In this chapter, we present a method for designing circular-polarization selective surfaces based on MEFSSs. The proposed CPSS is composed of two MEFSS-based LP-to-CP polarization converters [120] sandwiching a linear polarizer. Each polarization converter is composed of two-dimensional arrays of anisotropic sub-wavelength capacitive patches and inductive

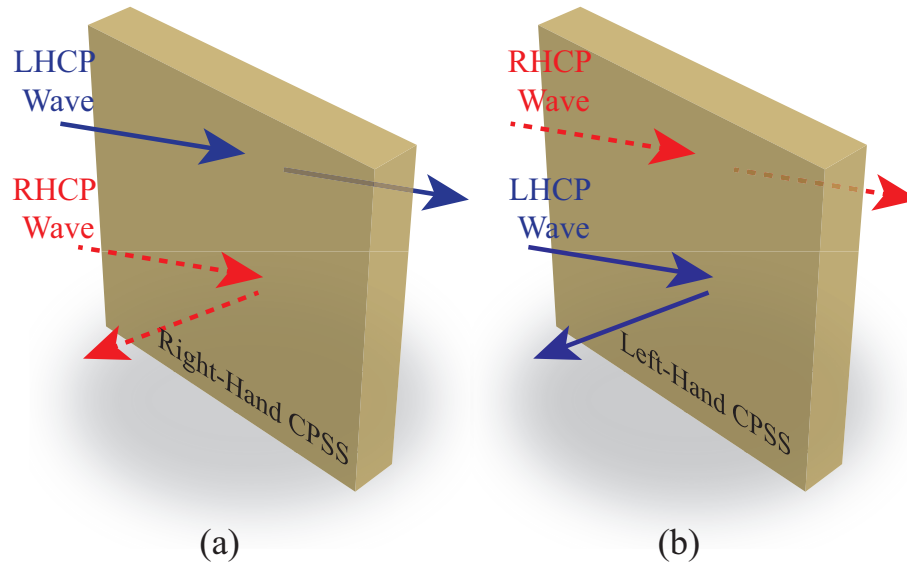


Figure 5.1 Schematic models of (a) right-handed and (b) left-handed circular-polarization selective surfaces.

wire grids that are separated from each other by thin dielectric substrates. The linear polarizer is an array of sub-wavelength strips located in between two polarization converters. Using wideband low-profile polarization converters, the proposed polarization-selective surface is capable of offering a very broadband operation. In addition, due to the low profile nature of the structure as well as its small unit cell dimensions, the proposed structure can demonstrate a stable performance within a wide field of view. Using this approach, a circular-polarization selective surface operating in the 12-18 GHz was designed. The full-wave simulated results show that the structure operates over a bandwidth of more than 40% and can provide a very consistent frequency response with respect to the angle of incidence of the EM wave with a wide field of view of  $\pm 60^\circ$ .

## 5.2 Principles of Operation

Fig. 5.1 presents the topology of a circular-polarization selective surface. This device is a slab of anisotropic medium and treats waves with left-hand circular polarization (LHCP) and right hand circular polarization (RHCP) in different ways. In this chapter, the polarization is defined from the point of view of the source. Therefore, RHCP and LHCP waves can be regarded as

clockwise and counter-clockwise, respectively. Depending on the polarization, two types of CPSSs can be envisioned. A left-handed circular-polarization selective surface (LH-CPSS) reflects an LHCP wave while transmitting an RHCP wave without changing its polarization and magnitude over the frequency band of operation. A right-handed circular-polarization selective surface (RH-CPSS), on the other hand, is transparent to LHCP waves and completely reflects RHCP waves within its operating frequency range. Similar to LH-CPSS, the polarization and magnitude of the LHCP incident wave remains unchanged after passing through the RH-CPSS. Figs. 5.1(a) and 5.1(b) show the schematic models for RH-CPSS and LH-CPSS, respectively. In both cases, the structure is reciprocal and symmetrical. Thus, the operating mechanism remains unchanged for wave propagation in  $\hat{z}$  or  $-\hat{z}$  directions. Therefore, a CPSS can be considered as a four-port network. Such a network can be described using a scattering parameter (S-parameter) matrix. An S-parameter matrix shows the relation between the incident power waves,  $a_n$ , and reflected power waves,  $b_n$ , in a network. Each element of this matrix is defined as  $S_{ij} = \frac{b_j}{a_i}$  where  $a_k = 0$  for  $k \neq i$ . The S-parameter matrix for a CPSS can be defined as follows:

$$\begin{bmatrix} b_1^L \\ b_1^R \\ b_2^L \\ b_2^R \end{bmatrix} = [S_{CPSS}] \begin{bmatrix} a_1^L \\ a_1^R \\ a_2^L \\ a_2^R \end{bmatrix} \quad (5.1)$$

$$[S_{CPSS}] = \begin{bmatrix} S_{11}^{LL} & S_{11}^{LR} & S_{12}^{LL} & S_{12}^{LR} \\ S_{11}^{RL} & S_{11}^{RR} & S_{12}^{RL} & S_{12}^{RR} \\ S_{21}^{LL} & S_{21}^{LR} & S_{22}^{LL} & S_{22}^{LR} \\ S_{21}^{RL} & S_{21}^{RR} & S_{22}^{RL} & S_{22}^{RR} \end{bmatrix}$$

where  $b_j^R$  and  $b_j^L$  denote the reflected power waves for right- and left-handed circularly-polarized power waves from port  $j$ , respectively. Also,  $a_j^R$  and  $a_j^L$  are respectively the incident power waves for right- and left-handed circularly-polarized power waves on port  $j$ . In addition,  $s_{ij}^{LL}$  and  $s_{ij}^{RR}$  denote the co-polarized components and  $s_{ij}^{LR}$  and  $s_{ij}^{RL}$  shows the cross-polarized components. The ideal S-parameter matrices for RH-CPSS and LH-CPSS are as follows:

$$[S_{RH-CPSS}] = \begin{bmatrix} 0 & 0 & 1 & 0 \\ 0 & 1 & 0 & 0 \\ 1 & 0 & 0 & 0 \\ 0 & 0 & 0 & 1 \end{bmatrix} \quad (5.2)$$

$$[S_{LH-CPSS}] = \begin{bmatrix} 1 & 0 & 0 & 0 \\ 0 & 0 & 0 & 1 \\ 0 & 0 & 1 & 0 \\ 0 & 1 & 0 & 0 \end{bmatrix} \quad (5.3)$$

For the ideal cases, the level of the cross-polarized components is considered to be zero. For a realistic design, however, this level is not zero but needs to be sufficiently low.

The CPSS shown in Fig. 5.1 is a combination of three planar structures. Fig. 5.2(a) shows the composition of the proposed CPSS which consists of two LP-to-CP polarization converters that are separated by a linear polarizer. The polarization converters are designed to transform a circularly-polarized wave to a linearly-polarized wave and vice versa. The linear polarizer is designed to completely reflect one linear polarization while maintaining its transparency for the orthogonal one. Knowing the functionalities of different stages of the proposed structure, we can examine the behavior of the structure for an incident circularly-polarized wave with a given polarization. The examined CPSS in this Section is considered to be an RH-CPSS. The same mechanism is transferable to LH-CPSS by a simple geometry transformation. In Figs. 5.2(b) and 5.2(c), the operating mechanism of the RH-CPSS is examined for the incoming LHCP and RHCP waves, respectively. As shown in Figs. 5.2(b) and 5.2(c), the structure is respectively illuminated with an LHCP and an RHCP wave with the electric field component of  $E^i$ . As discussed in Ref. [120], the operating mechanism of a polarization converter is based on behaving differently for two orthogonal components of the incident wave. Within the operational band, this device passes both components very efficiently with little or no attenuation while these components experience two distinct phase shifts with the phase difference of  $90^\circ$ . Therefore, after passing through the first polarization converter, the transmitted signal is a linearly-polarized wave with the electric field

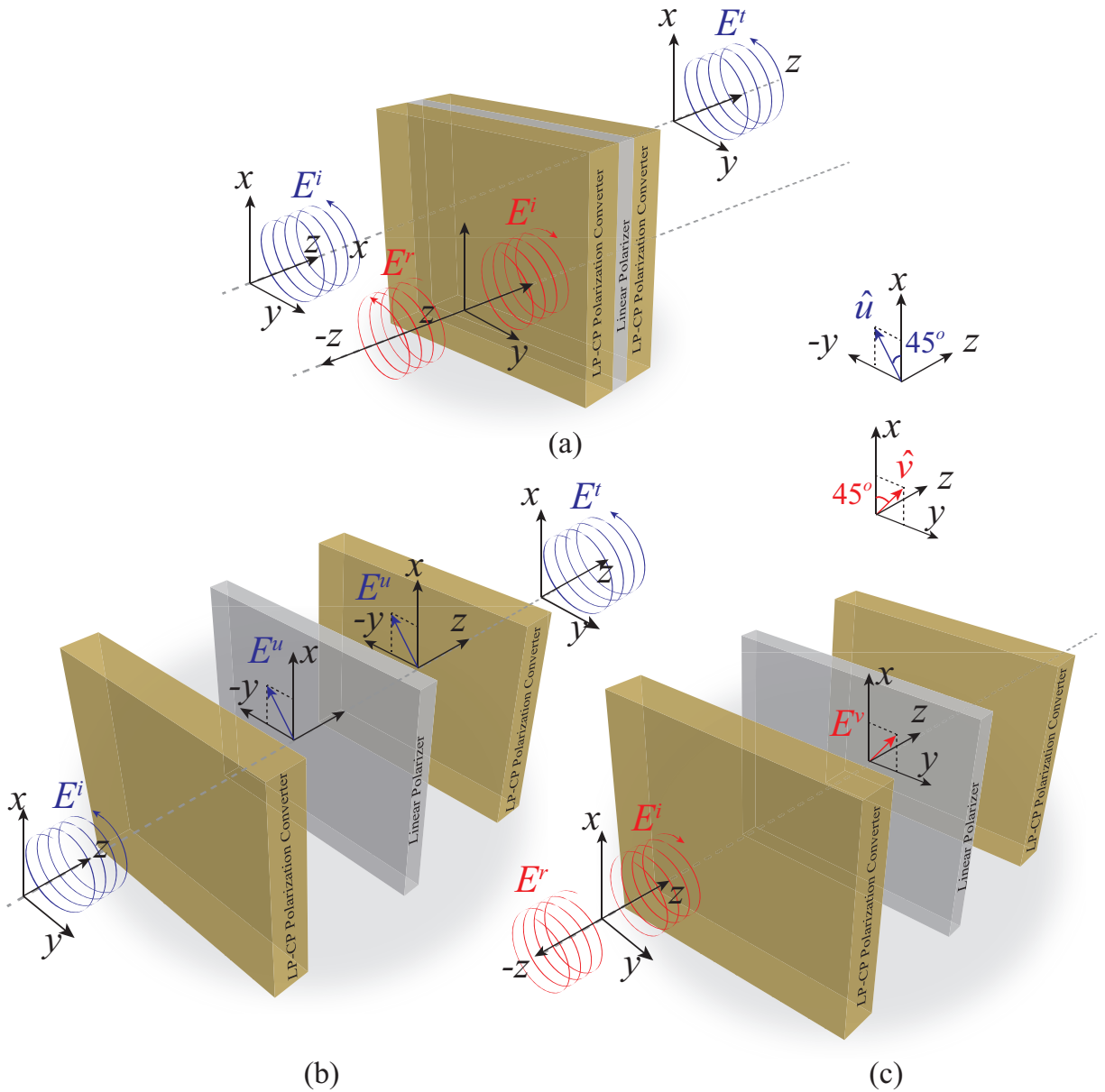


Figure 5.2 (a) Schematic model of an RH-CPSS. This CPSS is composed of two LP-to-CP polarization converters that are separated by a linear polarizer. (b) This structure is transparent to left-handed circularly-polarized waves and (c) it reflects the right-handed circularly polarized waves.

vector,  $E^u$  or  $E^v$ , depending on the polarization of the incoming wave.  $\hat{u}$  and  $\hat{v}$  are both tilted  $45^\circ$  relative to  $\hat{x}$  and  $\hat{y}$  directions, respectively. This transmitted linearly-polarized wave, then, passes through a linear polarizer. This polarizer is transparent to a linearly-polarized wave with a given

field vector while it completely reflects a wave whose field vector is directed orthogonal to that given direction. In this RH-CPSS case, the linear polarizer transmits the waves with field vectors directed towards  $\hat{u}$  while it reflects those with  $\hat{v}$ -directed field vectors. The reflected linearly-polarized wave passes through the first polarization converter again and is transformed to an RHCP wave propagating in the  $-\hat{z}$  direction. The linearly-polarized waves passing the linear polarizer, on the other hand, pass through the other polarization converter and are transformed to LHCP waves propagating in the  $\hat{z}$  direction. To do so, the second polarization converter needs to be  $90^\circ$  rotated with respect to the first one. This way, the cascaded RH-CPSS structure transmits the LHCP waves while it reflects RHCP waves over the frequency band of operation. This frequency band is set by the operating bands of LP-to-CP polarization converters as well as the linear polarizer.

The CPSS shown in Fig. 5.2(a) is implemented using miniaturized element frequency selective surfaces of the type reported in Ref. [1]. The structure includes two MEFSS-based polarization converters and a wire grid linear polarizer. MEFSS-based polarization converters [120] are multi-layer anisotropic structures composed of arrays of subwavelength capacitive patches and inductive wire grids separated from one another by thin dielectric substrates. The difference in the frequency response for two orthogonal polarizations in these polarization converters is achieved by using patches and wire grids with asymmetric features. In Ref. [120], it was shown that this type of converter can provide the unique combination of wide bandwidth, thin profile, and stable response with respect to the angle of incidence. The linear polarizer, on the other hand, is a periodic arrangement of metallic strips that are tilted  $45^\circ$  relative to  $\hat{x}$  and  $\hat{y}$  directions. If the polarization of the incident wave is aligned with the strips, the surface acts as an inductive impedance surface. On the other hand, if the incident electric field is perpendicular to the strips, the surface has a capacitive response. If the parameters are chosen such that the cut off frequency is much higher than the operating band, the surface can act as a short circuit for waves having polarizations aligned with the strips and as an open circuit for the waves with perpendicular polarizations. This way, for an RH-CPSS, the linear polarizer passes the incident waves polarized along the  $\hat{u}$  (see Fig. 5.2) while reflecting those waves polarized along the  $\hat{v}$ . The reflected wave then passes through the first converter and is transformed to an RHCP wave propagating along  $-\hat{z}$  while the transmitted

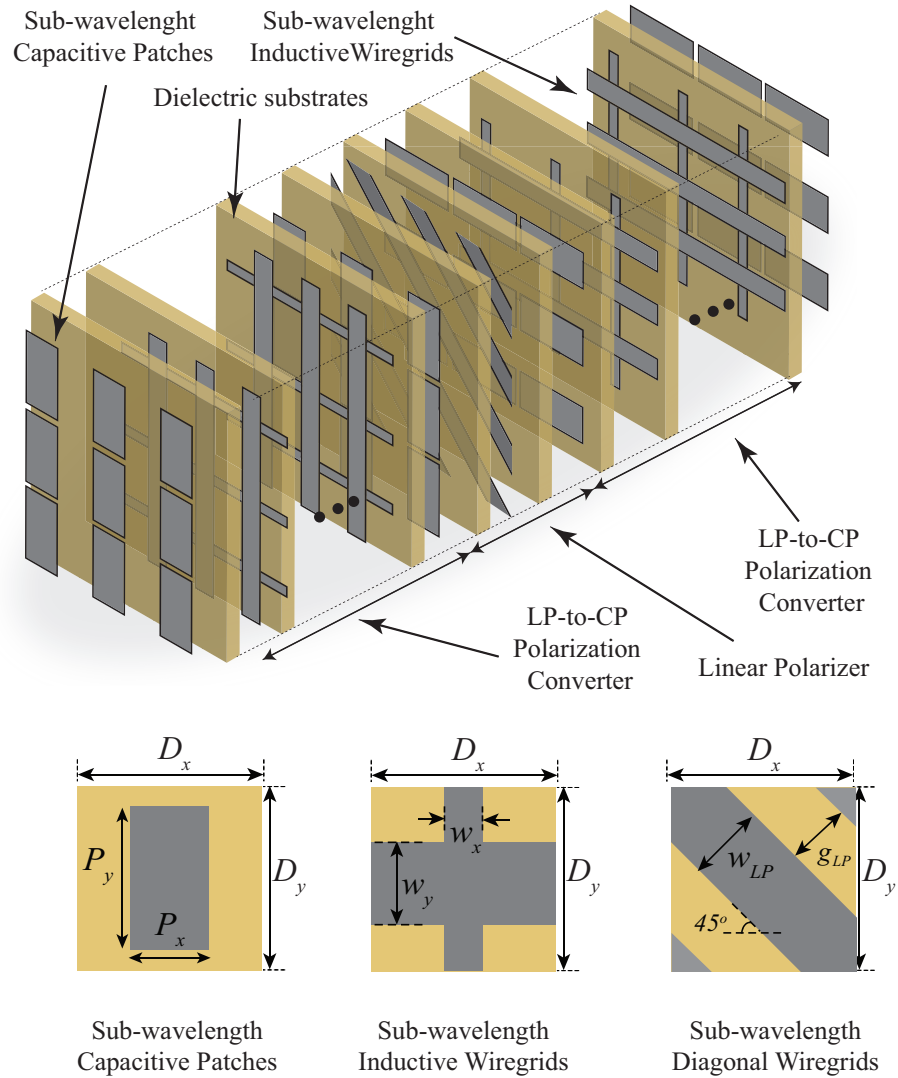


Figure 5.3 Topology of the proposed CPSS composed of two LP-to-CP polarization converters and a linear polarizer. The polarization converters are composed of two-dimensional arrays of sub-wavelength capacitive patches and inductive wire grids having different dimensions along the  $x$  and  $y$  directions. The layers are separated from each other by thin dielectric slabs. The linear polarizer is composed of an array of sub-wavelength strips that are titled  $45^\circ$  with respect to  $\hat{x}$ - and  $\hat{y}$ -directions and is sandwiched between two thin substrates.

wave passes through the second converter and is transformed to an LHCP wave. To maintain the same polarization in the incident and transmitted waves, the second polarization converter needs to be rotated by  $90^\circ$  relative to the first one. Fig. 5.3 shows the three-dimensional (3D) topology of the proposed CPSS. The top view of one unit cell of the capacitive layer, inductive layer, and

linear polarizer are shown in the inset of Fig. 5.3. The dimensions of the unit cell along the  $\hat{x}$  and  $\hat{y}$  directions are  $D_x = D_y = D$ . The capacitive patches are in the form of rectangular patches with dimensions of  $P_x$  and  $P_y$  in  $\hat{x}$  and  $\hat{y}$  directions, respectively. The inductive wire grids are the combination of two metallic strips with the widths of  $w_x$  and  $w_y$  oriented perpendicularly to each other. Finally, the width of the strips in the linear polarizer is  $w_{LP}$ , and the spacing between the strips is  $g_{LP}$ .

### 5.3 Design Procedure and Design Example

As discussed in Section 5.2, the proposed CPSS is a combination of two LP-to-CP polarization converters that are separated by a linear polarizer. Therefore, the design procedure consists of few steps including designing the converters and the linear polarizer and the integration. We assume that the desired operational bandwidth of the device,  $BW$ , and the types of available dielectric materials are known and use them as design parameters in this process. The first step in the design procedure of the CPSS is to design the polarization converters. The polarization converters used in the CPSS architecture are the same with the exception that one of them is rotated by  $90^\circ$  in the  $x-y$  plane relative to the other one. Therefore, only one converter needs to be designed. The required parameters to design the converters are its operating bandwidth,  $\Delta f_{pc}$ , and the dielectric constant of the substrates. To assure satisfying the bandwidth condition of the CPSS, the bandwidth of the polarization converters must be chosen to be larger than or equal to the bandwidth of the CPSS (i.e.,  $\Delta f_{pc} \geq BW$ ). The design procedure of the polarization converters are based on synthesizing the transmission characteristics of the required responses for vertical and horizontal polarizations. As discussed in Ref. [120], these response (e.g. order of the response and the frequency band) are determined based on the required bandwidth  $\Delta f_{pc}$ . After determining the required responses, the structure is first designed based on the equivalent circuit model (e.g. see Fig. 3 of Ref. [120]) and then the geometrical parameters including the wire widths and gap spacings are calculated using (23) and (24) in Ref. [120]. For brevity, the details of this design procedure will not be repeated here and the reader is referred to Section III of Ref. [120]. The next step in the design of CPSS is to design the linear polarizer. As discussed in Section 5.2, the linear polarizer is a capacitive

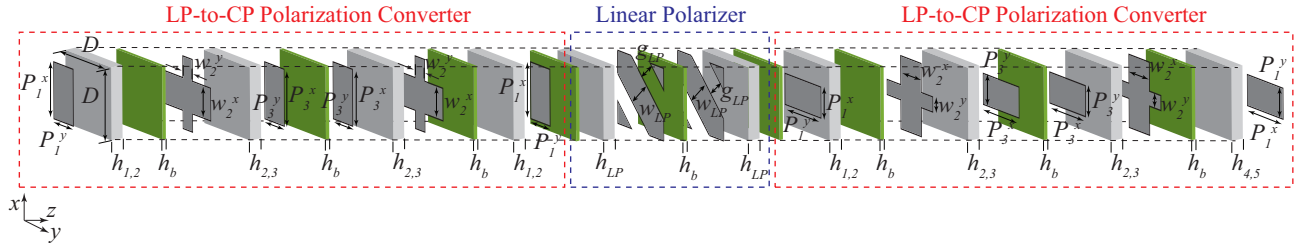


Figure 5.4 Unit cell of the proposed CPSS discussed in Section 5.3. The two middle capacitive patches for each converter are separated from one another by a thin bonding layer. This arrangement is used to maintain the symmetry in the structure.

impedance sheet that act as a low pass filter for the passing waves. The cut off frequency for this filter is  $1/Z_0C$ , where  $Z_0 = 377\Omega$  is the free-space impedance and  $C$  is the capacitance of the impedance sheet which can be calculated using equation (23) of Ref. [1]. The cut off frequency of the linear polarizer needs to be higher than the operating frequency band of the CPSS. Based on this, it can be shown that the widths of strips as well as the gap spacings between them should satisfy the following inequality:

$$4Z_0\varepsilon_0\varepsilon_{r,eff}(w_{LP} + g_{LP}) \times \ln\left(\frac{1}{\sin\left(\frac{\pi w_{LP}}{2(w_{LP} + g_{LP})}\right)}\right) \leq \frac{1}{f_{max}} \quad (5.4)$$

where  $w_{LP}$  is the width of the strips,  $g_{LP}$  is the spacing between strips,  $\varepsilon_0$  is the free-space permittivity,  $\varepsilon_{r,eff}$  represents the effective permittivity of the surrounding the strips,  $Z_0 = 377\Omega$  is the free-space impedance, and  $f_{max}$  is the upper frequency in the band of operation. Since the strips are assumed to be sandwiched between two dielectric substrates, the effective permittivity is the same as that of the substrates. The integration of the polarization converters and the linear polarizer is the final step. Depending on the design, some small modifications might be needed to compensate for the changes caused by the coupling between different components of the CPSS. In this design example, these modifications were done by slightly changing the dimensions of capacitive patches.

The abovementioned procedure was followed to design an RH-CPSS operating over the frequency range of 12-18 GHz. The bandwidth is defined as the frequency range over which the

Table 5.1 Physical parameters of the polarization converters and linear polarizer discussed in Section 5.3.

Parameter	$P_1^y = P_5^y$	$P_3^y$	$w_2^x = w_4^x$	$w_2^y = w_4^y$
value	1.55 mm	1.6 mm	0.5 mm	0.1 mm
Parameter	$P_1^x = P_5^x$	$P_3^x$	$h_{1,2} = h_{4,5}$	$h_{2,3} = h_{3,4}$
value	2.15 mm	1.95 mm	0.635 mm	0.635 mm
Parameter	$w_{LP}$	$g_{LP}$	$h_{LP}$	$D$
value	1 mm	1.15 mm	0.508 mm	3 mm

desired co-polarized transmission coefficient is higher than -3 dB. In this design, the dielectric substrates used for polarization converters were assumed to be nonmagnetic and having a dielectric constant of  $\epsilon_r=10.2$  (Rogers RT/duroid 6010). Based on the given parameters and the procedure described in Section III of Ref. [120], a third-order bandpass MEFSS with anisotropic unit cells and a Chebyshev response was used to design the polarization converters. After determining the parameters of the equivalent circuit model, the physical parameters were calculated. Fig. 5.4 shows one unit cell of the proposed CPSS, which uses this MEFSS-based polarization converter. The fabrication of the proposed structure requires multi-layer printed-circuit-board (PCB) fabrication technology. In such a case, the different metallic layers of the CPSS are fabricated on one or two sides of multiple dielectric substrates. The different dielectric substrates are then bonded together using bonding films. The presence of these bonding films does impact the response of the structure. Therefore, the effects of the bonding layers placed in between the adjacent substrates are also considered. The bonding material used in this design is Rogers 4450F prepreg with the dielectric constant of 3.52 and the thickness of  $h_b=0.1$  mm. Introduction of these bonding layers also creates an asymmetry in the topology of the structure, which can slightly change the frequency response of the structure. This asymmetry can be eliminated by using two closely spaced patches in two sides of the middle layer as shown in Fig. 5.4 instead of using just one patch placed on one side of this layer. The same method is also used for the linear polarizer to eliminate the asymmetry. The unit cell dimensions of the structure is selected to be 3 mm, which is equivalent to approximately

Table 5.2 Finalized physical parameters of the polarization converters and linear polarizer discussed in Section 5.3.

Parameter	$P_1^y = P_5^y$	$P_3^y$	$w_2^x = w_4^x$	$w_2^y = w_4^y$
value	1.0 mm	1.4 mm	0.5 mm	0.2 mm
Parameter	$P_1^x = P_5^x$	$P_3^x$	$h_{1,2} = h_{4,5}$	$h_{2,3} = h_{3,4}$
value	2.05 mm	2.05 mm	0.635 mm	0.635 mm
Parameter	$w_{LP}$	$g_{LP}$	$h_{LP}$	$D$
value	1 mm	1.15 mm	0.508 mm	3 mm

$0.15\lambda_0$ , where  $\lambda_0$  is the free-space wavelength at the center frequency of operation. Using these unit cell dimensions, the widths of the wire grids and capacitive gap spacings of the polarization converters are calculated and listed in Table 5.1. The polarization converter was simulated in CST Studio and its frequency response for both vertical and horizontal polarizations were calculated. Fig. 5.5(a) shows the full-wave simulated transmission coefficient of the polarization converter for both polarizations with the geometrical parameters reported in Table 5.1.

The phase difference between the transmission phases of both polarizations is also shown in Fig. 5.5(a). As can be seen, over the band of interest, the polarization converter is transparent for both polarizations and it creates a  $90^\circ$  difference between their transmission phases. Fig. 5.5(b) shows the axial ratio of the transmitted wave based on the full-wave simulated results shown in Fig. 5.5(a). Also, the total transmission coefficient of the polarization converter is shown in Fig. 5.5(b). Observe that the axial ratio remain below 3 dB and the insertion loss remains below 2 dB over the entire band of interest. The width of the strips in the linear polarizer is also reported in Table 5.1. This width is calculated using (5.4) considering that the linear polarizer is sandwiched between two 0.508-mm Rogers RT/duroid substrates ( $\epsilon_r = 2.2$ ). These substrate are chosen primarily based on the practical design considerations. Fig. 5.6 shows the transmission response of the linear polarizer. As can be seen, this polarizer is transparent to the waves with the electric field vector perpendicular to the direction of strips over the band of interest.

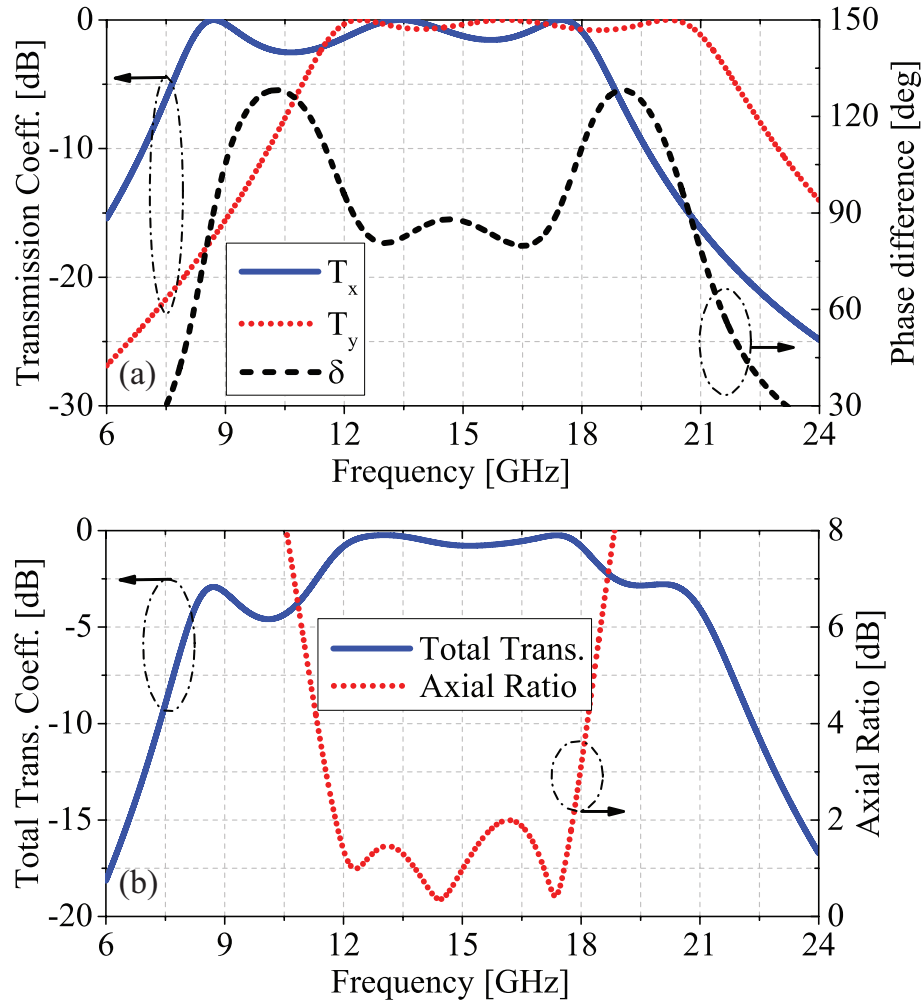


Figure 5.5 (a) Transmission characteristics of the polarization converter part of the proposed CPSS discussed in Section 5.3. These characteristics include the transmission coefficients for both vertical and horizontal polarizations as well as the difference between their corresponding transmission phases. (b) The total transmission coefficient and the axial ratio of the polarization converter used in the architecture of the CPSS described in Section 5.3. These results are all obtained based on the values reported in Table 5.1.

In the final step, the polarization converters and the linear polarizer are cascaded to form the CPSS. As discussed previously, some small modifications were needed to account for the effects of the coupling between different components. The finalized values of the geometrical parameters are listed in Table 5.2. Figs. 5.7(a) and 5.7(b) show the simulated transmission and reflection responses of the CPSS with the values reported in Table 5.2. As can be observed, the transmission window in

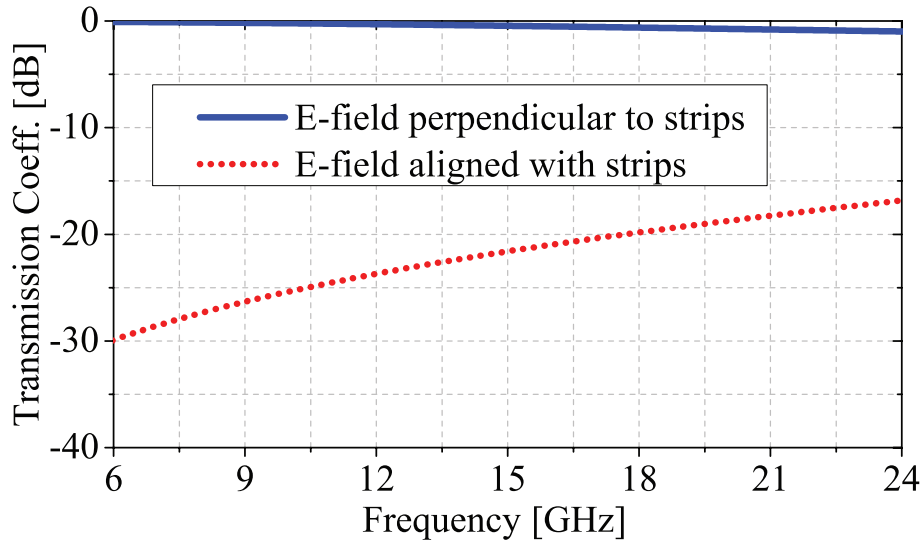


Figure 5.6 Transmission characteristics of the linear polarizer used in the design of the CPSS discussed in Section 5.3. The magnitude of the transmission responses are shown for two cases where the linear polarizer is illuminated with an E-field that is aligned with and perpendicular to the strips. These results are calculated based on the values listed in Table 5.1.

12-18 GHz is achieved. Also, the level of co-polarized transmission discrimination,  $S_{21}^{LL}/S_{21}^{RR}$ , is more than 15 dB over the band of interest. The co-polarized reflection coefficient discrimination,  $S_{11}^{RR}/S_{11}^{LL}$ , is also more than 10 dB over most of the operating band. The frequency response of the structure was also simulated for oblique incidence angles and the results are presented in Figs. 5.8(a) and (b). Observe that the for incidence angles in the range of  $\pm 60^\circ$ , the CPSS provides a stable frequency response as a function of incidence angle with a polarization isolation better than 15 dB over this entire frequency band of operation. Such stable response in a wide field of view is mainly attributed to the small dimensions of the unit cells.

## 5.4 Conclusions

A new technique for designing circular-polarization selective surfaces with wide fields of views and extremely wide bandwidths was presented. The proposed structure is composed of two MEFSS-based linear-to-circular polarization converters that are separated by a linear polarizer. Each polarization converter is designed by exploiting an anisotropic miniaturized-element

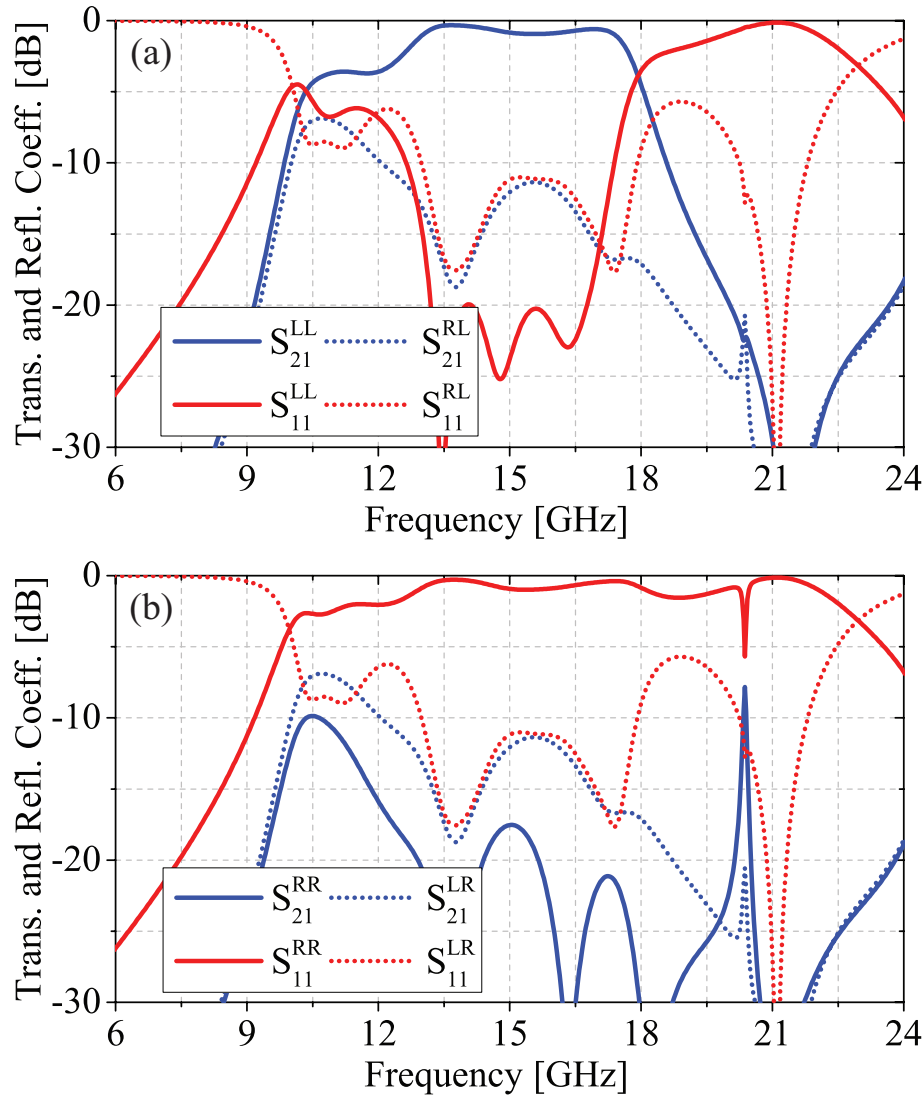


Figure 5.7 Transmission and reflection coefficient of the RH-CPSS prototype discussed in Section 5.3 for (a) LHCP and (b) RHCP incoming waves. These results are obtained with the parameter values listed in Table 5.2.

frequency selective surface. The the linear polarizer is an array of sub-wavelength strips. The multilayer combination of these two structures were used to design a circular-polarization selective surface that is transparent to left handed circularly polarized waves while being opaque to right handed CP waves. A design procedure was presented and used to design a prototype capable of operating over the entire Ku-band in the 12-18 GHz frequency band. The full-wave simulated results confirmed that the RH-CPSS prototype operates over a 40% fractional bandwidth. Also,

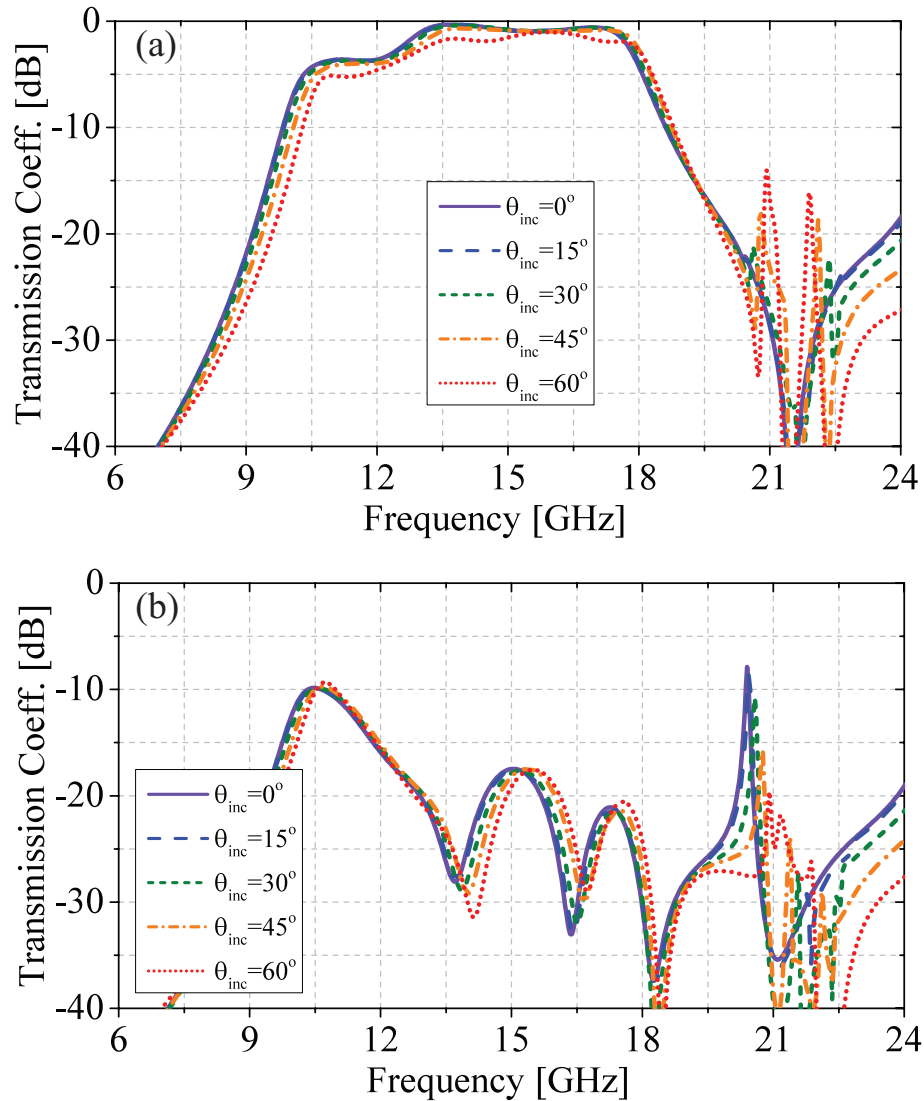


Figure 5.8 (a) Transmission characteristics of RH-CPSS prototype discussed in Section 5.3 for oblique incidence angles. (a) Transmission coefficient for incoming LHCP waves. (b) Transmission coefficient for incoming RHCP waves. The results are obtained with the parameters reported in Table 5.2.

it was shown that the structure provides a stable frequency response for oblique incidence angles in the  $\pm 60^\circ$ . The comparison between the performance of the proposed structure and a number of the other CPSSs reported in the literature is provided in Table 5.3. Despite having many metal and dielectric layers, the overall thickness of this structure remains below a quarter of wavelength.

Table 5.3 Comparison between the performance of the proposed structure and few other reported CPSSs.  $\lambda_c$  is the wavelength at center frequency.

Ref. Work	Bandwidth	Thickness	Oblique Performance
Ref. [51]	2%	$0.25\lambda_c$	$\pm 30^\circ$
Ref. [52]	<10%	$0.25\lambda_c$	N/A
Ref. [53]	12.5%	$0.25\lambda_c$	N/A
Ref. [54]	10%	$0.25\lambda_c$	$\pm 20^\circ$
Ref. [55]	<10%	$0.18\lambda_c$	N/A
Ref. [56]	7%	$0.25\lambda_c$	N/A
Ref. [59]	26%	$1.5\lambda_c$	N/A
Ref. [60]	40%	$0.45\lambda_c$	$\pm 20^\circ$
Present structure	40%	$0.23\lambda_c$	$\pm 60^\circ$

However, it provides one of the widest bandwidths reported to date and has the widest field of view among all similar structures that are reported to date.

## Chapter 6

# Design of Wideband, FSS-Based Multi-Beam Antennas Using the Effective Medium Approach

### 6.1 Introduction

Multi-beam antenna arrays have found applications in areas including wireless communications [121–123], radars [124,125], satellite communications [71], and surveillance systems to name a few. A number of different techniques have been used to design multi-beam arrays in the past. In active antenna arrays where each element of the array is backed by a complete transmit/receive module, multi-beam operation is achieved by exciting the array elements with the complex excitation coefficients required to generate the desired beams [126]. While these arrays offer a great flexibility in achieving multi-beam operation, they are rather costly and complex solutions for most commercial systems. In passive antenna arrays, a single microwave source feeds the array elements via a corporate feed network<sup>1</sup>. In such arrays, multi-beam operation is achieved through the use of an appropriately designed beam forming network (such as the Butler matrix, the Rotman lens, etc. [127]). However, in passive arrays that use corporate feed networks, as the aperture size is increased beyond a certain point, the losses in the feed network start to dominate, thereby reducing the efficiency of the antenna [128]. This problem is largely absent in a different class of passive arrays in which a microwave lens is spatially fed with a feed antenna. In such an architecture, multiple feed antennas illuminating the lens at different angles can be used to achieve multi-beam operation.

---

<sup>1</sup>In passive phased-arrays, variable phase shifters are integrated within the feed network to achieve beam steering.

Many types of microwave lenses have been presented in the literature. Dielectric lenses were among the first microwave lenses investigated [129–131]. Such lenses are generally heavy and bulky and suffer from internal reflection losses. Fresnel lenses are low-profile alternatives to traditional dielectric lenses [132]. However, they have a narrower bandwidth and increased losses due to the shadow blockage. Other planar microwave lenses have addressed many of the shortcomings of the traditional dielectric lenses at low RF and microwave frequencies. The majority of planar microwave lenses are composed of arrays of transmitting and receiving antennas coupled together using some sort of a phase shifting or time-delaying mechanism [61–69]. Multi-beam operation in spatially-fed lens antennas is commonly achieved by feed displacement. More advanced multi-beam lens antennas are obtained by using iterative design techniques to optimize the lens or using microwave lenses with multiple focal points [64]. Frequency selective surfaces (FSSs) have also been used to design microwave lenses [13, 14, 70]. In [13] and [14] miniaturized element frequency selective surfaces (MEFSSs) were used to address the main shortcomings of conventional planar lenses (namely, the poor scanning performance). These designs offer an excellent scanning performance in a wide field of view along with an extremely wide operating bandwidth.

Regardless of the implementation process, a major problem with high gain single- and multi-beam antennas obtained by spatially feeding a microwave lens is the relatively large spacing between the feed point and the lens aperture as quantified by the focal distance to the aperture diameter ratio ( $f/D$ ) of the lens. This results in a high-profile structure where the entire thickness of the antenna array, inclusive of the feed, is generally comparable to the aperture dimensions. This is not desired in many applications where low-profile antenna arrays are required or in scenarios where a low  $f/D$  ratio is needed to provide amplitude tapering over the aperture to reduce the side lobe levels. It is well-known that reducing the  $f/D$  ratio of a lens antenna increases the amplitude tapering and reduces the spillover losses at the expense of decreasing the aperture efficiency [133]. However, in situations where a low  $f/D$  ratio is needed (e.g. to get low sidelobe levels), most traditional lens design techniques fail to deliver practical designs for achieving wideband, low-profile, true-time-delay microwave lenses. In this chapter, we present a multi-beam antenna composed of a planar MEFSS-based lens of the type reported in [15] fed with a focal plane array. The antenna

is designed to have an  $f/D = 0.2$ , where  $f$  is the separation between the focal plane and the lens' aperture and  $D$  is the aperture diameter. This makes the overall profile of this antenna comparable to those of Farby-Perot-based antennas. However, unlike Fabry-Perot antennas [134–136], the proposed antenna is capable of having multiple beams and operates over a wide bandwidth. We also introduce a new technique for modeling MEFSS-based microwave lenses that allows for rapid design and optimization of both the lenses and the antenna arrays that exploit them. The proposed technique is based on treating the constituting-elements of these lenses as equivalent media having relative effective permittivity and permeability values of  $\mu_{r,eff} = \epsilon_{e,rf}$ . When homogenized in this manner, the MEFSS-based microwave lens can be easily simulated using commercially-available EM solvers with relatively low requirements for memory and computational resources. Using this procedure, a prototype of an antenna array with multiple beam in the  $\pm 45^\circ$  operating in the frequency range of 8-10 GHz is designed, fabricated, and experimentally characterized.

## 6.2 Principles of Operation

### 6.2.1 Why Use Effective Medium Approach?

MEFSS-based microwave lenses have numerous phase shifting (or time-delay) pixels with very small sub-wavelength features [14, 15]. Each pixel is composed of a number of different metallic patterns separated from each other with thin dielectric substrates. In each pixel, there are small variations between the shapes and dimensions of the metallic patterns occupying the different layers. Moreover, there are small variations between the dimensions of the different pixels occupying the lens. Because of the small minimum features and small variations between different pixels of the lens, simulating an MEFSS-based microwave lens using full-wave EM simulations requires an excessive amount of computational resources. Using the effective medium approach to model the lens offers a simple yet reasonably accurate method for simulating and optimizing lens-based antenna apertures using commercially-available full-wave tools.

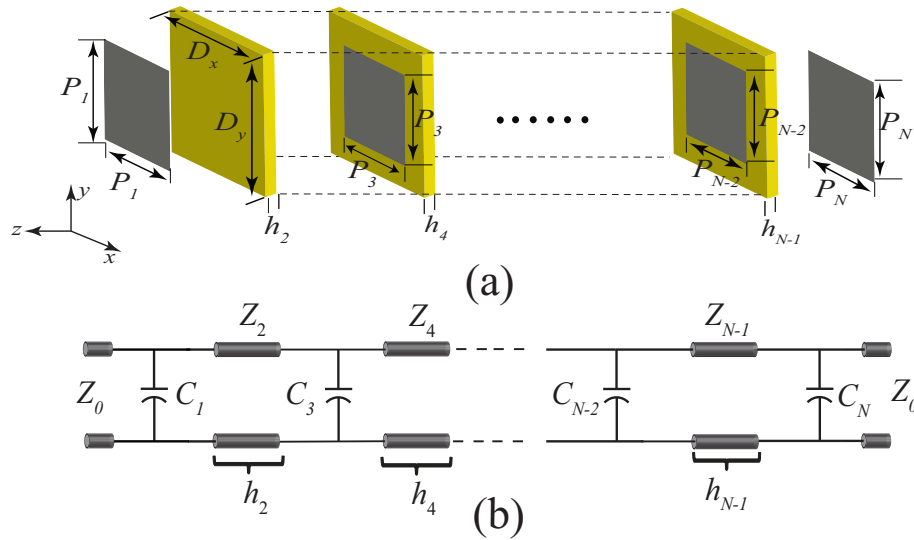


Figure 6.1 (a) Topology of a unit cell of lowpass MEFSS. (b) Equivalent circuit model of the MEFSS. The structure has  $\frac{N+1}{2}$  metal layers and acts as an FSS with an  $N^{\text{th}}$ -order lowpass response.

## 6.2.2 Effective Medium Approach for Modeling True-Time-Delay MEFSSs

Fig. 6.1(a) shows the unit cell of an MEFSS with a lowpass frequency response [15]. The structure is composed of multiple sub-wavelength capacitive patches separated from each other by thin dielectric substrates. The equivalent circuit model of this structure is shown in Fig. 6.1(b), where the capacitive patches are modeled with parallel capacitors and the dielectric substrates are modeled with transmission lines with small electrical lengths. Because of the small electrical lengths of these transmission lines, they can be approximated with series inductors. Therefore, the equivalent circuit model of this MEFSS is converted to that shown in Fig. 6.2, which is a classical lowpass filter. A lowpass MEFSS of this type was used in [15] to design a broadband true-time-delay microwave lens. Since the MEFSS shown in Fig. 6.1 has sub-wavelength unit cell dimensions, it can be treated as a homogenous, effective medium with an effective relative permittivity of  $\epsilon_{r,eff}$  and an effective relative permeability of  $\mu_{r,eff}$ .  $\epsilon_{r,eff}$  and  $\mu_{r,eff}$  are frequency dependent and in general they vary significantly as a function of frequency for most periodic structures. However, for (bandpass or lowpass) MEFSSs with linear phase responses,  $\mu_{r,eff}$  and  $\epsilon_{r,eff}$  are expected to

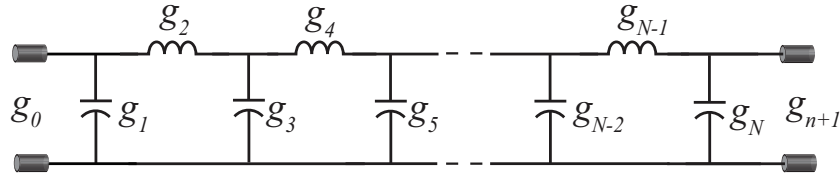


Figure 6.2 Lumped-element circuit model of a classical  $N^{\text{th}}$  order lowpass filter.

be constant in the frequency range where the MEFSS demonstrates a linear phase response. Moreover, because MEFSSs are designed to be impedance matched,  $\mu_{r,eff}$  and  $\epsilon_{r,eff}$  are expected to be equal to one another (i.e.,  $\mu_{r,eff} = \epsilon_{r,eff}$ ).

To demonstrate the system-level equivalency<sup>2</sup> between the lowpass MEFSS shown in Fig. 6.1 and a homogenous slab of a material with  $\mu_{r,eff} = \epsilon_{r,eff}$ , an MEFSS with a third-order, maximally-flat lowpass response with a cutoff frequency of 8.0 GHz is designed and simulated. Using the design procedure reported in [137], the parameters of the equivalent circuit model of the MEFSS (shown in Fig. 6.2) are determined to be  $C_1 = C_3 = 52.5$  fF and  $L_2 = 15$  nH. The synthesized equivalent circuit model of the MEFSS is then used to calculate its frequency response. Fig. 6.3(a) shows the calculated magnitude and phase of the transmission coefficient of this MEFSS in the frequency range of 0-8 GHz. As can be seen, the magnitude of the MEFSS transmission coefficient remains constant in the 0-4 GHz frequency range and its phase is approximately linear in this range.

The effective constitutive parameters of this MEFSS are extracted through a resonant inverse scattering approach reported in [138]. Using this procedure, the effective permittivity, permeability, and the refractive index of the MEFSS are retrieved from its complex transmission and reflection coefficients. In doing this, the MEFSS is assumed to be equivalent to a slab of a homogeneous material with a thickness of 1 mm. Notice that this thickness is chosen arbitrarily, since we are only concerned about the system level equivalency of the response of this MEFSS and that of a homogenous effective medium slab. Fig. 6.3(b) shows the real and imaginary parts of the permittivity and permeability of the effective homogenous slab with the same frequency response

<sup>2</sup>Notice that in this chapter, we are interested in this equivalency only to the extent that the overall system level performance of the MEFSS is concerned. In other words, the only important factor here is that the homogeneous effective medium slab demonstrates the same frequency response as that of the MEFSS.

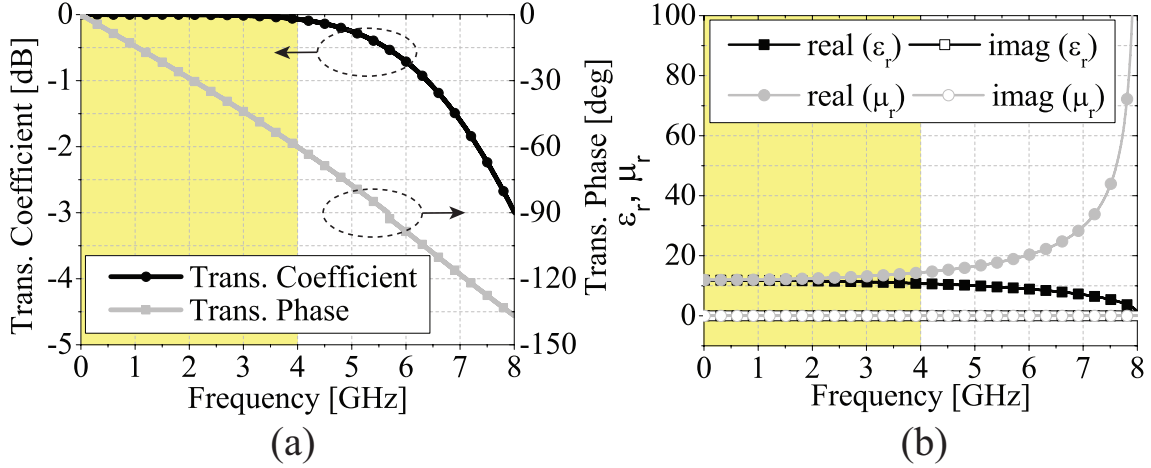


Figure 6.3 (a) Magnitude and phase of the transmission coefficient of a lumped-element third-order lowpass filter with cutoff frequency  $f_c = 8$  GHz. (b) Real and imaginary parts for the permittivity and permeability of a homogeneous slab with the same frequency response as the one shown in Fig. 6.3(a). The results are derived from calculated S-parameters for the third-order filter shown in Fig. 6.3(a). The thickness of the equivalent slab is considered to be 1 mm.

as that shown in Fig. 6.3(a) in the frequency range of 0-8 GHz. Since the MEFSS is assumed to be lossless in this stage, the algorithm correctly predicts  $\Im\{\mu_{r,eff}\} = \Im\{\epsilon_{r,eff}\} = 0$ . Fig. 6.3(b) shows that  $\Re\{\mu_{r,eff}\} = \Re\{\epsilon_{r,eff}\}$  in the frequency range of 0-4 GHz corresponding to the frequency range where the insertion loss of the MEFSS is close to 0 dB and its phase response is linear. As we get closer to the cutoff frequency of the MEFSS,  $\mu_{r,eff}$  and  $\epsilon_{r,eff}$  start to show significantly dispersive properties. Nonetheless, the results shown in Fig. 6.3(b) confirm that over a given frequency band, a lowpass MEFSS with a linear phase response and a small insertion loss can be modeled as an effective homogeneous medium with  $\mu_{r,eff} = \epsilon_{r,eff}$  and the transmission and reflection coefficients of the FSS can be calculated if the frequency-dependent  $\mu_{r,eff}$  and  $\epsilon_{r,eff}$  are known. If the transmission and reflection coefficients of a slab with these extracted effective material parameters are calculated, the filter response shown in Fig. 6.3(a) will be recovered. This confirms that the approximations made in the extraction procedure [138] do not significantly impact the accuracy of this process. This modeling approach can be used to significantly simplify the design process and optimization of MEFSS-based multi-beam antenna arrays as will be shown in the subsequent sections.

### 6.2.3 MEFSS-Based Microwave Lens Design Using the Effective Medium Approach

Fig. 6.4(a) and 6.4(b) show the top and the side views of the proposed multi-beam antenna. The structure is composed of a lens fed with multiple feed antennas located on a plane parallel to and in close proximity of the lens aperture. The lens is assumed to be formed from multiple concentric rings of magneto-dielectric slabs with  $\mu_{r,i} = \epsilon_{r,i}$ , all with the same thickness of  $t$ . The apertures of all feed antennas are assumed to be on the same plane located in parallel with the aperture of the lens. In the design example and experiments reported in the subsequent sections of this chapter, probe-fed patch antennas are used as the feed antennas. However, this is done purely for simplifying the experimental process and other types of antennas such as open ended waveguides, horns, slots, etc. can be used as well. The lens has aperture diameter of  $D$  and the distance between the feed plane and the input aperture of the lens is  $f$ .

The design procedure of the proposed antenna consists of a few different steps. The first step is to design the feed antenna. Once the feed antenna is designed, its physical dimensions and current distribution are determined either analytically or numerically. The next step is to choose the aperture diameter  $D$  and the separation between the feed plane and the input aperture of the lens,  $f$ . These parameters are largely determined from practical design considerations such as the maximum tolerable thickness of the antenna, the minimum tolerable side lobe level, and the desired 3dB beamwidth, which will impact the choice of  $f$  and  $D$  values. The lens thickness,  $t$ , is chosen arbitrarily<sup>3</sup>. The lens aperture then is divided into  $M$  concentric zones, where  $M$  is an integer. The  $i^{th}$  zone ( $1 \leq i \leq M$ ) is assumed to be composed of a homogeneous magneto-dielectric slab with a thickness of  $t$  with  $\mu_{r,i} = \epsilon_{r,i}$ . The number of different zones,  $M$ , is a design parameter that can be chosen by the designer. The upper bound for  $M$  can be determined from the aperture diameter  $D$  and the unit cell size of the MEFSSs that will be used to synthesize the homogeneous magneto-dielectric materials filling each zone of the lens. Once these physical parameters are determined, the relative permittivity and permeability of the magneto-dielectric materials filling each zone of

<sup>3</sup>We recommend choosing thicknesses in the 5-15 mm range. Although, the specific value of thickness does not significantly impact the subsequent design stages.

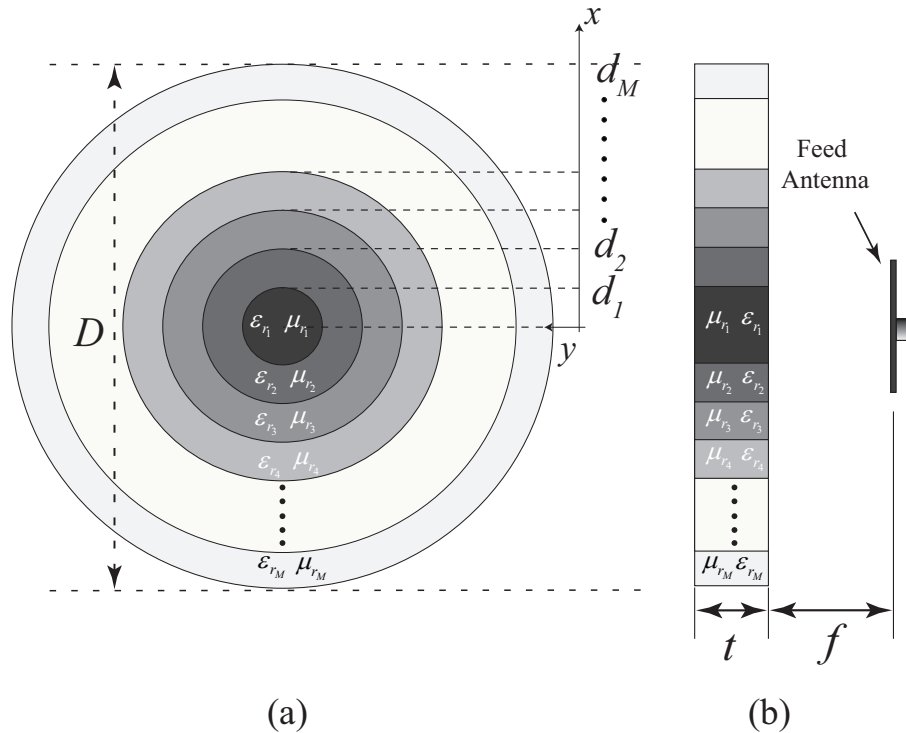


Figure 6.4 Topology of the proposed multi-beam antenna consisting of a zoned flat TTD lens and planar feed antenna.  $d_i$  is the radius of  $i^{th}$  zone. (a) Front view. (b) Side view.

the lens should be determined. This is carried out using a ray tracing approach similar to the one presented in [14] and [15].

#### 6.2.4 A Design Example

In this sub-section, we present a design example to demonstrate the procedure described in Section 6.2.3. In this example, we assume that the high-gain antenna aperture is achieved by feeding a flat lens of the type shown in Fig. 6.4 by a probe-fed microstrip patch antenna. The antenna is designed to operate at a center frequency of 9 GHz with an aperture diameter of 20 cm or equivalently  $6\lambda_0$ , where  $\lambda_0$  is the free-space wavelength at the center frequency of operation. The distance between the focal plane of the antenna and the input aperture of the lens is chosen to be equal to 4 cm. This yields an  $f/D$  ratio of 0.2 for this antenna, which is between 5 to 8 times smaller than the  $f/D$  values of other MEFSS-based microwave lenses reported previously

in [13], [14], and [15]<sup>4</sup>. The aperture of the lens is divided into  $M = 16$  concentric zones and the widths of the zones are assumed to be equal to each other. The lens thickness is chosen to be equal to  $t = 1$  cm. In this design example, the lens is designed to provide an planar wavefront at its output aperture when fed with a patch antenna symmetrically positioned at the center of its aperture on the focal plane. As described in Section 6.2.4, for this problem the indices of refraction of different zones of the lens can be determined using the ray tracing approach discussed in [14], [15]. Since the lens is composed of magneto-dielectric materials with  $\mu_{r,i} = \epsilon_{r,i}$ , this calculation only needs to be performed at one single frequency (e.g. the center frequency of operation in this case). Table 6.1 shows the indices of refraction of different zones of the lens obtained from this design procedure and also the final values after the lens was further optimized using full-wave EM simulations in CST Microwave Studio. The goal of these full-wave EM optimization was to achieve the desired aperture field distribution at the output of the lens when it was fed with a realistic model of the feed antenna.

Even though the  $n_i$  values for the different zones of this lens are obtained based on the assumption of having a single feed antenna located on its optical axis, the lens can be used for off-axis illumination/radiation conditions as well. In this design example, once the lens is designed (i.e., all  $n_i$  values are determined) we determine the location of the feed antennas on the focal plane that generate far field beams in different off-axis directions through full-wave EM simulations of the lens in CST Studio. To do this, the microwave lens shown in Fig. 6.4 is excited with plane waves arriving from different directions. Specifically, for each incidence angle of  $0^\circ$ ,  $15^\circ$ ,  $30^\circ$ , and  $45^\circ$ , the electric field distribution over the focal plane of the lens is calculated and the location of maximum power density is determined. Due to the TTD nature of the lens, this simulation only needs to be done at a single frequency, since this location will not change over the entire frequency range where  $\mu_{r,i} = \epsilon_{r,i}$ . Fig. 6.6(a)-(d) shows the simulated power patterns on (a line within) the focal plane of the lens obtained using these simulations. Using this procedure, the feed locations resulting in far field beams in the directions of  $0^\circ$ ,  $15^\circ$ ,  $30^\circ$ , and  $45^\circ$  referred to as  $x_{\theta=\theta_i}$ , are obtained

---

<sup>4</sup>Specifically, in these studies various MEFSS-based microwave lenses with  $f/D$  ratios ranging from 1.0 to 1.6 were reported

Table 6.1 The refractive index profile of the proposed lens composed of the effective media with equal permittivity and permeability.(MF: Matrix Formulation)

Zone	1	2	3	4
$n_i$ (MF)	7.5768	7.5260	7.3769	7.1389
$n_i$ (Final)	7.5739	7.5262	7.3879	7.1647
Zone	5	6	7	8
$n_i$ (MF)	6.8249	6.4485	6.0219	5.5556
$n_i$ (Final)	6.8651	6.5003	6.0813	5.6216
Zone	9	10	11	12
$n_i$ (MF)	5.0582	4.5360	3.9942	3.4367
$n_i$ (Final)	5.1331	4.6164	4.0795	3.5295
Zone	13	14	15	16
$n_i$ (MF)	2.8664	2.2857	1.6964	1.1000
$n_i$ (Final)	2.9552	2.3657	1.7467	1.1000

to be  $x_{\theta=0^\circ}=0$  mm,  $x_{\theta=15^\circ}=21.4$  mm,  $x_{\theta=30^\circ}=40.4$  mm,  $x_{\theta=45^\circ}=54$  mm, respectively. Because of reciprocity, placing feed antennas on the focal plane at these locations is expected to result in the generation of beams in the far field along these specific directions. This will be experimentally demonstrated in Section 6.3.

### 6.3 Physical Implementation

Once the indices of refraction of different zones of the lens are determined, the effective medium that occupies each zone of the lens is synthesized using lowpass MEFSSs of the type shown in Fig. 6.1. To do this, for the  $i^{th}$  zone of the lens, a lowpass MEFSS is designed to have the same complex transmission and reflection coefficients as those of a slab with a thickness of  $t$  and the index of refraction of  $n_i$ .

The design procedure for lowpass MEFSSs that provide the desired indices of refraction  $n_i$ 's is similar to what is reported in [15] and will not be repeated here. In the current design, the dimensions of all elements populating each zone of the proposed structure are considered to be  $6.5 \text{ mm} \times 6.5 \text{ mm}$  (or equivalently  $\approx 0.2\lambda_0 \times 0.2\lambda_0$ ). The implementation process starts by synthesizing an MEFSS that provides the same frequency response as that of a 1 cm thick slab of an effective medium with the index of refraction of  $n_1 = \sqrt{\mu_r \epsilon_r}$ . Since the zone occupying the center of the lens has the highest effective index, its optical path length determines the order of the lowpass MEFSS that needs to be used to synthesize the desired transfer function [15]. In this case, an MEFSS with a 17<sup>th</sup>-order lowpass response and a linear transmission phase over the frequency range of interest is used to emulate the transfer function needed from  $n_1$ . The remaining zones of the lens (corresponding to indices of refraction of  $n_2$  to  $n_{16}$ ) are also implemented using a similar procedure following the design guidelines provided in [15]. The lens considered in this example has a low  $f/D$  value. Therefore, the variations of the effective indices of refraction between zone 1 and zone 16 is very large (from 7.6 down to 1.1 as seen from Table 6.1). Implementation of the effective medium occupying zone 1 requires an MEFSS with a relatively high order of  $N = 17$ . On the other hand, implementing the effective medium occupying zone 16 requires an MEFSS with a lower order and fewer number of layers. Thus, to implement the lens shown in Fig. 6.4 in a true time delay fashion, MEFSSs with different orders must be used. MEFSSs with different orders, however, have different thicknesses [15]. Therefore, implementation of this lens in a TTD fashion using a completely planar structure is not practical<sup>5</sup>. Since moving to a non-planar structure (with different thicknesses at different locations along the lens' aperture) increases the fabrication difficulty and cost, a compromise was made in synthesizing the effective media occupying a few of the outer zones of the lens. Specifically, for the four outer zones (zones 13-16), phase wrapping was used to increase the optical path length of the rays passing through these zones by  $2\pi$  to allow higher-order MEFSSs to be used to implement the effective media occupying these zones. The drawback with using this technique is that it introduces distortion because of the non-TTD nature of the outer zones. However, as will be shown in Section 6.4.3, the effect of this distortion is

---

<sup>5</sup>This is a direct consequence of the low  $f/D$  ratio of this lens.

Table 6.2 Physical and electrical properties of the elements that populate each zone of the proposed lens. Time-delay values and physical dimensions are in *psec* and *mm* respectively. The lens has unit cell dimensions of  $6.5 \text{ mm} \times 6.5 \text{ mm}$ . The dielectric substrate used is Rogers 5880 and the thickness of all the substrates is  $h=3.175 \text{ mm}$ .

Zone	$P_1$	$P_2$	$P_3$	$P_4$	$P_5$
1	5.2	5.75	5.4	5.45	6
2	5.65	5.65	5.4	5.25	5.75
3	5.55	5.8	5.35	4.95	5.7
4	5.35	5.72	5.3	4.7	5.65
5	5.57	5.82	5	3.65	5.5
6	5.1	5.95	4.85	4	5
7	4.85	5.6	4.6	4.15	4.78
8	4.2	3.72	4.6	4.8	4.95
9	4	2.65	4.25	4.25	4.53
10	3.3	2.5	3.5	3.65	3.75
11	5.1	4.5	<i>CUT</i>	<i>CUT</i>	<i>CUT</i>
12	3.9	2	<i>CUT</i>	<i>CUT</i>	<i>CUT</i>
13	4.25	0	5.24	5	4.85
14	4.1	0	4.8	4.75	4.70
15	3.7	0	4.45	4.5	3.90
16	0	0	3.2	3.2	4.80

minimal, since it is introduced in the outer zones of the lens where the amplitude of the excitation tapers off from its peak at the center.

The 17<sup>th</sup>-order MEFSS occupying the center zone of the lens is formed by nine capacitive patch layers separated from one another by eight dielectric layers. The dielectric substrates are assumed to be non-magnetic and have a dielectric constant of  $\epsilon_r = 2.2$  (Rogers RT/duroid 5880). The thickness of each layer is 3.175 mm or equivalently  $0.095\lambda_0$ . Also, since this structure is

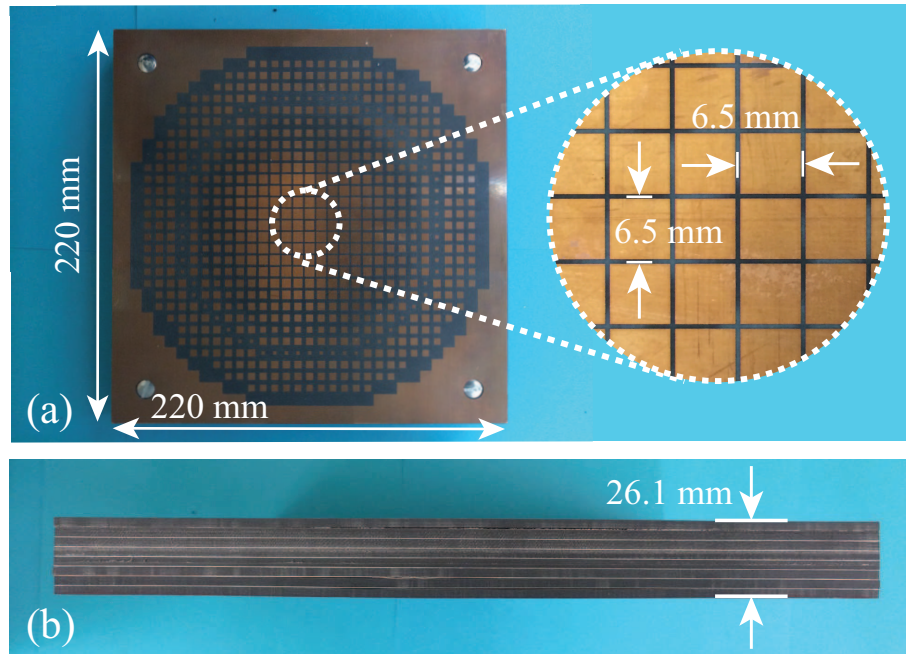


Figure 6.5 (a) Photograph of the fabricated lens. (b) Side view of the fabricated prototype.

composed of multiple substrates that need to be bonded together, the effect if the bonding materials on the response of each zone is taken into account. The bonding material used here is Rogers 4450F prepreg with the dielectric constant of  $\epsilon_r = 3.58$  and the thickness of 0.1 mm. The detailed physical parameters of the elements occupying each zone are provided in Table 6.2.

To facilitate the implementation procedure for the effective media occupying each zone of the lens, the structures of all elements are assumed to be symmetric with respect to the center capacitive layer. This requires  $P_1 = P_9$ ,  $P_2 = P_8$ ,  $P_3 = P_7$ , and  $P_4 = P_6$  as reported in Table 6.2. This simplification is used to greatly reduce the complexity of the implementation process. Nevertheless, it still yields satisfactory results. In certain layers of some zones of the lens, the dielectric substrates are loaded with cylindrical air holes with the diameter of 6 mm. In such cases, it is necessary to completely etch the patches at those layers. This is indicated by word “CUT” in Table 6.2.

## 6.4 Experimental Verification and Measurement Results

### 6.4.1 Multi-beam Antenna Prototype

A prototype of the high-gain antenna including the feed antenna and the lens was fabricated. The excitation feed is a microstrip antenna with the center frequency of 9 GHz printed on Rogers RT/duroid 5880 ( $\epsilon_r = 2.2$ ) substrate with the thickness of 0.508 mm. The antenna is fed with a coaxial cable connected to the antenna through the substrate. The realized gain of the feed antenna is approximately 8 dBi and its half power beam widths in the E- and H-planes are approximately  $80^\circ$  and  $72^\circ$ , respectively. The lens examined in Section 6.2.4 was fabricated using standard PCB lithography, substrate bonding, and milling (machining) techniques. The fabricated prototype has nine metal layers and eight substrate layers. Rogers RT/duroid 5880 substrate ( $\epsilon_r = 2.2$ ) with the thickness of 3.175 mm are used between metallic layers. All the dielectric substrates are bonded together using a 0.1 mm thick Rogers 4450F binding file with  $\epsilon_r = 3.58$ . The air holes in the dielectric substrates were machined into the substrates using a milling machine. The total thickness of the structure, including the bonding layers is 26.1 mm which is about  $0.78\lambda_0$  at 9 GHz. Fig. 6.5 shows a photograph of the fabricated lens as a part of the proposed high-gain antenna. As can be observed, the panel dimensions are 22 cm  $\times$  22 cm (or equivalently  $6.6\lambda_0 \times 6.6\lambda_0$ ).

### 6.4.2 Measurement Results

As described in Section 6.2.4, beam-steering is achieved by switching the feed location on the focal plane of the lens. Therefore, in the first set of measurements, the goal was to find the location of the feed antenna that generates a beam in the desired direction. To do so, the measurement setup described in Fig. 10 of [13] was used. The measurement setup consists of a large metallic screen with the dimensions of 1.8m  $\times$  1.2m with a rectangular shaped opening having the same dimensions as those of the lens at its center. The screen was placed between transmitting and receiving antennas both connected to the two ports of a vector network analyzer (VNA). An X-band horn antenna was used to illuminate the structure. The lens was placed in the far field region of the horn antenna, and illuminated by the generated plane waves with various incidence angles

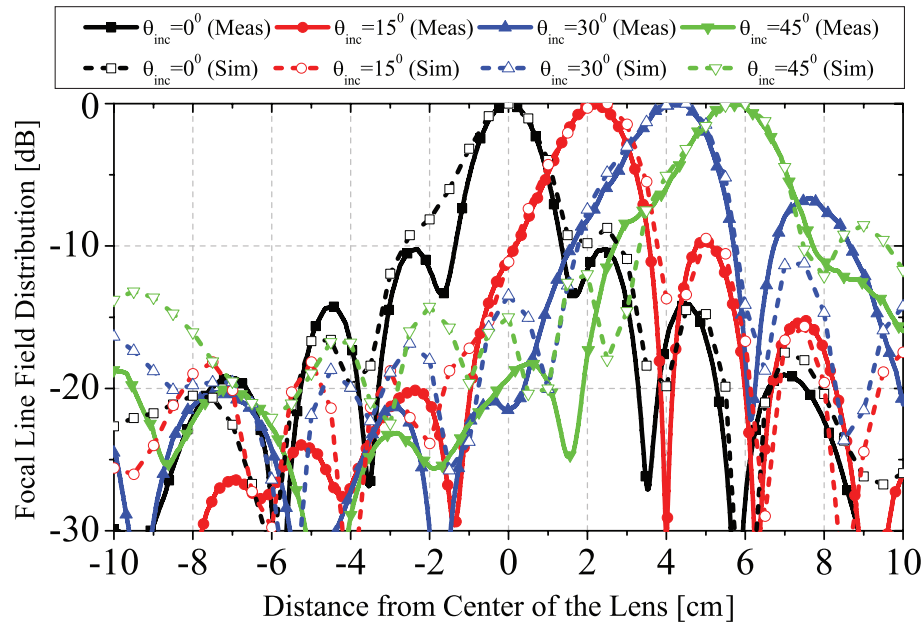


Figure 6.6 Measured and simulated power patterns on the focal line of the lens at the center frequency of 9 GHz. The results are shown for plane waves arriving from various incidence angles of  $0^\circ$ ,  $15^\circ$ ,  $30^\circ$ , and  $45^\circ$ . The point on the focal plane that results in maximum power level for a given incidence angle is the location where the feed antenna needs to be placed to get a beam in the desired direction in the far field.

ranging from normal to  $45^\circ$ . At the other side of the fixture an open-ended semi-rigid coaxial cable with the center conductor extended by about 1 cm, was used to sample the electric field on a line within the focal plane. The structure was illuminated by vertically-polarized plane waves with incident angles of  $0^\circ$ ,  $15^\circ$ ,  $30^\circ$ , and  $45^\circ$ , and the received power patterns were measured over the frequency range of interest while the probe was swept over the focal line with an increment of 5 mm. Fig. 6.6 shows the measured received power pattern alongside the simulation results at the center frequency of 9 GHz for various incidence angles of the electromagnetic waves. For each incidence angle, the location of the field maximum of the measured curve is considered to determine the physical location of the feed antenna on the focal plane that generates a far field beam pointed towards that direction. As can be seen from Fig. 6.6, a good agreement between the measurement results and the simulation results employing the simplified equivalent medium of the lens (see Fig. 6.4) is observed.

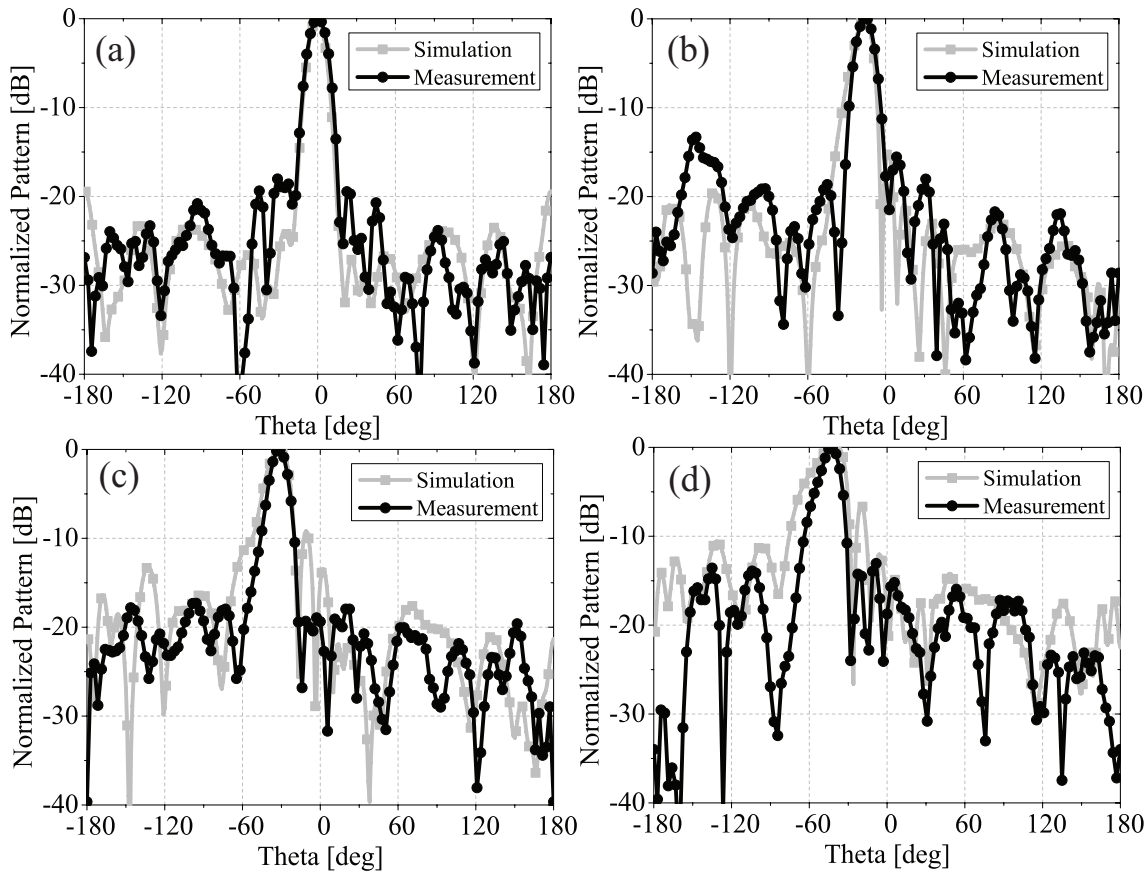


Figure 6.7 Measured and simulated radiation patterns of the proposed antenna at the center frequency of operation (9 GHz). The feed antennas are placed at locations  $x_{\theta=0^\circ}$ ,  $x_{\theta=15^\circ}$ ,  $x_{\theta=30^\circ}$ , and  $x_{\theta=45^\circ}$ , obtained using the measurement results shown in Fig. 6.6. (a)  $0^\circ$ , (b)  $15^\circ$ , (c)  $30^\circ$ , and (d)  $45^\circ$ . The measurements were carried out using a multi-probe near field system. The simulated results are obtained using full-wave simulations of the structure using the effective medium technique presented in Section 6.2.2.

Once the feed locations were experimentally verified, the feed antennas were positioned on the focal plane of the lens and the radiation characteristics of the lens were measured. To do this, a multi-probe spherical near field system was used over the frequency band of 8-10 GHz. Fig. 6.7 shows the measured and simulated radiation patterns of the multi-beam antenna with four feeds corresponding to far field beams along  $\theta = 0^\circ$ ,  $15^\circ$ ,  $30^\circ$ , and  $45^\circ$  directions at the center frequency. The radiation patterns are normalized to their peak values. The simulation results are obtained using full-wave EM simulations in CST Microwave Studio with the simplified model of the lens shown in Fig. 6.4. In general, a good agreement is observed between the simulation and

measurement results despite the approximations made in the modeling and implementation of the lens as discussed in Sections 6.2 and 6.3. As can be observed from Fig. 6.7, by selecting the appropriate feed antenna, the direction of the peak radiation can be steered towards the desired direction in the far-field region of the antenna. Due to the TTD nature of the lens, the antenna maintains consistent radiation characteristics across its entire band of operation. Therefore, for all frequencies within the operating band, when the feed antenna was placed at  $x_{\theta=\theta_i}$ , the main beam was always steered towards  $\theta_i$  and beam squinting was not observed. Additionally, because of the amplitude tapering caused by the small  $f/D$  ratio of the antenna, the side-lobe level for the broadside beam is considerably smaller than that of a uniformly illuminated aperture as can be seen from Fig. 6.7(a). The discrepancies observed between the simulation and measurement results shown in Fig. 6.7 can be attributed to the accuracy of the extraction of the effective material parameters. Since the lens has low  $f/D$  ratio, some of the regions of the lens are illuminated with large oblique incidence angles. Under oblique incidence angles, the response of a homogeneous effective medium slab differs slightly from that of the MEFSS with a linear phase response. For example, for the center fed case, the incidence angles of the rays for the central zones are close to normal and they gradually increase as we move towards the outer zones. Due to the tapering of the excitation amplitude at the edges, the effect of outer zones is minimal. Therefore, the agreement between the simulation results and the measurement results in Fig. 6.7(a) is reasonably good. This issue becomes more visible as the feed is moved on the focal line away from the center of the lens to get the beams pointed at other desired directions. In these cases, the agreement between the simulation and the measurement results deteriorates as can be observed from Figs. 6.7(b), 6.7(c), and 6.7(d).

The gain and directivity of the antenna were measured using the same near field system for different frequency bands and different beam directions and the results are shown in Fig. 6.8. The difference between the directivity and realized gain is mainly attributed to ohmic and dielectric losses as well as the impedance mismatch losses of the feed. Also, as expected, the antenna gain drops as the scanning angle increases. Fig. 6.9(a) shows the aperture efficiency of the antenna as a function of frequency for normal incidence. The relatively low aperture efficiency values are a

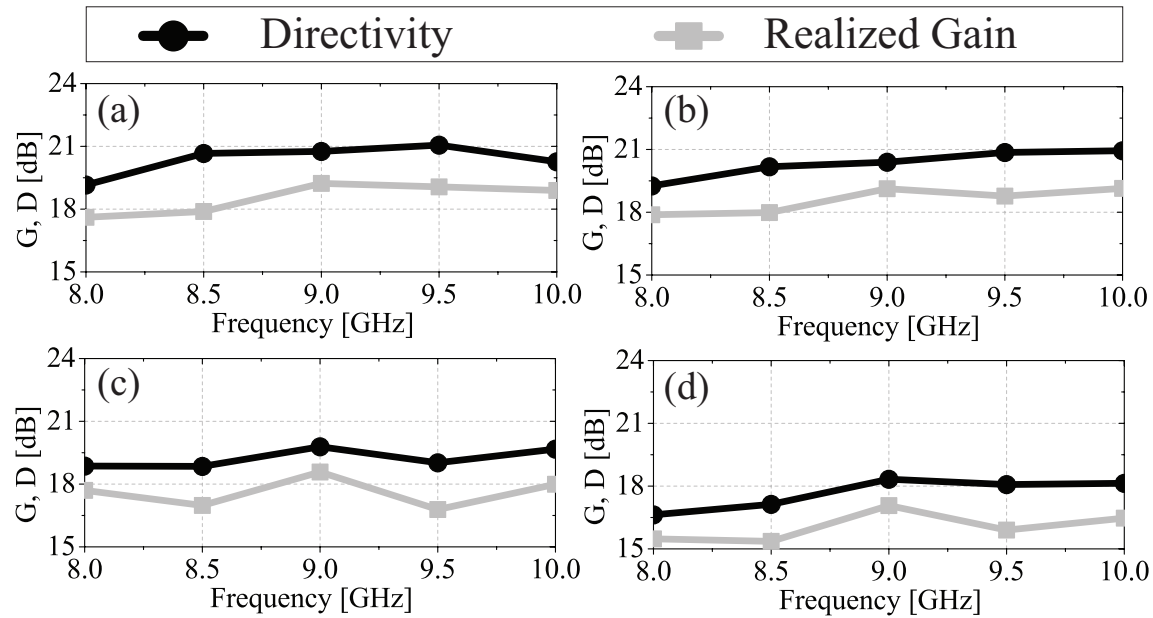


Figure 6.8 Measured realized gain and directivity of the proposed antenna for different beam directions of (a) 0°, (b) 15°, (c) 30°, and (d) 45°.

consequence of the small  $f/D$  ratio of the antenna, which creates amplitude tapering over the lens aperture and results in reduced side-lobe levels compared to uniformly illuminated apertures (e.g. see Fig. 6.7(a)).

### 6.4.3 Time-Domain Analysis

As described in Section 6.2.4, in the implementation of the lens, it was necessary to use phase wrapping to implement the MEFSSs occupying the outer zones of the lens. To quantify the potential impact of this in introducing distortion in the lens response, a series of time-domain measurements were performed on the lens itself. Specifically, the fidelity factor of the lens was measured for time-domain signals with different incidence angles. To do this, the procedure described in [14] and [15] are used. The fidelity factor quantifies the correlation between the incidence and transmitted pulses through the lens' aperture. Fig. 6.9(b) shows the measured fidelity factors for the four different beams with the center frequency of 9 GHz and the bandwidths equal to the bandwidth of the implemented structure (8-10 GHz). As can be seen, a very high fidelity factor can be achieved when the structure is illuminated with wideband pulses. The fidelity factor decreases with

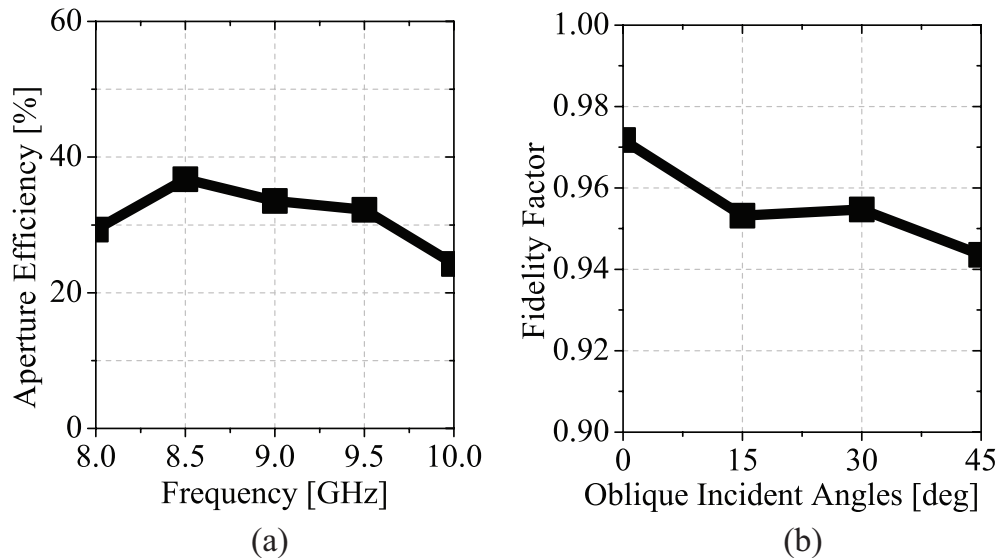


Figure 6.9 (a) Measured aperture efficiency as a function of the frequency. (b) Measured fidelity factors of the proposed lens under oblique angles of incidence for a modulated Gaussian pulse centered at 9 GHz and the bandwidth of 8-10 GHz.

increasing the angle of incidence. Nonetheless, in almost every case, the fidelity factor remains relatively high as expected. This confirms that the phase wrapping technique used to implement the MEFSSs of the outer zones of the lens does not significantly deteriorate the performance of the lens for wideband pulses.

## 6.5 Conclusion

A multi-beam antenna consisting of a planar MEFSS-based microwave lens fed with a focal plane array and a new method for modeling MEFSS-based true-time-delay microwave lenses were presented and discussed. It was demonstrated that an MEFSS with a linear phase response can be treated as a slab of an effective medium having the same effective permittivity and permeability values over the frequency range where its transmission phase remains linear. Using this system-level equivalency, an MEFSS-based true-time-delay microwave lens can be modeled as a collection of a number of different homogeneous dielectric rings with the same thickness and different inner and outer radii. This method eliminates the need to model the different metallic and dielectric layers constituting each different unit cell of an MEFSS used in the lens and can be especially

useful in modeling FSSs with sub-wavelength dimensions and complex unit cell designs such as the one reported in [24]. This offers a practical method for simulating and optimizing MEFSS-based microwave lenses with large aperture dimensions using full-wave EM simulation tools. Using this approach, a multi-beam antenna consisting of a planar lens fed with a focal plane array was designed and experimentally characterized. The proposed antenna has a significantly lower profile compared to other spatially-fed apertures such as reflectarrays and lens antennas. A focal plane array placed in parallel with the lens aperture is used to feed the antenna and achieve multiple independent beams in the  $\pm 45^\circ$  range. The structure operates over the frequency band of 8-10 GHz and demonstrates consistent radiation characteristics within this frequency range. Experimental measurement results demonstrated a good agreement with the simulation results obtained using the proposed simple modeling technique reported in this chapter.

## Chapter 7

# Ultra-Wideband, True-Time-Delay Reflectarray Antennas Using Ground-Plane-Backed, Miniaturized-Element Frequency Selective Surfaces

### 7.1 Introduction

The conventional parabolic antennas were among the first reflective type aperture antennas investigated for high-gain antenna applications. Using their three-dimensional geometrical parameters, these antennas are designed to work in a true-time-delay fashion over a broad range of frequencies (provided that a suitable feed is used). Although they are widely used in many systems due to their wideband characteristics, ease of design, and relatively low cost, they are generally bulky because of their inherent three-dimensional structures. Over the past few decades, significant developments have been made in the area of flat phased arrays employed in high-gain antenna applications. These structures are generally implemented using active or passive antenna array architectures. The tradeoffs existing between the cost, power handling capability, and thermal management of the transmit/receive (T/R) modules used in active electronically-steerable antenna arrays have hindered their widespread deployments in many commercial systems. On the other hand, large-aperture passive electronically steerable arrays suffer from excessive losses in their feed networks and the cost and power handling capability of their phase shifters [139, 140]. With the recent progress in the areas of periodic structures and metamaterials, numerous innovative designs of reflectarray antenna systems have been reported as potential replacements of parabolic antennas. Reflectarrays have also found applications in flat phased arrays that are used for many high-gain antenna applications such as satellite communications [71, 141–144]. There has been a

growing interest in reflectarray antennas for a number of reasons. First, they offer the advantages that conventional parabolic reflectors offer but they are planar and potentially conformal structures. Additionally, spatial feeding in reflectarrays eliminates the feed network losses that are a common problem in large-aperture passive phased array systems [128]. Finally, using multiple feeds to illuminate the reflectarray offers a low-cost and simple means of designing multi-beam or beam switchable, high-gain antenna apertures. Moreover, new techniques are being developed to tune the phase shift gradient of the elements in a reflectarray aperture that can result in beam steerable reflectarrays [90, 145].

Reflectarray antennas are generally composed of locally-periodic structures with unit cells that act as spatial phase shifters (SPSs) or spatial time-delay units (TDUs). These unit cells are commonly implemented from resonant building blocks. Numerous types of elements for designing reflectarrays have been reported in the past [71–77]. These structures are generally made of single-resonant elements. More recently, various attempts have been made to increase the bandwidth of reflectarrays by using multiple layers of elements [16, 146, 147], using multi-resonant elements fabricated on a single substrate [148–150], or using apertures with faceted shapes [151, 152]. However, such reflectarrays are not true-time-delay structures and tend to be highly dispersive when illuminated with broadband pulses. Moreover, in situations where reflectarrays are fed with multiple feed antennas to achieve a multi-beam aperture, the sensitivity of the responses of their elements to the angle of incidence of the electromagnetic waves can seriously deteriorate the response of the structure. In [153], a TDU-based reflectarray is presented. Each element in the reported structure is based on a patch antenna aperture-coupled to a delay line. Although an improvement in the bandwidth is demonstrated by using time-delay elements instead of spatial-phase-shifters, a limitation in bandwidth is still imposed because of using radiating elements (i.e., resonant patches) as constituting spatial time delay units of this device. In addition, the performance of the reported reflectarray is expected to degrade when illuminated with an obliquely incident wave due to large element separations. Recently, non-resonant sub-wavelength elements have also been used in printed reflectarrays to address the shortcomings of the conventional structures using resonant elements [154, 155] and achieve broadband responses. Although these reported reflectarrays

demonstrate wideband performances, they are non-TTD reflectarrays. Therefore, such structures are not suitable for broadband pulsed applications.

Over the past few years, a new class of frequency selective surfaces with sub-wavelength unit cell dimensions - referred to as miniaturized-element frequency selective surfaces (MEFSSs) - has been studied by various research groups. Unlike traditional FSSs that are composed of periodic arrangement of resonant elements, MEFSS are periodic structures having highly-miniaturized, non-resonant unit cells. Recently, these structures have been used in designing wideband planar microwave lenses [13–15]. In [14, 15], each pixel of the lens is a unit cell of appropriately designed MEFSS that act as a time-delay unit. Lately, a reflectarray antenna that uses the unit cells of a single layer MEFSS as its spatial phase shifters was reported in [156]. It was demonstrated that using this MEFSS, a low-profile reflectarray with a relatively wideband response could be designed. However, this reflectarray suffers from chromatic aberration as it uses MEFSS unit cells as its spatial phase shifters and not time-delay units. Also, the phase wrapping technique used in the design of this structure causes distortion in the response of the antenna when the structure is excited with broadband pulses. Therefore, such a reflectarray is not suitable for broadband pulsed applications. In applications where signals with instantaneously broad bandwidths are used, reflectarray antennas free of chromatic aberration must be employed.

In this chapter, we propose a new technique for designing low-profile, ultra-wideband, and true-time-delay reflectarray antennas. The proposed antenna is composed of numerous spatial time delay units distributed over a planar surface that provide a desired time delay over a wide frequency range. Each spatial TDU is a unit cell of an appropriately designed, ground-plane-backed miniaturized-element frequency selective surface. The MEFSS is composed of stacked non-resonant patches separated from one another by thin dielectric substrate. Each TDU is designed to provide a frequency-independent time delay within the frequency band of interest. A prototype of the TTD reflectarray with focal length to aperture diameter ratio ( $f/D$ ) of 0.87 fed with an X-band horn located at its optical axis is designed to operate at the center frequency of 10 GHz. The overall thickness of the proposed structure is less than 4.8 mm (or equivalently  $0.16\lambda_0$ ),

where  $\lambda_o$  is the free space wavelength at the center frequency of operation), and the lateral dimensions of the aperture are  $253.5 \text{ mm} \times 253.5 \text{ mm}$  (or equivalently  $\approx 8.5\lambda_o \times 8.5\lambda_o$ ). A prototype of the proposed structure is also fabricated and experimentally characterized in the lab. It is demonstrated that the structure provides a gain of 23 dB with a variation of less than 4 dB over a relative gain-bandwidth of 40%. Measurement of the fidelity factor of this device demonstrates that it can operate relatively free of chromatic aberrations over this entire 8-12 GHz frequency range.

## 7.2 Reflectarray Elements

Fig. 7.1(a) shows the topology of the proposed center-fed TTD reflectarray antenna. The structure is composed of a reflectarray fed with a horn antenna. The reflectarray has aperture diameter of  $D$  and the distance between the feed horn and the aperture of the reflectarray is  $f$ . The reflectarray is illuminated by the feed horn and it is designed to correct and transform the incoming wave front from the feed horn to a planar wave front with a pencil beam in a desired direction. Since the feed horn does not have a uniform phase pattern at the location of the reflectarray's aperture, the phase response of the feed is also taken into account in designing the reflectarray.

The aperture of the reflectarray is formed from numerous sub-wavelength spatial TDUs. These TDUs provide the desired time delay over the entire aperture within the frequency range of interest. This desired time delay over the aperture is determined from the focal distance,  $f$ , the aperture diameter,  $D$ , and the field and phase patterns of the feed antenna. In this structure, each TDU is the unit cell of a ground-plane backed MEFSS with a lowpass frequency response. Each TDU is composed of multiple sub-wavelength capacitive patches, a ground plane, and a number of thin dielectric substrates. The ground plane is located on the bottom surface of the unit cell and the other metallic layers (sub-wavelength capacitive patches) are placed above it. All the metal layers are separated from one another by thin dielectric substrates. The detailed topology and the equivalent circuit model of this unit cell are shown in Fig. 7.1(b), where the capacitive patches are modeled with parallel capacitors and the thin dielectric substrates are modeled with transmission lines with small electrical lengths. The ground plane is modeled as a short load at one side. Mapping between the element values of the equivalent circuit model shown in Fig. 7.1(b) and the physical parameters

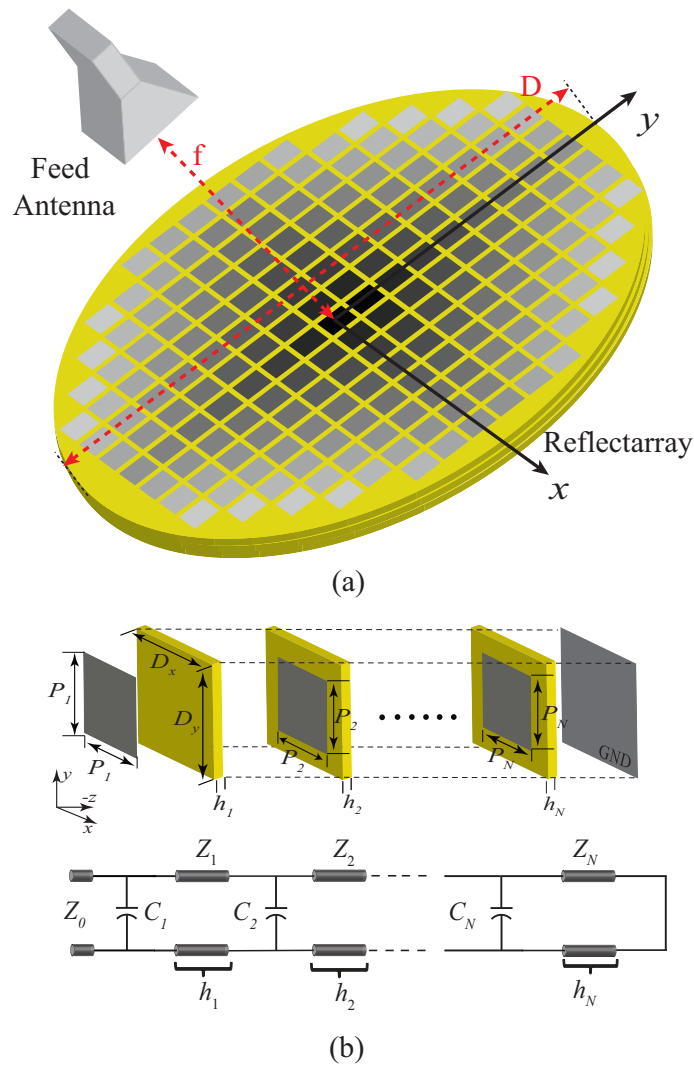


Figure 7.1 (a) Topology of the proposed reflectarray antenna. (b) The composition of each TDU and its equivalent circuit model.

of the unit cell (patch and unit cell dimensions, etc.) can be done using the procedure described in [1] and will not be repeated here for brevity. Due to the sub-wavelength nature of the MEFSS unit cells, the dimensions of adjacent unit cells are not drastically different. Therefore, each unit cell can be analyzed as if it is in a periodic structure. This periodic structure can be characterized by its frequency response when it is illuminated with an incident plane wave from the side starting with a patch layer. The magnitude of the reflected wave for the unit cell shown in Fig. 7.1(b) is unity, assuming that all the materials are lossless. As far as the phase response is concerned,

the wave experiences a phase shift behavior similar to the phase shift incurred by propagating through a lowpass type MEFSS with  $2N$  layers of patches (i.e., the phase response of a  $(4N - 1)^{th}$ -order lowpass MEFSS). The presence of the metal ground adds a constant phase shift as well. In the proposed TTD reflectarray, a relatively constant group delay over large bandwidths can be achieved. To achieve a constant group delay, the phase of the reflected wave needs to exhibit a linear response versus frequency, as the slope of its response determines the group delay of the filter. Therefore, the proposed elements with linear phase responses are used to synthesize the TDUs of the proposed reflectarray.

To design the proposed reflectarray, different time-delay values are required for different elements over the reflectarray aperture. There are a number of parameters that influence the time-delay value provided by a TDU. These include the number of the capacitive patch layers, the lateral dimensions of the elements, the size of the capacitive patches, and the thicknesses and the dielectric constants of the separating substrates. The dielectric substrates and the unit cell size are largely determined from practical design considerations (e.g., the accessibility of substrates with given dielectric constants and thicknesses, the tolerances of the printed circuit board lithography technique used, and the minimum feature that can be fabricated reliably). Assuming these two parameters are fixed, the group delay can be controlled by the number of patch layers and their respective dimensions. The number of patch layers determines the maximum delay variation that can be achieved using a given MEFSS design. As the number of the patch layers increases, the maximum delay variation within the frequency range of interest increases. Therefore, the number of the patch layers is determined from the difference between the maximum and minimum time delays required to achieve broadband beam collimation over the entire desired frequency band of operation. Once the number of the patch layers is determined, they need to be tuned to obtain different group delays for each TDU over the reflectarray aperture. Moreover, for a given range of group delay values, increasing the number of patch layers can be used as a means of increasing the bandwidth of the reflectarray.

### 7.3 Design Procedure

The design procedure of the proposed reflectarray consists of a few different steps. The first step is to choose the aperture diameter,  $D$ , and the separation between the feed antenna and the aperture of the reflectarray,  $f$ . These parameters are largely determined from the practical design consideration such as the 3 dB beamwidth, available volume, and the maximum tolerable thickness of the reflectarray. Another important factor in choosing such parameters is the trade-off between the spillover loss and aperture efficiency. To increase the efficiency of the antenna, spillover loss should be minimized. Spillover loss, however, is a function of the radiation pattern of the antenna and the  $f/D$  ratio of the reflectarray. For a given feed antenna, spillover loss can be reduced by reducing the  $f/D$  ratio while ensuring the tapering over the aperture caused by this does not significantly decrease the aperture efficiency of the antenna. For these TTD reflectarrays, the maximum bandwidth of the entire antenna is primarily limited by the bandwidth of the feed.

The reflectarray aperture is then divided into  $M$  concentric zones<sup>1</sup>, where  $M$  is an integer. The elements of each zone are assumed to be identical. The number of different zones,  $M$ , is a design parameter that can be chosen by the designer. As  $M$  increases, the accuracy of time-delay correction over the aperture of the reflectarray increases. The upper bound of  $M$  can be determined from the aperture diameter,  $D$ , and the unit cell size of the MEFSSs that are used to synthesize the TDUs of different zones of the proposed TTD reflectarray.

Once these physical parameters are determined, the time-delay profile required from the TDUs occupying each zone should be determined. The time-delay profile can be determined from the phase delay profile as each element offers a linear phase response. To obtain the phase delay profile, the level of illumination at each element by the feed horn is determined using full-wave simulations. Since the reflectarray is composed of TDUs, this calculation only needs to be performed at one single frequency (e.g. the center frequency of operation in this case) [14]. The final

---

<sup>1</sup>Dividing the aperture into concentric zones simplifies the design procedure, since all the elements within a specific zone are identical to each other. However, more advanced design techniques can also be used where each TDU of the reflectarray can be designed and optimized separately based on its illumination level from the feed. This is particularly useful in scenarios where the reflectarray is illuminated with an offset feed. In such cases, the same design procedure (with the exception of zoning) can still be used.

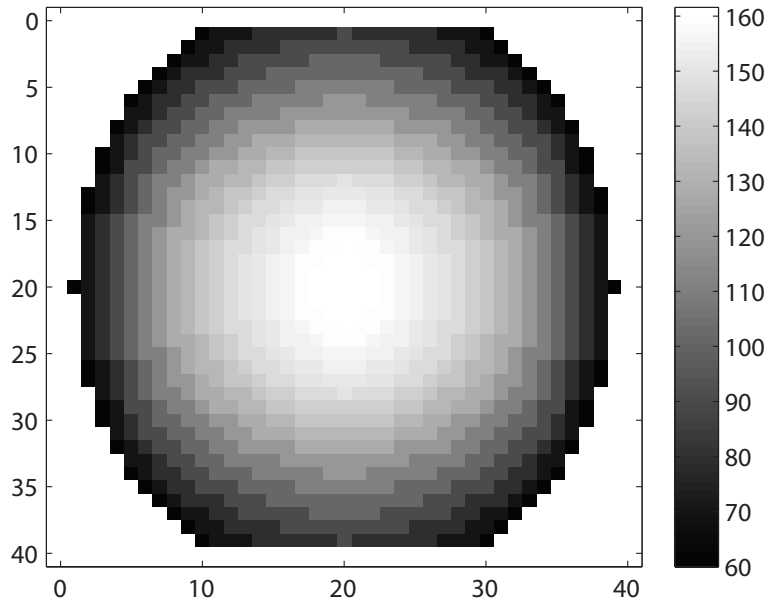


Figure 7.2 The time-delay profile required from the TDUs distributed over the aperture of the reflectarray. The values are in psec.

step is to use the procedure described in Section 7.2 to design the TDUs that populate the aperture of the reflectarray based on the calculated time delay profile.

## 7.4 Design Example

The procedure presented in Section 7.3 was followed to design an MEFSS-based center-fed reflectarray antenna. The proposed antenna is designed to operate within the frequency range of 8-12 GHz. The reflectarray has an aperture diameter of 253.5 mm or equivalently  $\approx 8.5\lambda_0^2$  where  $\lambda_0$  is the wavelength at the center frequency of operation. As described in Section 7.3, the  $f/D$  ratio is determined by the radiation pattern of the feed antenna considering the tradeoff between the spillover loss and the efficiency. For this design, a commercial X-band horn antenna (AT-39/AP) is used as the feed antenna. The directivity of the feed antenna is  $\approx 17.5$  dB at 10 GHz. The half power beam widths of the horn in the E- and H-planes are approximately  $24^\circ$  and  $21^\circ$ , respectively. In the design process, a 15 dB illumination tapering is considered over

<sup>2</sup>The dimensions of the reflectarray aperture are chosen primarily for ease of measurements. The concept proposed in this chapter can easily be applied to design reflectarrays with larger apertures.

the aperture for the compromise between the spillover and aperture efficiency. In other words, the illumination energy is 15 dB down at the edges of the reflectarray compared to its center. Considering this allowed tapering and the radiation pattern of the horn antenna, the  $f/D$  ratio is calculated to be approximately 0.87, which leads to a focal distance of approximately 22 cm. The aperture of the reflectarray is divided into 20 concentric zones. The time delays required from the TDUs populating the aperture of reflectarray are calculated and shown in Fig. 7.2. The maximum time-delay variation across the aperture is 101.6 psec for this combination of  $f$  and  $D$ . The maximum time delay required is for the center element and it gradually decreases as we move towards the outer zones. The minimum time delay required is for the outermost zone and it is synthesized with the proposed MEFSS when all patches are etched. Following the design guidelines provided in Section 7.3, an MEFSS structure composed of a stack of two layers of patches backed with a ground plane is found to be needed to compensate the required time-delay difference and achieve linear phase response within the frequency range of interest for all elements. The dielectric substrates used in this design are non-magnetic and have a dielectric constant of  $\epsilon_r = 3.4$  (Rogers RO4003C). Since the proposed unit cell is composed of multiple dielectric substrates that need to be bonded together, the effect of the bonding material on the response of each element must also be taken into account. The bonding material used here is Rogers 4450F prepreg layer with the dielectric constant of  $\epsilon_r = 3.52$  and the thickness of 0.1 mm. The topology of each TDU populating the aperture of the proposed reflectarray is shown in Fig. 7.3. The detailed physical parameters of the TDUs occupying each zone of reflectarray are provided in Table 7.1. Fig. 7.4 shows the simulated phase responses of the elements occupying different zones of the reflectarray. Specifically, this figure shows the comparison between the full-wave simulated phase response of the designed elements and the desired ideal case for each TDU occupying different zones. Within the frequency range of interest, slight discrepancies are observed between both cases for some elements. However, as will be shown in Section 7.5.2, the effect of these discrepancies on the time-domain performance of the proposed reflectarray is minimal as they happen at the frequency band edges. With regards to the magnitude of reflection coefficient, all elements of the

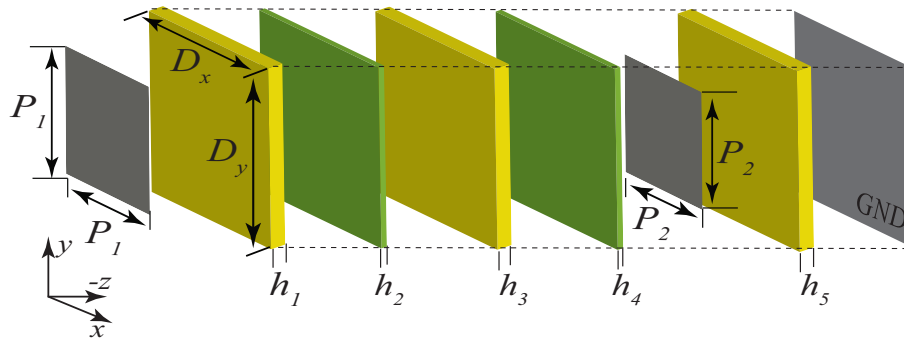


Figure 7.3 The composition of TDUs populating the proposed reflectarray aperture discussed in Section 7.4.

Table 7.1 Physical parameters of the TDUs that populate each zone of the proposed reflectarray.

All physical dimensions are in  $mm$ . For all these TDUs,  $D_x = D_y = 6.5mm$ ,  $h_1 = h_3 = h_5 = 1.524mm$ , and  $h_2 = h_4 = 0.1mm$ . The dielectric substrates with the thickness of  $1.524mm$  are Rogers RO4003C with the dielectric constant of 3.4. The bonding layers with the thickness of  $0.1mm$  are Rogers 4450F with the dielectric constant of 3.52.

Zone	1	2	3	4	5
$P_1$	4.50	4.50	4.45	4.40	4.33
$P_2$	6.30	6.30	6.30	6.30	6.30
Zone	6	7	8	9	10
$P_1$	4.22	4.16	4.09	3.93	3.83
$P_2$	6.30	6.30	6.30	6.30	6.28
Zone	11	12	13	14	15
$P_1$	3.66	3.46	3.22	2.96	2.69
$P_2$	6.22	6.15	6.02	5.84	5.45
Zone	16	17	18	19	20
$P_1$	2.66	2.66	2.47	1.5	0
$P_2$	5.03	4.45	3.50	1.50	0

reflectarray demonstrate losses of less than 0.2 dB which is mainly attributed to the Ohmic and dielectric losses of the elements.

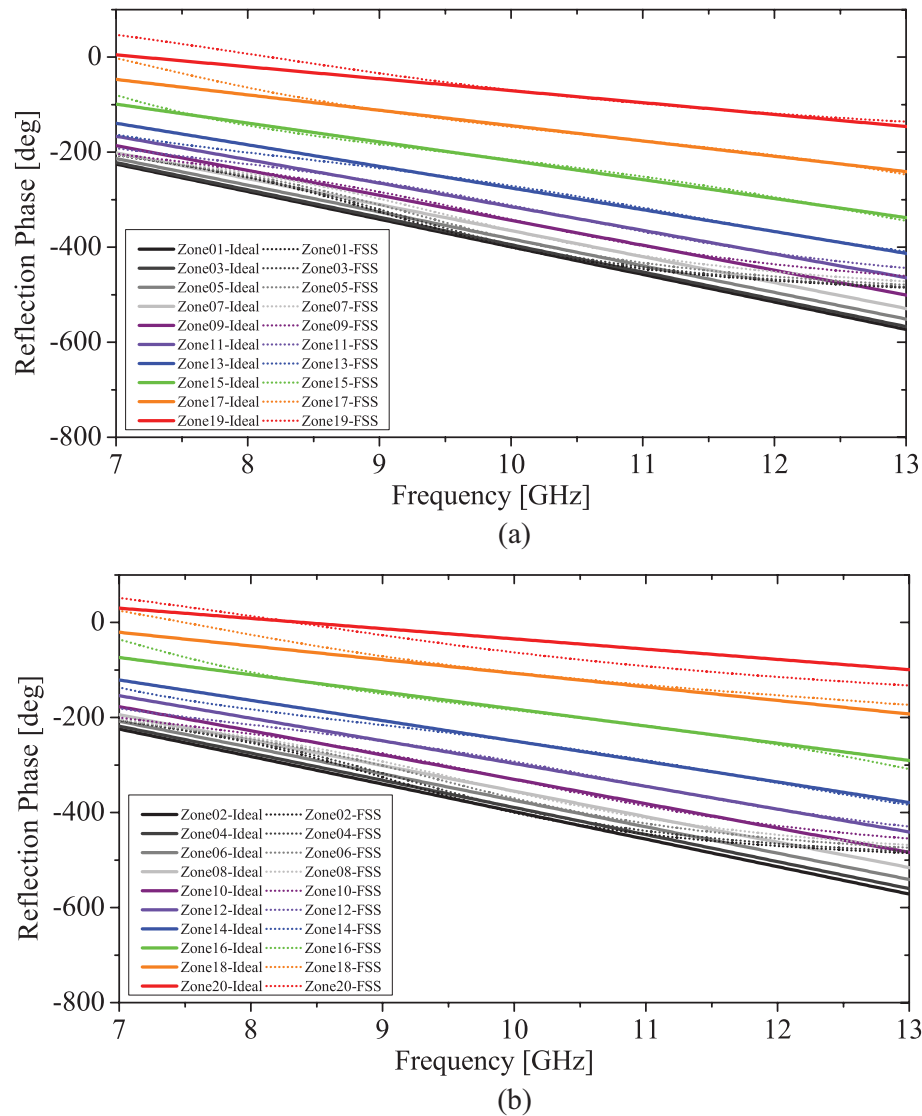


Figure 7.4 The comparison between the full-wave simulated phase responses of the designed elements and the desired ideal responses for each TDU occupying different zones. The topology of the designed elements is shown in Fig. 7.3 and their dimensions are reported in Table 7.1. The ideal case represents the desired linear reflection phase with the desired time delay. (a) The responses for the TDUs occupying the odd zones. (b) The responses for the TDUs occupying the even zones.

As can be seen in Table 7.1, there are very small variations between different pixels of the reflectarray. Due to these small variations and also the small features of the proposed reflectarray,

simulating the proposed structure using full-wave electromagnetic simulations requires an excessive amount of computational resources. For example, to simulate this structure using the finite difference time domain (FDTD) technique, the minimum cell size needs to be smaller than the minimum feature size in the structure. Considering the dimensions of the patches reported in Table 7.1, the cell sizes need be as small as  $20 \mu m$  for the aperture with the dimensions of  $253.5 \text{ mm} \times 253.5 \text{ mm}$ . Therefore, simulation of such MEFSS based reflectarray using full-wave EM simulations is extremely challenging. In [100], a new approach is proposed to reduce the difficulty of the full-wave electromagnetic simulations of such structures with very small features but relatively large aperture sizes. In this method, the constituting elements of the aperture are treated as effective media. In [100], it was shown that, at the system level, an MEFSS with a linear phase response can be modeled as an effective medium having the same effective permittivity and permeability values over the frequency range where its phase response is linear. The same concept can be used here to simulate the proposed reflectarray antenna. Using the effective medium approach, each TDU of the reflectarray can be treated as a slab of homogenous medium with the refractive index of  $n_{eff,i}$  and the thickness of  $d$  which is backed with a ground plane. Here the thickness  $d$  is chosen to be the same as that of the actual reflectarray. As the response of each element is relatively linear within the frequency range of interest, the effective permittivity and permeability are the same for each element ( $\epsilon_{r,eff} = \mu_{r,eff}$ ). These effective constitutive parameters can be extracted through a resonant inverse scattering approach reported in [138]. Table 7.2 shows the indices of refraction obtained for different zones of the reflectarray. The simulated radiation patterns of the reflectarray antenna in the E-plane ( $yz$ -plane) and the H-plane ( $xz$ -plane) in the frequency range of 8-12 GHz are shown in Fig. 7.6. The reflectarray is fed with an X-band horn antenna with the electric field oriented in the  $\hat{y}$ -direction.

## 7.5 Experimental Verification and Measurement Results

### 7.5.1 Reflectarray Antenna Prototype

The reflectarray prototype examined in Section 7.4 was fabricated and experimentally characterized. The feed antenna is a commercial X-band horn antenna located on the optical axis of the

Table 7.2 The refractive index profile of the simplified model of the proposed reflectarray composed of the effective media with the thickness of 4.8 mm.

Zone	1	2	3	4	5
$n_{eff}$	5.076	5.066	5.036	4.990	4.930
Zone	6	7	8	9	10
$n_{eff}$	4.859	4.779	4.689	4.588	4.474
Zone	11	12	13	14	15
$n_{eff}$	4.341	4.185	3.998	3.770	3.495
Zone	16	17	18	19	20
$n_{eff}$	3.178	2.844	2.517	2.199	1.884

reflectarray at the distance of  $f \approx 22$  cm from the center of the reflectarray aperture. Standard lithography as well as substrate bonding techniques were used to fabricate the reflectarray. The fabricated prototype has three metal layers and three substrate layers. The metal layers include two patch layers and the ground plane. Rogers RO4003C dielectric substrates ( $\epsilon_r = 3.4$ ) with the thickness of 1.524 mm were used for each substrate layer, and all the dielectric substrates were bonded together using a 0.1 mm thick Rogers 4450F binding film with  $\epsilon_r = 3.52$ . The total thickness of the reflectarray prototype including the bonding layers is  $\approx 4.8$  mm, which is equivalent to  $0.16\lambda_0$  at 10 GHz. Each time-delay unit, as shown in Fig. 7.5, has the dimensions of 6.5 mm  $\times$  6.5 mm (or equivalently  $\approx 0.22\lambda_0 \times 0.22\lambda_0$ ) in the proposed structure. Fig. 7.5 shows the photographs of the fabricated TTD reflectarray prototype. The total dimensions of the structure are 253.5 mm  $\times$  253.5 mm (or equivalently  $\approx 8.5\lambda_0 \times 8.5\lambda_0$ ).

## 7.5.2 Measurement Results

The measurements of the radiation characteristics of the proposed reflectarray antenna were carried out using a multi-probe spherical near-field system. For a feed horn located with the electric

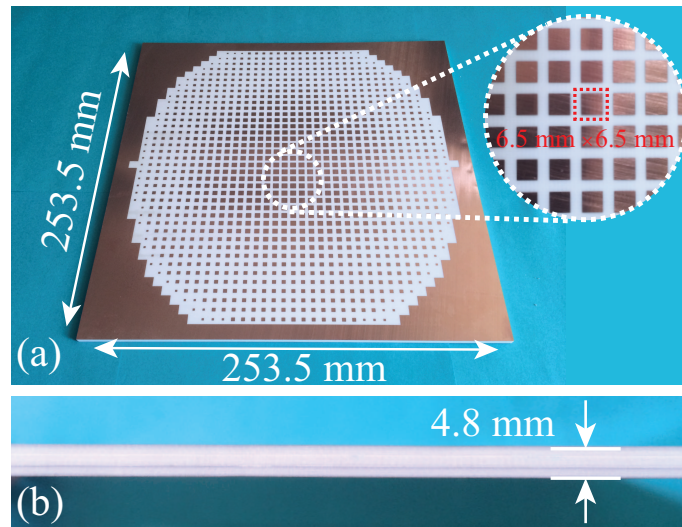


Figure 7.5 (a) Photograph of the fabricated reflectarray. (b) Side view of the fabricated prototype.

field oriented in the  $\hat{y}$ -direction, Fig. 7.6 shows the measured and simulated far-field co- and cross-polarized radiation patterns of the antenna in the E-plane ( $yz$ -plane) and the H-plane ( $xz$ -plane) in the frequency range of 8-12 GHz. The radiation patterns are normalized to the peak values of their corresponding co-polarized components. The simulation results were obtained using full-wave EM simulations in CST Microwave Studio with the simplified model of the reflectarray using effective media. In general, a good agreement is observed between the simulation and measurement results despite the approximations made in the modeling of the reflectarray using effective medium theory. Observe that the proposed antenna provides a focused beam with side-lobe level (SLL) better than -10 dB across the entire band. The side-lobe levels of the measured and simulated radiation patterns are generally above the side-lobe levels that are expected from an aperture illumination with a 15 dB tapering. The primary cause of this is the aperture blockage caused by the feed horn antenna. Specifically, the feed horn antenna has aperture dimensions of  $3.05\lambda_0 \times 2.62\lambda_0$ , which directly blocks the center part of the aperture of the reflectarray. Another drawback of this large aperture blockage is the reduction of the aperture efficiency of the reflectarray. These issues, however, can be resolved relatively easily by using an offset feed to illuminate the aperture of the reflectarray. The measured cross-polarized radiation of the antenna is at least 20 dB below that of the co-pol for all cases over the entire band of interest. The gain and the directivity of the antenna were also

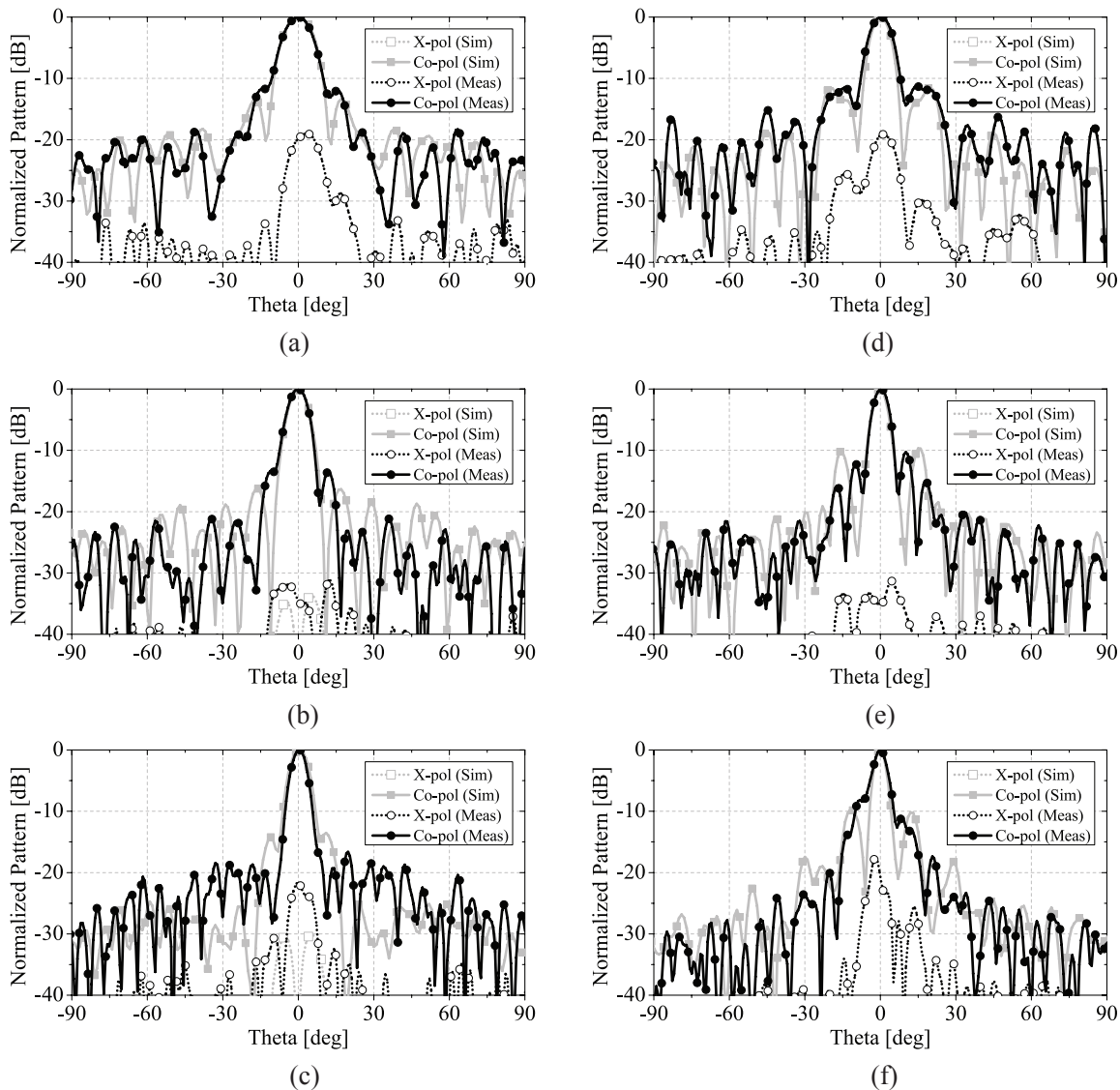


Figure 7.6 Measured and simulated normalized radiation patterns of the proposed reflectarray antenna described in Section 7.4 and shown in Fig. 7.5 in the (a)-(c)  $xz$ - and (d)-(e)  $yz$ -planes at (a), (d) 8 GHz, (b), (e) 10 GHz, and (c), (f) 12 GHz. The measurements were carried out using a multi-probe spherical near field system. The simulated results are obtained using full-wave EM simulations of simplified model of the reflectarray using effective medium approach. All the patterns are normalized to the peak values of their corresponding co-polarized components.

measured using the same near field system over the frequency range of 8-12 GHz and the results are shown in Fig. 7.7. The antenna gain is 23 dB at 10 GHz and does not vary more than 4 dB

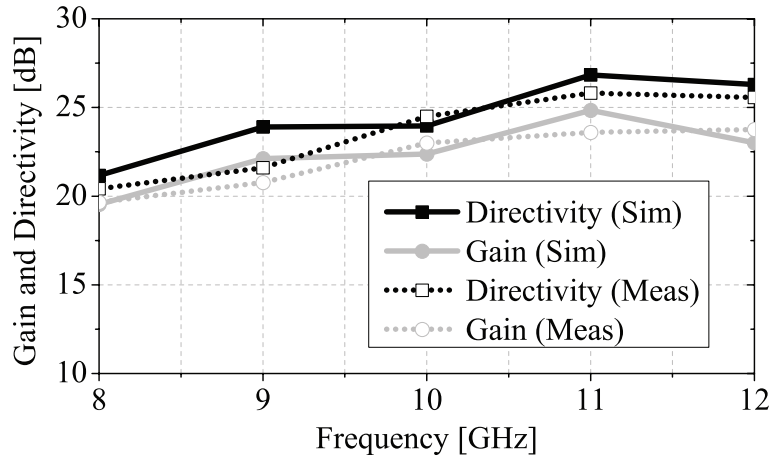


Figure 7.7 Measured and simulated realized gain and directivity of the proposed antenna shown in Fig. 7.5 across the band of interest. The measurements are done using a multi-probe near-field system and the full-wave EM simulation results are obtained by simulating the reflectarray antenna, using the effective medium approach, in CST Microwave Studio.

within 8-12 GHz frequency range. This variation of the gain is due to the change in the electrical dimensions of the reflectarray. The gain for electrically larger reflectarrays is expected to be higher. Therefore, the gain gradually increases as the frequency increases. Also, the difference between the directivity and realized gain is mainly attributed to ohmic and dielectric losses.

The reflectarray can serve as a multi-beam aperture with a wide field of view when fed with multiple feed antennas. Fig. 7.8 shows the measured co-polarized gain patterns of the reflectarray antenna with four feeds placed on the focal arc illuminating the reflectarray aperture under oblique incident angles of  $0^\circ$ ,  $15^\circ$ ,  $30^\circ$ , and  $45^\circ$  in the  $xz$ -plane (H-plane). As can be seen, by selecting the appropriate feed antenna, the direction of the far-field pattern can be steered towards the desired direction. As expected, the main beam steers towards the angle  $\theta_i$  when the reflectarray was illuminated under an incident angle of  $\theta_i$ . The proposed antenna demonstrates a good scanning performance in a relatively wide field of view of  $\pm 45^\circ$  without beam squinting. However, this capability comes at the expense of slight degradation of the side-lobe level.

As described in Section 7.4, the phase responses of the TDUs over the aperture are not quite linear over the entire band, especially at the band edges. To quantify the potential influence of

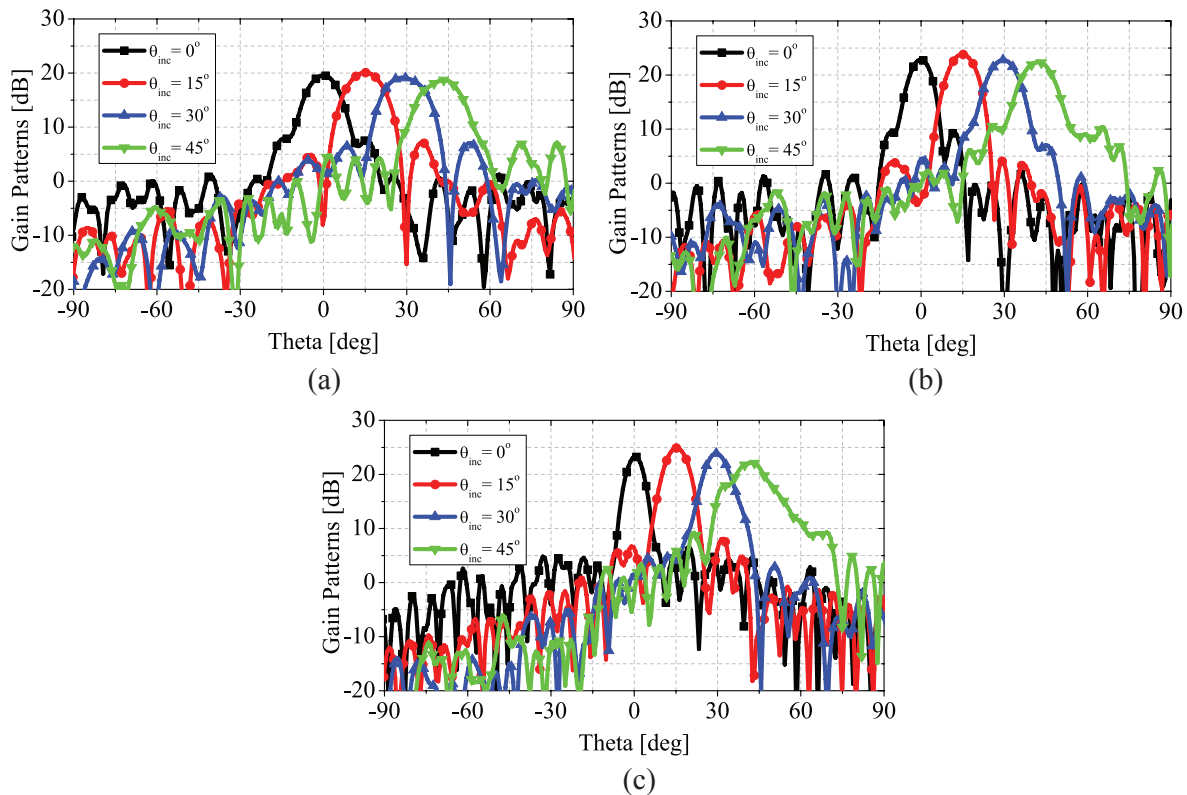


Figure 7.8 Measured co-polarized components of the gain patterns of the proposed reflectarray antenna at (a) 8 GHz, (b) 10 GHz, and (c) 12 GHz in the H-plane ( $xz$ -plane). For each frequency, four feed antennas are located on the focal arc illuminating the reflectarray at incident angles of  $0^\circ$ ,  $15^\circ$ ,  $30^\circ$ , and  $45^\circ$  to steer the main beam towards  $0^\circ$ ,  $15^\circ$ ,  $30^\circ$ , and  $45^\circ$ , respectively.

this nonlinearity in introducing distortion in the antenna response, a series of time-domain measurements were carried out. The purpose of such measurements is to examine the true-time-delay performance of the proposed reflectarray antenna. In this set of measurements, the fidelity factor of the reflectarray was measured for time-domain signals with different fractional bandwidths. The fidelity factor quantifies the correlation between the incident and reflected pulses from the reflectarray aperture [157, 158]. The setup for doing such measurements is shown in Fig. 7.9(a). It consists of a large metallic screen with an opening having the same dimensions as those of the reflectarray. The screen was used to minimize the effect of diffractions. A transmitting X-band horn antenna was used to illuminate the reflectarray with plane waves as the reflectarray was located in the far field of the transmitting antenna. A receiving probe was also placed on the focal point

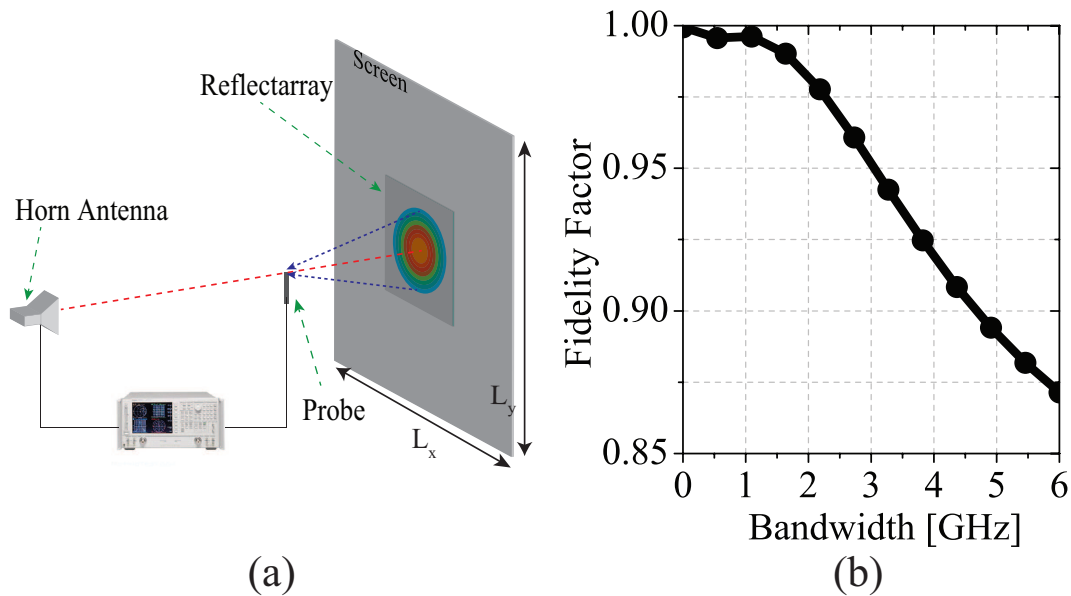


Figure 7.9 (a) The measurement setup used to experimentally characterized the time-domain performance of the proposed reflectarray. (b) Measured fidelity factor of the proposed reflectarray when it is illuminated with a modulated Gaussian pulse centered at 10 GHz with different fractional bandwidths up to 6 GHz.

of the reflectarray to sample the received electric field. Both transmitting and receiving antennas were connected to the two ports of the vector network analyzer (VNA) to measure the transmission coefficient. This measurement was performed with and without the presence of the reflectarray, and the latter measurement was used as the base line to calibrate the effect of the metallic screen out. Additionally, the range gating in the VNA was used to eliminate the direct transmission between the transmitting and receiving antennas. This technique allows us to only capture the waves reflected back from the reflectarray. Fig. 7.9 shows the measured fidelity factors for modulated Gaussian incident pulses centered at 10 GHz with different fractional bandwidths up to 6 GHz. As can be seen, a very high fidelity factor is achieved when the reflectarray is illuminated with such pulses with wide fractional bandwidths. Observe that the fidelity factor decreases as the fractional bandwidth increases which is due to the nonlinearity of the phase responses at the edges of the operating band of the reflectarray. However, a relatively high fidelity factor (more than 0.92) is achieved when the reflectarray is illuminated with signals with fractional bandwidths less than

or equal to its operational bandwidth. This further confirms the TTD behaviour of the proposed reflectarray antenna.

## 7.6 Conclusions

In this chapter, a broadband true-time-delay reflectarray antenna composed of a low-profile planar MEFSS-based reflectarray fed with a horn antenna was presented. The proposed reflectarray exploits the unit cells of appropriately designed MEFSSs as its spatial TDUs to operate in a true-time-delay fashion and to reduce chromatic aberrations within a wide frequency band. A prototype of such TTD MEFSS-based reflectarray was fabricated and experimentally characterized. The fabricated structure was designed to operate at the center frequency of 10 GHz. It was experimentally verified that the reflectarray antenna demonstrates relatively consistent radiation properties within the 8-12 GHz frequency range or equivalently 40% bandwidth. For the same aperture dimensions, reflectarrays of the type reported in this chapter are expected to demonstrate larger bandwidths than those of the previously-reported TTD reflectarrays. The TTD performance of the reflectarray was also verified by characterizing its fidelity factor as a measure of distortion that the structure introduces to wideband incident pulses. It was demonstrated that the reflectarray is indeed free of any significant chromatic aberrations over its entire operational band. Therefore, such reflectarrays are expected to be useful for applications where instantaneously broadband pulses are used.

## Chapter 8

# Broadband True-Time-Delay Circularly-Polarized Reflectarray With Linearly-Polarized Feed

### 8.1 Introduction

Reflectarray antennas have recently been proposed as a replacement to traditional reflectors in applications such as beam-switchable [101, 159] and beam-steerable antenna designs [145, 160]. In recent years, a number of studies have examined the design of circularly-polarized reflectarrays [161–171]. This interest primarily stems from the fact that circularly-polarized waves are more robust to various environmental interferences including multipath fading. Thus, circularly-polarized antennas are widely used in modern satellite and point to point communication systems.

A reflectarray antenna is composed of a flat reflecting surface illuminated by a feed antenna. The reflectarray aperture is treated as a locally-periodic structure. The unit cells of this structure act as spatial phase shifters or spatial time-delay units. Both linearly-polarized and circularly-polarized sources have been employed as the primary feed for the existing circularly-polarized reflectarray antennas. For reflectarrays with circularly-polarized feeds, various element shapes have been presented in the literature [161–165]. In most cases, the angular rotation of the elements is used to vary the phase shift or time delay introduced by it. Circularly-polarized reflectarrays can be also designed using linearly-polarized feeds. In such architectures, the feed can be rotated by  $45^\circ$  with respect to the aperture axis, and the circularly-polarized radiated beam is provided by generating a  $90^\circ$  phase shift between the two orthogonal polarization components of the incident wave. Numerous types of elements for such reflectarrays have been reported in the past. These include dual layer T-shaped elements [166], aperture coupled patches with slot

and two lines of variable lengths [167], cross-shaped elements with varying arms [168], and rectangular patch elements [169]. These structures tend to be relatively narrowband, since they are made of resonant elements. Moreover, they have seldom been employed as a part of multibeam apertures due to the sensitivity of the response of their constituting elements to the angle of incidence. Single layer non-resonant elements employing asymmetric features have also been used to design linearly-polarized-fed, circularly-polarized reflectarrays [170, 171]. Although some of these reported reflectarrays demonstrate wide bandwidths, they are not true-time-delay structures. In such structures, when the aperture is illuminated with a broadband pulse whose spectral content falls within the bandwidth of the reflectarray, the radiated pulse will be significantly distorted [101, 153]. Therefore, such reflectarrays are not suitable for broadband pulsed signal applications.

In this chapter, we present a method for designing low-profile, broadband, and true-time-delay circularly-polarized reflectarray antennas. The proposed antenna consists of a planar surface populated with spatial time-delay units (TDUs). These TDUs are the unit cells of anisotropic ground-plane-backed miniaturized-element frequency selective surfaces (MEFSS). MEFSSs have been previously employed to design spatial filters [97, 102, 115, 119], transmitarrays [13], true-time-delay microwave lenses [14, 15], multi-beam antennas [100], polarization converters [120], and linearly-polarized reflectarrays [101]. The multilayer TDUs employed in the proposed structure are capable of providing constant time delays over wide bandwidths. To generate a circularly-polarized wave, TDUs are designed to behave differently for the two orthogonal polarizations. They feature asymmetric elements to create  $90^\circ$  phase shift between two orthogonal components of the output wave while providing the desired time delay over the wide frequency range of interest. Using this approach, a linearly-polarized-fed reflectarray prototype capable of providing a circularly-polarized output is designed, fabricated, and characterized. The prototype operates over the frequency band of 8-12 GHz (a 40% bandwidth) and provides a gain of 23.7 dB with a variation of less than 3 dB. Additionally, the time-domain properties of the proposed reflectarray are characterized by measuring its fidelity factor for broadband pulsed excitations. The antenna demonstrates a fidelity factor greater than 0.91 for wideband pulses with bandwidths as wide as 40%.

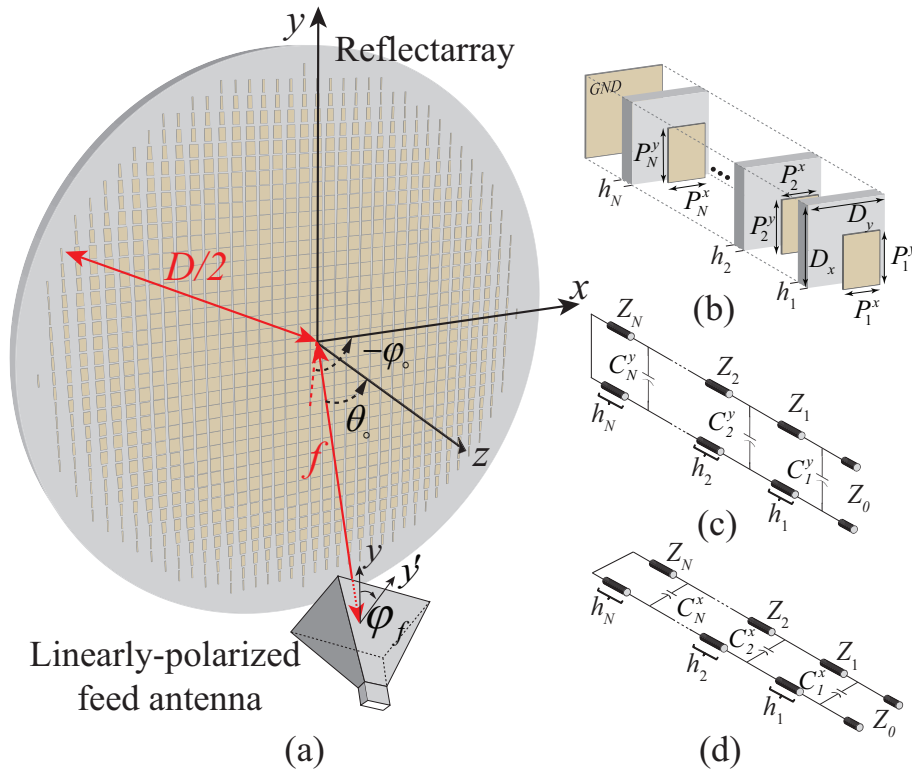


Figure 8.1 (a) Topology of the proposed reflectarray whose aperture is populated with FSS-based spatial TDUs. (b) The composition of each TDU. (c)-(d) The equivalent circuit model of each TDU for the two orthogonal ( $\hat{x}$ - and  $\hat{y}$ -directed) polarizations.

## 8.2 Reflectarray Elements

Fig. 8.1(a) shows the topology of the proposed true-time-delay, circularly-polarized reflectarray antenna. The structure is composed of a reflectarray and a feed horn antenna. The aperture diameter of the reflectarray is  $D_{ap}$  and the distance between the reflectarray and the feed horn is  $f$ . The feed horn is linearly polarized and is rotated  $45^\circ$  with respect to the  $\hat{y}$  axis. The far-field phase pattern of the feed horn is not uniform. Due to this and the spherical wavefront of the fields radiated by the feed, the incident field over the aperture will not have a uniform phase front over the aperture of the reflectarray. Therefore, the reflectarray is designed to both correct the phase variations of the feed antenna and transform the spherical incoming wave striking its aperture to a planar wave front with a circularly-polarized pencil beam in the far field in the desired direction. The aperture of the reflectarray is populated with numerous sub-wavelength time-delay unit pixels. These pixels

provide the desired time delay over the entire aperture of the reflectarray within the intended frequency range. This ensures that, within the desired frequency band of operation, the reflectarray does not demonstrate any chromatic aberrations. The TDUs also create a constant phase difference of  $90^\circ$  between the two orthogonal polarization components of the radiated field. These time-delay and phase-delay profiles are determined from the focal distance,  $f$ , the aperture diameter,  $D_{ap}$ , and the phase pattern of the feed antenna. Since the structure transforms the linearly-polarized incoming wave to a circularly-polarized wave, it needs to behave differently for the two orthogonal polarization components of the incoming wave. The time-delay profile, however, is the same for both of these two components. The phase-delay profile, on the other hand, is different for the horizontal and vertical components of the incident wave. To generate a circularly-polarized wave, these two orthogonal components need to experience two different phase shifts with the phase differences of  $\pm 90^\circ$  as they are reflected from the reflectarray's aperture. Depending on the sign of the phase difference, the radiated beam can be right-handed or left-handed circularly polarized. The radiated beam is left-handed circularly-polarized if  $\angle R_x - \angle R_y = -90^\circ$  and right-handed circularly-polarized if  $\angle R_x - \angle R_y = +90^\circ$ . To satisfy both the time-delay and the phase-delay conditions, the pixels must be designed to provide linear phase responses for both polarization components with desired slopes versus frequency. This is to ensure that the pixels provide constant group delays and to minimize the chromatic aberrations in the reflectarray when it is excited with a broadband pulse. Moreover, a phase difference of  $90^\circ$  must exist between the phase responses of the pixels for the two polarizations over the entire frequency band of operation. This is to ensure that the radiated field of the antenna is circularly polarized. Finally, the magnitude of the reflection coefficient for both components needs to be ideally equal over this intended frequency range. These phase and amplitude requirements of the time-delay units are visually depicted in Fig. 8.2. In this figure,  $R_x$  and  $R_y$  are the reflection responses of each pixel for  $\hat{x}$  and  $\hat{y}$  polarizations, respectively. As discussed,  $|R_x| = |R_y|$ ,  $\angle R_x - \angle R_y = 90^\circ$ , and the phases of  $R_x$  and  $R_y$  are linear functions of frequency across the entire band of operation of the reflectarray antenna.

Each pixel of the reflectarray is the unit cell of an anisotropic, ground-plane-backed miniaturized-element frequency selective surface. The composition of each pixel is shown in Fig. 8.1(b). Each

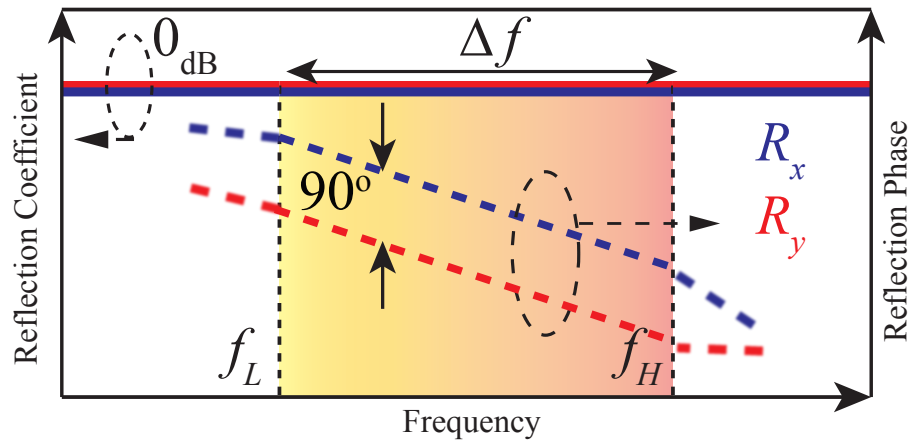


Figure 8.2 Conceptual depiction of the idealized response needed from the TDUs populating the aperture of the proposed reflectarray. The magnitudes and phases of the reflection coefficient of each TDU for the two orthogonal polarizations are shown.

pixel is composed of a stack of multiple subwavelength capacitive patches. These patches are separated from one another by a number of thin dielectric substrates. The entire structure is backed by a ground plane. As discussed in [101], such a configuration is capable of providing linear phase responses having different slopes versus frequency over a wide bandwidth. This wide bandwidth is due to the phase shift behaviour that the wave experiences as it propagates through the pixel, which is similar to that of a low-pass type MEFSS with twice number of layers. Since a flat group delay response can be achieved using low-pass filters, the proposed pixel can provide constant group delay over a wide bandwidth. The pixels also employ asymmetric elements to generate two distinct frequency responses for the vertical and the horizontal components of the incident wave. Therefore, the capacitive patches are in the form of rectangular metallic patches with the dimensions of  $P_i^x$  and  $P_i^y$ . The dimensions of the unit cells are  $D \times D$ . The equivalent circuit model of each pixel is shown in Figs. 8.1(c) and 8.1(d). In this model, the capacitive patches are modeled with parallel capacitors. The short sections of transmission lines with characteristic impedances of  $Z_1, Z_2, \dots, Z_N$  model the thin dielectric substrates. The ground plane is also modeled with a short circuit. Since the asymmetry of the structure is only in the capacitive patches, the equivalent circuit model is the same for both polarizations with the exception of the capacitance values.

To design the proposed reflectarray, pixels with various time-delay and phase-delay values are required to populate the aperture. These two values are functions of a number of geometrical parameters including the unit cell dimensions, dielectric constants and thicknesses of the substrates, the number of patch layers, and the size of patches in each layer. The choice of the pixel dimension,  $D$ , is arbitrary as long as it is small compared to the wavelength. The characteristics of the substrates are largely determined from the practical design considerations. These include the accessibility of the substrates with given dielectric constant and thickness, the resolution of the employed printed circuit board lithography techniques as well as the minimum features that can be reliably fabricated. Assuming that the pixel dimensions and the substrate characteristics are known, the number of patch layers and their respective dimensions can control the time and phase delays. The number of patch layers mainly determines the maximum variation of time and phase delays that can be achieved with a given pixel design. To compensate a larger delay variation and achieve broadband collimation over the band of interest, a higher number of layers is required. Also, for a given range of delay values, using a higher number of patch layers can be used as a means of increasing the operational bandwidth of the reflectarray. Once the number of the layers is determined, the dimensions of the patches can be varied to obtain the required responses for each pixel. This variation is in between the minimum and maximum available delays. The minimum delay available for such configuration is synthesized when the patches in all layers are etched and the maximum available delay can be obtained when the gaps in between the patches are equal to the minimum features that can be reliably fabricated using the specific lithography technique employed for fabricating the device. For a more detailed discussion about designing TDUs of the type used in this chapter to achieve a desired time delay value, the interested reader is referred to [101].

### 8.3 Design Procedure and Design Example

The design procedure of the proposed reflectarray starts with the choice of the focal distance,  $f$ , and the aperture diameter,  $D_{ap}$ . These two parameters are determined based on the practical design considerations as well as the tradeoff between the spillover loss and the aperture efficiency.

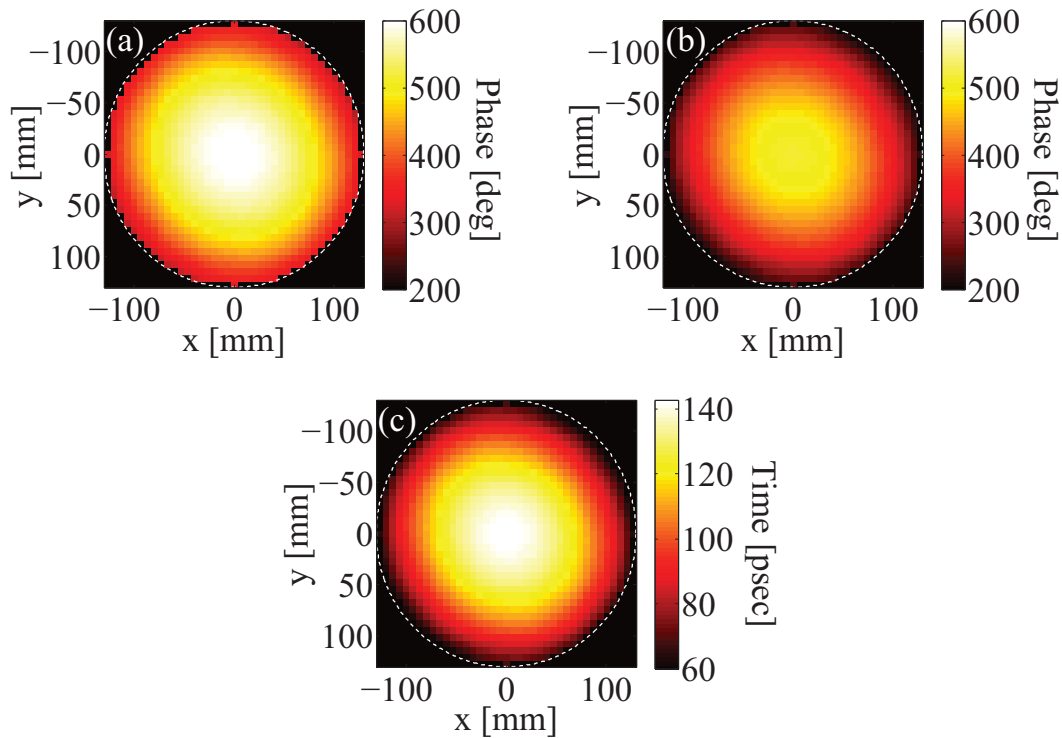


Figure 8.3 (a)-(b) The phase-delay profile required from the pixels distributed over the aperture of the reflectarray for (a)  $\hat{x}$ - and (b)  $\hat{y}$ -directed polarizations. (c) The time-delay profile required by the time delay units populating the reflectarray aperture.

The spillover loss can be reduced by decreasing the aperture  $f/D$  while ensuring the aperture efficiency is within an acceptable range. Once these physical parameters are determined, the required time- and phase-delay profiles for each pixel can be determined based on its level of illumination from the feed. To simplify the design procedure, the reflectarray aperture is divided into concentric zones assuming that the elements in each zone are identical. The number of zones is an arbitrary parameter that determines the accuracy of time-delay correction over the aperture. For more advanced design techniques, each time delay unit can be designed separately based on its illumination level from the feed. In the final step, once the number of zones is determined, the procedure described in Section 8.2 can be used to design the pixels populating the aperture of the reflectarray.

This design procedure was followed to design a center fed reflectarray antenna radiating a right-handed circularly-polarized wave. The proposed reflectarray with the aperture diameter of 235.5

mm<sup>1</sup> is designed to operate at X-band. For this design, an X-band horn antenna (AT-39/AP) is used as the linearly-polarized feed antenna. The directivity of the feed antenna is 17.5 dB and its half power beam width in the  $x$ -plane and  $y$ -plane are 24° and 21°, respectively. The gain variation of the feed antenna is considered negligible in the design process. Considering a 15 dB illumination tapering allowed over the aperture, the approximate focal distance is calculated to be 220 mm (i.e.  $f/D=0.87$ ). The phase-delay for both  $\hat{x}$  and  $\hat{y}$  polarizations and the time-delay profile are shown in Fig. 8.3. Following the design guidelines discussed in Section 8.2, a stack of two layers of asymmetric, ground-plane-backed patches is used to implement each pixel of the reflectarray. Collectively, the pixels generate the required time-delay and phase-delay profiles shown in Fig. 8.3 over the entire aperture. The pixel dimensions in this design are 6.5 mm × 6.5 mm. The dielectric substrates used in the design have dielectric constant of  $\epsilon_r = 3.4$  (Rogers RO4003C). Since the design is a multilayer structure, different layers are bonded together using a bonding material with a dielectric constant of  $\epsilon_r=3.52$  (Rogers 4450F) and thickness of 0.1 mm. The topology of each pixel is shown in Fig. 8.4. The physical parameters of the pixels populating each zone are listed in Table 8.1. Figs. 8.5(a) and 8.5(b) show the full-wave simulated frequency responses of the different pixels populating each zone of the aperture for the  $\hat{x}$  and  $\hat{y}$  polarizations, respectively. For brevity, only the responses of the pixels occupying the odd zones of the reflectarray are presented. In each graph, the ideal responses desired from each pixel are also shown. As can be seen, each pixel provides a relatively linear phase response for both orthogonal polarizations while maintaining a 90° phase difference between its response for the  $\hat{y}$  and  $\hat{x}$  polarizations. The full-wave simulated radiation patterns of the reflectarray in the  $x - z$  and  $y - z$  planes in the frequency range of 8-12 GHz are also calculated in CST Microwave Studio<sup>®</sup> and the results are presented in Fig. 8.6 for a reflectarray fed with a horn antenna whose polarization is tilted 45° with respect to the axis (the polarization of the antenna is along the unit vector  $\hat{e} = \frac{1}{\sqrt{2}}\{\hat{x} + \hat{y}\}$ ). The radiation patterns are normalized to the peak values of their corresponding co-polarized components.

---

<sup>1</sup>The aperture dimensions of the reflectarray are selected primarily for the ease of measurements. The proposed concept can be simply applied to design structures with larger apertures.

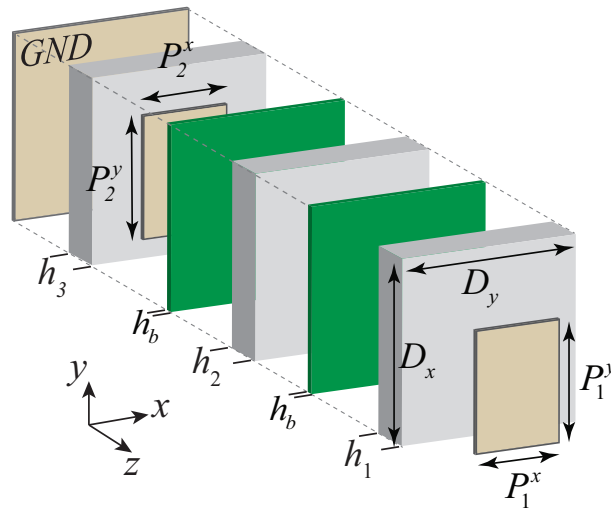


Figure 8.4 Topology of the TDUs used in the design of the prototype reflectarray discussed in Section 8.3.

Table 8.1 Physical properties of the time-delay units that populate each zone of the proposed TTD reflectarray. The unit of all the physical dimensions is *mm*. The unit cell dimensions for each time-delay unit is  $D_x = D_y = 6.5 \text{ mm}$ . The substrate thicknesses are  $h_1 = h_3 = h_5 = 1.524 \text{ mm}$  and  $h_2 = h_4 = 0.1 \text{ mm}$ . The substrates with the thickness of  $1.524 \text{ mm}$  are all Rogers RO4003C with the dielectric constant of 3.4. The  $0.1\text{-mm}$ -thick bonding layers are Rogers 4450F with the dielectric constant of 3.52.

Zone	$P_1^x$	$P_2^x$	$P_1^y$	$P_2^y$	zone	$P_1^x$	$P_2^x$	$P_1^y$	$P_2^y$
1	3.70	5.90	4.70	6.30	11	3.50	5.20	3.45	6.25
2	3.70	5.90	4.70	6.30	12	3.50	5.10	3.30	6.15
3	3.60	5.90	4.70	6.30	13	3.50	4.90	3.10	6.05
4	3.60	5.90	4.60	6.30	14	3.50	4.60	3.00	5.85
5	3.60	5.80	4.50	6.30	15	3.00	4.20	3.00	5.70
6	3.60	5.80	4.40	6.30	16	2.50	3.80	3.00	5.50
7	3.60	5.70	4.30	6.30	17	2.50	3.00	3.00	5.40
8	3.60	5.60	4.15	6.30	18	2.00	1.90	3.00	5.30
9	3.50	5.50	3.90	6.30	19	1.00	1.00	3.00	5.40
10	3.50	5.40	3.70	6.30	20	0.50	0.50	3.00	5.30

## 8.4 Experimental Results

A prototype of the proposed reflectarray was fabricated. As shown in Fig. 8.4, two substrates with thicknesses of  $h_1$  and  $h_2$  are bonded together to achieve the required separation between

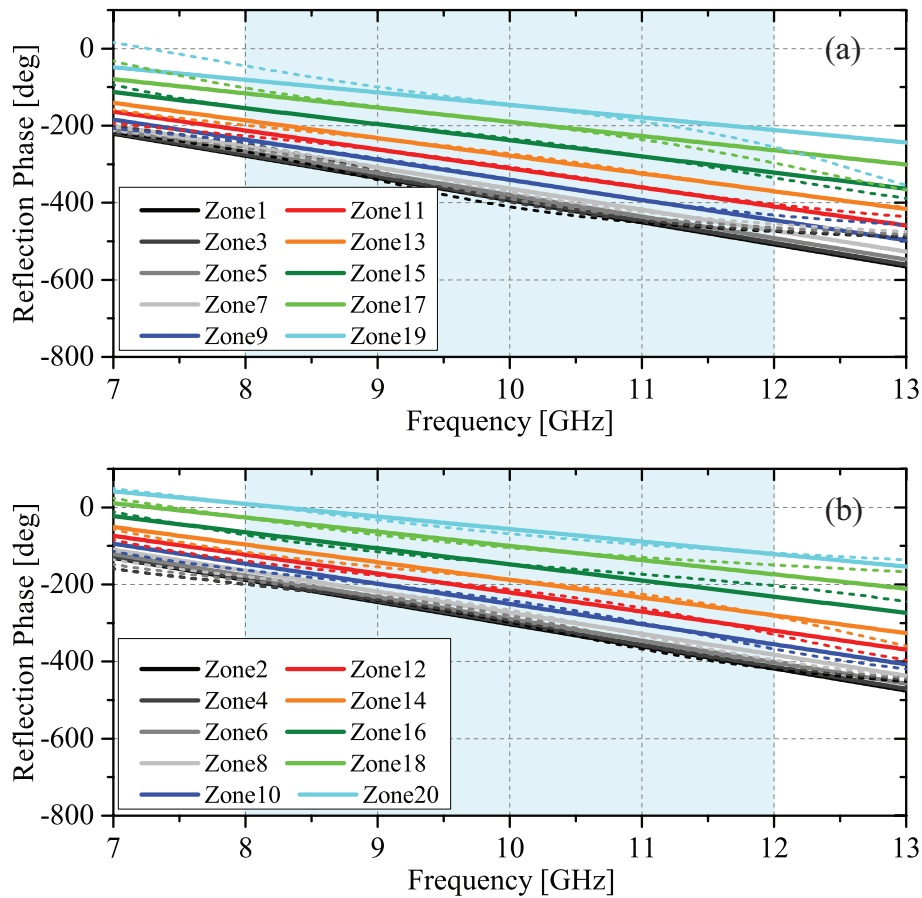


Figure 8.5 The full-wave simulated phase responses alongside the desired ideal phase responses for time-delay units populating different zones. (a) The phase responses of TDUs occupying the odd zones for  $\hat{x}$ -polarization. (b) The phase responses of TDUs occupying the odd zones for  $\hat{y}$ -polarization. Solid line: ideal phase response. Dashed line: full-wave simulated phase responses.

patches. The aperture diameter of the prototype is 235 mm and its total thickness including the bonding layers is 5.4 mm. This corresponds to  $0.18\lambda_0$  where  $\lambda_0$  is the wavelength at the center frequency of operation. Fig. 8.7(a) shows the photograph of the fabricated device. The feed was located on the optical axis of the reflectarray. The distance between the feed and the reflectarray aperture was approximately 22 cm. Radiation patterns of the antenna were measured using a multi-probe spherical near-field system. Fig. 8.6 shows the measured far-field co- and cross-polarized radiation patterns of the antenna in the  $x - z$  and  $y - z$  planes alongside the full-wave simulated results. As can be seen, the proposed reflectarray provides a focused RHCP beam with side lobe

level better than 10 dB over the entire band of operation. The measured and simulated side-lobe levels of the radiation patterns are generally above those expected from an aperture illumination of 15 dB. This is caused by the aperture blockage created by the feed antenna, which has dimensions of  $3.05\lambda_0 \times 2.62\lambda_0$ . This feed blocks the center part of the reflectarray's aperture, which has the diameter of  $8.5\lambda_0$ . The reduction of the aperture efficiency from the expected values does occur in all center-fed reflectarrays due to the feed blockage. Fig. 8.6 shows that the measured cross-polarized radiation level is at least 8 dB below that of co-polarization for all cases over the band of interest. One factor contributing to the measured cross-polarized radiation is the scattering by the relatively large feed horn placed in front of the aperture. The cross-polarization discrimination can be improved by minimizing the phase deviations of the responses of the designed TDUs from the ideal responses and possibly by using an offset feed to illuminate the aperture.

The directivity and gain of the antenna were also measured using the near-field system. The simulated and measured gain and directivity of the antenna are shown in Fig. 8.7(b). Observe that the antenna gain is 23.7 dB at the center frequency with gain variations less than 3 dB within the X-band. These variations are mainly due to the increasing of the electrical dimensions of the aperture and the decreasing of the beam width of the feed antenna as frequency increases. This is similar to the behavior of other broadband aperture antennas where the gain increases with frequency. In this regard, the behaviour of the proposed reflectarray differs from those employing narrow-band, resonant-type elements. In those structures, the gain variations are mainly determined by the narrow-band nature of the beam collimation. The difference between the gain and the directivity is primarily due to the Ohmic and dielectric losses.

If the reflectarray is fed with multiple feed antennas, it can potentially be used as a multi-beam antenna. To examine this, the radiation patterns of the reflectarray are also measured when the feed horn is placed off of the optical axis of the reflectarray and illuminates it with an oblique incidence angle. Fig. 8.8(a) shows the co-polarized gain patterns (RHCP) of the reflectarray antenna at the center frequency with four feeds placed on the focal arc illuminating its aperture off axis under incident angles of  $0^\circ$ ,  $15^\circ$ ,  $30^\circ$ , and  $45^\circ$  in the  $x - z$  plane. Fig. 8.8(b) shows the axial ratios of the antenna for these four different feeding arrangements. Observe that the antenna demonstrates

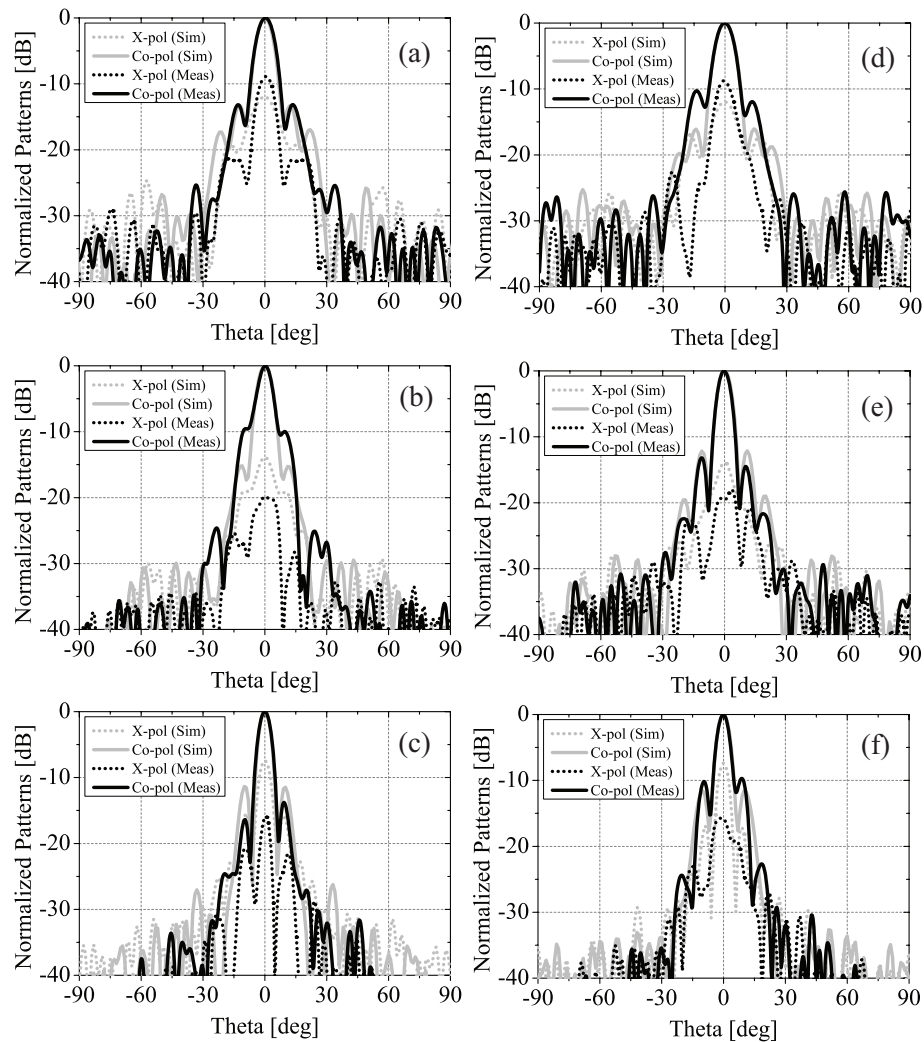


Figure 8.6 Full-wave simulated and measured normalized radiation patterns of the prototype discussed in Section 8.3 at (a), (d) 8 GHz, (b), (e) 10 GHz, and (c), (f) 12 GHz in both (a)-(c)  $x - z$ - and (d)-(f)  $y - z$ -planes. The full-wave simulated results were obtained using CST Microwave Studio and the experiments were carried out using a multiprobe spherical near-field system.

a very good scanning performance for incidence angles in the range of  $\pm 30^\circ$ . At  $45^\circ$ , the antenna shows an axial ratio below 1.5 across the entire X-band. However, its radiation pattern starts to deteriorate. This is mostly due to the variations of the amplitude illumination tapering over the aperture as well as the spillover losses. Nevertheless, in all these cases, the antenna demonstrates

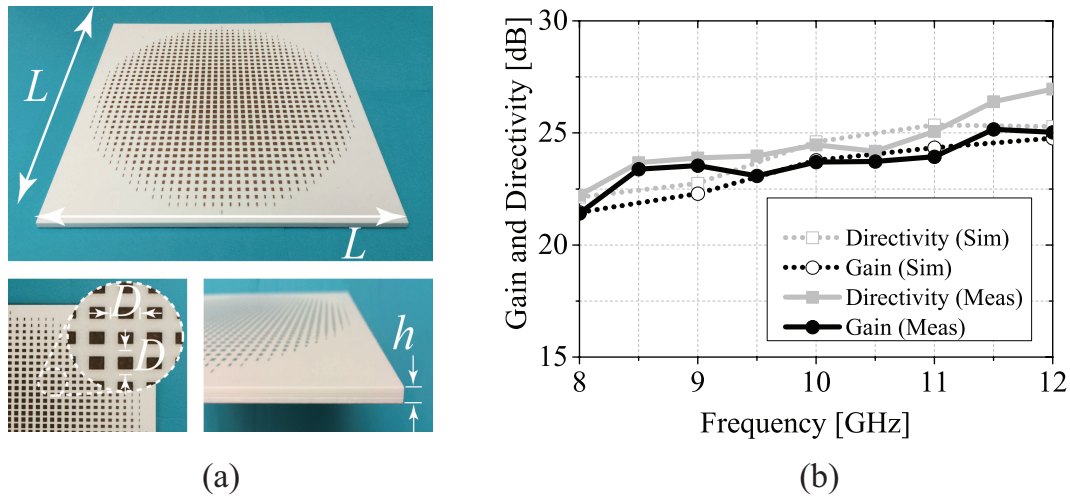


Figure 8.7 (a) Photograph of the fabricated reflectarray prototype. In this prototype,  $L = 253.5$  mm,  $h = 4.8$  mm, and  $D = 6.5$  mm. (b) Full-wave simulated and measured directivity and realized gain of the prototype discussed in Section 8.3 and shown in Fig. 8.7(a).

an axial ratio better than 2 over most of the operating band and the radiation pattern of the antenna remains stable without any beam squinting. This is due to the TTD nature of the reflectarray.

As can be seen in Fig. 8.5, the phase responses of the time-delay units occupying the reflectarray aperture shows some minor nonlinearity especially at the band edges. These nonlinearities can potentially cause distortions in the antenna response. To quantify the impact of these, a number of time-domain experiments were carried out in which the fidelity factor of the reflectarray was characterized for pulsed excitations with different fractional bandwidths. The fidelity factor is a measure of the correlation between the time-domain incident and reflected pulses from the reflectarray aperture [157, 158] and its value is unity in a distortion-less system. The fidelity factor measurements were carried out in the transmitting mode for which the transfer function of the reflectarray was measured using the multi-probe near-field system. Fig. 8.9 shows the measured fidelity factors of the reflectarray antenna for the cases where the antenna is illuminated with modulated Gaussian pulses with a center frequency of 10 GHz with different fractional bandwidths up to 6 GHz. The fidelity factor results shown in Fig. 8.9 are impacted by the response of the reflectarray itself and that of the feed antenna. Observe that a high fidelity factor close to unity is achieved when the reflectarray is illuminated with pulses with bandwidths less than 4 GHz. As expected, as

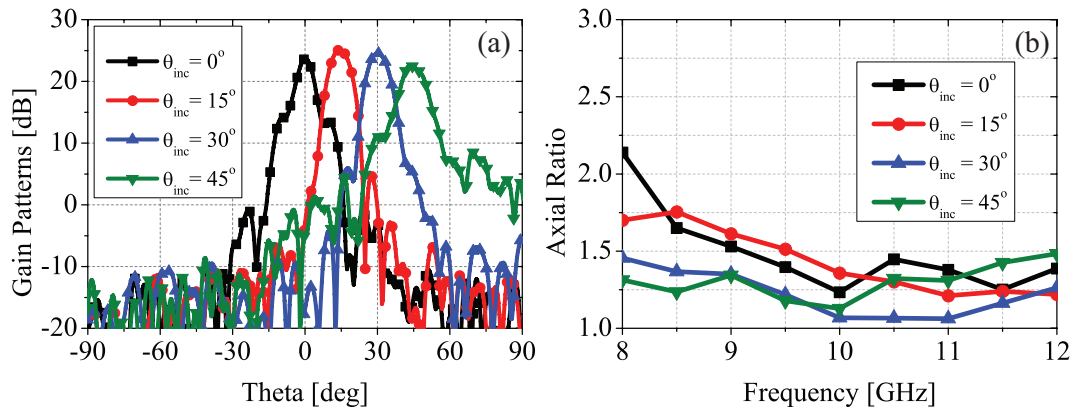


Figure 8.8 (a) Measured RHCP gain pattern of the prototype discussed in Section 8.3 at 10 GHz in the  $x - z$  plane. These patterns are measured when the feed is moved on the focal arc to illuminate the aperture off axis with angles of  $0^\circ$ ,  $15^\circ$ ,  $30^\circ$ , and  $45^\circ$ . This steers the beam toward  $0^\circ$ ,  $15^\circ$ ,  $30^\circ$ , and  $45^\circ$ , respectively. (b) Measured axial ratios of the radiated beams in all these four cases over the entire band of operation.

the fractional bandwidth of the incident pulse increases, the fidelity factor decreases. This is in part due to the nonlinearity of the phase responses of the time-delay units at the band edges. Another factor contributing to this is the frequency dispersion of the response of the standard horn antenna used to feed the reflectarray. Nevertheless, a relatively high fidelity factors ( $\geq 0.91$ ) is achieved when the bandwidth of the illuminating pulses are less than or equal to the operational bandwidth of the reflectarray. This indicates that the proposed reflectarray does not significantly impact the temporal characteristics of the incident pulse and confirms its TTD behavior.

## 8.5 Conclusions

A broadband true-time-delay circularly-polarized reflectarray antenna was presented. The antenna is composed of a low-profile MEFSS-based reflectarray fed with a linearly-polarized horn antenna. The constituting elements of the reflectarray are unit cells of anisotropic, low-pass, ground-plane backed MEFSSs. Within the desired frequency band of operation, these structures provide linear phase responses with different slopes to achieve the desired time-delay profiles over the aperture of the reflectarray. Moreover, each pixel provides a  $90^\circ$  phase difference between the reflection phase of the two different polarizations. A prototype of the proposed TTD MEFSS-based

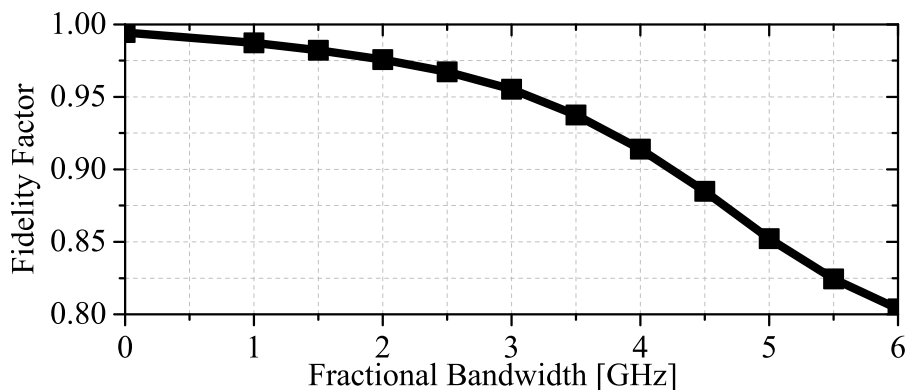


Figure 8.9 Measured fidelity factor of the prototype discussed in Section 8.3 when the antenna transmits modulated Gaussian pulses with a center frequency of 10 GHz and the fractional bandwidths up to 6 GHz.

circularly-polarized reflectarray was fabricated and experimentally characterized. The fabricated prototype was designed to operate within the X-band and it was experimentally demonstrated to be capable of providing a wideband, true-time-delay equivalent operation over a 40% bandwidth. The offset-fed version of the fabricated prototype were demonstrated to be capable of providing off-axis RHCP beams with directions of maximum radiation ranging up to  $45^\circ$  off the main axis. The TTD nature of the reflectarray was demonstrated by measuring its fidelity factor for broadband pulsed excitations. It was demonstrated that, when the reflectarray antenna was fed with a rectangular horn, the device shows fidelity factors greater than 0.91 for pulses with bandwidths as high as 40%.

## Chapter 9

# Exploiting Mechanical Flexure as a Means of Tuning the Responses of Large-Scale Periodic Structures

### 9.1 Introduction

Periodic structures are used in a wide range of applications spanning the microwave and millimeter-wave to THz and optical bands of the spectrum. With the emergence of the field of metamaterials in recent years, the number of applications of such structures has skyrocketed. At RF/microwave frequencies, some of the applications of periodic structures include the design of frequency selective surfaces [2, 8], radar absorbers [91, 92], artificial magnetic conductors [11, 12], metamaterials [9, 172], microwave lenses [13–15, 100], and reflectarray antennas [16, 101]. With the ever-growing development and deployment of multifunctional systems, the need for designing periodic structures with agile frequency responses is also growing.

To date, significant research has been devoted to developing periodic structures with dynamically reconfigurable responses. The most common approach used in the design of a reconfigurable periodic structure is to incorporate electronically-tunable elements into its unit cells [78–82]. Examples of this approach include using solid state or micro-electro-mechanical system switches [78, 79] and varactors [80–82] to switch or tune the response of the structure. This approach, however, suffers from several challenges. First, each of the unit cells of the structure must be loaded with at least one switch or varactor (two if polarization independence is needed in planar structures) that must be biased. Since even a medium-sized periodic structure may have tens of thousands of unit cells<sup>1</sup>, integration of so many switches or varactors with the structure presents a significant

---

<sup>1</sup>e.g. Consider an FSS operating at 10 GHz with an aperture of 1 m × 1 m and a period of 5 mm (see [80] for example). In this panel size 40,000 unit cells are present.

challenge. Moreover, these elements need to be biased. Also, depending on the design technique, they may need to have integrated RF/DC isolation which presents an additional level of difficulty into the design of large-scale periodic structures. Finally, the nonlinearity of varactors limits the power handling capability of varactor-tunable periodic structures [89]. In addition to electronic tuning, other techniques used to tune the responses of periodic structures have included using ferroelectric dielectrics [83], magnetically controlled materials [84], liquid crystals [85], optically controlled materials [86], and fluidic tuning techniques [89, 90]. While these techniques have certain advantages that make them interesting for particular applications, they are not as widely studied as electronic tuning techniques. Consequently, more research and development is needed to determine whether or not they can be suitable to design large-scale tunable periodic structures.

One way to overcome the aforementioned challenges of using electronically-tunable periodic structures is to use mechanical reconfiguration. Using mechanical reconfiguration in periodic structures has been examined before [173–178]. For instance, frequency tuning of coupled splitting resonators (SRRs) is obtained by changing the near-field coupling using in-plane displacement of layers [173, 174] and folding of the surface in a corrugated fashion [175]. In addition, stretching or folding in an origami fashion of a periodic arrangement of conducting cross-shaped elements have been also studied in [176, 177]. In [178], tuning is achieved in stacked ring resonators by mechanically adjusting the spacing between elements using spring-like spacers. While the earlier works conducted in this area demonstrate the possibility of using mechanical techniques to tune the responses of periodic structures, they tend to focus on specific types periodic structures that often use complex resonant-type unit cells (e.g. see [173–175]). Consequently, the findings reported in one study may not necessarily be applicable to the design of a different mechanically-tunable structure.

In this chapter, we first examine how three different mechanical techniques can be used to tune the responses of two elementary types of periodic structures with non-resonant capacitive or inductive response types. These techniques include overlapping combined with relative movement, stretching/compression, and flexure. The importance of the elementary capacitive and inductive structures examined here is that they are the fundamental building blocks of a wide range

of other different periodic structures with more complex unit cells and response types. For example, by combining these inductive and capacitive surface impedances in single- or multi-layer periodic structures, devices with more complex response types and functions such as FSSs [2, 8], lenses [13–15, 100], and reflectarrays [16, 101] can be obtained. Therefore, understanding how the inductance or capacitance of these elementary structures change when mechanical deformation is introduced into the picture is critical in understanding how different periodic structures with more complicated unit cells behave under the same conditions. Towards that end, in Section 9.2, we study how mechanical techniques can be used to tune the responses of these elementary periodic structures to obtain variable inductance and capacitance values. For each case examined in this section, we derive analytic expressions for calculating the effective inductance or capacitance of the structure under the specific mechanical deformations considered. The accuracy of these closed-form formulas is verified through full-wave EM simulations. In Section 9.3, we demonstrate the application of the findings of Section 9.2 in understanding the behavior of mechanically-tunable periodic structures with more complicated unit cells. Specifically, we examine the operation of a mechanically-tunable frequency selective surface whose unit cells are composed of the series combination of the inductive and capacitive structures presented in Section 9.2. We demonstrate that the change in frequency response of this structure under contraction and expansion conditions can be predicted using the theoretical studies presented in Section 9.2. In Section 9.4, we discuss the fabrication and experimental characterization of a prototype of this mechanically-tunable FSS. The simulation and measurement results presented in Sections 9.3 and 9.4 demonstrate the validity of the proposed concepts and verify the efficiency of the analytical methods developed. Finally, in Section 9.5, we discuss a number of practical issues and challenges that must be overcome before such mechanically-tunable periodic structure can be used in practical applications.

## **9.2 Mechanically-Tunable Periodic Structures with Inductive or Capacitive Responses**

To demonstrate the concepts proposed in this chapter, we start with a simple one-dimensional periodic structure composed of long metallic strips arranged in one dimension as shown in Fig. 9.1.

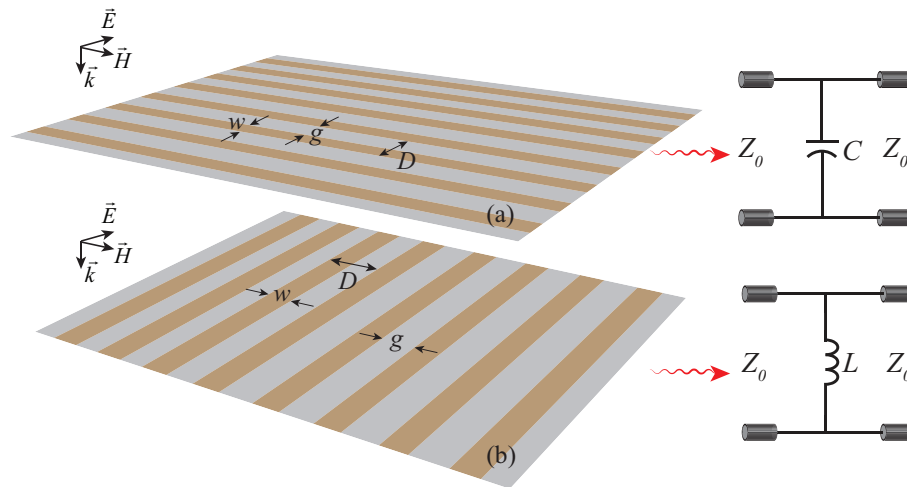


Figure 9.1 Topology of a periodic arrangement of metallic strips. (a) If the incident electric field is perpendicular to the strips, the plane wave creates positive and negative charges on the edges of adjacent strips, which produces a capacitive effect. (b) If the electric field is parallel to the strips, the structure acts as a reactive impedance surface with inductive impedance. The metallic pattern and the substrate are shown in brown and gray, respectively.

These one-dimensional periodic structures present capacitive or inductive surface impedances to a plane wave depending on the polarization of the incident electromagnetic (EM) wave. If the polarization of the incident wave is aligned with the strips, the surface transmits high-frequency content and reflects the lower frequencies. Therefore, such a structure acts as an inductive impedance surface. On the other hand, if the incident electric field is perpendicular to the strips, the surface has a capacitive response and acts as a low-pass filter. These two reactive surfaces are the fundamental building blocks of a number of other periodic structures with more complex functionalities and response types. Examples include microwave lenses [13–15, 100], reflectarrays [16, 101], and miniaturized-element frequency selective surfaces [20–27, 97, 98, 102, 114, 115, 119]. Therefore, understanding how the responses of the elementary structures shown in Fig. 9.1 change in response to mechanical deformations is critical for designing more complex tunable devices that use a combination of these inductive or capacitive structures in single- or multi-layer periodic structures.

The frequency response of an inductive or capacitive impedance surface is a function of its geometrical parameters as well as the material parameters of the substrate it is implemented on. The approximate analytic solutions for the reactance value of these surfaces have been reported in

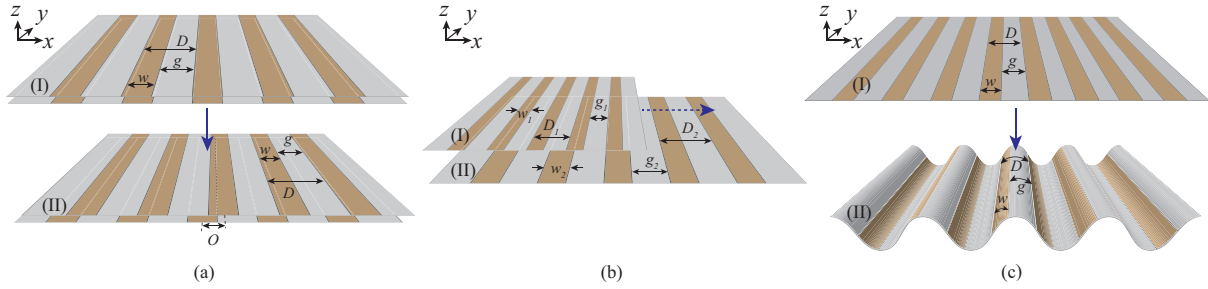


Figure 9.2 Illustration of the three concepts of (a) overlapping along with relative movement, (b) stretching and contraction, and (c) deforming used to mechanically tune the frequency responses of reactive impedance sheets shown in Fig.9.1. The metallic pattern and substrates are respectively shown in brown and gray.

the literature. The effective capacitance of the periodic arrangement of capacitive strips shown in Fig. 9.1(a) can be calculated using the following formula [179]:

$$C = \varepsilon_0 \varepsilon_{r,eff} \frac{2D}{\pi} \ln \left( \csc \left( \frac{\pi g}{2D} \right) \right). \quad (9.1)$$

Here,  $D$  is the unit cell size,  $g$  is the gap between adjacent capacitive strips,  $\varepsilon_0$  is the free-space permittivity, and  $\varepsilon_{r,eff}$  represents the effective permittivity of the medium surrounding the capacitive strips. The effective inductance of the periodic arrangement of inductive strips, shown in Fig. 9.1(b), can be approximated using the following formula [179]:

$$L = \mu_0 \mu_{r,eff} \frac{D}{2\pi} \ln \left( \csc \left( \frac{\pi w}{2D} \right) \right) \quad (9.2)$$

where  $D$  is the period of the structure,  $w$  is the strip width,  $\mu_0$  is the free-space permeability, and  $\mu_{r,eff}$  is the effective permeability of the medium surrounding the inductive strips. Details of the derivation and proof of the validity of (9.1) and (9.2) are presented in [179]. These expressions confirm that the impedance of a capacitive or inductive layer can be changed by changing the physical dimensions of the structure's features or by dynamically changing the effective dielectric constant or permeability of the medium surrounding it. The focus in this chapter is on the first technique. According to (9.1)-(9.2), the reactance of the surfaces can be varied by changing the unit cell dimensions  $D$  or the ratio of the width of the metallic strips to the unit cell dimensions  $w/D$ . Based on these parameters, different techniques to tune the frequency response of the impedance surfaces

can be envisioned. To do so, three concepts are proposed in this chapter: overlapping combined with relative movement, stretching/contraction, and deforming. These concepts are illustrated in Fig. 9.2.

### 9.2.1 Overlapping and Relative Movement of Layers

Fig. 9.2(a) shows a three-dimensional view of two cascaded layers of periodic metallic strips separated by a very thin substrate. This arrangement functions like a single reactive layer with a tunable effective reactance value. There are different parameters controlling the effective reactance of this structure. These include the widths of the metallic strips ( $w$ ), the gap sizes ( $g$ ), the thickness and the dielectric constant of the separating substrate, and the offset overlap between two cascaded reactive surfaces ( $O$ ). Here, we propose that the offset overlap can be used as the tuning parameter. This requires one of the reactive surfaces to have the ability to move with respect to the other. The maximum movement in this case is half of the unit cell dimension (i.e.,  $D/2$ ). To demonstrate the effect of offset overlapping, we examined a periodic structure composed of two layers sharing the metallic strip width  $w = 2$  mm, the strip separation  $g = 3$  mm, and the unit cell size  $D = 5$  mm. Both layers were assumed to be in free space ( $\epsilon_{r,eff} = 1$ ) and the spacing between layers was  $h = 0.1$  mm. As shown in Fig. 9.2(a), the overlap was modeled with an offset vector,  $O$ , connecting the centers of two strips within each unit cell of the structure together. To compute the effective inductance and capacitance, the transmission coefficient of the structure for a normally-incident wave was calculated for two orthogonal polarizations using full-wave simulations in CST Studio<sup>®</sup>. The electric field is oriented along the  $\hat{x}$ - and  $\hat{y}$ -directions for the capacitive and inductive cases, respectively. Figs. 9.3(a) and 9.3(c) show the full-wave simulation results obtained for both cases. Subsequently, the full-wave simulation results were matched to the frequency responses of the simplified equivalent circuit models of the structures, shown in the inset of Fig. 9.1, and the effective inductance and capacitance of each surface was extracted. Figs. 9.3(b) and 9.3(d) display the ratios of  $L_{eff}/L_0$  and  $C_{eff}/C_0$  versus the offset dimension,  $O$ , where  $L_0$  and  $C_0$  are the inductance and capacitance values when two strips are aligned, i.e.  $O = 0$  mm. Fig. 9.3(b) shows that increasing the offset  $O$  decreases the effective inductance. Therefore, the maximum

inductance happens when the two layers are aligned with each other. For the case where the electric field is oriented in  $\hat{x}$ -direction, increasing the length of the offset  $O$  increases the effective capacitance. It means that the minimum value of the capacitance corresponds to the case where the two strips are aligned. In this case, the maximum value of capacitance happens when the offset is maximum.

To better understand the impact of the offset overlap, approximate analytical formulas are developed to determine the effective inductance and capacitance as a function of offset value. Because of the very thin substrate between the two layers, this two-layer structure can be approximated as a single periodic layer of metallic strips where the widths of the strips are variable and dependent on the offset. Replacing  $w$  with  $w + O$  in (9.1) and (9.2), the effective inductance and capacitance values can be approximated using the following formulas:

$$L_{eff} = \mu_0 \mu_{r,eff} \frac{D}{2\pi} \ln \left( \csc \left( \frac{\pi(w + O)}{2D} \right) \right) \quad (9.3)$$

$$C_{eff} = \epsilon_0 \epsilon_{r,eff} \frac{2D}{\pi} \ln \left( \csc \left( \frac{\pi(D - w - O)}{2D} \right) \right) \quad (9.4)$$

Fig. 9.3(b) and 9.3(d) show the inductance and capacitance values calculated using these formulas and compare the results with the reactance values extracted from full-wave simulations. As can be seen, (9.3) and (9.4) can be used to accurately predict the effective inductance and capacitance of the two periodic structures. In a practical application, one can envision that the two layers can be fabricated on two separate substrates where one of the substrates can be mechanically moved by small distances. Specifically, the maximum useful linear movement of one layer with respect to the other layer is half of the unit cell dimension ( $D/2$ ). Therefore, the tuning speed is determined by how fast this movement can be accomplished. Some implementation challenges that may arise in using this technique in practice include maintaining the flatness of, the separation height between, and the alignment between the layers over a large area.

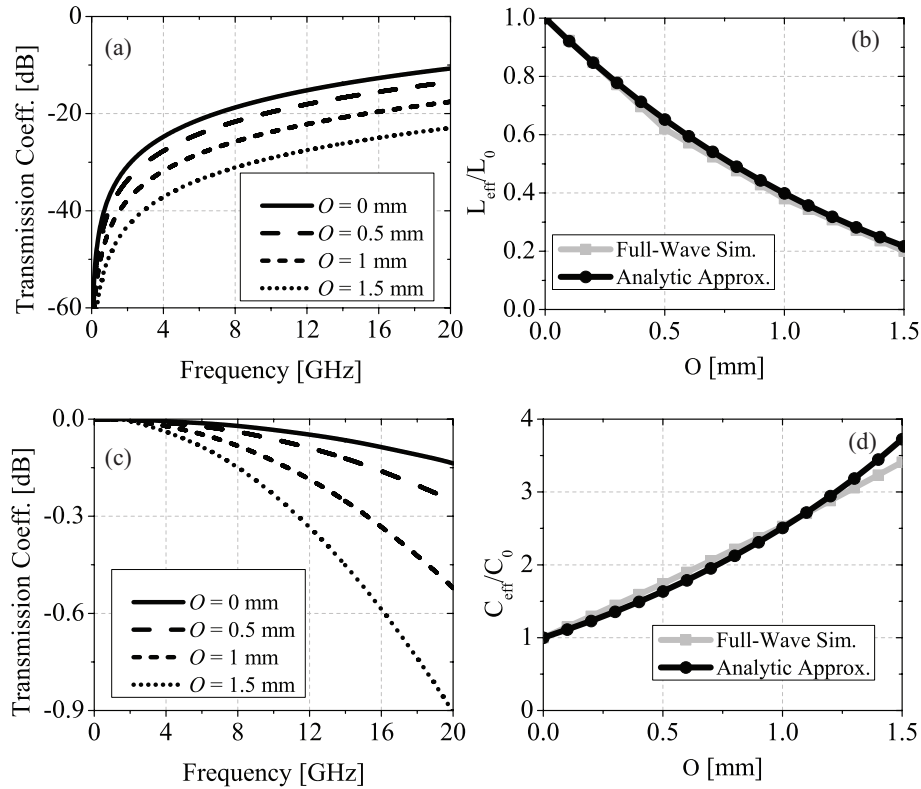


Figure 9.3 (a) Transmission coefficients of the structure shown in Fig. 9.2(a) with  $w = 2$  mm,  $g = 3$  mm, and  $h = 0.1$  mm and different overlappings once excited by a plane wave with a polarization aligned with the direction of strips. (b) Calculated effective inductance using the full-wave simulation results shown in Fig. 9.3(a) and equation (9.3).  $L_0$  refers to the effective inductance value at  $O=0$  mm. (c) Transmission coefficients of the same structure with  $w = 2$  mm and  $g = 3$  mm where the incident electric field is perpendicular to the direction of strips. (d) The effective capacitance computed using the simulated results shown in Fig. 9.3(c) alongside the calculated values using equation (9.4).  $C_0$  refers to the capacitance inductance value at  $O=0$  mm.

## 9.2.2 Stretching

Changing the dimensions of the metallic strips' widths and spacings of the structures shown in Fig. 9.1 can tune their inductance and capacitance values. However, dynamically changing such parameters in conventional metallized and patterned structures is not easily achievable since they are typically fabricated by etching metallic films on a fixed rigid substrate. With the recent progress in stretchable and flexible electronics, a number of techniques have been proposed to

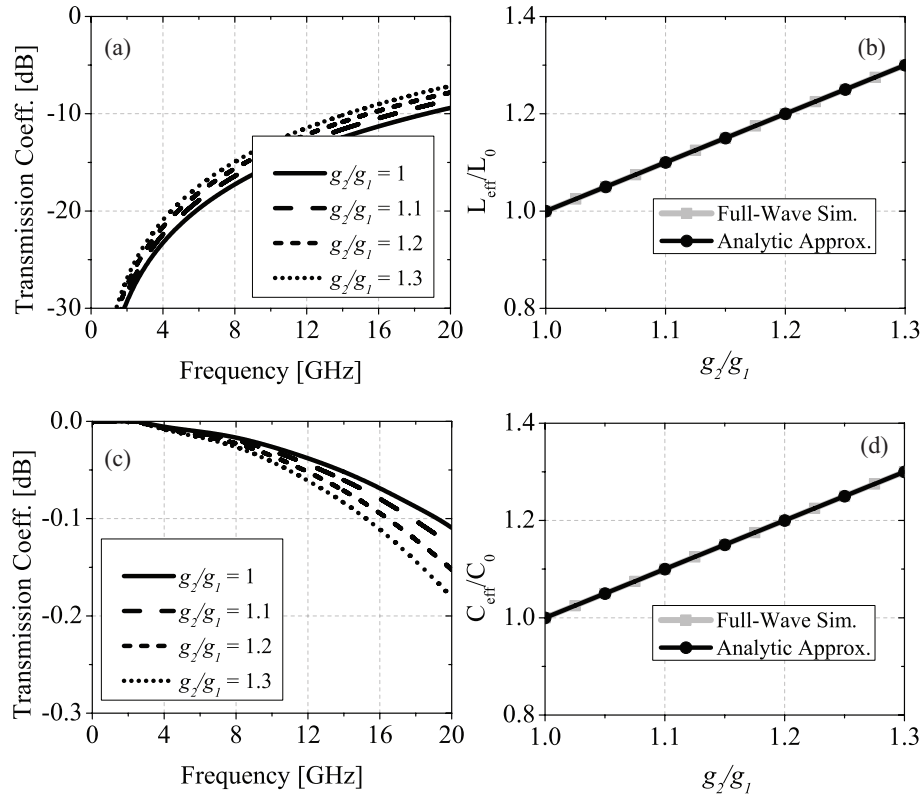


Figure 9.4 (a) Transmission coefficients of the stretched reactive surface, shown in Fig. 9.2(b) composed of inductive strips with  $w_1 = 2$  mm and  $g_1 = 3$  mm for  $g_2/g_1 = 1, 1.1, 1.2,$  and  $1.3$ . (b) The calculated effective inductance using the full-wave simulation results shown in Fig. 9.4(a) alongside the predicted value from  $L_{\text{eff}}/L_0 = g_2/g_1$ .  $L_0$  refers to the effective inductance value at  $g_2/g_1=1$ . (c) Transmission coefficients of the stretched impedance sheet, shown in Fig. 9.2(b) composed of capacitive strips with  $w_1 = 2$  mm and  $g_1 = 3$  mm for  $g_2/g_1 = 1, 1.1, 1.2,$  and  $1.3$ . (d) The effective capacitance computed using the simulated results shown in Fig. 9.4(c) alongside the calculated values using  $C_{\text{eff}}/C_0 = g_2/g_1$ .  $C_0$  refers to the effective capacitance value at  $g_2/g_1=1$ .

design stretchable reconfigurable devices [180]- [181]. For example, in [180] a fluidic dipole antenna obtained by injecting liquid metal into an elastomeric microfluidic channel is proposed. This antenna is mechanically stretchable and this property was used to tune its response over a relatively broad frequency range. In [181], stretchable electronics, circuits, and antennas consisting of fractal-shaped metallic patterns and interconnects fabricated on elastomeric substrates are proposed. The aforementioned techniques can also be used to design periodic structures with tunable frequency responses. Fig. 9.2(b) shows a periodic arrangement of metallic strips on a stretchable substrate. A driving external force in the direction perpendicular to and in the plane of the strips

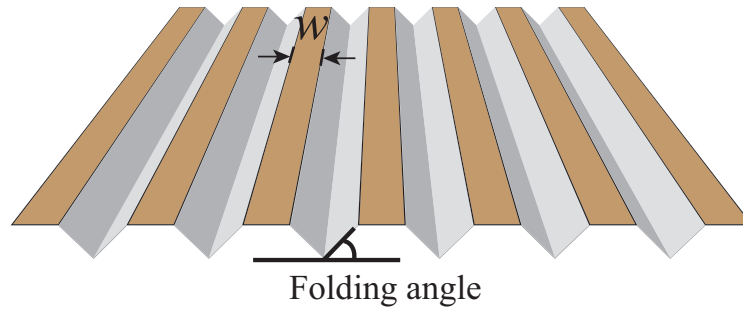


Figure 9.5 A method for emulating stretching in the periodic structures shown in Fig. 9.1. This method does not rely on stretching of an elastic substrate to change the  $w/D$  ratio.

can change the unit cell dimensions while the  $w/D$  ratio is fixed assuming that the substrate and metallic strips are stretched at an equal rate. (9.1)-(9.2) confirm that these variations change the reactances of the surfaces. To demonstrate this effect, a case study for a periodic arrangement of metallic strips with the width of  $w_1 = 2$  mm and the gap spacing of  $g_1 = 3$  mm was conducted.  $w_2$  and  $g_2$  show the strip width and gap spacing after exerting the force. For simplicity to prove the the concept, the substrate was assumed to be extremely thin having a low dielectric constant. Therefore, the effective dielectric constant of the substrate was assumed to be 1. Similar to the case study for the overlapping technique, the transmission coefficients of the structure for a normally incident wave were calculated for both orthogonal polarizations. Fig. 9.4(a) and 9.4(c) show the full-wave simulation results obtained for both cases. Based on these responses, the effective inductance and capacitance were calculated as a function of  $g_2/g_1$  and are shown in Figs. 9.4(b) and 9.4(d). As expected, the values of inductance and capacitance increase as the structure is stretched. This behavior can be explained by examining (9.1) and (9.2). As described for both cases, after exerting the force, the  $w/D$  ratio was assumed to remain constant while the unit cell dimension,  $D$ , changed. Therefore, the effective values of inductance and capacitance, which are directly proportional to the unit cell dimensions, increased. The predicted values using  $L_{eff}/L_0 = g_2/g_1$  and  $C_{eff}/C_0 = g_2/g_1$  are also shown in Figs. 9.4(b) and 9.4(d).

In practical implementation, the effective substrate thickness will also change due to the stretching and contraction. This variation depends on the stretching displacement. This is generally small compared to the unit cell dimensions. Thus, the impact of this variation on the structure's response

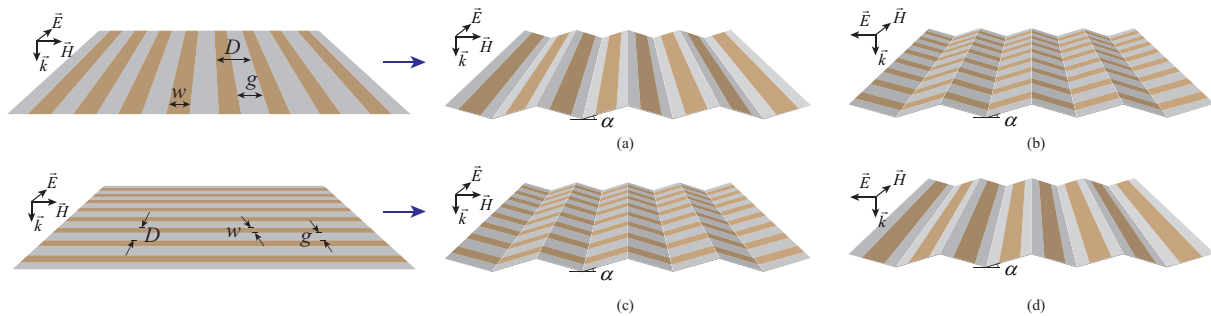


Figure 9.6 Different cases for folding an impedance sheet composed of parallel metallic strips in an accordion-like fashion. Case (a): The incident electric field is along the direction of strips (inductive) and folding is parallel to the metallic strips. Case (b): The incident electric field is along the direction of strips (inductive) but the surface is folded perpendicular to the strips. Case (c): The incident electric field and the folds are both perpendicular to the direction of strips. Case (d): The incident electric field is perpendicular to the direction of the strips (capacitive) and the folds are parallel to the metallic strips. The metallic pattern and the substrate are shown in brown and gray, respectively.  $\alpha$  is the folding angle.

is not expected to be significant. This is particularly the case for single-layer structures as the response is primarily determined by the physical dimensions of the elements. Fig. 9.5 shows a technique for emulating a stretchable version of the structures shown in Fig. 9.1. In this case, the substrate on which the inductive/capacitive grids are fabricated is folded in parallel and between each two strips. This way, by compressing or expanding the structure, the unit cell dimensions of the periodic structure change. This technique can be used to emulate the stretching concept shown in Fig. 9.2(b) without the need to use stretchable or elastic dielectric substrates. Using this technique may also alleviate some of the practical implementation concerns discussed earlier in this paragraph.

### 9.2.3 Mechanical Flexure

An alternative technique for dynamically tuning the frequency response of the reactive surfaces is shown in Fig. 9.2(c). This technique is based on deforming the surface in such a way that the effective dimensions of the unit cells can be changed without needing to stretch the substrate. Let's assume that a plane wave polarized in the  $\hat{y}$  direction is incident on the structure shown in Fig. 9.2(c). When the structure is deformed from its planar version as shown in Fig. 9.2(c), the inductive

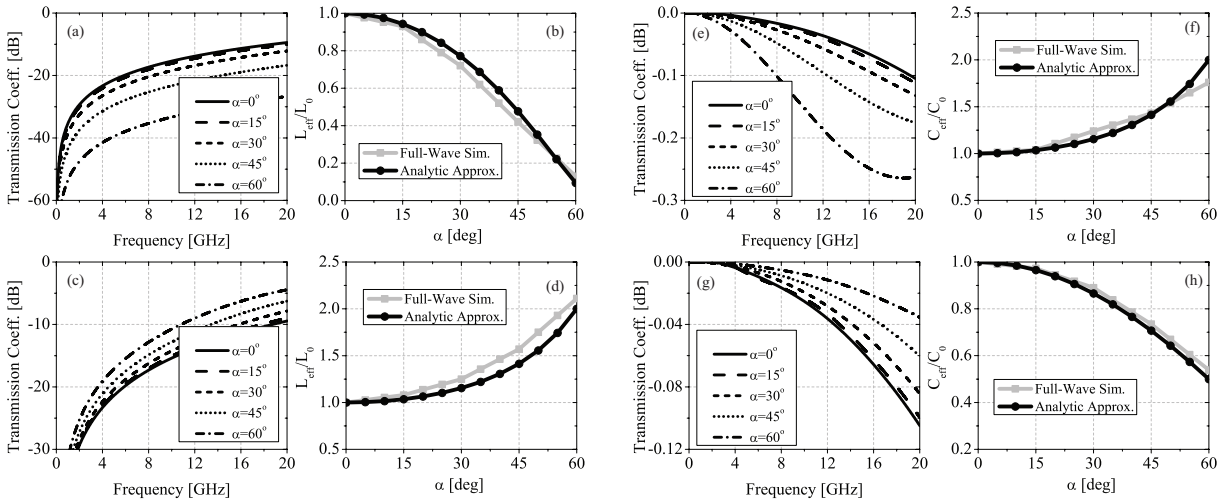


Figure 9.7 (a), (c), (e), and (g) The transmission coefficients of the structures shown in Figs. 9.6(a), 9.6(b), 9.6(c), and 9.6(d), respectively. In all cases,  $w = 2$  mm and  $g = 3$  mm. (b), (d), (f), and (h) The effective reactance values calculated using simulated results shown in Figs. 9.7(a), 9.7(b), 9.7(c), and 9.7(d), respectively. These results are also compared with the predicted values calculated from equations (9.5), (9.6), (9.7), and (9.8), respectively. In (b) and (d),  $L_0$  refers to the effective inductance value at  $\alpha = 0^\circ$ . In (f) and (h),  $C_0$  refers to the effective capacitance value at  $\alpha = 0^\circ$ .

strips are brought closer together. Intuitively, this is similar to reducing the dimensions of the unit cell without changing the width of the inductive strips. Consequently, the overall inductance of the structure should decrease as the structure is flexed. Using a similar argument, when the polarization of the incident EM wave is along the  $\hat{x}$  direction, flexing the surface will increase its capacitance.

This intuitive prediction was confirmed by conducting full-wave EM simulations for a periodic arrangement of metallic strips with the width of  $w$ . The strips were assumed to be in free space with spacing between two adjacent strips of  $g$ . To simplify the simulation and eventual fabrication of the structure, a simpler version of this flexure was investigated. Specifically, rather than sinusoidally deforming the planar structure as shown in Fig. 9.2(c), a folded, accordion-like substrate was used. The folds of this structure were identical and parallel to each other. Also, the effects of placing the folds both perpendicular and parallel to the direction of metallic strips were studied. These different cases are illustrated in Fig. 9.6.

In the first two cases of this study, we investigated an inductive structure as illustrated in Figs. 9.6(a)-(b). In both cases,  $w = 2$  mm and  $g = 3$  mm, and the polarization of the incident wave was aligned with the metallic strips. Fig. 9.7(a) shows the transmission coefficients of the inductive surface when it was folded along the direction of the strips. The distance between two adjacent folds in the flattened planar version of the structure is  $D$ , and the folding angle,  $\alpha$ , is measured from the horizontal plane. The calculated inductance value as a function of  $\alpha$  is shown in Fig. 9.7(b). The figure shows that the inductance decreases by increasing the folding angle. To explain this, consider a fixed unit area of  $1 \text{ m} \times 1 \text{ m}$  coinciding with the equi-phase plane of the incident wave. When the structure is bent as shown in Fig. 9.6(a), the number of metallic strips that occupy this area increase, or equivalently the unit cell dimension decreases while the widths of the inductive strips remain fixed. This is equivalent to placing multiple inductors in parallel, reducing the effective inductance of the overall surface. The effective inductance value for this type of folding can be approximated using the following formula:

$$L_{eff} = \mu_0 \mu_{r,eff} \frac{D}{2\pi} \ln \left( \csc \left( \frac{\pi w}{2D \cos(\alpha)} \right) \right) \quad (9.5)$$

The predicted inductance values using (9.5) are also shown in Fig. 9.7(b). It is seen that for  $\alpha$  angles between  $0^\circ - 60^\circ$ , (9.5) predicts the change of inductance reasonably well. Fig. 9.6(b) shows the situation where the inductive surface is folded perpendicularly to the direction of strips. In this case, the number of strips that occupy a reference  $1 \text{ m} \times 1 \text{ m}$  area does not change but the overall conductive path length of each strip within the reference area increases. This results in an increase of the effective inductance of the surface. Figs. 9.7(c) and 9.7(d) show the transmission coefficient and also the computed effective inductance value, respectively. The figures show that the inductance increases as the folding angle increases. Mathematically, in this case, the  $w/D$  ratio remains constant while the lengths of the strips in a fixed area increase. Therefore, the effective inductance value can be approximated using the following formula:

$$L_{eff} = \mu_0 \mu_{r,eff} \frac{D}{2\pi \cos(\alpha)} \ln \left( \csc \left( \frac{\pi w}{2D} \right) \right) \quad (9.6)$$

The predicted inductance values using (9.6) are shown alongside the full-wave simulated results in Fig. 9.7(d). Observe that (9.6) provides an acceptable approximation of the change of inductance for fold angles,  $\alpha$ , between  $0^\circ - 60^\circ$ .

Figs. 9.6(c)-(d) show these scenarios for both cases where the capacitive surface is folded along and perpendicular to the direction of the strips. For these cases, the strip widths and the gap spacings are  $w = 2$  mm and  $g = 3$  mm, respectively. Figs. 9.7(e) and 9.7(f) show the full-wave simulated transmission coefficients and the corresponding calculated effective capacitance values, respectively. The figures show that when the surface is folded perpendicularly to the direction of the strips, the capacitance value increases as the folding angle increases. The effective capacitance values can be approximated using the following formula:

$$C_{eff} = \epsilon_0 \epsilon_{r,eff} \frac{2D}{\pi \cos(\alpha)} \ln \left( \csc \left( \sin \left( \frac{\pi(D-w)}{2D} \right) \right) \right) \quad (9.7)$$

The capacitance values predicted using (9.7) are shown in Fig. 9.7(f). Fig. 9.7(g) shows the full-wave simulated transmission coefficient of the structure when the surface is folded parallel to the direction of the strips. Fig. 9.7(h) shows that the effective capacitance decreases as the folding angle increases. The analytic approximation for the effective capacitance for this case can be represented as:

$$C_{eff} = \epsilon_0 \epsilon_{r,eff} \frac{2D \cos(\alpha)}{\pi} \ln \left( \csc \left( \sin \left( \frac{\pi(D-w)}{2D} \right) \right) \right) \quad (9.8)$$

Fig. 9.7(h) shows the effective capacitance value calculated using (9.8). Table 9.1 shows the summary of this study. Observe that all types of control on the impedances of an inductive or a capacitive reactive surface can be achieved through these deformations. Potential challenges that need to be addressed before this technique can be used in commercial applications include maintaining the folding angle throughout a large panel, ensuring the repeatability of the folding process over large areas, and maintaining the material integrity and electrical connections at critical pinch points, such as folds and creases where the support structure undergoes significant strain.

Despite the practical challenges associated with the use of the techniques reported in Sections 9.2.1, 9.2.2, and 9.2.3, the results presented in these sections demonstrate the possibility of using

Table 9.1 The variations of the impedances of the inductive and capacitive metallic sheets with increasing folding angle  $\alpha$ . The sheets are composed of periodic arrangement of metallic strips where the folding is along and perpendicular to the direction of the strips. (EQC: Equivalent Circuit Model)

Impedance	Folding Type	Trans. Mag.	EQC
Inductive	Along $\vec{E}$	$\searrow$	$L \searrow$
Inductive	Perp. to $\vec{E}$	$\nearrow$	$L \nearrow$
Capacitive	Along $\vec{E}$	$\searrow$	$C \nearrow$
Capacitive	Perp. to $\vec{E}$	$\nearrow$	$C \searrow$

mechanical techniques to design periodic structures with tunable inductance or capacitance values. These results and equations (9.1)-(9.8) can be used to design or analyze other mechanically-tunable periodic structures that use a combination of these inductive and capacitive building blocks to obtain more complicated unit cells and more elaborate functionalities. For example, by combining these inductive and capacitive structures in single- or multi-layer structures frequency selective surfaces [8], microwave lenses [13], or reflectarrays [101] may be obtained. In the subsequent sections, we will demonstrate this in practice by examining a mechanically tunable FSS, which is obtained by combining the inductive and capacitive structures examined in this section in a single-layer periodic structure. The FSS demonstrates a bandstop response that can be mechanically tuned over a relatively wide frequency band. We show that the behavior of this tunable FSS can be understood by examining how the responses of its inductive or capacitive constituting elements change as a function of mechanical flexure and present simulation and measurement results of a fabricated prototype. We emphasize that the specific example presented in Sections 9.3 and 9.4 is meant to be an illustrative example demonstrating how the findings presented in Section 9.2 can be used to analyze more complex structures. A similar analysis can be used to design or analyze a variety of other structures that use the same inductive and capacitive building blocks.

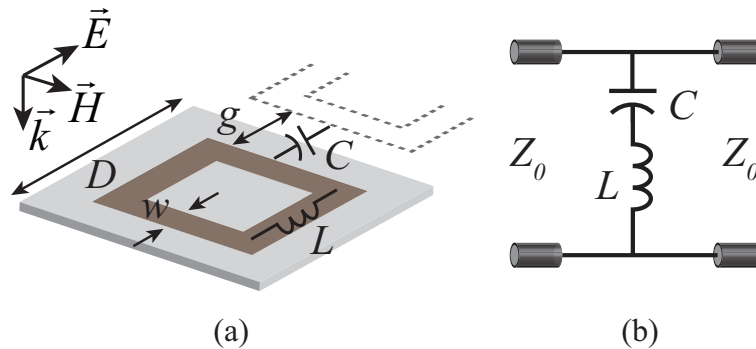


Figure 9.8 (a) The unit cell of a bandstop frequency selective surface formed by combining the inductive and capacitive strips discussed in Section 9.2 in series on a single layer. (b) The equivalent-circuit model of the structure shown in part (a).

### 9.3 Design Example

To demonstrate the application of the tunable inductive and capacitive structures discussed in Section 9.2 in designing more complex devices, we examine a surface consisting of a periodic arrangement of metallic square loops. The unit cell of this structure is shown in Fig. 9.8(a). This unit cell is obtained by combining the inductive and capacitive strips discussed in Section 9.2 in a single layer. The sides of the loop that are parallel to the  $E$ -field of the incident wave act as inductors and the sides that are perpendicular to it form coplanar-strip capacitors with the similarly-oriented sides of the two adjacent loops. Therefore, this structure represents a series combination of inductive and capacitive surface impedances in the same layer. The equivalent circuit model of the structure is shown in Fig. 9.8(b). At the frequency where the  $L$  and  $C$  values resonate, a filter with a first-order bandstop response is obtained. As an example, a structure with strip width  $w = 1.5$  mm, strip spacing  $g = 1$  mm, and unit cell dimensions of  $15$  mm  $\times$   $15$  mm was examined. We assumed the structure was illuminated by a normally incident plane wave with the electric field polarized along the  $\hat{y}$ -direction. Also, we assumed that structure is fabricated on an accordion-like substrate where the folds were along the electric field polarization as shown in Fig. 9.9. As discussed in Section 9.2.3, contraction and expansion of the substrate causes the inductance and capacitance values of this structure (see Fig. 9.8(b)) to change. Therefore, the frequency response of this FSS can be tuned by changing the folding angle.

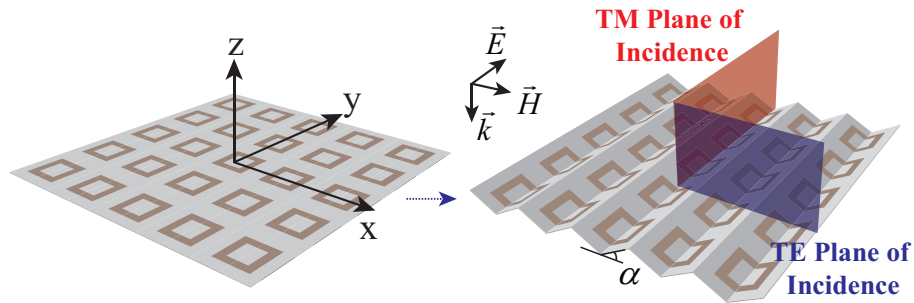


Figure 9.9 The bandstop FSS composed of metallic squares of the type shown in Fig. 9.8(a) can be folded to tune its frequency response.  $\alpha$  is the folding angle.

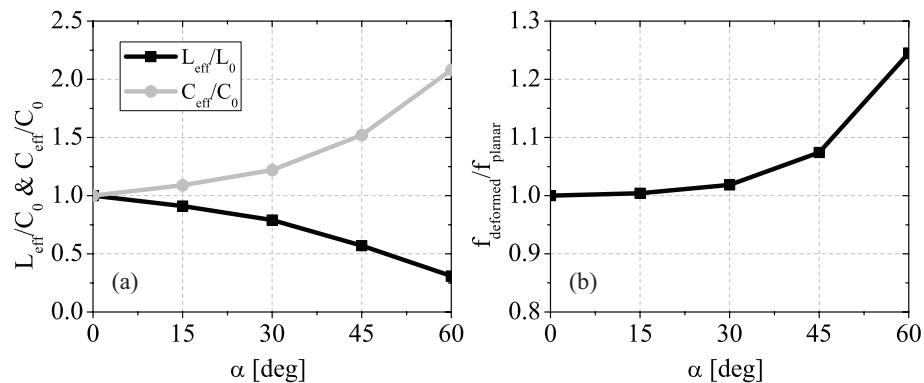


Figure 9.10 (a) Effective inductance and capacitance values of the structure shown in Fig. 9.8(a) as a function of folding angle. The results obtained using full-wave EM simulations and those predicted using equations (9.5) and (9.7) are shown. Physical dimensions of the structure are  $w = 1.5$  mm,  $g = 1$  mm, and unit cell dimensions of  $15$  mm  $\times$   $15$  mm. (b) The predicted resonant frequency of the bandstop FSS shown in Fig. 9.9 based on the calculated effective reactance values shown in Fig. 9.10(a).

To predict the frequency response tuning, the behavior of both capacitive and inductive sections of each loop should be taken into account when the structure is stretched or contracted. For this setup, the inductive strips are along the folding. Therefore, according to the results of Section 9.2.3, increasing the folding angle reduces the inductance. On the other hand, the capacitive strips are perpendicular to the folds. Thus, increasing the folding angle increases the capacitance. Similar to the procedure described in Section 9.2.3, the variation of inductance and capacitance for this particular combination of strip widths and gap spacings are calculated and shown in Fig. 9.10(a). Fig. 9.10(a) also shows the variations of inductance and capacitance predicted by the closed form

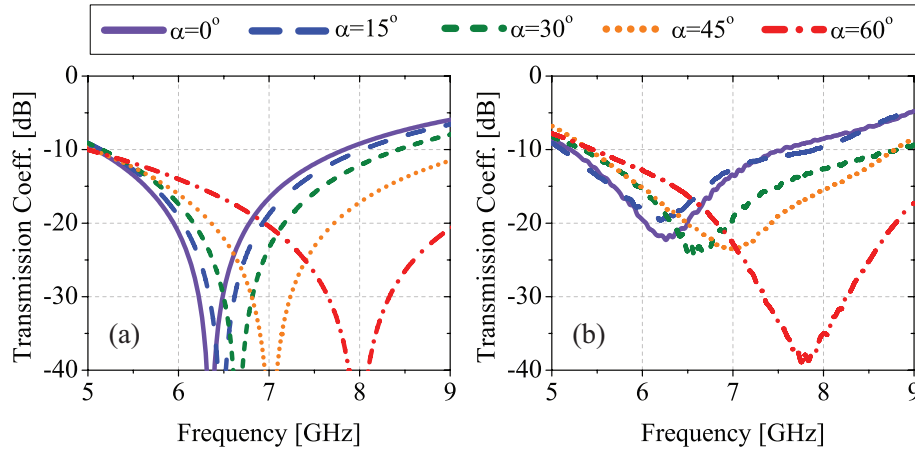


Figure 9.11 (a) Full-wave simulated and (b) measured frequency responses of the mechanically-tunable bandstop FSS prototype shown in Fig. 9.9 having folding angles of  $\alpha = 0^\circ$ ,  $15^\circ$ ,  $30^\circ$ ,  $45^\circ$ , and  $60^\circ$ .

formulas presented in Section 9.2.3. Observe that equations (9.5) and (9.7) predict the variations of the inductance and capacitances of the equivalent-circuit model shown in Fig. 9.8(b) accurately. The resonant frequency of the bandstop filter with the equivalent circuit model shown in Fig. 9.8(b), is proportional to  $\frac{1}{\sqrt{LC}}$ . Therefore, the resonant frequency of the deformed structure can be predicted using the calculated values of  $L_{eff}/L_0$  and  $C_{eff}/C_0$  shown in Fig. 9.10(a). Fig. 9.10(b) shows the predicted resonant frequency as a function of the folding angle obtained using full-wave EM simulations and the values predicted from (9.5) and (9.7). Therefore, we expect the resonant frequency to increase as the folding angle increases. Fig. 9.11(a) shows the simulated frequency responses of the structure for a normally-incident plane wave and folding angles of  $\alpha=0^\circ$ ,  $15^\circ$ ,  $30^\circ$ ,  $45^\circ$ , and  $60^\circ$ . Consistent with the predictions of the analytical methods presented in Section 9.2.3, the resonant frequency increases from 6.35 GHz to 8 GHz (or equivalently over a 23% fractional bandwidth) as the folding angle increases from  $0^\circ$  to  $60^\circ$ .

## 9.4 Experimental Verification and Measurement Results

We fabricated a prototype of the FSS analyzed in Section 9.3. The square loops were etched on strips of copper tape and attached to a 0.1 mm-thick sheet of paper which was manually folded into the accordion shape of Fig. 9.9. The prototype has panel dimensions of 180 mm  $\times$  240 mm

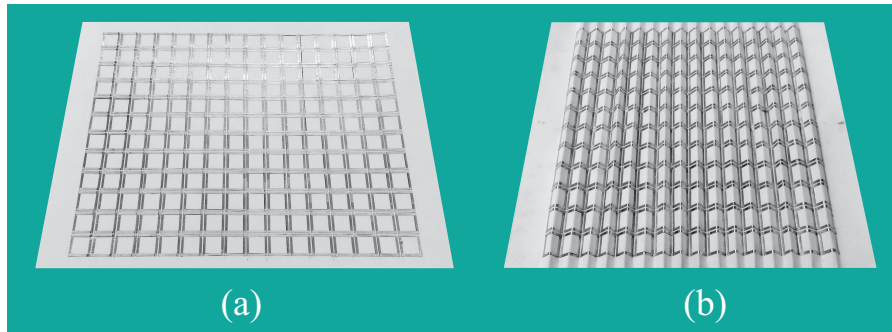


Figure 9.12 The photographs of the fabricated prototype of the mechanically-tunable bandstop FSS where the folding angle is (a)  $0^\circ$  and (b)  $45^\circ$ .

when stretched completely flat. Fig. 9.12 shows a photograph of the fabricated prototype for two folding angles of  $0^\circ$  (Fig. 9.12(a)) and  $45^\circ$  (Fig. 9.12(b)). The measurement setup consisted of a large metallic screen with a rectangular opening having the same dimensions as those of the FSS at its center. The transmitting and receiving antennas were placed on each side of the structure such that the FSS was located in the far field of each of the antennas. The large fixture was used to ensure that all transmitted waves passed through the FSS. Absorbers were also used to reduce diffractions from the surrounding environment. Additionally, range gating techniques were used to eliminate the effect of multiple reflections between transmitting and receiving antennas. The transmission coefficient in the absence of FSS was measured and used for calibration. The FSS panel was then placed in the opening of the fixture and its transmission coefficients under different conditions were measured and calibrated (using the transmission coefficient of the fixture without the presence of the FSS). The measured transmission coefficients of the FSS for the five different folding angles examined in this chapter are shown in Fig. 9.11 along with the simulated results. To maintain the folding angle of the structure during the measurement process, a styrofoam panel was used to support the structure. Each of the bottom corners of the folded structure was attached to the styrofoam panel. During the measurement, the placement of these attached corners were adjusted to maintain the folding angle at the desired angle. The measured resonant frequencies agree well with the simulation predictions, typically within 4%. These results confirm the feasibility of using the proposed mechanical technique to dynamically tune the response of a large-scale periodic

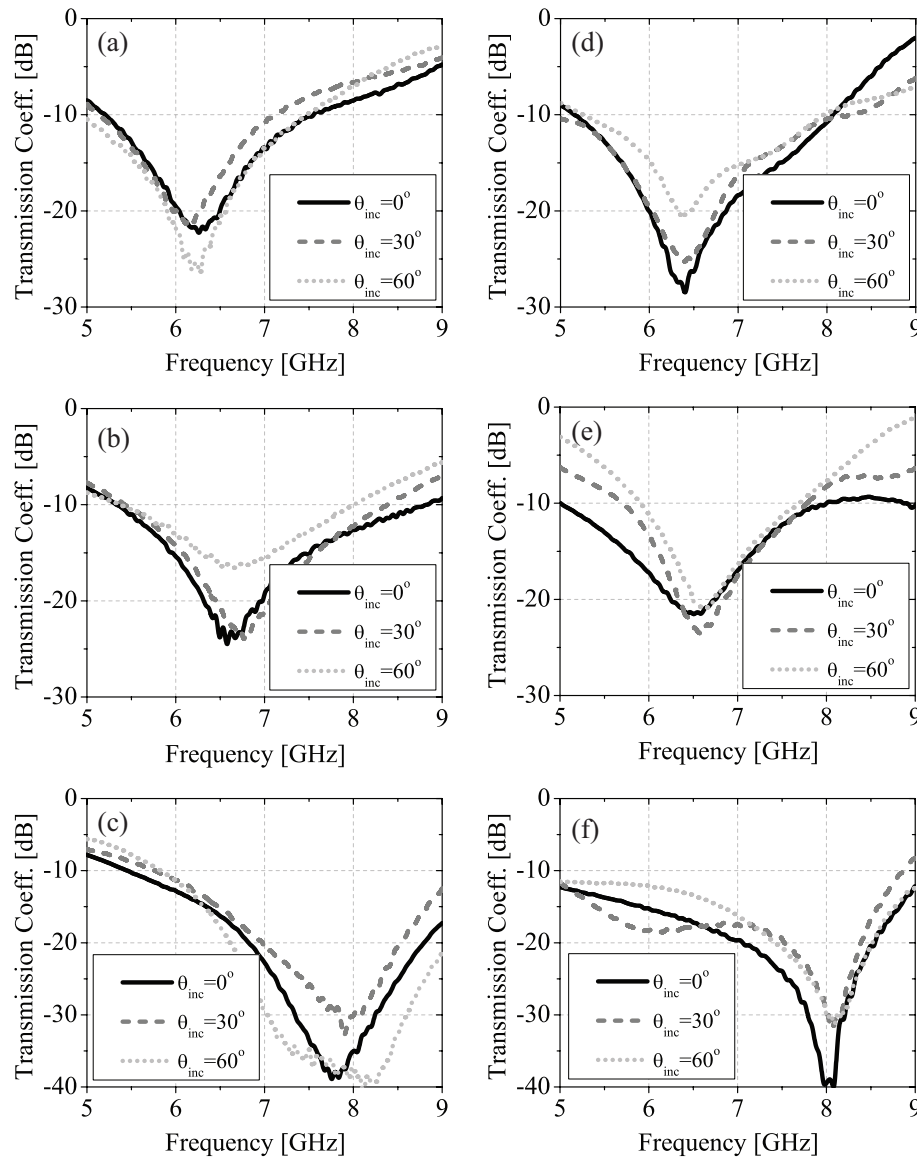


Figure 9.13 Measured transmission coefficients of the fabricated prototype shown in Fig. 9.12 with three folding angles of  $0^\circ$ ,  $30^\circ$ , and  $60^\circ$ . (a) Polarization: TE,  $\alpha = 0^\circ$ , (b) Polarization: TE,  $\alpha = 30^\circ$ , (c) Polarization: TE,  $\alpha = 60^\circ$ , (d) Polarization: TM,  $\alpha = 0^\circ$ , (e) Polarization: TM,  $\alpha = 30^\circ$ , and (f) Polarization: TM,  $\alpha = 60^\circ$ .

structure. Additionally, there is a good agreement between the measured center frequencies of operation of the FSS with those predicted using the analytical formulas presented in Section 9.2.3. This further highlights the importance of the understanding gained from the analysis presented in Section 9.2 in analyzing periodic structures with more complicated unit cells.

The sensitivity of the frequency response of the fabricated structure to the angle of incidence was also examined by measuring the transmission coefficient of the structure for various oblique angles of incidence for three folding angles. The measurements were carried out in the range of  $\theta_{inc} = 0^\circ - 60^\circ$  for both TE and TM polarizations of incidence and the results are shown in Fig. 9.13. These results demonstrate that the change in the resonant frequency of the structure (versus the folding angle) is rather insensitive to the incident angle and the polarization of incidence of the EM wave for incidence angles between  $0^\circ$  and  $60^\circ$ .

## 9.5 Discussion

We presented several approaches for using mechanical flexure to design tunable periodic structures with elementary inductive and capacitive responses. These included the overlapping and relative translation of multiple metallic structures, stretching/compression, and flexure or deformation. It was demonstrated that these tuning techniques can be used to control the surface impedances of inductive and capacitive reactive surfaces. A wide range of devices with different response types (e.g. frequency selective surfaces, lenses, and reflectarrays) can be designed by combining these elementary inductive and capacitive structures in single- or multi-layer structures. Such devices can be made tunable using the proposed mechanical tuning techniques. We also presented an example of such a device whose unit cell consists of the series combination of the elementary inductive and capacitive elements in a single layer. The device was fabricated on an accordion-like substrate that could be contracted or expanded mechanically. We demonstrated both theoretically and experimentally that the frequency response of this FSS can be tuned over a relatively large bandwidth. The experimental results were in good agreement with the results predicted by the analytical models developed for the tunable inductive and capacitive structures.

The analytical and experimental studies presented in this chapter demonstrate the capabilities that mechanical tuning techniques offer in developing large-scale tunable periodic structures. However, similar to any other idea that is at its infancy, significant research and development is needed to take the proposed ideas from these initial demonstration stage to the higher maturation level needed to make them ready for use in a real-life application. The practical challenges that one may

face in this process were also briefly discussed in Section 9.2. One advantage of these mechanical tuning techniques over electronic tuning techniques include the elimination of numerous electronic switches or varactors and their associated dc bias networks. This elimination also alleviates the thermal management of the aperture. Furthermore, mechanically-tunable periodic structures are expected to be capable of handling significantly higher power levels than their electronically-tunable counterparts as they do not use any nonlinear devices that can drastically limit the power handling capability of the device as demonstrated in [89]. In any practical application, however, these advantages must be carefully weighed against the additional complexity introduced by using mechanical movements in the structure as discussed in Section 9.2. Finally, one obvious disadvantage of the proposed technique over electronic tuning techniques is its slower tuning speed. However, the mechanical movements involved in the proposed techniques are generally small (in the order of half a unit cell dimension). Therefore, using electro-mechanical actuation mechanisms (e.g., piezoelectric devices, linear motors, etc.), reconfiguration rates of tens of Hertz or possibly greater are expected to be achievable.

## Chapter 10

# MAcro-Electro-Mechanical Systems (MÆEMS) Based Concept for Beam Steering in Reflectarray Antennas

### 10.1 Introduction

In recent years, there has been a growing interest in employing phased-array antennas in various applications ranging from satellite and airborne communications to radars and imaging systems. While a number of phased-array systems have been deployed, their extreme cost and complexity have limited their application only to the most expensive pieces of military hardware. Therefore, many systems that can potentially benefit from the capabilities offered by phased arrays are left behind [140]. Thus, new ideas for developing affordable phased arrays are needed to enable the widespread use of this technology. Beam steerable reflectarray antennas have been considered as a promising approach for realizing affordable phased arrays. Tuning approaches in the existing beam steering reflectarrays can be categorized into either feed switching techniques or element tuning techniques [182]. In the feed switching techniques, the spatial delay profile over the aperture can be tuned by displacement of the feed [101]. Although this technique is simple to implement, it does not provide a continuous beam scanning and requires multiple feed antennas to illuminate the aperture. Using multiple feed antennas can reduce the aperture efficiency of the system, due to aperture blockage, as the number of feeds increases. In the element tuning technique, on the other hand, a tunable phase shifting mechanism needs to be incorporated into each spatial phase shifting element on the aperture of the reflectarray to achieve beam steering. Various designs of element tuning techniques have been reported in the literature over the years.

Examples of these include using mechanically actuated patch antennas [183] or integrating varactors [184], micro-electromechanical systems (MEMS) switches [185], PIN diodes [186], and functional materials [83, 87, 88, 187–190] with the constituting elements of the aperture. The cost and complexity of the fabrication, reliability issues, and relatively low scanning rates are the primary challenges of the approach reported in [183]. Varactors and MEMS switches, on the other hand, offer faster scanning speed and have lower power consumption compared to the previous technique. However, reflectarray antennas that use such electronically tunable elements to achieve tunability suffer from several major problems. First and foremost, these structures suffer from limited power handling capability due to the nonlinearity of these electronically tunable devices. In [89], it was demonstrated that the phase shift provided by a tunable spatial phase shifter used in a typical reflect- or transmit-array employing BST or GaAs varactors would drastically change as the incident RF power level of it was increased from low to moderate power levels. This is a major factor that limits the use of electronically-reconfigurable reflectarrays to relatively low power applications. Moreover, a moderate-size electronically-tunable reflectarray may have hundreds to thousands of pixels that need to be tuned individually. Varactors need to be integrated with each pixel and must be appropriately biased. Often times, it is required to have RF/dc isolation mechanisms (e.g. dc block capacitors) integrated with the unit cell as well. These factors increase the cost and complexity of the design and control of the reflectarray. Additionally, the ohmic losses of the electronically-tunable elements as well as the bias line losses also deteriorate the radiation efficiency of the reflectarray and generate unwanted heat that needs to be dissipated, complicating the thermal managements of the aperture in high power applications. These issues are significantly exacerbated as we move from microwave frequencies to millimeter-wave (MMW) and sub-MMW frequencies. Functional materials including liquid crystals [187–189], ferroelectric dielectrics [83], photonically-controlled materials [190], and graphene [87, 88] have also been used to design beam steerable reflectarrays. While these technologies have certain advantages that make them interesting for particular applications, they are not as widely studied as other techniques and most of the demonstrations of these techniques have been done at the unit cell level as opposed to

the full size apertures. Therefore, more research and development is required to determine if these techniques are suitable to design large-scale reflectarray antenna apertures with tunable responses.

Over the past few years, innovative mechanical reconfiguration techniques have been used to overcome the aforementioned challenges of using electronic tuning and to achieve tuning in reflective and transmissive type apertures [89, 114, 160, 173, 174, 191, 192]. In [191], a reconfigurable beam steering reflector based on mechanical motion of a movable board with respect to a fixed board was presented. In the proposed structure, a mushroom-like high impedance surface is topped with rotating periodic arrangement of capacitive patches. As the top layer moves, the phase gradient over the aperture changes which consequently steers the reflecting beam. In-plane displacement of layers were also used to achieve tunability in the response of periodic arrangement of coupled split-ring resonators in [173, 174]. This tunability of the response could be used to change the phase gradient over the aperture and achieve beam steering. In [192], a tunable high impedance surface was achieved by changing the displacement between two layers. Liquid tuning of the responses of transmissive spatial phase shifters is examined in [89, 114]. In [175–177], stretching or folding of the layer were used to achieve reconfigurability in periodic structures. Finally, in [160], several techniques for designing large-scale tunable periodic structures are presented. One of these techniques is used to design a mechanically-tunable reflecting type spatial phase shifter. It was shown that tunability of the response can be achieved through flexure of the surface. Such tunable spatial phase shifter can be used to design beam steering reflectarrays.

In this chapter, we propose a new mechanical beam steering technique that exploits macro-scale mechanical movements over parts of a reflecting-type aperture to achieve beam steering [193]. Since we envision that these mechanical movements will ideally be performed using electro-mechanical actuators, we refer to this technique as MACRO-ELECTRO-MECHANICAL SYSTEMS (MÆEMS) based beam steering. Beam steering using this concept does not require the use of any solid state phase shifters, varactors, or switches. Consequently, the proposed technique is expected to address many of the shortcomings of electronically-tunable reflectarray antennas discussed earlier in this section and is expected to enable the development of affordable, high-power capable phased-array antennas. Moreover, the spatial phase shifters constituting the reflectarrays do not need to

be individually controlled. Rather, they are controlled collectively, over a macro scale, which significantly reduces the complexity of two dimensional (2D) beam steering in a reflectarray antenna. We present a design example where a MÆEMS-based tuning technique is applied to an aperture composed of reflecting type spatial phase shifters. This spatial phase shifter is the unit cell of a non-resonant sub-wavelength periodic structure similar to the one reported in [101]. The elements of such sub-wavelength periodic structures have been previously used in the design of reflectarrays [101], spatial filters [8,24,97,102], transmitarrays [14,15,100], and polarization converters [120]. Subsequently, the proposed tunable spatial phase shifters are used in the design of a beam steering reflective type aperture where only small tilting of the ground plane underneath the entire aperture is used to change the direction of the radiated beam in two dimensions. Finally, we discuss the fabrication and experimental characterization of a prototype of this MÆEMS-based reflective aperture.

## 10.2 MÆEMS-based Spatial Phase Shifters

Fig. 10.1(a) shows a reflecting-type spatial phase shifter of the type used in [101]. The structure is composed of an array of sub-wavelength capacitive patches separated from a ground plane with a thin dielectric substrate. To an incident electromagnetic wave, this surface acts as a resonator with the equivalent circuit model shown in Fig. 10.1(b). In this configuration, the patch array is modeled with a capacitor and the small separation between the patch and the ground plane is modeled with two short transmission line sections representing the dielectric substrate and the separation between the dielectric substrate and the ground plane. Assuming that  $t, h \ll \lambda$ , this short circuited transmission line has an inductive input impedance. Therefore, the structure shown in Fig. 10.1 can be modeled with a parallel  $LC$  resonator with the resonant frequency of  $\omega_0 = \frac{1}{\sqrt{LC}}$ . Far from the resonance frequency, this structure acts as a perfect electric conductor (PEC). Therefore, it reflects the wave with a  $\pm\pi$  phase shift. At resonance, the phase of the reflection coefficient is zero and the structure acts as a perfect magnetic conductor (PMC). Assuming that the structure is lossless, the magnitude of the reflection coefficient is always equal to 1. The capacitance and

inductance values of the equivalent circuit model shown in Fig. 10.1 can be calculated using the following formulas:

$$L_{total} = \frac{Z_0}{\omega} \left\{ \frac{1}{\sqrt{\varepsilon_r}} \tan(\omega \sqrt{\mu_0 \varepsilon_0 \varepsilon_r} t) + \tan(\omega \sqrt{\mu_0 \varepsilon_0} h) \right\} \quad (10.1)$$

$$C = \varepsilon_0 \varepsilon_{r,eff} \frac{2D}{\pi} \ln \left( \csc\left(\frac{\pi s}{2D}\right) \right) \quad (10.2)$$

where  $D$  is the dimension of the unit cell,  $s$  is the gap spacing between two adjacent patches,  $t$  is the thickness of the substrate on which the patches are etched,  $\varepsilon_r$  is the dielectric constant of the substrate, and  $h$  is the spacing between the ground plane and the bottom of the substrate. Also,  $\varepsilon_{r,eff}$  is the effective dielectric constant for the capacitive patch array,  $\omega$  is the operating frequency, and  $Z_0 = 377 \Omega$ . For the structure under discussion in this section,  $\varepsilon_{r,eff} \approx \frac{1+\varepsilon_r}{2}$ . To change the reflection phase at a certain fixed operating frequency, the resonant frequency of the effective  $LC$  resonator shown in Fig. 10.1 needs to be tuned. This can be done by tuning the inductance or the capacitance values of this structure. In the vast majority of periodic structures of this type the literature, the response tunability is achieved by tuning the capacitance values. In doing so, various techniques including loading of varactors and MEMS switches [33, 80, 184, 194, 195] and fluidic tuning [90] were employed. Unlike most previous studies, however, we propose to tune the response of this spatial phase shifter by changing its effective inductance as opposed to changing the capacitance values. We first reported this tuning technique in [193]. To change the inductance value, the separation between the ground plane and the capacitive patch layer can be changed as shown in Fig. 10.1(c). Therefore, the tuning parameter that controls the value of the inductance in this case is  $h$ . The inductance value continuously changes as the separation between the capacitive patches and the ground plane changes. This, however, does not significantly impact the value of the capacitance of the structure, since most of the fringing effects are negligible and most of the fields in the capacitive layer are confined in the gap region between adjacent capacitive patches. Thus, a continuous tuning can be performed without using any solid-state devices. Moreover, since the separation between the ground plane and the patch is sub-wavelength, only small movements of the ground plane are needed to change of the phase shift over a wide range.

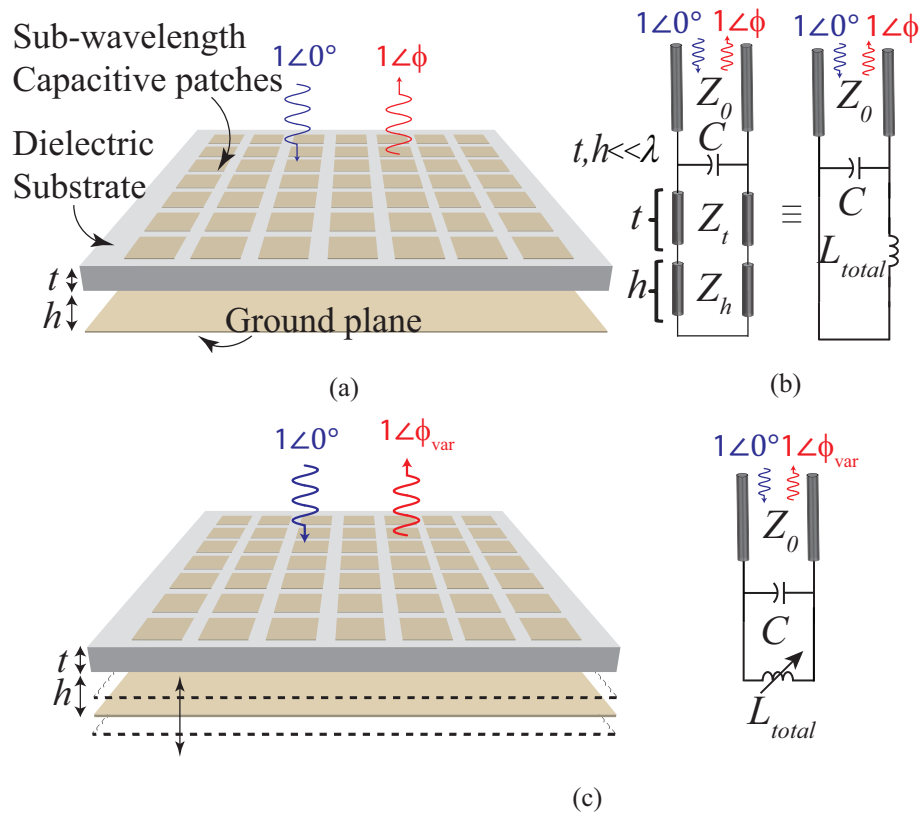


Figure 10.1 (a) Topology of a phase shifting surface composed of an array of sub-wavelength capacitive patches backed with a ground plane. Each unit cell of this phase shifting surface is considered to be a single spatial phase shifter. (b) The equivalent circuit model of the spatial phase shifter and the phase shifting surface shown in Fig. 10.1(a). (c) Topology of the MÆEMS-based phase shifting surface and its equivalent circuit model.

To demonstrate the capabilities of the proposed tuning technique, we examined a high-impedance surface designed to operate at 9.5 GHz. The design parameters for this structure are the dielectric constant and thickness of the substrates, the unit cell size, the gap spacing between patches, and the maximum variation of the spacing between ground plane and the bottom of the patch. The choice of the unit cell size is arbitrary as long as it is small compared to the wavelength. The needed resonant frequency scanning to achieve a fixed phase shift is smaller for a resonator with higher quality factor. However, increasing the quality factor of reduces the bandwidth of the structure. In our initial experiments, we focused on narrow-band operation around a single frequency (9.5 GHz) to demonstrate the fundamentals of beam steering using this concept. Therefore, a resonator with

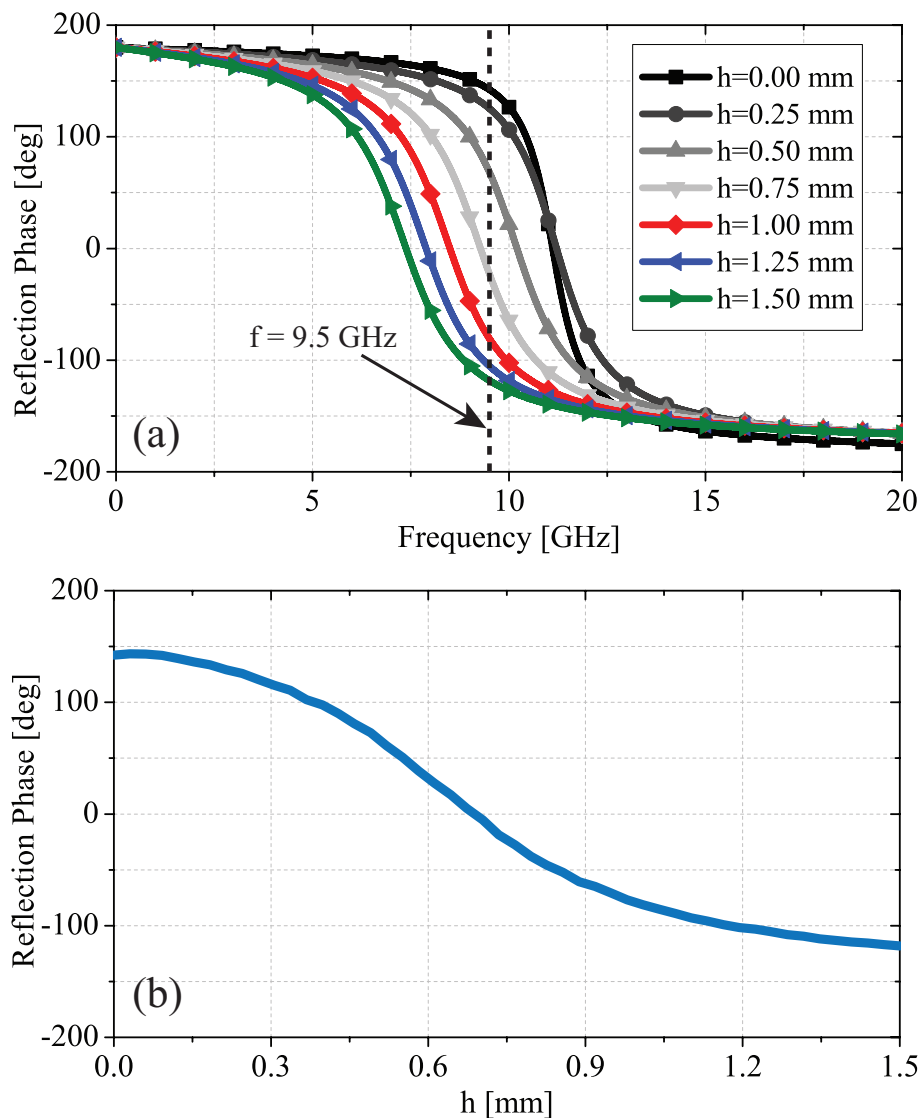


Figure 10.2 (a) The phase of the reflection coefficient of the spatial phase shifters discussed in Section 10.2 as a function of frequency and for different  $h$  values.  $h$  represents the separation between the ground plane and the bottom of the dielectric substrate on the top surface of which the two-dimensional array of sub-wavelength capacitive patches are printed. (b) The reflection phase of the SPS described in Section 10.2 at the operating frequency of 9.5 GHz as a function of the tuning parameter,  $h$ .

a moderate quality factor was chosen. In wideband applications, resonators with a higher-order response (e.g. using multiple capacitive patch layers) may be used in conjunction with similar tuning techniques. For a first-order parallel  $LC$  resonator, the quality factor is proportional to

$\sqrt{C/L}$ . Thus, to tune the response with minimized mechanical movements, a higher capacitance value and a smaller inductance value is needed. To achieve a higher capacitance, the gap spacing between the adjacent capacitive patches should be decreased for a fixed unit cell size,  $D$ , and relative permittivity of the substrate,  $\epsilon_r$ . Smaller inductance values can be achieved by using a thinner substrate. Then, considering all these values including the substrate characteristics and the gap spacing between patches are known *a priori*, the required variation range for the distance between the ground plane and the capacitive patch array can be calculated. The unit cell size in this example is  $D = 6.5$  mm or equivalently  $\approx 0.2\lambda_0$ , where  $\lambda_0$  is the free-space wavelength at the center frequency of operation. The dielectric constant and thickness of the substrate used in this design are  $\epsilon_r = 3.4$  (Rogers RO4003C) and 0.5 mm, respectively. The minimum gap spacing is limited by the fabrication technology. In this example, a relatively small gap spacing of  $s = 0.45$  mm, which can be reliably fabricated, is considered. Knowing all these parameters, the range of the ground plane movements needed to achieve the desired phase shift range can be obtained. The capacitance value can be calculated using (10.1). Using this value and knowing the center frequency of operation, the inductance value can be determined. Then,  $h$  can be calculated using (10.2). For the center frequency of 9.5 GHz,  $h$  is calculated to be 0.75 mm. Therefore, the range of variations for the spacing between ground plane and the substrate is considered to be 0-1.5 mm. Fig. 10.2(a) shows the reflection phase of the structure shown in Fig. 10.1 as a function of frequency for different values of  $h$ . As can be observed, for a fixed operating frequency (9.5 GHz), the reflection phase changes as the value of  $h$  is changed. Also, the reflection phase at 9.5 GHz as a function of the tuning parameter,  $h$ , is shown in Fig. 10.2(b). Observe that small movements of the ground plane with a maximum variation of 1.5 mm allow for changing the phase shift over a wide range of  $\approx 270^\circ$ . As discussed, to achieve a wider phase shift range using the same mechanical movements, a larger capacitance value in the equivalent circuit model is needed. The higher capacitance can be achieved by either reducing the gap spacings between the patches or using a dielectric substrate with a higher dielectric constant.

### 10.3 MÆEMS-Based Beam Steering

The unit cell of the spatial phase shifter discussed in Section 10.2 can be used in the design of MÆEMS-based beam-steerable reflectarrays. Fig. 10.3 shows the basics of beam steering in a MÆEMS-based reflector. The structure is composed of a planar uniform reflector surface illuminated by a feed antenna. The reflector's aperture is populated by identical spatial phase shifters that locally manipulate the phase of the reflected wave. In this structure, the ground plane backing the reflectarray can be tilted freely by small distances compared to the wavelength. In doing so, the other parts of the structure including the capacitive patch layer and its supporting dielectric substrate remain fixed and do not move. The tilting of the ground plane locally changes the resonant frequencies of the SPSs located at different points on the aperture. At a fixed operating frequency, this change in the resonant frequency of the SPSs changes the phase shift that each SPS provides. Therefore, the SPSs occupying different locations on the aperture can provide different phase shifts simply by tilting the ground plane underneath the structure while maintaining the remaining parts of the structure fixed. In the simplest form, if all SPSs are composed of capacitive patches with identical physical dimensions, the tilting of the ground-plane creates a phase shift gradient over the aperture of the reflectarray. This phase shift gradient determines the direction of maximum radiation (or the direction of main lobe of the radiation pattern) of the antenna in the far field. For an aperture with a linear phase gradient of  $\frac{\partial\phi}{\partial r}$ , where  $\phi$  is the phase of the reflection coefficient from the aperture, a normally incident wave will be reflected towards the angle of  $\theta = \pm \arcsin\left(\frac{\lambda}{2\pi} \frac{\partial\phi}{\partial r}\right)$ . By dynamically changing this phase shift gradient ( $\frac{\partial\phi}{\partial r}$ ) over the aperture of the reflector, the direction of maximum radiation can be changed dynamically and the scattered beam can be steered. The beam scanning range in this structure is a function of several factors. In a narrow-band application as is the case studied here, the range increases as the reflector's aperture dimension decreases or the maximum phase shift provided by the SPSs increases. For a single, first-order resonant spatial phase shifter of the type examined in this chapter, the maximum variation of the phase is less than  $2\pi$ . Therefore, the phase gradient in the extreme case can be approximated as  $\frac{\partial\phi}{\partial r} \approx \frac{2\pi}{D}$ , where  $D$  is the aperture dimension. For this case, the scanning range is limited in the range of  $\pm \arcsin\left(\frac{\lambda}{D}\right)$ .

The spatial phase shifters discussed in Section 10.2 are used to design a flat, non-focusing beam-steerable reflector. The surface is designed to operate at 9.5 GHz and has aperture dimensions of approximately  $5.6\lambda_0 \times 5.6\lambda_0$ . The reflecting surface is illuminated with a horn antenna placed at a distance of  $\approx 7\lambda_0$  away from it. The structure is fabricated on a 0.5-mm thick RO4003C substrate (from Rogers Corp.) with a dielectric constant of 3.4. In this embodiment, all of the capacitive patches are identical. Therefore, unlike a reflectarray antenna, this reflecting surface does not perform any collimation of the beam. Nevertheless, the beam steering concepts can be demonstrated equally well without having beam collimation. The ground plane is located underneath the substrate separated by 0.75 mm from the bottom of the substrate. Assuming that the ground plane is fixed at its center, it can be tilted up or down along this pivot point by a maximum distance of 1.5 mm. This tilting allows for achieving a phase shift gradient over the surface of the reflector along any desired direction. This way, two dimensional continuous beam scanning can be performed. Fig. 10.4(a) shows the phase profile over the aperture for three different ground plane tilts. For the first case (State A), the ground plane is fixed and not tilted. For the second and third cases (State B and State C), the ground plane is tilted by the maximum distance along either edge of the aperture to steer the beam in the  $x - z$  plane along  $+\hat{x}$  or  $-\hat{x}$ . Fig. 10.4(b) shows the simulated co-polarized normalized radiation patterns of this structure for these three cases. Observe that by tilting of the ground plane up or down by a maximum distance of 1.5 mm, the direction of the reflected beam can be steered in the range of  $\pm 10^\circ$ .

The beam scanning technique described in the previous paragraph relies on creating a phase shift gradient over the aperture by locally manipulating the resonant frequencies of its constituting spatial phase shifters. Because of the resonant nature of the structure, small shifts in the ground plane distance can cause significant changes in the resonant frequency of its spatial phase shifters. Consequently, large phase shift gradients can be achieved using this approach that cause a larger beam scanning field of view. In comparison, if one were to rotate the whole reflectarray structure (excluding its feed) and tilt it with the same maximum distance of 1.5 mm (or equivalently a rotation angle of  $\alpha \approx 1^\circ$ ), the beam steering would be only in the range of  $\pm 2^\circ$ . On the other hand, if the reflector surface is maintained and the feed is rotated by an angle of  $\pm 1^\circ$ , the maximum

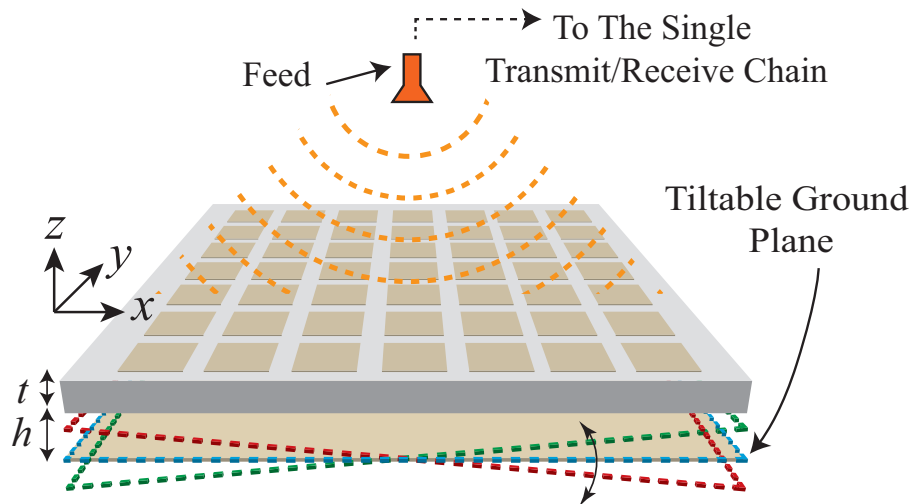


Figure 10.3 A possible implementation of a MÆMS-based beam-steerable reflectarray antenna. In this structure, the ground plane underneath the array of capacitive patches can be freely tilted in two dimensions along a pivot point located at its center. This locally changes the resonant frequencies of the spatial phase shifters occupying different locations in the aperture and the phase shift that they provide. The phase shift gradient created by this technique will determine the direction of the radiated beam in the far field. Using this approach the radiated beam can be steered in two dimensions using a single control variable.

beam scanning range that can be achieved is limited to  $\pm 1^\circ$ . Both of these scanning ranges are much smaller than the scanning range provide by tilting only the ground plane. This is due to the fact that neither of these two alternative techniques impact the resonant frequency of the SPSs occupying the aperture of the reflectarray. This  $\pm 10^\circ$  scanning range is in agreement with the predicted result in which  $\theta = 2 \arctan\left(\frac{\lambda}{2\pi} \frac{\partial\phi}{\partial r}\right)$  where  $\frac{\partial\phi}{\partial r} \approx \frac{2\pi}{5.6\lambda}$ . The transition within this range is not abrupt and the beam steers continuously as the ground plane tilts along the pivot point between state A and states B and C. The side lobe levels of the far field scattered pattern are generally above the expected values. This is mainly attributed to the aperture blockage caused by the feed antenna. The feed horn antenna used in the experiments has aperture dimensions of  $3.21\lambda_0 \times 2.76\lambda_0$ , which directly blocks the center part of the reflector's aperture. The issue of feed blockage can be resolved relatively easily by using offset feed to illuminate the reflector's aperture. Nonlinearity of the reflection phase as a function of displacement also contributes to enhance the level of side lobes.

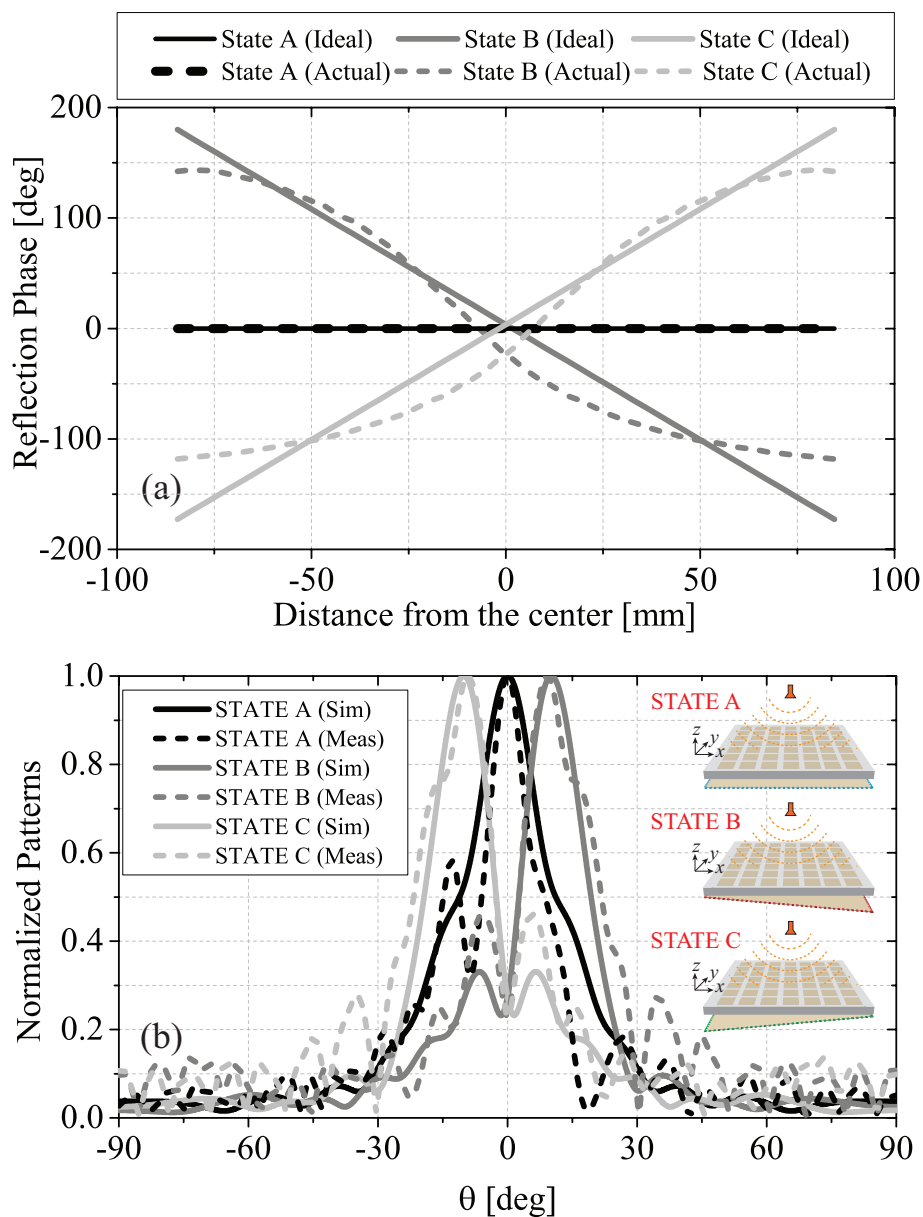


Figure 10.4 (a) Phase profile over the aperture for three cases where the ground plane is not-tilted and fully-tilted along the  $\hat{x}$  or the  $-\hat{x}$  axes. (b) Simulated and measured far field radiation patterns of the structure shown in Fig. 10.3 and described in Section 10.3 for the three tilting cases described earlier.

## 10.4 Experimental Results

An experimental prototype of the beam-steerable flat reflector surface analyzed in Section 10.3 was fabricated using standard PCB lithography. The prototype panel dimensions are 175.5 mm

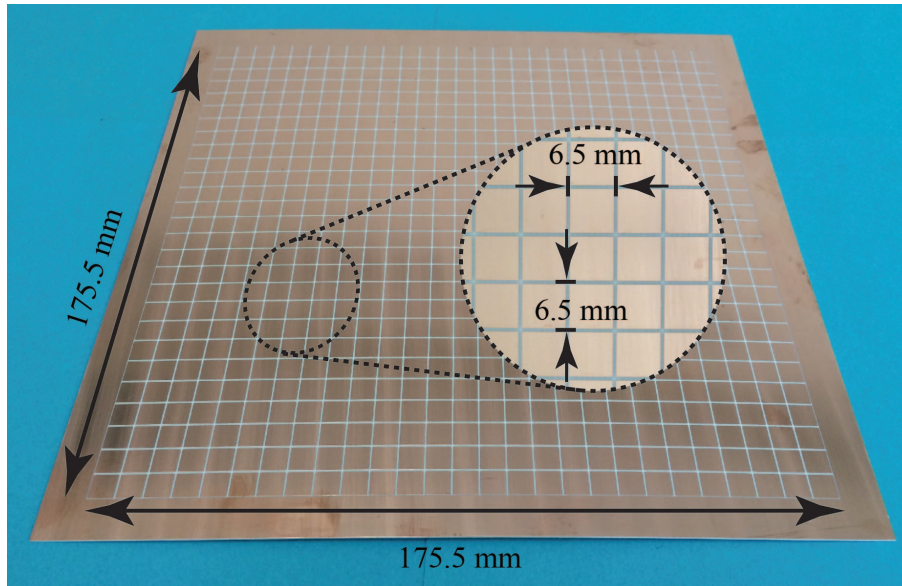


Figure 10.5 Photograph of the fabricated prototype.

× 175.5 mm. Fig. 10.5 shows the photograph of the fabricated prototype. The feed antenna is a commercial X-band horn antenna located on the optical axis of the structure at a distance of  $\approx 22$  cm from its center. For initial characterization, dielectric spacers were used to fix the separation between the ground plane and the substrate panel and the measurements were performed for a static prototype. To dynamically tilt the ground plane, these dielectric spacers can be replaced by spacers whose lengths can be electrically controlled (e.g. using piezoelectric actuators). Fig. 10.6 shows an illustration of a potential implementation of the structure with two-dimensional dynamic beam steering. In this structure, four piezoelectric actuators are placed at four corners of the reflecting surface and are employed to control the tilt angle of the ground plane. The displacement of each actuator from its idle position depends on the voltage applied to its two bias lines. When a positive voltage is applied, the actuator will displace in the positive  $z$ -axis and when a negative voltage is applied, the actuators will displace the same distance in position direction from its idle position. By controlling the voltage applied to each actuator, the desired tilt vector of the ground plane can be achieved. In this arrangement, two dimensional beam steering can be performed by simply controlling the heights of the piezoelectric actuators, which determines the tilt vector of the ground plane. Based on the maximum displacement provided by actuators, bending actuators appear to

be suitable for microwave frequencies (e.g. X-band) while stacked actuators are better options to be used at higher frequencies (e.g. MMW). Commercially-available bending actuators (e.g. [196]) provide maximum displacement of 2-3 mm with speeds up to few KHz. These characteristics make them a good candidate to be used in this design example.

The far-field scattering patterns of this structure were measured using a multi-probe spherical near-field system. For our static prototype, Fig. 10.4(b) shows the co-polarized normalized radiated fields from this structure at the center frequency of operation. In general, a good agreement is observed between the simulation and measurement results. Observe that the main beam is steered towards the expected direction by tilting the ground plane.

When all the parameters including the aperture dimensions, distance between feed and the aperture, and bandwidth are fixed, the scan range is only a function of the phase variation over the aperture. For a single resonant structure, the maximum variation of the phase is less than  $2\pi$ . This limits the scanning range of the structure. However, the scan range of the array can still be improved if minor modifications are made to the architecture of the array shown in Fig. 10.3. An effective method for enhancing the phase shift range over the aperture is to use multiple independently-controlled tiltable ground planes instead of the single tiltable ground plane. This way, a saw-tooth-shaped phase function over the aperture can be created. This broadens the achievable phase shift gradient over the aperture for given  $f$  and  $D$  parameters. However, since  $2\pi$  discontinuities created by the adjacent ground planes are required to achieve a monotonic phase function, the beam scanning is abrupt and the resulting structure can be used as a beam switching reflector. To demonstrate the capabilities offered by this new feature, the same flat reflector surface discussed in Section 10.3 is examined again but this time with three independently-controlled tiltable ground planes as shown in Fig. 10.7. Each ground plane can now be tilted freely up or down by a maximum distance of 1.5 mm. Fig. 10.8(a) shows the phase profile over the aperture for two states. For “State A”, all three ground planes are fixed and not tilted. For “State B”, all the ground planes are tilted by the maximum values to achieve beam-steering in  $x - z$  plane along  $+\hat{x}$ . Since the structure is symmetric, the state corresponding to “State C” of the structure with

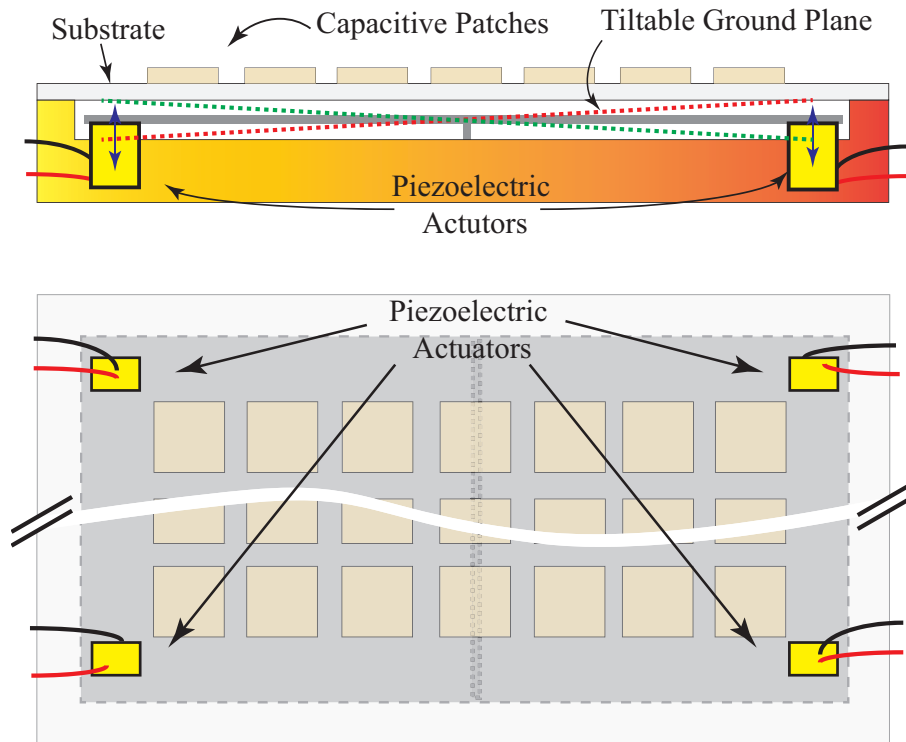


Figure 10.6 Illustration of a potential implementation of a MÆMS-based reflectarray antenna with dynamic beam steering. Four piezo-electric actuators are placed on the corners of the ground plane of the structure below the ground plane. By applying a DC bias voltage to each actuator, its height can be controlled. Changing the relative heights of the piezoelectric actuators allows for tilting the ground plane in any desired direction. This can be used to control the phase shift gradient vector over the aperture of the structure in the  $x - y$  plane and achieve the desired two-dimensional steering. Finally, placement of the actuators below the ground plane shields them from the incident antenna thereby ensuring that they do not impact the radiation patterns of the reflectarray antenna.

one ground plane scanning along in  $-\hat{x}$  is not shown for brevity. The simulated and measured co-polarized normalized radiation patterns of the reflector for both cases are shown in Fig. 10.8(b). As can be observed, using multiple independently-controlled ground planes successfully steers the beam to larger angles by increasing the range of phase gradient over the aperture. For the case of three ground planes tilted, the maximum reflection occurs at  $\pm 30^\circ$  when the aperture is illuminated under normal incidence. Other than nonlinearity of the reflection phase response as a function of displacement, the relatively high level of the side lobes here (compared to the case of single ground

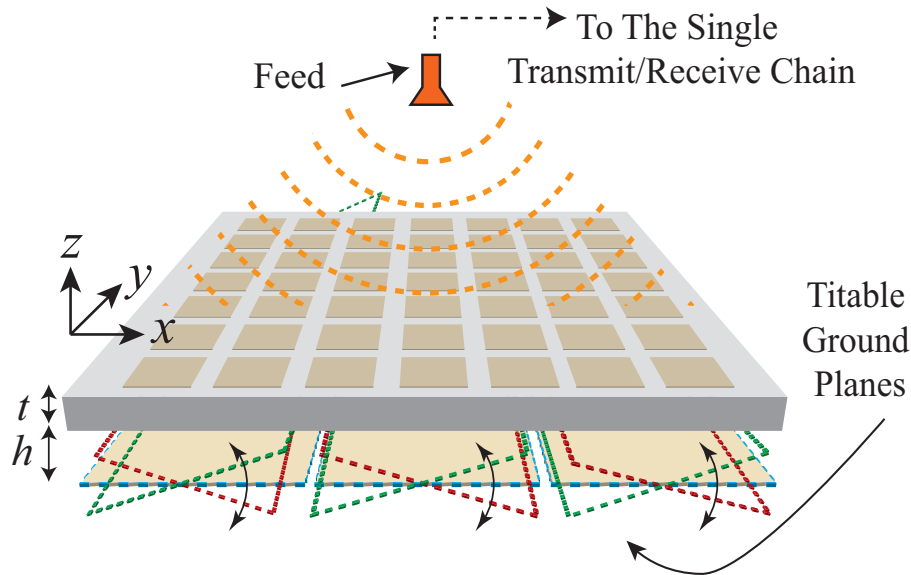


Figure 10.7 Topology of a MÆEMS based reflecting surface with a segmented ground plane. In this structure the continuous ground plane is replaced with three segments of independently controllable ground planes. This allows for creating phase wrapping over the aperture of the reflectarray and widening the beam scanning range of the structure.

plane) is mostly due to the imperfect  $2\pi$  phase discontinuities created by each two adjacent ground planes.

## 10.5 Discussion

We investigated a new approach for designing passive phased arrays based on electro-mechanical beam steering. We discussed a specific design where MÆEMS tuning techniques were applied to a planar, high-impedance surface (HIS) to achieve a beam-steerable flat reflector. We demonstrated that beam-scanning in this reflector can be achieved without the need for integrating individual electronic tuning elements with each unit cell of the structure. Rather, small, macro-scale mechanical movements of the ground plane of the high-impedance surface were exploited to achieve the same beam steering that would have been provided by integrating individual electronic tuning

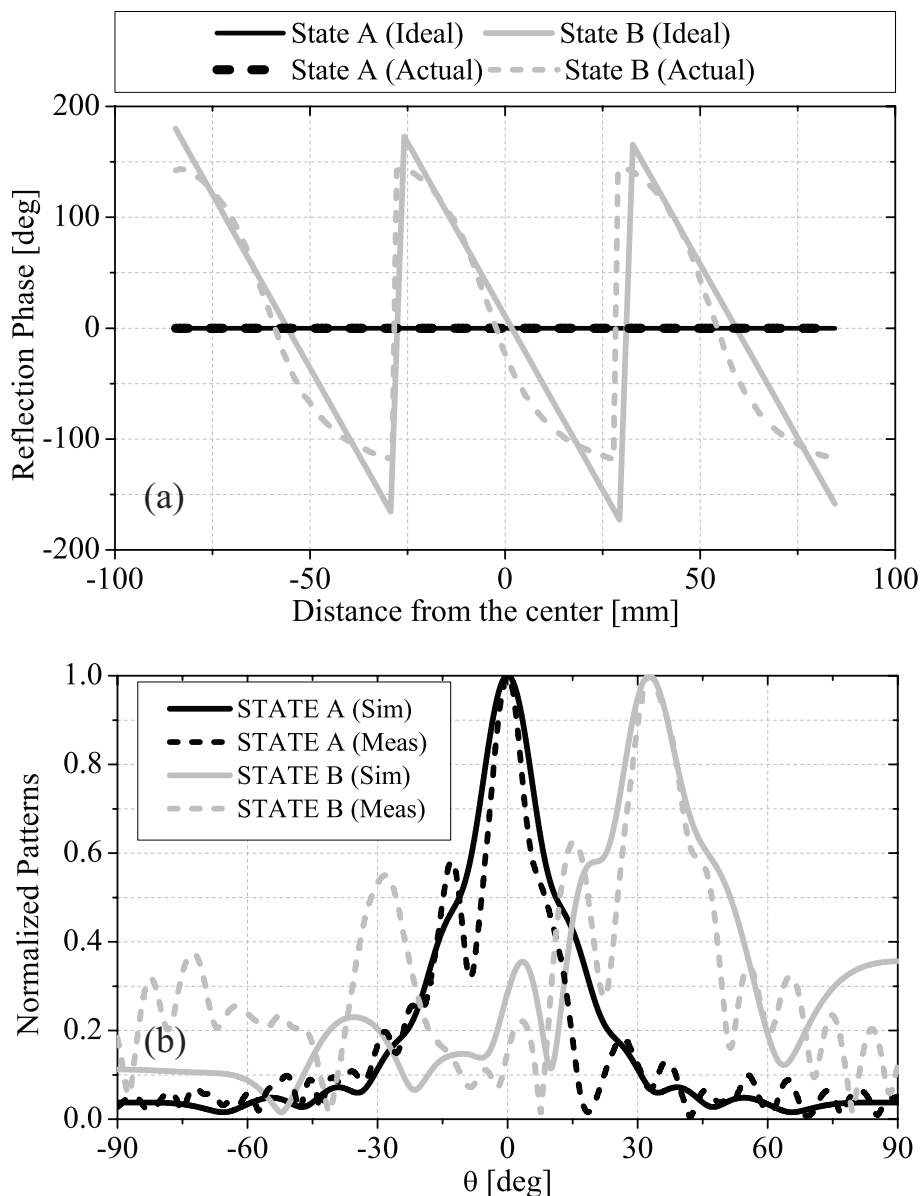


Figure 10.8 (a) Phase profiles over the aperture of the structure shown in Fig. 10.6 for the two cases where none of the three ground planes are tilted or all of them are tilted with the maximum values of tilt. (b) The simulated and measured far field patterns of the structure for these two different tilt conditions.

elements (e.g. varactors) with each unit cell of the HIS. If the proof-of-concept prototype structure demonstrated in this chapter was to be made tunable using varactors, 1458 varactors<sup>1</sup> would

<sup>1</sup>The structure has 27 unit cells in each direction and each unit cell needs two varactors to ensure dual-polarization operation. This results in a total of 1458 varactors.

have needed to be integrated with the unit cells of the structure and appropriately biased to achieve the same phase tuning and beam scanning range. In sharp contrast with this alternative electronic tuning technique, the proposed technique achieves two-dimensional beam steering by controlling significantly fewer variables. Namely, the tilt vector(s) of the ground plane (segmented ground planes). Moreover, unlike other mechanical beam steering techniques where the entire reflecting surface of a reflector (or a reflectarray) antenna and its feed are rotated to scan the beam, in the proposed technique most of the structure (including the feed horn and the capacitive patch array constituting the high-impedance surface) remains stationary and only the ground plane is moved by small distances.

This proposed concept is expected to make the task of designing large-scale tunable reflectarray and transmitarrays considerably simpler and more practical. Compared to their electronically-tunable counterparts, MÆMS-based reflect- and transmit-arrays have several unique advantages. These include the capability to handle significantly higher power levels, reduced design and control complexity, reduction of losses associated with electronic tuning elements, and ease of thermal management. These attributes are expected to make this technology a promising candidate for development of affordable phased-array antennas at microwave, millimeter-wave, and THz frequency bands. One area where electronically-tunable structures have an advantage over MÆMS-based structures is the tuning speed. However, because the mechanical movements involved in a MÆMS-based phased array are very small and the parts of the structure that need to be moved are light weight, mechanical movements are expected to be performed quite rapidly using commercially-available electro-mechanical actuators (e.g. piezoelectric actuators). While further research and development is needed before all practical issues involved in implementing phased-array antennas based on this technology are addressed, we expect MÆMS-based phased arrays to be capable of providing beam scanning speeds of at least several tens to several hundreds of Hertz<sup>2</sup>. Finally, we like to emphasize that the proof-of-concept structure demonstrated in this chapter was meant to demonstrate the feasibility of using the proposed concepts to perform passive beam steering. Several practical engineering issues regarding the implementation, actuation, and control of such

---

<sup>2</sup>This estimate is based on existing commercially-available electro-mechanical actuators.

structures need to be addressed before MÆMS-based phased arrays can be commercialized. Many of these issues, however, are addressed in the field of adaptive optics where optical devices (e.g. mirrors) are reconfigured using electro-mechanical actuation techniques similar to the ones that would be needed to be used by a MÆMS-based phased array antenna.

## **Chapter 11**

### **Future Work**

This dissertation work arose from the need to advance the current state-of-the-art in spatial filters, reflectarrays, and transmitarrays in order to satisfy the demands in both commercial and military sectors. To this end, each chapter of this dissertation was devoted to address one of the existing limitations in the design of these devices. For instance, two major challenges in the design of spatial filters were addressed in chapters 2 and 3. The new presented capabilities are highly desired in low-observable and stealth platforms. In chapters 4 and 5, new techniques for designing broadband polarization converters and polarization selective surfaces were introduced. These devices are key elements in many applications including satellite and point-to-point communications. In chapters 6 to 8, novel approaches in designing wideband true-time-delay reflectarrays and transmitarrays were presented. In addition to the wide-angle scanning performance, demonstrating wideband bandwidths and chromatic aberration free operation are the unique features of the proposed devices. These features are highly desired in applications where signals with intravenously broad bandwidths are used. Finally, in chapters 9 and 10, novel approaches for designing periodic structures with tunable frequency responses were presented. Affordable phased arrays, active camouflage skins offering adaptive stealth capabilities, and adaptive emissivity control against imagers are some of the applications expected to be enabled by this proposed technology. To continue the efforts undertaken in this dissertation, some ideas about the future work is listed in the following subsections.

## 11.1 Random Frequency Selective Surfaces

As discussed in chapter 2, the suppression of spurious harmonics of an FSS is highly desired in stealth applications since they can potentially lead to a significant large RCS at high frequencies. As also discussed in the same chapter, since these spurious passbands of the FSSs are generally caused by natural harmonics of their constituting elements, the studies in this area are commonly focused on reducing the unit cell size of the FSS and shifting these harmonics to considerably higher frequencies to achieve a wideband harmonic suppressed region. Using conventional printed circuit board (PCB) fabrication technology, however, there is a miniaturization level that can be reliably achieved. This issue makes it challenging to achieve harmonic-free operation over wide bandwidths using single-layer structures. Therefore, new approaches are needed to enable the suppression of harmonics as opposed to shift them to very high frequencies. One suggested solution is to use random frequency selective surfaces whose aperture is populated by numerous different resonant elements. These resonant structures share the same main transmission band while having vastly different spurious transmission windows. At the main transmission band, the FSS is transparent allowing the transmission of EM waves with little attenuation. At other frequencies, however, the random nature of the responses of elements causes the re-radiated fields of all the elements to interfere destructively, thereby significantly reducing the magnitude of the transmitted wave. This way, the transparency of the FSS at higher frequencies is substantially reduced over a very wide bandwidth and its spurious harmonics are suppressed. Fig. 11.1 shows a conceptual depiction of the proposed concept.

## 11.2 MÆMS-Based Beam Steering in Leaky-Wave Antennas

A major part of this dissertation was centered around high-gain antennas including transmitarrays and reflectarrays. In chapters 6, 7, and 8, the design of broadband transmitarrays and reflectarrays using non-resonant sub-wavelength periodic structures were presented. These antenna prototypes, however, were not tunable and had fixed beams only. In chapter 10, then, a new concept referred to as MÆMS-based beam steering were introduced to make these arrays tunable.

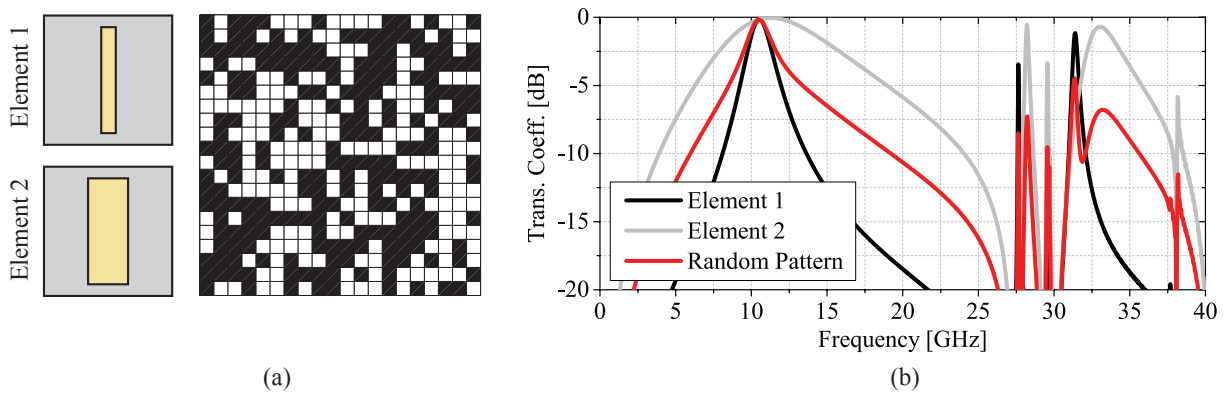


Figure 11.1 (a) A random frequency selective surface whose aperture is populated with two resonant slot elements. Black pixels represent “Element 1” and white pixels represent “Element 2”. (b) The frequency response of a frequency selective surface with pattern shown in Fig. 11.1(a). The transmission coefficient is compared with two cases in which the aperture is uniformly populated.

As discussed, the capabilities offered by these technologies are highly desired in many applications ranging from satellite communication to radars and imaging systems. However, a major practical problem with such arrays is the relatively high profile of their configurations due to their spatial feeding schemes. A potential solution to this issue is to use leaky-wave antennas instead of spatially-fed arrays. Leaky-wave antenna is a type of travelling-wave antennas for which no protruding feed is needed. In future studies, the applicability of the MÆMS-based techniques in the design of leaky-wave antennas with reconfigurable beams will be examined.

### 11.3 Infrared Spatial Filters and Lenses

As discussed in the earlier chapters, the focus of this dissertation was on the design of spatial filters, reflectarrays, and transmitarrays in the microwave domain. A potential research direction to continue these existing efforts is to extend these concepts to higher frequencies such as IR and MMW. For instance, IR filters are key devices in any astronomical instrument including telescopes. These devices reject the out-of-band radiation before reaching the detector. This way, they allow for reducing the noise level and improving the detection sensitivity. In recent years, long mid-infrared (LMIR) frequency range has attracted attention in astronomy since they allow

for observation of highly reddened sources as well as a wide variety of molecular and atomic features. The development of filters at this frequency window, however, has been hindered due to the practical issues. These include the need for high accuracy fabrication techniques in dielectric interference filters and robustness issues in air-gap metal mesh filters. One possible solution to this problem is to use the concept of inductively-coupled spatial filters introduced in chapter 3. Structural rigidity for a self-standing design and simple/low-cost fabrication techniques are some of the main advantages of the proposed filter that are well suited for space applications. Alternatively, another solution is to design reflecting-type spatial filters. These spatial filters are inspired by monochromators in Optics. The general operating mechanism of these devices is to reflect a selected narrowband of wavelengths of the incident wave to another chosen direction from a wider range of wavelengths in the incident waveform. This scheme eliminates the need for multilayer fabrications which are potentially challenging at IR and MMW frequencies.

Another niche area to continue the research efforts in this dissertation is to investigate the design of aberration free lenses at optical wavelengths. Chromatic aberration is an important phenomenon observed in most lenses operating at optical wavelengths. Overcoming this issue is necessary in various imaging systems ranging from conventional microscopy and photography to sophisticated astronomical spectroscopy and coherence tomography. The goal of the research activity in this area can be to use the concepts introduced in chapters 6, 7, and 8 to develop optical true-time-delay lenses free of any chromatic aberrations.

**DISCARD THIS PAGE**

## Appendix A: List of Publications

The work in this dissertation has been published in the following peer-reviewed journal papers and conference proceedings.

### A.1 Journal Papers

- [1] S. M. A. Momeni Hasan Abadi, M. Li, and N. Behdad, "Harmonic-suppressed miniaturized element frequency selective surfaces with higher order bandpass responses," *IEEE Trans. Antennas Propag.*, vol. 62, no. 5, pp. 2562-2571, May 2014.
- [2] S. M. A. Momeni Hasan Abadi and N. Behdad, "An electrically small, vertically polarized ultrawideband antenna with monopole-like radiation characteristics," *IEEE Antennas Wireless Propag. Lett.*, vol. 13, pp. 742-745, 2014.
- [3] S. M. A. Momeni Hasan Abadi and N. Behdad, "Design of wideband, FSS-based multi-beam antennas using the effective medium approach," *IEEE Trans. Antennas Propag.*, vol. 62, no. 11, pp. 5557-5564, Nov. 2014.
- [4] S. M. A. Momeni Hasan Abadi, K. Ghaemi, and N. Behdad, "Ultra-wideband, true-time-delay reflectarray antennas using ground-plane-backed, miniaturized-element frequency selective surfaces," *IEEE Trans. Antennas Propag.*, vol. 63, no. 2, pp. 534-542, Feb. 2015.
- [5] S. M. A. Momeni Hasan Abadi and N. Behdad, "Inductively-coupled miniaturized-element frequency selective surfaces with narrowband, high-order bandpass responses," *IEEE Trans. Antennas Propag.*, vol. 63, no. 11, Nov. 2015.
- [6] S. M. A. Momeni Hasan Abadi and N. Behdad, "Wideband linear-to-circular polarization converters based on miniaturized-element frequency selective surfaces," *IEEE Trans. Antennas Propag.*, vol. 64, no. 2, pp. 525-534, Feb. 2016.

- [7] S. M. A. Momeni Hasan Abadi and N. Behdad, "Exploiting mechanical flexure as a means of tuning the responses of large-scale periodic structures," *IEEE Trans. Antennas Propag.*, vol. 64, no. 3, pp. 933-943, Mar. 2016.
- [8] M. Gao, S. M. A. Momeni Hasan Abadi and N. Behdad, "A dual-band, inductively-coupled miniaturized element frequency selective surface with higher-order bandpass response," *IEEE Trans. Antennas Propag.*, vol. PP, no. 99, pp. 1-1, doi:10.1109/TAP.2016.2580181.
- [9] S. M. A. Momeni Hasan Abadi and N. Behdad, "A broadband, circular-polarization selective surface," *J. Appl. Phys.*, vol. 119, no. 24, pp. 244901, Jun. 2016.
- [10] S. M. A. Momeni Hasan Abadi and N. Behdad, "Broadband true-time-delay circularly-polarized reflectarray with linearly-polarized feed," *IEEE Trans. Antennas Propag.*, *IEEE Trans. Antennas Propag.*, vol. PP, no. 99, pp. 1-1, doi:10.1109/TAP.2016.2596900.
- [11] M. Gao, S. M. A. Momeni Hasan Abadi and N. Behdad, "A hybrid miniaturized-element frequency selective surface with a third-order bandpass response," *IEEE Antennas Wireless Propag. Lett.*, In press, Aug. 2016.
- [12] S. M. A. Momeni Hasan Abadi and N. Behdad, "MAcro-Electro-Mechanical Systems (MÆMS) based concept for beam steering in reflectarray antennas ", *J. Appl. Phys.*, vol. 120, no. 5, pp. 054901, Aug. 2016.

## **A.2 Conference Papers and Abstracts**

- [1] S. M. A. Momeni Hasan Abadi and N. Behdad, "True-time-delay UWB reflectarray with linear to circular polarization transformation," *IEEE International Symposium on Antennas and Propagation and USNC-URSI Radio Science Meeting (APS/URSI)*, Fajardo, Puerto Rico, Jun. 2016.
- [2] S. M. A. Momeni Hasan Abadi and N. Behdad, "Random frequency selective surfaces with harmonic suppressed frequency responses," *IEEE International Symposium on Antennas and*

- Propagation and USNC-URSI Radio Science Meeting (APS/URSI), Fajardo, Puerto Rico, Jun. 2016.
- [3] M. Gao, S. M. A. Momeni Hasan Abadi, and N. Behdad, "Dual-band miniaturized-element frequency selective surface with independently controllable transmission frequencies," IEEE International Symposium on Antennas and Propagation and USNC-URSI Radio Science Meeting (APS/URSI), Fajardo, Puerto Rico, Jun. 2016.
- [4] S. M. A. Momeni Hasan Abadi, J. H. Booske, and N. Behdad, "Macro Electro Mechanical Systems (MÆMS) based beam steering in reflectarray antennas," USNC-URSI National Radio Science Meeting, Boulder, CO, Jan. 2016.
- [5] S. M. A. Momeni Hasan Abadi and N. Behdad, "Wideband polarization converters based on miniaturized element frequency selective surfaces," won *Third Place Award* at CNC/USNC-URSI Radio Science Meeting, Vancouver, Canada, July 2015.
- [6] M. Gao, S. M. A. Momeni Hasan Abadi, J. H. Booske, and N. Behdad, "Low-cost phased-array antenna technology enabled by Macro-Electro-Mechanical Systems (MÆMS)," *Invited Talk* at IEEE International Symposium on Antennas and Propagation and USNC-URSI Radio Science Meeting (APS/URSI), Vancouver, Canada, July 2015.
- [7] S. M. A. Momeni Hasan Abadi, J. H. Booske, and N. Behdad, "Exploiting mechanical flexure to design tunable periodic structures," IEEE International Symposium on Antennas and Propagation and USNC-URSI Radio Science Meeting (APS/URSI), Vancouver, Canada, July 2015.
- [8] S. M. A. Momeni Hasan Abadi and N. Behdad, "Miniaturized-element frequency selective surfaces with narrowband, higher-order bandpass responses," IEEE International Symposium on Antennas and Propagation and USNC-URSI Radio Science Meeting (APS/URSI), Vancouver, Canada, July 2015.

- [9] S. M. A. Momeni Hasan Abadi and N. Behdad, "True-time-delay reflectarray and transmitarrays based on miniaturized element frequency selective surfaces," *Invited Talk* at The 9th European Conference on Antennas and Propagation (EuCAP 2015), Lisbon, Portugal, Apr. 2015.
- [10] S. M. A. Momeni Hasan Abadi and N. Behdad, "Design of lens-based, broadband multi-beam antenna apertures using effective medium theory approach," *Invited Talk* at International Conference on Electromagnetics in Advanced Applications (ICEAA), Palm Beach, Aruba, Aug 2014.
- [11] S. M. A. Momeni Hasan Abadi and N. Behdad, "Wideband multi-beam antenna apertures using metamaterial-based superstrates," won *Honorable Mention Award* at IEEE International Symposium on Antennas and Propagation and USNC-URSI Radio Science Meeting (APS/URSI), Memphis, TN, July 2014.
- [12] S. M. A. Momeni Hasan Abadi and N. Behdad, "A harmonic-suppressed miniaturized-element frequency selective surface with a second-order bandpass response," IEEE International Symposium on Antennas and Propagation and USNC-URSI Radio Science Meeting (APS/URSI), Memphis, TN, July 2014.
- [13] S. M. A. Momeni Hasan Abadi and N. Behdad, "A miniaturized, low-profile, omni-directional ultra-wideband antenna," IEEE International Symposium on Antennas and Propagation and USNC-URSI Radio Science Meeting (APS/URSI), Memphis, TN, July 2014.
- [14] S. M. A. Momeni Hasan Abadi, K. Ghaemi, and N. Behdad, "Ultra-wideband, true-time-delay, metamaterial-based reflectarray antenna," IEEE International Symposium on Antennas and Propagation and USNC-URSI Radio Science Meeting (APS/URSI), Memphis, TN, July 2014.
- [15] S. M. A. Momeni Hasan Abadi and N. Behdad, "Multi-beam antennas using planar lenses fed with focal plane arrays," IEEE International Symposium on Antennas and Propagation and USNC-URSI Radio Science Meeting (APS/URSI), Orlando, FL, July 2013.

- [16] S. M. A. Momeni Hasan Abadi and N. Behdad, "Harmonic-suppressed miniaturized-element frequency selective surfaces for low-observable antenna applications," IEEE International Symposium on Antennas and Propagation and USNC-URSI Radio Science Meeting (APS/URSI), Orlando, FL, July 2013.

## Appendix B: List of Acronyms

BST: Barium Strontium Titanate

CPSS: Circular-Polarization Selective Surface

EM: Electromagnetic

EQC: Equivalent Circuit Model

f/D ratio: Focal Length to Aperture Diameter Ratio

FDTD: Finite Difference Time Domain

FSS: Frequency Selective Surface

GaAs: Gallium Arsenide

HIS: High Impedance Surface

IR: Infrared

LHCP (RHCP): Left(Right)-Handed Circularly-Polarized

LH-CPSS (RH-CPSS): Left(Right)-Handed Circular-Polarization Selective Surface

MÆEMS: MAcro-Electro-Mechanical Systems

MEFSS: Miniaturized-Element Frequency Selective Surface

MEMS: Micro-Electro-Mechanical Systems

MMW: Millimeter-Wave

PCB: Printed Circuit Board

PEC (PMC): Perfect Electric (Magnetic) Conductor

PS: Periodic Structure

RCS: Radar Cross Section

SPS: Spatial Phase Shifter

SRR: Split-Ring Resonator

TDU: Time-Delay Unit

TE (TM): Transverse Electric (Magnetic)

TTD: True-Time-Delay

VNA: Vector Network Analyzer

## LIST OF REFERENCES

- [1] M. A. Al-Joumayly and N. Behdad, "A generalized method for synthesizing low-profile, band-pass frequency selective surfaces with non-resonant constituting elements," *IEEE Trans. Antennas Propag.*, vol. 58, pp. 4033–4041, Dec. 2010.
- [2] B. A. Munk, *Frequency Selective Surfaces: Theory and Design*. New York: Wiley- Interscience, 2001.
- [3] B. Monacelli, J. B. Pryor, B. A. Munk, D. Kotter, and G. D. Boreman, "Infrared frequency selective surface based on circuit-analog square loop design," *IEEE Trans. Antennas Propag.*, vol. 53, pp. 745–752, Feb. 2005.
- [4] J. A. Bossard, D. H. Werner, T. S. Mayer, J. A. Smith, Y. U. Tang, R. P. Drupp, and L. Li, "The design and fabrication of planar multiband metallodielectric frequency selective surfaces for infrared applications," *IEEE Trans. Antennas Propag.*, vol. 54, pp. 1265–1276, Apr. 2006.
- [5] G. I. Kiani, L. G. Olsson, A. Karlsson, and K. P. Esselle, "Transmission of infrared and visible wavelengths through energy-saving glass due to etching of frequency-selective surfaces," *IET Microw. Antennas Propag.*, vol. 4, pp. 955–961, July 2010.
- [6] A. Ebrahimi, S. Nirantar, W. Withayachumnankul, M. Bhaskaran, S. Sriram, S. F. Al-Sarawi, and D. Abbott, "Second-order terahertz bandpass frequency selective surface with miniaturized elements," *IEEE Trans. THz Sci. Technol.*, vol. 5, pp. 761–769, Sept. 2015.
- [7] C. Saeidi and D. van der Weide, "Nanoparticle array based optical frequency selective surfaces: theory and design," *Opt. Express*, vol. 21, p. 16170, July 2013.
- [8] N. Behdad, "A second-order band-pass frequency selective surface using nonresonant sub-wavelength periodic structures," *Microw. Opt. Technol. Lett.*, vol. 50, pp. 1639–1643, June 2008.
- [9] N. Engheta and R. Ziolkowski, *Metamaterials: physics and engineering explorations*. Wiley-IEEE Press, 2006.

- [10] N. Yu, P. Genevet, M. A. Kats, F. Aieta, J.-P. Tetienne, F. Capasso, and Z. Gaburro, "Light propagation with phase discontinuities: generalized laws of reflection and refraction," *Science*, vol. 334, pp. 333–337, Oct. 2011.
- [11] A. Monorchio, G. Manara, and L. Lanuzza, "Synthesis of artificial magnetic conductors by using multilayered frequency selective surfaces," *IEEE Antennas Wireless Propag. Lett.*, vol. 1, no. 1, pp. 196–199, 2002.
- [12] M. A. Hiranandani, A. B. Yakovlev, and A. A. Kishk, "Artificial magnetic conductors realised by frequency-selective surfaces on a grounded dielectric slab for antenna applications," *IEE Proc. Microw. Antennas Propag.*, vol. 153, pp. 487–493, Oct. 2006.
- [13] M. A. Al-Joumayly and N. Behdad, "Wideband planar microwave lenses using sub-wavelength spatial phase shifters," *IEEE Trans. Antennas Propag.*, vol. 59, pp. 4542–4552, Dec. 2011.
- [14] M. Li, M. A. Al-Joumayly, and N. Behdad, "Broadband true-time-delay microwave lenses based on miniaturized element frequency selective surfaces," *IEEE Trans. Antennas Propag.*, vol. 61, pp. 1166–1179, Mar. 2013.
- [15] M. Li and N. Behdad, "Wideband True-Time-Delay Microwave Lenses Based on Metallo-Dielectric and All-Dielectric Lowpass Frequency Selective Surfaces," *IEEE Trans. Antennas Propag.*, vol. 61, pp. 4109–4119, Aug. 2013.
- [16] J. A. Encinar, "Design of two-layer printed reflectarrays using patches of variable size," *IEEE Trans. Antennas Propag.*, vol. 49, pp. 1403–1410, Oct. 2001.
- [17] G. H. h. Sung, K. W. Sowerby, M. J. Neve, and A. G. Williamson, "A frequency-selective wall for interference reduction in wireless indoor environments," *IEEE Antennas Propag. Mag.*, vol. 48, pp. 29–37, Oct. 2006.
- [18] G. I. Kiani, K. L. Ford, L. G. Olsson, K. P. Esselle, and C. J. Panagamuwa, "Switchable frequency selective surface for reconfigurable electromagnetic architecture of buildings," *IEEE Trans. Antennas Propag.*, vol. 58, pp. 581–584, Feb. 2010.
- [19] K. Sarabandi and N. Behdad, "A frequency selective surface with miniaturized elements," *IEEE Trans. Antennas Propag.*, vol. 55, pp. 1239–1245, May 2007.
- [20] H. Liu, K. L. Ford, and R. J. Langley, "Miniaturised bandpass frequency selective surface with lumped components," *Electron. Lett.*, vol. 44, pp. 1054–1055, Aug. 2008.
- [21] F. Bayatpur and K. Sarabandi, "Multipole spatial filters using metamaterial-based miniaturized-element frequency-selective surfaces," *IEEE Trans. Microw. Theory Tech.*, vol. 56, pp. 2742–2747, Dec. 2008.

- [22] H. L. Liu, K. L. Ford, and R. J. Langley, "Design methodology for a miniaturized frequency selective surface using lumped reactive components," *IEEE Trans. Antennas Propag.*, vol. 57, pp. 2732–2738, Sept. 2009.
- [23] C. N. Chiu and K. P. Chang, "A novel miniaturized-element frequency selective surface having a stable resonance," *IEEE Antennas Wireless Propag. Lett.*, vol. 8, pp. 1175–1177, 2009.
- [24] N. Behdad and M. A. Al-Joumayly, "A generalized synthesis procedure for low-profile, frequency selective surfaces with odd-order bandpass responses," *IEEE Trans. Antennas Propag.*, vol. 58, pp. 2460–2464, July 2010.
- [25] G. Yang, T. Zhang, W. Li, and Q. Wu, "A novel stable miniaturized frequency selective surface," *IEEE Antennas Wireless Propag. Lett.*, vol. 9, pp. 1018–1021, 2010.
- [26] C. N. Chiu and W. Y. Wang, "A dual-frequency miniaturized-element fss with closely located resonances," *IEEE Antennas Wireless Propag. Lett.*, vol. 12, pp. 163–165, 2013.
- [27] F. Deng, X. Yi, and W. Wu, "Design and performance of a double-layer miniaturized-element frequency selective surface," *IEEE Antennas Wireless Propag. Lett.*, vol. 12, pp. 721–724, 2013.
- [28] R. Dubrovka, J. Vazquez, C. Parini, and D. Moore, "Equivalent circuit method for analysis and synthesis of frequency selective surfaces," *IEE Proc. Microw. Antennas Propag.*, vol. 153, pp. 213–220, June 2006.
- [29] R. J. Langley and E. A. Parker, "Equivalent circuit model for arrays of square loops," *Electron. Lett.*, vol. 18, pp. 294–296, Apr. 1982.
- [30] P. W. B. Au, L. S. Musa, E. A. Parker, and R. J. Langley, "Parametric study of tripole and tripole loop arrays as frequency selective surfaces," *IEE Proc. Microw. Antennas Propag.*, vol. 137, pp. 263–268, Oct. 1990.
- [31] A. Kondo, "Design and characteristics of ring-slot type FSS," *Electronics Letters*, vol. 27, no. 3, p. 240, 1991.
- [32] R. J. Langley and A. J. Drinkwater, "Improved empirical model for the Jerusalem cross," *Microwaves, Optics and Antennas, IEE Proceedings H*, vol. 129, pp. 1–6, Feb. 1982.
- [33] F. Bayatpur and K. Sarabandi, "Single-layer high-order miniaturized-element frequency-selective surfaces," *IEEE Trans. Microw. Theory Tech.*, vol. 56, pp. 774–781, Apr. 2008.
- [34] D. Lerner, "A wave polarization converter for circular polarization," *IEEE Trans. Antennas Propag.*, vol. 13, pp. 3–7, Jan. 1965.
- [35] L. Young, L. Robinson, and C. Hacking, "Meander-line polarizer," *IEEE Trans. Antennas Propag.*, vol. 21, pp. 376–378, May 1973.

- [36] M. A. Joyal and J. J. Laurin, "Analysis and design of thin circular polarizers based on meander lines," *IEEE Trans. Antennas Propag.*, vol. 60, pp. 3007–3011, June 2012.
- [37] M. Letizia, B. Fuchs, C. Zorraquino, J.-F. Zurcher, and J. R. Mosig, "Oblique incidence design of meander-line polarizers for dielectric lens antennas," *Progr. Electromagn. Res. B*, vol. 45, pp. 309–335, 2012.
- [38] E. Arnaud, R. Chantalat, M. Koubeissi, T. Monediere, E. Rodes, and M. Thevenot, "Global design of an ebg antenna and meander-line polarizer for circular polarization," *IEEE Antennas Wireless Propag. Lett.*, vol. 9, pp. 215–218, 2010.
- [39] G. Kiani and V. Dyadyuk, "Low loss FSS polarizer for 70 GHz applications," in *Proceedings of the 2012 IEEE International Symposium on Antennas and Propagation*, pp. 1–2, July 2012.
- [40] I. Sohail, Y. Ranga, K. P. Esselle, and S. G. Hay, "A linear to circular polarization converter based on Jerusalem-Cross frequency selective surface," in *2013 7th European Conference on Antennas and Propagation (EuCAP)*, pp. 2141–2143, Apr. 2013.
- [41] M. Euler, V. Fusco, R. Cahill, and R. Dickie, "Comparison of frequency-selective screen-based linear to circular split-ring polarisation convertors," *IET Microw. Antennas Propag.*, vol. 4, pp. 1764–1772, Nov. 2010.
- [42] M. Euler, V. Fusco, R. Cahill, and R. Dickie, "325 GHz single layer sub-millimeter wave fss based split slot ring linear to circular polarization convertor," *IEEE Trans. Antennas Propag.*, vol. 58, pp. 2457–2459, July 2010.
- [43] S. Yan and G. A. E. Vandenbosch, "Compact circular polarizer based on chiral twisted double split-ring resonator," *Appl. Phys. Lett.*, vol. 102, p. 103503, Mar. 2013.
- [44] M. Biscarini, G. M. Sardi, E. Martini, F. Caminita, and S. Maci, "A simple broadband fss polarizer," in *7th. Eur. Conf. Antennas Propag. (EuCAP2013)*, 2013.
- [45] L. Martinez-Lopez, J. Rodriguez-Cuevas, J. I. Martinez-Lopez, and A. E. Martynyuk, "A multilayer circular polarizer based on bisected split-ring frequency selective surfaces," *IEEE Antennas Wireless Propag. Lett.*, vol. 13, pp. 153–156, 2014.
- [46] S. Zhang, Y.-S. Park, J. Li, X. Lu, W. Zhang, and X. Zhang, "Negative refractive index in chiral metamaterials," *Phys. Rev. Lett.*, vol. 102, p. 023901, Jan. 2009.
- [47] S. Yan and G. A. Vandenbosch, "Chiral structure based on bilayered displaced U pair," *Europhy. Lett.*, vol. 103, no. 1, p. 18002, 2013.
- [48] M. Mutlu, A. E. Akosman, A. E. Serebryannikov, and E. Ozbay, "Asymmetric chiral metamaterial circular polarizer based on four U-shaped split ring resonators," *Opt Lett.*, vol. 36, p. 1653, May 2011.

- [49] R. Pierrot, "Reflector for circularly polarized waves," Mar. 1970.
- [50] G. A. Morin, "A simple circular polarization selective surface (CPSS)," in *Antennas and Propagation Society International Symposium, 1990. AP-S. Merging Technologies for the 90's. Digest.*, pp. 100–103 vol.1, May 1990.
- [51] V. F. Fusco and B. Nair, "Circular polarisation selective surface characterisation and advanced applications," *Antennas and Propagation IEE Proceedings - Microwaves*, vol. 153, pp. 247–252, June 2006.
- [52] I. Lopez and J. J. Laurin, "A circular polarization selective surface implemented on a flexible substrate," *IEEE Trans. Antennas Propag.*, vol. 62, pp. 3847–3852, July 2014.
- [53] W. V. Tilston, S. E. Tilston, M. Tilston, D. Tilston, and T. Tralman, "Polarization selective surface for circular polarization," Oct. 1991.
- [54] A. Ericsson and D. Sjberg, "A resonant circular polarization selective structure of closely spaced Morin helices," in *General Assembly and Scientific Symposium (URSI GASS), 2014 XXXIth URSI*, pp. 1–4, Aug. 2014.
- [55] I. Y. Tarn and S. J. Chung, "A new advance in circular polarization selective surface mdash;a three layered cpss without vertical conductive segments," *IEEE Trans. Antennas Propag.*, vol. 55, pp. 460–467, Feb. 2007.
- [56] J. Sanz-Fernndez, E. Saenz, and P. d. Maagt, "A circular polarization selective surface for space applications," *IEEE Trans. Antennas Propag.*, vol. 63, pp. 2460–2470, June 2015.
- [57] J. E. Roy, L. Shafai, and L. Shafai, "Reciprocal circular-polarization-selective surface," *IEEE Antennas Propag. Mag.*, vol. 38, pp. 18–33, Dec. 1996.
- [58] Y. Zhao, M. A. Belkin, and A. Al, "Twisted optical metamaterials for planarized ultrathin broadband circular polarizers," *Nat. Commun.*, vol. 3, p. 870, May 2012.
- [59] M. A. Joyal and J. J. Laurin, "Design and analysis of a cascade circular polarization selective surface at k band," *IEEE Trans. Antennas Propag.*, vol. 62, pp. 3043–3053, June 2014.
- [60] D. Sjberg and A. Ericsson, "A multi layer meander line circular polarization selective structure (MLML-CPSS)," in *The 8th European Conference on Antennas and Propagation (EuCAP 2014)*, pp. 464–468, Apr. 2014.
- [61] A. Abbaspour-Tamijani, K. Sarabandi, and G. M. Rebeiz, "A millimetre-wave bandpass filter-lens array," *IET Microw. Antennas Propag.*, vol. 1, pp. 388–395, Apr. 2007.
- [62] A. Abbaspour-Tamijani, K. Sarabandi, and G. M. Rebeiz, "Antenna-filter-antenna arrays as a class of bandpass frequency-selective surfaces," *IEEE Trans. Antennas Propag.*, vol. 52, pp. 1781–1789, Aug. 2004.

- [63] D. T. McGrath, "Slot coupled microstrip constrained lens," Feb. 1990.
- [64] D. McGrath, "Planar three-dimensional constrained lenses," *IEEE Trans. Antennas Propag.*, vol. 34, pp. 46–50, Jan. 1986.
- [65] M. Barba, E. Carrasco, and J. A. Encinar, "Suitable planar transmit-arrays in x-band," vol. 626, p. 533.1, Oct. 2006.
- [66] P. Padilla de la Torre and M. Sierra-Castaer, "Design and prototype of a 12-GHz transmit-array," *Microw. Opt. Technol. Lett.*, vol. 49, pp. 3020–3026, Dec. 2007.
- [67] R. H. Phillion and M. Okoniewski, "Lenses for circular polarization using planar arrays of rotated passive elements," *IEEE Trans. Antennas Propag.*, vol. 59, pp. 1217–1227, Apr. 2011.
- [68] Y. Zhou, S. Rondineau, D. Popovic, A. Sayeed, and Z. Popovic, "Virtual channel space-time processing with dual-polarization discrete lens antenna arrays," *IEEE Trans. Antennas Propag.*, vol. 53, pp. 2444–2455, Aug. 2005.
- [69] D. M. Pozar, "Flat lens antenna concept using aperture coupled microstrip patches," *Electron. Lett.*, vol. 32, pp. 2109–2111, Nov. 1996.
- [70] Y. Fan, B. L. Ooi, H. D. Hristov, and M. S. Leong, "Compound diffractive lens consisting of fresnel zone plate and frequency selective screen," *IEEE Trans. Antennas Propag.*, vol. 58, pp. 1842–1847, June 2010.
- [71] R. E. Munson, H. A. Haddad, and J. W. Hanlen, "Microstrip reflectarray for satellite communication and radar cross-section enhancement or reduction," Aug. 1987.
- [72] J. Huang, "Microstrip reflectarray," in *Antennas and Propagation Society International Symposium, 1991. AP-S. Digest*, pp. 612–615 vol.2, June 1991.
- [73] R. D. Javor, X.-D. Wu, and K. Chang, "Design and performance of a microstrip reflectarray antenna," *IEEE Trans. Antennas Propag.*, vol. 43, pp. 932–939, Sept. 1995.
- [74] D.-C. Chang and M.-C. Huang, "Multiple-polarization microstrip reflectarray antenna with high efficiency and low cross-polarization," *IEEE Trans. Antennas Propag.*, vol. 43, pp. 829–834, Aug. 1995.
- [75] D. M. Pozar and T. A. Metzler, "Analysis of a reflectarray antenna using microstrip patches of variable size," *Electron. Lett.*, vol. 29, pp. 657–658, Apr. 1993.
- [76] D. M. Pozar, S. D. Targonski, and H. D. Syrigos, "Design of millimeter wave microstrip reflectarrays," *IEEE Trans. Antennas Propag.*, vol. 45, pp. 287–296, Feb. 1997.

- [77] M. Bozzi, S. Germani, and L. Perregrini, "Performance comparison of different element shapes used in printed reflectarrays," *IEEE Trans. Antennas Propag.*, vol. 2, no. 1, pp. 219–222, 2003.
- [78] S. V. Hum, G. McFeetors, and M. Okoniewski, "Integrated mems reflectarray elements," in *2006 First European Conference on Antennas and Propagation*, pp. 1–6, Nov. 2006.
- [79] C. C. Cheng, B. Lakshminarayanan, and A. Abbaspour-Tamijani, "A programmable lens-array antenna with monolithically integrated mems switches," *IEEE Trans. Microw. Theory Tech.*, vol. 57, pp. 1874–1884, Aug. 2009.
- [80] C. Mias, "Varactor-tunable frequency selective surface with resistive-lumped-element biasing grids," *IEEE Microw. Compon. Lett.*, vol. 15, pp. 570–572, Sept. 2005.
- [81] F. Bayatpur and K. Sarabandi, "Tuning performance of metamaterial-based frequency selective surfaces," *IEEE Trans. Antennas Propag.*, vol. 57, pp. 590–592, Feb. 2009.
- [82] J. Y. Lau and S. V. Hum, "A planar reconfigurable aperture with lens and reflectarray modes of operation," *IEEE Trans. Antennas Propag.*, vol. 58, pp. 3547–3555, Dec. 2010.
- [83] J. B. L. Rao, D. P. Patel, and V. Krichevsky, "Voltage-controlled ferroelectric lens phased arrays," *IEEE Trans. Antennas Propag.*, vol. 47, pp. 458–468, Mar. 1999.
- [84] R. V. Petrov, R. Pandey, G. Srinivasan, and M. I. Bichurin, "A magnetic field controlled negative-index microwave lens," *Microw. Opt. Technol. Lett.*, vol. 50, pp. 2804–2807, Nov. 2008.
- [85] W. Hu, M. Y. Ismail, R. Cahill, H. S. Gamble, R. Dickie, V. F. Fusco, D. Linton, S. P. Rea, and N. Grant, "Tunable liquid crystal reflectarray patch element," *Electron. Lett.*, vol. 42, pp. 509–511, Apr. 2006.
- [86] H. Su, X. Liu, D. Li, X. Chen, R. S. Donnan, C. G. Parini, and T. Kreouzis, "Study of optically controlled active frequency selective surfaces with organic semiconductor," in *35th International Conference on Infrared, Millimeter, and Terahertz Waves*, pp. 1–2, Sept. 2010.
- [87] E. Carrasco, M. Tamagnone, and J. Perruisseau-Carrier, "Tunable graphene reflective cells for THz reflectarrays and generalized law of reflection," *Appl. Phys. Lett.*, vol. 102, p. 104103, Mar. 2013.
- [88] E. Carrasco, M. Tamagnone, J. R. Mosig, T. Low, and J. Perruisseau-Carrier, "Gate-controlled mid-infrared light bending with aperiodic graphene nanoribbons array," *Nanotechnology*, vol. 26, no. 13, p. 134002, 2015.
- [89] M. Li and N. Behdad, "Fluidically tunable frequency selective/phase shifting surfaces for high-power microwave applications," *IEEE Trans. Antennas Propag.*, vol. 60, pp. 2748–2759, June 2012.

- [90] T. Bhattacharjee, H. Jiang, and N. Behdad, "Large-scale fluidic tuning of subwavelength periodic structures," *IEEE Antennas Wireless Propag. Lett.*, vol. 14, pp. 190–193, 2015.
- [91] S. Chakravarty, R. Mittra, and N. R. Williams, "On the application of the microgenetic algorithm to the design of broad-band microwave absorbers comprising frequency-selective surfaces embedded in multilayered dielectric media," *IEEE Trans. Microw. Theory Tech.*, vol. 49, pp. 1050–1059, June 2001.
- [92] A. Fallahi, A. Yahaghi, H. R. Benedickter, H. Abiri, M. Shahabadi, and C. Hafner, "Thin wideband radar absorbers," *IEEE Trans. Antennas Propag.*, vol. 58, pp. 4051–4058, Dec. 2010.
- [93] W. S. Arceneaux, R. D. Akins, and W. B. May, "Absorptive/transmissive radome," Mar. 1995.
- [94] B. Li and Z. Shen, "Synthesis of quasi-elliptic bandpass frequency-selective surface using cascaded loop arrays," *IEEE Trans. Antennas Propag.*, vol. 61, pp. 3053–3059, June 2013.
- [95] F. Costa and A. Monorchio, "A frequency selective radome with wideband absorbing properties," *IEEE Trans. Antennas Propag.*, vol. 60, pp. 2740–2747, June 2012.
- [96] E. A. Parker and A. N. A. E. Sheikh, "Convolutd array elements and reduced size unit cells for frequency-selective surfaces," *IEE Proc. H (Microwaves, Antennas and Propagation)*, vol. 138, pp. 19–22, Feb. 1991.
- [97] M. Li and N. Behdad, "Frequency selective surfaces for pulsed high-power microwave applications," *IEEE Trans. Antennas Propag.*, vol. 61, pp. 677–687, Feb. 2013.
- [98] M. Al-Joumayly and N. Behdad, "A new technique for design of low-profile, second-order, bandpass frequency selective surfaces," *IEEE Trans. Antennas Propag.*, vol. 57, pp. 452–459, Feb. 2009.
- [99] O. Luukkonen, C. Simovski, G. Granet, G. Goussetis, D. Lioubtchenko, A. V. Raisanen, and S. A. Tretyakov, "Simple and accurate analytical model of planar grids and high-impedance surfaces comprising metal strips or patches," *IEEE Trans. Antennas Propag.*, vol. 56, pp. 1624–1632, June 2008.
- [100] S. M. A. M. H. Abadi and N. Behdad, "Design of wideband, fss-based multibeam antennas using the effective medium approach," *IEEE Trans. Antennas Propag.*, vol. 62, pp. 5557–5564, Nov. 2014.
- [101] S. M. A. M. H. Abadi, K. Ghaemi, and N. Behdad, "Ultra-wideband, true-time-delay reflectarray antennas using ground-plane-backed, miniaturized-element frequency selective surfaces," *IEEE Trans. Antennas Propag.*, vol. 63, pp. 534–542, Feb. 2015.

- [102] S. M. A. M. H. Abadi, M. Li, and N. Behdad, "Harmonic-suppressed miniaturized-element frequency selective surfaces with higher order bandpass responses," *IEEE Trans. Antennas Propag.*, vol. 62, pp. 2562–2571, May 2014.
- [103] N. Behdad, M. Al-Joumayly, and M. Salehi, "A low-profile third-order bandpass frequency selective surface," *IEEE Trans. Antennas Propag.*, vol. 57, pp. 460–466, Feb. 2009.
- [104] A. C. d. Lima and E. A. Parker, "Narrow bandpass single layer frequency selective surfaces," *Electron. Lett.*, vol. 29, pp. 710–711, Apr. 1993.
- [105] R. Pous and D. M. Pozar, "A frequency-selective surface using aperture-coupled microstrip patches," *IEEE Trans. Antennas Propag.*, vol. 39, pp. 1763–1769, Dec. 1991.
- [106] D. S. Lockyer and C. Vardaxoglou, "Reconfigurable FSS response from two layers of slotted dipole arrays," *Electron. Lett.*, vol. 32, pp. 512–513, Mar. 1996.
- [107] A. K. Rashid and Z. Shen, "A novel band-reject frequency selective surface with pseudo-elliptic response," *IEEE Trans. Antennas Propag.*, vol. 58, pp. 1220–1226, Apr. 2010.
- [108] G. Q. Luo, W. Hong, Q. H. Lai, K. Wu, and L. L. Sun, "Design and experimental verification of compact frequency-selective surface with quasi-elliptic bandpass response," *IEEE Trans. Microw. Theory Tech.*, vol. 55, pp. 2481–2487, Dec. 2007.
- [109] H. Zhou, S. Qu, Z. Pei, J. Zhang, B.-Q. Lin, J. Wang, H. Ma, C. Gu, Z. Xu, P. Bai, and others, "Narrowband frequency selective surface based on substrate integrated waveguide technology," *Progr. Electromagn. Res. B*, vol. 22, pp. 19–28, 2011.
- [110] G. L. Matthaei, L. Young, and E. M. Jones, "Design of microwave filters, impedance-matching networks, and coupling structures.," tech. rep., DTIC Document, 1963.
- [111] D. G. Swanson, "Narrow-band microwave filter design," *IEEE Microw. Mag.*, vol. 8, pp. 105–114, Oct. 2007.
- [112] R. R. Mansour, F. Huang, S. Fouladi, W. D. Yan, and M. Nasr, "High-q tunable filters: challenges and potential," *IEEE Microw. Mag.*, vol. 15, pp. 70–82, July 2014.
- [113] D. M. L. Vine and S. Abraham, "The effect of the ionosphere on remote sensing of sea surface salinity from space: absorption and emission at L band," *IEEE Trans. Geosci. Remote Sens.*, vol. 40, pp. 771–782, Apr. 2002.
- [114] M. Li, B. Yu, and N. Behdad, "Liquid-tunable frequency selective surfaces," *IEEE Microw. Compon. Lett.*, vol. 20, pp. 423–425, Aug. 2010.
- [115] S. M. A. M. H. Abadi and N. Behdad, "Inductively-coupled miniaturized-element frequency selective surfaces with narrowband, high-order bandpass responses," *IEEE Trans. Antennas Propag.*, vol. 63, pp. 4766–4774, Nov. 2015.

- [116] A. Edalati and K. Sarabandi, "Reflectarray antenna based on grounded loop-wire miniaturised-element frequency selective surfaces," *IET Microw. Antennas Propag.*, vol. 8, pp. 973–979, Sept. 2014.
- [117] C.-H. Liu and N. Behdad, "High-power microwave filters and frequency selective surfaces exploiting electromagnetic wave tunneling through -negative layers," *J. Appl. Phys.*, vol. 113, p. 064909, Feb. 2013.
- [118] G. Marconi and C. S. Franklin, "Reflector for use in wireless telegraphy and telephony," Apr. 1919.
- [119] M. A. Al-Joumayly and N. Behdad, "Low-profile, highly-selective, dual-band frequency selective surfaces with closely spaced bands of operation," *IEEE Trans. Antennas Propag.*, vol. 58, pp. 4042–4050, Dec. 2010.
- [120] S. M. A. M. H. Abadi and N. Behdad, "Wideband linear-to-circular polarization converters based on miniaturized-element frequency selective surfaces," *IEEE Trans. Antennas Propag.*, vol. 64, pp. 525–534, Feb. 2016.
- [121] X. Wu, G. V. Eleftheriades, and T. E. v. Deventer-Perkins, "Design and characterization of single- and multiple-beam mm-wave circularly polarized substrate lens antennas for wireless communications," *IEEE Trans. Microw. Theory Tech.*, vol. 49, pp. 431–441, Mar. 2001.
- [122] P. Chen, W. Hong, Z. Kuai, J. Xu, H. Wang, J. Chen, H. Tang, J. Zhou, and K. Wu, "A multibeam antenna based on substrate integrated waveguide technology for mimo wireless communications," *IEEE Trans. Antennas Propag.*, vol. 57, pp. 1813–1821, June 2009.
- [123] M. Barba, J. E. Page, J. A. Encinar, and J. R. Montejo-Garai, "A switchable multiple beam antenna for GSM-UMTS base stations in planar technology," *IEEE Trans. Antennas Propag.*, vol. 54, pp. 3087–3094, Nov. 2006.
- [124] B. Schoenlinner, X. Wu, J. P. Ebling, G. V. Eleftheriades, and G. M. Rebeiz, "Wide-scan spherical-lens antennas for automotive radars," *IEEE Trans. Microw. Theory Tech.*, vol. 50, pp. 2166–2175, Sept. 2002.
- [125] L. Schulwitz and A. Mortazawi, "A compact dual-polarized multibeam phased-array architecture for millimeter-wave radar," *IEEE Trans. Microw. Theory Tech.*, vol. 53, pp. 3588–3594, Nov. 2005.
- [126] A. K. Bhattacharyya, "Active Phased Array Antenna," in *Phased Array Antennas*, pp. 417–457, John Wiley & Sons, Inc., 2006.
- [127] A. K. Bhattacharyya, "Beam Forming Networks in Multiple-Beam Arrays," in *Phased Array Antennas*, pp. 379–416, John Wiley & Sons, Inc., 2006.
- [128] R. J. Mailloux, "Phased array antenna handbook," *Boston, MA: Artech House, 1994.*, 1994.

- [129] G. Bekefi and G. W. Farnell, "A homogeneous dielectric sphere as a microwave lens," *Can. J. Phys.*, vol. 34, pp. 790–803, Aug. 1956.
- [130] T. A. Rhys, "The design of radially symmetric lenses," *IEEE Trans. Antennas Propag.*, vol. 18, pp. 497–506, July 1970.
- [131] S.-W. Lee, M. S. Sheshadri, V. Jamnejad, and R. Mittra, "Refraction at a curved dielectric interface: geometrical optics solution," *IEEE Trans. Microw. Theory Tech.*, vol. 30, pp. 12–19, Jan. 1982.
- [132] D. N. Black and J. C. Wiltse, "Millimeter-wave characteristics of phase-correcting fresnel zone plates," *IEEE Trans. Microw. Theory Tech.*, vol. 35, pp. 1122–1129, Dec. 1987.
- [133] J. D. Kraus and R. J. Marhefka, "Lens Antennas," in *Antennas: For All Applications*, McGraw Hill, 3rd edition ed., 2001.
- [134] G. V. Trentini, "Partially reflecting sheet arrays," *IRE Trans. Antennas Propag.*, vol. 4, pp. 666–671, Oct. 1956.
- [135] L. Leger, T. Monediere, and B. Jecko, "Enhancement of gain and radiation bandwidth for a planar 1-D EBG antenna," *IEEE Microw. Compon. Lett.*, vol. 15, pp. 573–575, Sept. 2005.
- [136] D. R. Jackson and A. A. Oliner, "A leaky-wave analysis of the high-gain printed antenna configuration," *IEEE Trans. Antennas Propag.*, vol. 36, pp. 905–910, July 1988.
- [137] A. I. Zverev, *Handbook of filter synthesis*. Wiley-Interscience, New York, 1967.
- [138] N. G. Alexopoulos, C. A. Kyriazidou, and H. F. Contopanagos, "Effective parameters for metamorphic materials and metamaterials through a resonant inverse scattering approach," *IEEE Trans. Microw. Theory Tech.*, vol. 55, pp. 254–267, Feb. 2007.
- [139] E. Brookner, "Phased array radars-past, present and future," in *RADAR 2002*, pp. 104–113, Oct. 2002.
- [140] E. Brookner, "Phased-array radars: past, astounding breakthroughs and future trends.," *Microw. Journal*, vol. 51, no. 1, pp. 30–50, 2008.
- [141] D. M. Pozar, S. D. Targonski, and R. Pokuls, "A shaped-beam microstrip patch reflectarray," *IEEE Trans. Antennas Propag.*, vol. 47, pp. 1167–1173, July 1999.
- [142] J. A. Encinar and J. A. Zornoza, "Three-layer printed reflectarrays for contoured beam space applications," *IEEE Trans. Antennas Propag.*, vol. 52, pp. 1138–1148, May 2004.
- [143] J. A. Encinar, L. S. Datashvili, J. A. Zornoza, M. Arrebola, M. Sierra-Castaner, J. L. Besada-Sanmartin, H. Baier, and H. Legay, "Dual-polarization dual-coverage reflectarray for space applications," *IEEE Trans. Antennas Propag.*, vol. 54, pp. 2827–2837, Oct. 2006.

- [144] J. A. Encinar, M. Arrebola, L. F. d. I. Fuente, and G. Toso, "A transmit-receive reflectarray antenna for direct broadcast satellite applications," *IEEE Trans. Antennas Propag.*, vol. 59, pp. 3255–3264, Sept. 2011.
- [145] P. R. Herz and D. Sievenpiper, "Electronically tunable microwave reflector," Mar. 2012.
- [146] J. A. Encinar and J. A. Zornoza, "Broadband design of three-layer printed reflectarrays," *IEEE Trans. Antennas Propag.*, vol. 51, pp. 1662–1664, July 2003.
- [147] N. Misran, R. Cahill, and V. F. Fusco, "Design optimisation of ring elements for broadband reflectarray antennas," *IEE Proc. Microw. Antennas Propag.*, vol. 150, pp. 440–444, Dec. 2003.
- [148] S. Dieter, C. Fischer, and W. Menzel, "Single-layer unit cells with optimized phase angle behavior," in *2009 3rd European Conference on Antennas and Propagation*, pp. 1149–1153, Mar. 2009.
- [149] M. R. Chaharmir, J. Shaker, M. Cuhaci, and A. Ittipiboon, "Broadband reflectarray antenna with double cross loops," *Electron. Lett.*, vol. 42, pp. 65–66, Jan. 2006.
- [150] P. D. Vita, A. Freni, G. L. Dassano, P. Pirinoli, and R. E. Zich, "Broadband element for high-gain single-layer printed reflectarray antenna," *Electron. Lett.*, vol. 43, Nov. 2007.
- [151] S. R. Rengarajan, "Reflectarrays of rectangular microstrip patches for dual-polarization dual-beam radar interferometers," *Progr. Electromagn. Res. B*, vol. 133, pp. 1–15, 2013.
- [152] H. Legay, D. Bresciani, E. Labiole, R. Chiniard, and R. Gillard, "A multi facets composite panel reflectarray antenna for a space contoured beam antenna in Ku band," *Progr. Electromagn. Res. B*, vol. 54, pp. 1–26, 2013.
- [153] E. Carrasco, J. A. Encinar, and M. Barba, "Bandwidth improvement in large reflectarrays by using true-time delay," *IEEE Trans. Antennas Propag.*, vol. 56, pp. 2496–2503, Aug. 2008.
- [154] D. M. Pozar, "Wideband reflectarrays using artificial impedance surfaces," *Electron. Lett.*, vol. 43, pp. 148–149, Feb. 2007.
- [155] P. Nayeri, F. Yang, and A. Z. Elsherbeni, "Broadband reflectarray antennas using double-layer subwavelength patch elements," *IEEE Antennas Wireless Propag. Lett.*, vol. 9, pp. 1139–1142, 2010.
- [156] A. Edalati and K. Sarabandi, "Wideband reflectarray antenna based on miniaturized element frequency selective surfaces," in *2012 6th European Conference on Antennas and Propagation (EUCAP)*, pp. 362–364, Mar. 2012.
- [157] D. Lamensdorf and L. Susman, "Baseband-pulse-antenna techniques," *IEEE Antennas Propag. Mag.*, vol. 36, pp. 20–30, Feb. 1994.

- [158] G. Quintero, J. F. Zurcher, and A. K. Skrivervik, "System fidelity factor: a new method for comparing uwb antennas," *IEEE Trans. Antennas Propag.*, vol. 59, pp. 2502–2512, July 2011.
- [159] E. Carrasco, M. Barba, and J. A. Encinar, "X-band reflectarray antenna with switching-beam using pin diodes and gathered elements," *IEEE Trans. Antennas Propag.*, vol. 60, pp. 5700–5708, Dec. 2012.
- [160] S. M. A. M. H. Abadi, J. H. Booske, and N. Behdad, "Exploiting mechanical flexure as a means of tuning the responses of large-scale periodic structures," *IEEE Trans. Antennas Propag.*, vol. 64, pp. 933–943, Mar. 2016.
- [161] C. Han and K. Chang, "Ka-band reflectarray using ring elements," *Electron. Lett.*, vol. 39, pp. 491–493, Mar. 2003.
- [162] B. Strassner, C. Han, and K. Chang, "Circularly polarized reflectarray with microstrip ring elements having variable rotation angles," *IEEE Trans. Antennas Propag.*, vol. 52, pp. 1122–1125, Apr. 2004.
- [163] A. Yu, F. Yang, A. Z. Elsherbeni, and J. Huang, "An X-band circularly polarized reflectarray using split square ring elements and the modified element rotation technique," in *2008 IEEE Antennas and Propagation Society International Symposium*, pp. 1–4, July 2008.
- [164] A. Yu, F. Yang, A. Z. Elsherbeni, and J. Huang, "Design and measurement of a circularly polarized Ka-band reflectarray antenna," in *2009 3rd European Conference on Antennas and Propagation*, pp. 2769–2773, Mar. 2009.
- [165] M. Y. Zhao, G. Q. Zhang, X. Lei, J. M. Wu, and J. Y. Shang, "Design of new single-layer multiple-resonance broadband circularly polarized reflectarrays," *IEEE Antennas Wireless Propag. Lett.*, vol. 12, pp. 356–359, 2013.
- [166] L. S. Ren, Y. C. Jiao, F. Li, J. J. Zhao, and G. Zhao, "A dual-layer T-shaped element for broadband circularly polarized reflectarray with linearly polarized feed," *IEEE Antennas Wireless Propag. Lett.*, vol. 10, pp. 407–410, 2011.
- [167] M. Albooyeh, N. Komjani, and M. S. Mahani, "A circularly polarized element for reflectarray antennas," *IEEE Antennas Wireless Propag. Lett.*, vol. 8, pp. 319–322, 2009.
- [168] M. R. Chaharmir, J. Shaker, M. Cuhaci, and A. Sebak, "Circularly polarised reflectarray with cross-slot of varying arms on ground plane," *Electron. Lett.*, vol. 38, pp. 1492–1493, Nov. 2002.
- [169] Z. H. Wu, W. X. Zhang, Z. G. Liu, and W. Shen, "Circularly polarised reflectarray with linearly polarised feed," *Electron. Lett.*, vol. 41, pp. 387–388, Mar. 2005.

- [170] G. Zhao, Y. C. Jiao, F. Zhang, and F. S. Zhang, "A subwavelength element for broadband circularly polarized reflectarrays," *IEEE Antennas Wireless Propag. Lett.*, vol. 9, pp. 330–333, 2010.
- [171] L. Guo, P. K. Tan, and T. H. Chio, "A simple method to realize polarization diversity in broadband reflectarrays using single-layered rectangular patch elements," in *2015 IEEE International Symposium on Antennas and Propagation USNC/URSI National Radio Science Meeting*, pp. 2161–2162, July 2015.
- [172] V. M. Shalaev, "Optical negative-index metamaterials," *Nat. Photon.*, vol. 1, pp. 41–48, Jan. 2007.
- [173] E. Ekmekci, A. C. Strikwerda, K. Fan, G. Keiser, X. Zhang, G. Turhan-Sayan, and R. D. Averitt, "Frequency tunable terahertz metamaterials using broadside coupled split-ring resonators," *Phys. Rev. B*, vol. 83, p. 193103, May 2011.
- [174] M. Lapine, D. Powell, M. Gorkunov, I. Shadrivov, R. Marquardt, and Y. Kivshar, "Structural tunability in metamaterials," *Appl. Phys. Lett.*, vol. 95, p. 084105, Aug. 2009.
- [175] K. Fuchi, A. R. Diaz, E. J. Rothwell, R. O. Ouedraogo, and J. Tang, "An origami tunable metamaterial," *J. Appl. Phys.*, vol. 111, p. 084905, Apr. 2012.
- [176] J. Li, C. M. Shah, W. Withayachumnankul, B. S.-Y. Ung, A. Mitchell, S. Sriram, M. Bhaskaran, S. Chang, and D. Abbott, "Flexible terahertz metamaterials for dual-axis strain sensing," *Opt. Lett.*, vol. 38, pp. 2104–2106, June 2013.
- [177] K. Fuchi, J. Tang, B. Crowgey, A. R. Diaz, E. J. Rothwell, and R. O. Ouedraogo, "Origami tunable frequency selective surfaces," *IEEE Antennas Wireless Propag. Lett.*, vol. 11, pp. 473–475, 2012.
- [178] S. N. Azemi, K. Ghorbani, and W. S. T. Rowe, "Mechanically tunable and reconfigurable FSS using spring loaded ring resonators," in *Microwave Conference (EuMC), 2013 European*, pp. 932–935, Oct. 2013.
- [179] S. Tretyakov, *Analytical modeling in applied electromagnetics*. Artech House, 2003.
- [180] M. Kubo, X. Li, C. Kim, M. Hashimoto, B. J. Wiley, D. Ham, and G. M. Whitesides, "Stretchable microfluidic radiofrequency antennas," *Adv. Mater.*, vol. 22, pp. 2749–2752, July 2010.
- [181] J. A. Fan, W.-H. Yeo, Y. Su, Y. Hattori, W. Lee, S.-Y. Jung, Y. Zhang, Z. Liu, H. Cheng, L. Falgout, M. Bajema, T. Coleman, D. Gregoire, R. J. Larsen, Y. Huang, and J. A. Rogers, "Fractal design concepts for stretchable electronics," *Nat. Commun.*, vol. 5, p. 3266, Feb. 2014.

- [182] P. Nayeri, F. Yang, and A. Z. Elsherbeni, "Beam-scanning reflectarray antennas: a technical overview and state of the art.," *IEEE Antennas Propag. Mag.*, vol. 57, pp. 32–47, Aug. 2015.
- [183] J. P. Gianvittorio and Y. Rahmat-Samii, "Reconfigurable patch antennas for steerable reflectarray applications," *IEEE Trans. Antennas Propag.*, vol. 54, pp. 1388–1392, May 2006.
- [184] D. F. Sievenpiper, J. H. Schaffner, H. J. Song, R. Y. Loo, and G. Tangonan, "Two-dimensional beam steering using an electrically tunable impedance surface," *IEEE Trans. Antennas Propag.*, vol. 51, pp. 2713–2722, Oct. 2003.
- [185] H. Legay, B. Pinte, M. Charrier, A. Ziaei, E. Girard, and R. Gillard, "A steerable reflectarray antenna with MEMS controls," in *IEEE International Symposium on Phased Array Systems and Technology, 2003*, pp. 494–499, Oct. 2003.
- [186] H. Kamoda, T. Iwasaki, J. Tsumochi, and T. Kuki, "60-GHz electrically reconfigurable reflectarray using p-i-n diode," in *Microwave Symposium Digest, 2009. MTT '09. IEEE MTT-S International*, pp. 1177–1180, June 2009.
- [187] W. Hu, R. Cahill, J. A. Encinar, R. Dickie, H. Gamble, V. Fusco, and N. Grant, "Design and measurement of reconfigurable millimeter wave reflectarray cells with nematic liquid crystal," *IEEE Trans. Antennas Propag.*, vol. 56, pp. 3112–3117, Oct. 2008.
- [188] G. Perez-Palomino, M. Barba, J. A. Encinar, R. Cahill, R. Dickie, P. Baine, and M. Bain, "Design and demonstration of an electronically scanned reflectarray antenna at 100 GHz using multiresonant cells based on liquid crystals," *IEEE Trans. Antennas Propag.*, vol. 63, pp. 3722–3727, Aug. 2015.
- [189] S. Bildik, S. Dieter, C. Fritsch, W. Menzel, and R. Jakoby, "Reconfigurable folded reflectarray antenna based upon liquid crystal technology," *IEEE Trans. Antennas Propag.*, vol. 63, pp. 122–132, Jan. 2015.
- [190] M. R. Chaharmir, J. Shaker, M. Cuhaci, and A. R. Sebak, "Novel photonically-controlled reflectarray antenna," *IEEE Trans. Antennas Propag.*, vol. 54, pp. 1134–1141, Apr. 2006.
- [191] D. Sievenpiper, J. Schaffner, R. Loo, G. Tangonan, S. Ontiveros, and R. Harold, "A tunable impedance surface performing as a reconfigurable beam steering reflector," *IEEE Trans. Antennas Propag.*, vol. 50, pp. 384–390, Mar. 2002.
- [192] M. Mavridou, K. Konstantinidis, and A. P. Feresidis, "Continuously Tunable mm-Wave High Impedance Surface," *IEEE Antennas Wireless Propag. Lett.*, vol. 15, pp. 1390–1393, 2016.
- [193] M. Gao, A. Momeni, J. H. Booske, and N. Behdad, "Low-cost phased-array antenna technology enabled by MAcro-Electro-Mechanical Systems (MAEMS)," in *Radio Science Meeting (Joint with AP-S Symposium), 2015 USNC-URSI*, pp. 331–331, July 2015.

- [194] F. Costa, A. Monorchio, S. Talarico, and F. M. Valeri, "An active high-impedance surface for low-profile tunable and steerable antennas," *IEEE Antennas Wireless Propag. Lett.*, vol. 7, pp. 676–680, 2008.
- [195] D. Chicherin, M. Sterner, J. Oberhammer, S. Dudorov, J. berg, and A. V. Rinsen, "Analog type millimeter wave phase shifters based on MEMS tunable high-impedance surface in rectangular metal waveguide," in *Microwave Symposium Digest (MTT), 2010 IEEE MTT-S International*, pp. 61–64, May 2010.
- [196] "Steminc Piezo, <http://www.steminc.com/piezo/SMBA4510t05m.asp>."